NSLS-II Project

PRELIMINARY DESIGN REPORT for the

HARD X-RAY NANOPROBE (HXN) BEAMLINE

First Draft September 2010

Intentionally blank.

Approvals and Reviewers

Compiled by	**Signature**	**Date**
Dr. Yong Chu, Beamline Scientist		
Approved		
Qun Shen, XFD Director, NSLS-II		
Reviewers		
Dr. Ismail Cev Noyan, BAT Spokesperson, signing on behalf of the BAT		
Andy Broadbent, Beamlines Manager		
Nicholas Gmür, ESH Coordinator, NSLS-II		
Sushil Sharma, Mechanical Engineering Group Leader, NSLS-II		

Document Updates

The Preliminary Design Report for the HXN beamline at NSLS-II is a controlled document, revised under change control.

Version No.	Date	Changes made
A	9/01/2010	Initial draft
1		Final draft, submitted to BAT

Acknowledgment

Compiling the preliminary design report for the Hard X-ray Nanoprobe Beamline was an extensive task, requiring significant technical support not only from the HXN group members but also from the external contributors. I would like to extend special thanks to many contributors:

- Larry Margulies: for sharing responsibility for designing the beamline. For establishing specifications and requirements for beamline components, compiling control requirements and contributing to section 2. Also, for meticulously proofreading the PDR.
- Steve O'Hara: for providing mechanical engineering support for the beamline design and producing 3D models and drawings, working closely with Brian Mullany. And, for writing most of section 5.
- Brian Mullany: for proving drafting support and producing beamline drawings by working closely with Steve. Also, completing Bremsstrahlung and synchrotron ray tracing.
- Evgueni Nazaretski: for leading the NSLS-II nanopositioning R&D and developing a conceptual design of the compact MLL module. And, for writing a significant part of section 3 describing the HXN microscope and section 4.
- Deming Shu (Argonne National Laboratory): for actively collaborating with the HXN team on developing the HXN microscope, for developing flexure-based stages and conceptual design of several modules for the HXN microscope, and for providing his expertise on various nanopositioning challenges. And for writing a part of section 3.
- Hanfei Yan: for performing calculations for MLLs and Be CRLs, providing theoretical basis for the optimized application of the MLL optics for the HXN beamline, and engaging in numerous discussions on the optical scheme. And for writing section 3.2 and Appendix 3 and providing useful discussion on various calculations in the PDR.
- Ray Conley: for leading the development of the MLL optics fabrication at NSLS-II and collaborating on determining the target specifications for the HXN nanofocusing optics. And for writing Appendix 4.
- Ken Evans-Lutterodt: for leading the CD2 and early conceptual design of the HXN beamline and for developing of Si kinoform lens. And for writing a section on the Si kinoform lens.
- Andy Broadbent: for managing all interactions between the HXN team and the rest of the NSLS-II, working closely with the beamline scientists and mechanical engineers, and playing a critical role in conceptual design of the HXN Satellite Building.
- Nickolas Simos: for performing numerous simulations and measurements the NSLS-II ring and the HXN Satellite Building and for actively participating in the conceptual and architectural design of the HXN Satellite Building. And for writing Appendix 5.
- Oleg Chubar: for calculating all aspects of the NSLS-II undulator properties and performances, and for performing partially-coherent wavefront propagation calculations for the HXN beamline. And for writing Appendix 6.
- Viswanath Ravindranath: for performing finite element analysis for high heat load optics for the HXN beamline.
- Ove Dyling: for coordinating all aspects of architectural and engineering design of the HXN Satellite Building and for leading the construction of the HXN Satellite Building. And for supplying all the Satellite Building drawings for the PDR.
- Scott Mowat (FMB-Oxford): for providing extensive details on the current and near-future capabilities of FMB-Oxford and advising on achievable specifications for the beamline optics and components. And for providing a 3D model for the HXN beamline in section 2.8.3.
- Paul Murray (IDT): for providing detailed technical discussions on the beamline components developed by IDT and for providing finite element analysis using the realistic boundary conditions for the HXN high heat load optics.
- Ricccardo Signorato (Bruker): for providing useful discussion on the current and near-future capabilities of Bruker.
- Kathleen Robinson: for meticulous proofreading and document design of the HXN PDR. And for teaching me many advanced formatting techniques.

Yong S. Chu, Hard X-ray Nanoprobe Beamline Group Leader

Contents

1 INTRODUCTION 1

1.1 SCIENTIFIC REQUIREMENTS 1
1.2 THE HXN TEAM 3
1.3 BEAMLINE ADVISORY TEAM (BAT) 5

2 BEAMLINE LAYOUT 6

2.1 OVERVIEW 6
2.2 INSERTION DEVICE 6
2.3 FRONT END (FE) 12
2.4 OPTICAL CONCEPT 15
2.5 OPTICAL LAYOUT 19
2.6 HIGH HEATLOAD OPTICS 21
2.7 MONOCHROMATIC BEAM OPTICS 37
2.8 LIST OF MAJOR COMPONENTS 43
2.9 SHADOW RAY TRACING 53
2.10 PERFORMANCE ESTIMATE 58

3 ENDSTATION INSTRUMENTATION 63

3.1 OVERVIEW 63
3.2 OPTIMIZED USE OF MLL OPTICS 64
3.3 PRELIMINARY DESIGN OF THE MICROSCOPE 67
3.4 LASER ENCODER SYSTEM 71
3.5 HIGH-STIFFNESS WEAK-LINK BASE STAGES 73
3.6 MLL MODULE 74
3.7 ZP MODULE 77
3.8 SAMPLE MODULES 77
3.9 SUMMARY AND TIMELINE FOR THE DEVELOPMENT OF THE HXN MICROSCOPE 78
3.10 DETECTORS 79

4 SATELLITE BUILDING FOR THE HXN BEAMLINE 82

4.1 OVERVIEW 82
4.2 TECHNICAL REQUIREMENTS AND SPECIFICATIONS 82
4.3 ARCHITECTURAL AND ENGINEERING DESIGN OF THE SATELLITE BUILDING 84

5 INFRASTRUCTURE FOR BEAMLINE AND USER SUPPORT 96

5.1 ENCLOSURES 96
5.2 ENVIRONMENTAL CONSIDERATIONS 99
5.3 SURVEYING REQUIREMENTS 99
5.4 VACUUM SYSTEM 99
5.5 UTILITIES REQUIREMENTS 100
5.6 CONTROL REQUIREMENTS 103

6 SPECIAL BEAMLINE REQUIREMENTS 105

7 SAFETY 105

8 FUTURE UPGRADE OPTIONS 105

8.1 HIGH-RESOLUTION MODE 105
8.2 VERTICAL FOCUSING USING X-RAY MIRRORS 105
8.3 PIXEL ARRAY DETECTOR FOR NANODIFFRACTION 106
8.4 DEVELOPMENT OF X-RAY MICROSCOPY CAPABILITY AT 1~10 NM 106
8.5 DEVELOPMENT OF VARIABLE TEMPERATURE CONTROL FOR THE HXN MICROSCOPE 107

APPENDIX 1: SCHEDULE 108

APPENDIX 2: REFERENCE DRAWINGS 109

APPENDIX 3: MULTILAYER LAUE LENS (MLL) 124

APPENDIX 4: MLL FABRICATION CAPABILITIES 126

APPENDIX 5: VIBRATION STABILITY CONSIDERATIONS 128

APPENDIX 6: PARTIALLY-COHERENT WAVEFRONT PROPAGATION CALCULATIONS FOR THE HARD X-RAY NANOPROBE BEAMLINE 137

Acronyms

ANL	Argonne National Laboratory
APS	Advanced Photon Source
AS	Australian Synchrotron
BAT	Beamline Advisory Team
BLW	Bellows
BMPS	Bending Magnet Photon Shutter
BNL	Brookhaven National Laboratory
BP	Beampipe
BPM	Beam Position Monitor
BRS	Bremsstrahlung Stop
bw	Band Width
CCD	Charge-Coupled Device
CDI	Coherent Diffractive Imaging
CDR	Conceptual Design Report
CFN	Center for Functional Nanomaterials
CMOS	Complementary Metal-Oxide Semiconductor
CNM	Center for Nanoscale Materials
CO	Collimator
CRL	Compound Refractive Lens
CVD	Chemical Vapor Deposition
DCM	Double Crystal Monochromator
DI	De-Ionized
DPC	Differential Phase Contrast
dr_N	Outmost zone width for MLL or ZP
DW	Damping Wiggler
ESRF	European Synchrotron Radiation Facility
FAM	Fixed Aperture Mask
FE	Front End
FEA	Finite Element Analysis
FGV	Fast Gate Valve
FLSM	Fluorescent Screen, Mono
FLSW	Fluorescent Screen, White
FLT	Filter
FOE	First Optical Enclosure
fMLL	Flat Multilayer Laue Lens
FWHM	Full Width at Half Maximum
GV	Gate Valve
HCM	Horizontal Collimating Mirror
HFM	Horizontal Focusing Mirror
HVAC	Heating, Ventilation, & Air Conditioning
HXN	Hard X-ray Nanoprobe
ID	Insertion Device
IP	Incidence Power
IVU	In-vacuum Undulator
IVU20	In-vacuum Undulator with 20mm period
LOB	Lab Office Building
LOI	Letter of Intent
MLL	Multilayer Laue Lens
MOM	MLL Optic Module
MOU	Memorandum of Understanding
MSK	Mask
MSKnFE	Mask, Front End *number 'n'*
NA	Numerical Aperture
NSLS	National Synchrotron Light Source
NSLS-II	National Synchrotron Light Source II
OSA	Order Sorting Aperture
PAD	Pixel Array Detector
PDR	Preliminary Design Report
PLC	Programmable Logic Controllers
PPS	Personnel Protection System
PSH	Photon Shutter
PZT	Piezoelectric Transducer
QBPM	Quad Diode and Screen Monitor
RCO	Ratchet Wall Collimator
RMS	Root Mean Squared
RSI	Requirements, Specifications, and Interfaces
SAM1D	Sample Module for 1-axis Diffraction
SAM3D	Sample Module for 3-axis Diffraction
SAMF	Sample Module for X-ray Fluorescence
SDD	Silicon Drift Diode
SEM	Scanning Electron Microscopy
SGV	Slow Gate Valve
SLT	Slits
SLTnFE	Slits, Front End *number 'n'*
SR	Storage Ring
SSA	Secondary Source Aperture
SSH	Safety Shutter
UHV	Ultra-High Vacuum
UR	Undulator Radiation
VC	Vibration Criteria
wMLL	Wedged Multilayer Laue Lens
WBS	White Beam Stop
WIN	Be Window
XBPM	X-ray Beam Position Monitor (Front End)
XRD	X-ray Diffraction
XRF	X-ray Fluorescence
ZOM	Zone Plate Optic Module
ZP	(X-ray) Zone Plate

Coordinate Conventions

Beam Direction	Unless otherwise noted x-ray beam travel from right to left in all drawings.	
Coordinate System	X-axis	Outboard of the beam direction
	Y-axis	Vertical
	Z-axis	Along the beam

1 INTRODUCTION

1.1 Scientific requirements

The hard x-ray nanoprobe beamline and endstation instruments (HXN) are designed to explore new frontiers of hard x-ray microscopy applications with the highest achievable spatial resolution. Currently the available spatial resolution for scientific applications, provided by scanning x-ray microscopes in the hard x-ray regime, is limited to ~30nm [1.1.1], which is still insufficient for probing many nanoscale interfacial structures critical in determining properties and functionalities of material and biological systems. The HXN beamline aims to enable x-ray experiments at spatial resolutions ranging from 30 nm to its ultimate goal of ~1 nm. The proposed range of the spatial resolution will effectively bridge the current gap between x-ray microscopy and electron microscopy, opening up new scientific opportunities. Weak interaction of x-rays with matter enables probing buried structures sufficiently under the surface or under realistic sample environments. In addition, the measurements can be quantified using a kinematical approximation, without the necessity to account for multiple scattering effects. The ability to adjust the spatial resolution between 1 nm and 100 nm is crucial in studying how structural hierarchy is related to the functional properties of materials. This relationship between hierarchical structure and properties exist in nearly all classes of materials, from simple metal alloys to complex biological systems, and the ability to investigate nanoscale structures is critical to furthering the development of the next generation of technological materials. In order to achieve this unprecedented spatial resolution and sensitivity, the HXN beamline and endstation instruments will be designed as a scanning microscope, taking full advantage of the high brightness offered by the NSLS-II lattice.

The letter of intent (LOI) for the HXN beamline elaborated four key modalities of x-ray microscopy, which have been fully endorsed by the HXN Beamline Advisory Team as well as the Experimental Facilities Advisory Committee and DOE review panels. These are:

- x-ray fluorescence and nanodiffraction as main techniques
- coherent diffraction imaging and differential phase-contrast imaging as supporting techniques

Photon-stimulated x-ray fluorescence offers one of the most sensitive ways to detect the presence of specific atomic elements embedded within a hosting matrix. The proposed x-ray energy range of the HXN beamline, 6-25 keV, enables detection of most of the elements in the periodic table through the fluorescence process induced by K or L-edge excitation. The ability to detect extremely low quantities of isolated atoms or small clusters of atoms is extremely important in understanding how small concentration of impurities in semiconducting or condensed materials affects electronic, magnetic, or catalytic properties of the hosting matrix. In addition, the ability to image and quantify trace metal distribution in cells and tissues is extremely important in understanding metal-mediated biological processes, including understanding many diseases and the development of therapeutic and diagnostic agents to treat them.

Diffraction is an essential structural tool to quantify crystalline phase, strain, orientation, and texture. At the atomic level, virtually all hard materials organize themselves in crystalline form at varying length scales when thermally annealed, and the spatial arrangement of the crystalline grains and grain boundaries can profoundly influence the material properties. Unlike the x-ray fluorescence process, the diffraction process channels the incident x-rays into well-defined directions, thereby providing high measurement efficiency without collecting signals over a large solid angle. Virtually all nanodiffraction investigation requires simultaneous measurement of the x-ray fluorescence signal in order to validate the positioning accuracy of the probe and quantify the structural environment around the crystalline phase. Consequently, x-ray fluorescence and nanodiffraction are complementary tools, extremely valuable for nanoscale structural characterization of hard materials.

Coherent diffraction imaging is a powerful and fast-growing technique, with its ultimate spatial resolution limited only by the wavelength of the x-ray. There are several varieties of this imaging modality, classified by the type of sample (crystalline vs. noncrystalline) and the details on how the reconstruction is carried out. All types of coherent

diffraction imaging have demonstrated extreme sensitivity for weakly absorbing specimens with a demonstrated spatial resolution below 10 nm [1.1.2, 1.1.3]. With this potential to reach nanometer spatial resolution in low contrast materials, coherent diffraction imaging is an important complementary technique at the HXN beamline. In particular, it is feasible to combine x-ray fluorescence measurement with coherent diffraction imaging in a Ptychography method to obtain both spectroscopic and electronic density images from a single experiment [1.1.4]. In addition, the far-field data collected in this way can be used for differential phase-contrast imaging by performing straightforward manipulation of the digital data set without reconstruction [1.1.5] to provide high-throughput direct imaging.

An important aspect of these different x-ray microscopy techniques is that they are mutually compatible with one another, providing feasibility for implementing methods to perform simultaneous or parallel measurements with two or more different techniques. This is an important instrumentation approach because the intense photon density over the focal spot can lead to significant radiation damage for soft and even some of the hard materials. Acquiring as much information from the specimen over a given exposure time will be one of the key instrumentation principles in developing a HXN microscope.

Designing, building, and operating the HXN beamline are intimately connected to the two critical instrumental challenges: development of high spatial resolution nanofocusing optics, and development of an x-ray microscope with adequate positioning and scanning capabilities. In order to tackle the technical challenges, NSLS-II has launched 1nm X-ray Optic R&D and Nanopositioning R&D programs. Both of these major R&D programs are currently carried out by the HXN team members. The 1nm Spatial Resolution R&D is aiming at fabricating high-resolution multilayer Laue lenses (MLL) with the outmost zone width as small as 1nm (see Appendix 3 for details). An advanced multilayer deposition system capable of fabricating wedged and flat MLLs with an aperture up to 150 microns has been commissioned in May 2010 (see Appendix 4 for details) and is presently used for investigating challenges associated with growing large aperture MLLs [1.1.6]. Considerable efforts of the Nanopositioning R&D are directed at designing a MLL microscope with a mechanical stability of ~1nm while ensuring the compatibility for using zone plate (ZP) optics. Though both MLL and ZP have similar aspects, positioning MLLs requires fundamentally different approaches in that both translational and rotational degrees of freedom are needed to focus the x-ray beam. Maintaining high stability through laser interferometer feedback loops while providing adequate degrees of freedom are the primary technical challenges. This preliminary design report (PDR) presents a well-defined modular instrument approach for the HXN microscope to offer both x-ray fluorescence and diffraction capabilities using MLL or ZP optics.

Maintaining an adequate level of vibration and temperature stability is an essential requirement for using a nanofocused beam to carry out scientific measurements. The spatial resolution of fluorescence or diffraction images obtained by a 2D raster scan of the sample with respect to the focused beam is determined not by the size of the probe alone. Positioning accuracy of the probe with respect to the sample, affected by ambient vibrations and temperature drift, plays a dominant role in determining the final resolution of the images. In order to provide sufficient vibration and temperature stability for the x-ray microscopy experiments, a dedicated satellite building will be built around the HXN endstation. Extensive vibration measurements and numerical simulations have been performed to determine the ideal site of the HXN beamline and validate specific details of the architectural design for the satellite building (see Appendix 5 for details). The design of the HXN beamline optics also took considerable attention to ensure the highest stability for the x-ray source. All the high heat load x-ray optics are designed to manipulate the x-ray beam in a horizontal geometry, in order to deliver high mechanical stability. In addition, a stable effective x-ray source is created using a secondary source aperture downstream of all the beamline optics. Consequently, any x-ray source motion induced by possible instability of the electron beam or resulting from vibration of the monochromator or x-ray mirrors cannot cause undesired displacement of the position of the nanofocused beam.

X-ray nanofocusing research is evolving rapidly and several groups in the world are developing novel technologies with the goal of achieving a nm-scale focus. This includes the latest results from Japan based on multilayer mirrors, where a 7 nm line focus has been demonstrated [1.1.7]. Though the current design of the HXN beamline enables

effective use of MLL and ZP optics, the beamline does not have any potential technical limitations for taking full advantage of other types of nanofocusing optics, if a significant technical breakthrough should occur in the near future. While achieving a high spatial resolution toward its ultimate spatial resolution of ~1nm is an important goal for the HXN beamline and a critical milestone achievement for x-ray microscopy, considerable technical challenges exist for both achieving a ~1nm x-ray beam and using it for scientific applications. Therefore, the initial goal of the HXN beamline will be to enable scientific applications at a spatial resolution of 10 nm. Development efforts for achieving higher spatial resolution will be made after the initial goal has been achieved.

As the baseline goal, multilayer Laue lenses will be used to achieve a 10 nm resolution with a 2 mm working distance in the energy range of 10-25 keV. With a target efficiency of 1.5%, integrated flux of ~6×10^8 is expected over a 10 nm focus. Wedged MLLs with a higher target efficiency of 22% can achieve focused flux of ~1×10^{10} over a 10 nm focus. In the energy range of 6-12 keV, zone plates will be used to provide a longer working distance of ~7 mm and a spatial resolution of 30 nm with an estimated focus flux of ~4×10^8 at 10keV.

In summary, the HXN beamline aims to become a world-leading scanning microscopy facility, enabling the highest spatially resolved structural and spectroscopic x-ray imaging techniques on day 1 at 10 nm spatial resolution with unprecedented elemental sensitivity. The x-ray microscopy capabilities offered at the HXN beamline will open new frontiers of hard x-ray microscopy applications in a wide range of scientific disciplines.

[1.1.1] J. Maser, et al., "The Hard X-ray Nanoprobe Beamline at the Advanced Photon Source," Proceedings of the 8th International Conference on X-ray Microscopy, Institute of Pure and Applied Physics, pp 26 - 29. (2006). For the current instrument capabilities, visit http://nano.anl.gov/facilities/xray_cap.html

[1.1.2] Jianwei Miao, Tetsuya Ishikawa, Erik H. Anderson et al., "Phase retrieval of diffraction patterns from noncrystalline samples using the oversampling method," *Physical Review B* **67** (17), 174104 (2003).

[1.1.3] C. G. Schroer, P. Boye, J. M. Feldkamp et al., "Coherent X-Ray Diffraction Imaging with Nanofocused Illumination," *Physical Review Letters* **101** (9), 090801 (2008).

[1.1.4] Pierre Thibault, Martin Dierolf, Andreas Menzel et al., "High-Resolution Scanning X-ray Diffraction Microscopy," *Science* **321** (5887), 379-382 (2008).

[1.1.5] M. D. de Jonge, B. Hornberger, C. Holzner et al., "Quantitative Phase Imaging with a Scanning Transmission X-Ray Microscope," *Physical Review Letters* **100** (16), 163902 (2008).

[1.1.6] Ray Conley, Nathalie Bouet, James Biancarosa et al., "The NSLS-II multilayer Laue lens deposition system," *Proc. SPIE - Int. Soc. Opt. Eng.* **7448** (2009).

[1.1.7] Hidekazu Mimura, Soichiro Handa, Takashi Kimura et al., "Breaking the 10 nm barrier in hard-X-ray focusing," *Nat Phys* **6** (2), 122-125 (2010).

1.2 The HXN team

The Hard X-ray Nanoprobe beamline at NSLS-II plans to achieve scientific and technical goals that are beyond the current state-of-the-art. Development and construction of the HXN beamline is coordinated with two supporting R&D programs: 1nm Spatial Resolution R&D and Nanopositioning R&D. Consequently, the HXN Team consists of many members. It is also important to acknowledge that the effort for developing high spatial resolution multilayer Laue lenses (MLLs) initially started at the Advanced Photon Source (APS) and the Center for Nanomaterials (CNM) at Argonne National Laboratory. The HXN team members are actively engaged in continuing collaboration. The following list summarizes the HXN team and multi-faceted support and collaboration.

HXN beamline

Yong Chu: Group Leader

Lawrence Margulies: Beamline Scientist

Ken Evans-Lutterodt: MOU Staff from NSLS and kinoform development

Steve O'Hara: Beamline Mechanical Engineer

1nm spatial resolution R&D

Hanfei Yan: MLL theory and testing

Enju Lima: MLL testing using coherent phase retrieval methods

Ray Conley: MLL fabrication, processing and metrology

Nathalie Bouet (postdoc): MLL processing

James Biancarosa (technician): MLL fabrication

Kenneth Lauer (MS student): Software development for MLL deposition control

Nanopositioning R&D

Evgueni Nazaretski: Nanopositioning research and development of the HXN x-ray microscope

Daejin Eom (postdoc): Nanopositioning research

Denis Kuhne (technician): Maintenance of nanopositioning lab and prototype machining

Deming Shu (ANL): Collaboration through a joint work project.

Other support

Andy Broadbent: Interfacial management and coordination

Nikolaos Simos: Vibration measurement, analysis and modeling

Brian Mullany: Technical drawing and designing support

Oleg Chubar: Numerical simulations of undulator radiation and wave propagation of partially coherent x-rays.

Viswanath Ravindranath: Numerical simulations on high heat load optics

Ove Dyling: Management of the HXN Satellite Building construction

Tom Joos: Structural engineering support for the HXN Satellite Building design and construction

Tom Nehring: Electrical engineering support for the HXN Satellite Building design and construction

John Gosman: Mechanical engineering support for the HXN Satellite Building design and construction

Kathleen Robinson: Scientific editing and document design

External collaboration

Deming Shu (Argonne National Laboratory): Collaboration on nanopositioning

Jörg Maser (Argonne National Laboratory): Collaboration on MLL theory and experiment

Hyon-Chol Kang (Chosun University, South Korea): Collaboration on MLL experiment

Volker Rose (Argonne National Laboratory): Collaboration on x-ray characterization of MLLs

Martin Holt: (Argonne National Laboratory): Collaboration on MLL experiment

Robert Winarski (Argonne National Laboratory): Collaboration on MLL experiment

Albert Macrander (Argonne National Laboratory): Collaboration on MLL fabrication and experiment

Chian Liu (Argonne National Laboratory): Collaboration on MLL fabrication

Nima Jihedi (Argonne National Laboratory): Collaboration on MLL polishing and metrology

Brian Stephenson (ANL): Collaboration on MLL experiment

1.3 Beamline Advisory Team (BAT)

BAT Member	Affiliation
Ismail Cev Noyan*	Columbia University
Chris Jacobsen	Argonne National Laboratory, Northwestern University
Don Bilderback	Cornell University
Tonio Buonassisi	Massachusetts Institute of Technology
Ken Evans-Lutterodt	Brookhaven National Laboratory
Tony Lanzirotti	University of Chicago
Stefan Vogt	Argonne National Laboratory
Martin Holt	Argonne National Laboratory

* BAT Spokesperson

2 BEAMLINE LAYOUT

2.1 Overview

The overall beamline layout is shown in Figure 2.1.1. The HXN beamline is a moderately long beamline, occupying a low-beta straight section with an in-vacuum undulator with a 20mm period, IVU20. The beamline extends out of the experimental hall and has a dedicated satellite building located adjacent to the storage ring building and the laboratory-office building (LOB). The furthest external wall of the satellite building is 115 m from the source. The official alpha-numerical label for the HXN beamline is 3-ID. The HXN beamline has three experimental stations.

- Experimental station 3-ID-A: the first optical enclosure (FOE) adjacent to the synchrotron storage ratchet wall with white beam shielding requirement.
- Experimental station 3-ID-B: the second optical enclosure located on the NSLS-II experimental hall with monochromatic shielding requirement.
- Experimental station 3-ID-C: the third optical enclosure or endstation located in the HXN Satellite Building with monochromatic shielding requirement.

Experimental station 3-ID-A contains the beam conditioning optics and other essential components required for stable and safe operation of the beamline. Experimental station 3-ID-B houses the first secondary source aperture (SSA1), which is one of two possible secondary source apertures of the HXN beamline. The primary function of station B is to extend the nanofocusing capability of the HXN beamline. In addition, it will be used to perform beamline diagnostic measurements and to develop beam position monitoring methods, in order to ensure the highest level of beam stability for x-ray microscope experiments. Presently, station B is not in the baseline scope of the HXN beamline.

Monochromatic x-rays are transported through a long beam transport pipe running over the bypass corridor, out of the main storage ring building, into the HXN satellite building, and into station C. With an interior dimension of 20 m (length) x 5 m (width) x 3.5 m (height), the endstation contains the secondary source aperture 2 (SSA2) and endstation instruments that will provided the world-leading hard x-ray microscopy capabilities. The HXN Satellite Building and the endstation are designed to meet the stringent stability requirements for vibrations and temperature. Presently, the architectural and engineering design of the satellite building is 100% complete. The technical details are summarized in section 4.

2.2 Insertion device

Table 2.2.1: Electron beam size and divergence at NSLS-II.

Type	Low-Beta Straight Section (6.6 m)	High-Beta Straight Section (9.3 m)	0.4T Bend Magnet	1T Three-Pole Wiggler
σ_h (μm)	33.3	107	125	167
$\sigma_{h'}$(μrad)	16.5	5.1	91	98
σ_v (μm)	2.9	5.2	13.4	12.3
$\sigma_{v'}$(μrad)	2.7	1.5	0.80	0.82

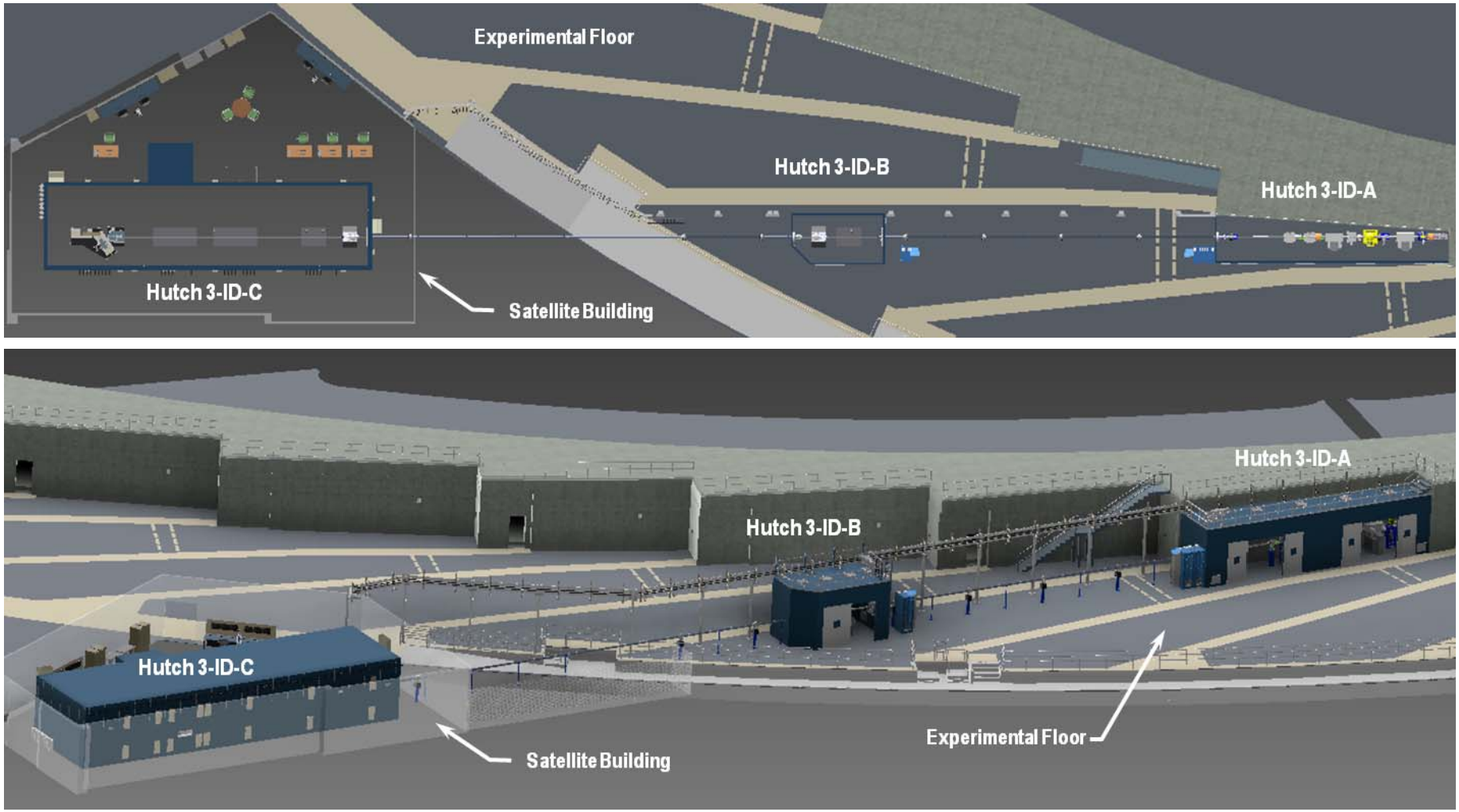

Figure 2.1.1: Overview of the HXN beamline with three experimental stations, 3-ID-A, -B, and -C (from right to left). Top panel: horizontal cross-section of the beamline seen from the top. Bottom panel: 3D perspective view of the beamline. Translucent boundary around the endstation indicates the external walls of the HXN Satellite Building. The designated access paths and corridors, ensuring the required clearance space, are indicated by a light grey color. A bypass corridor under the beam transport pipe ensures the convenient passage of people and equipment.

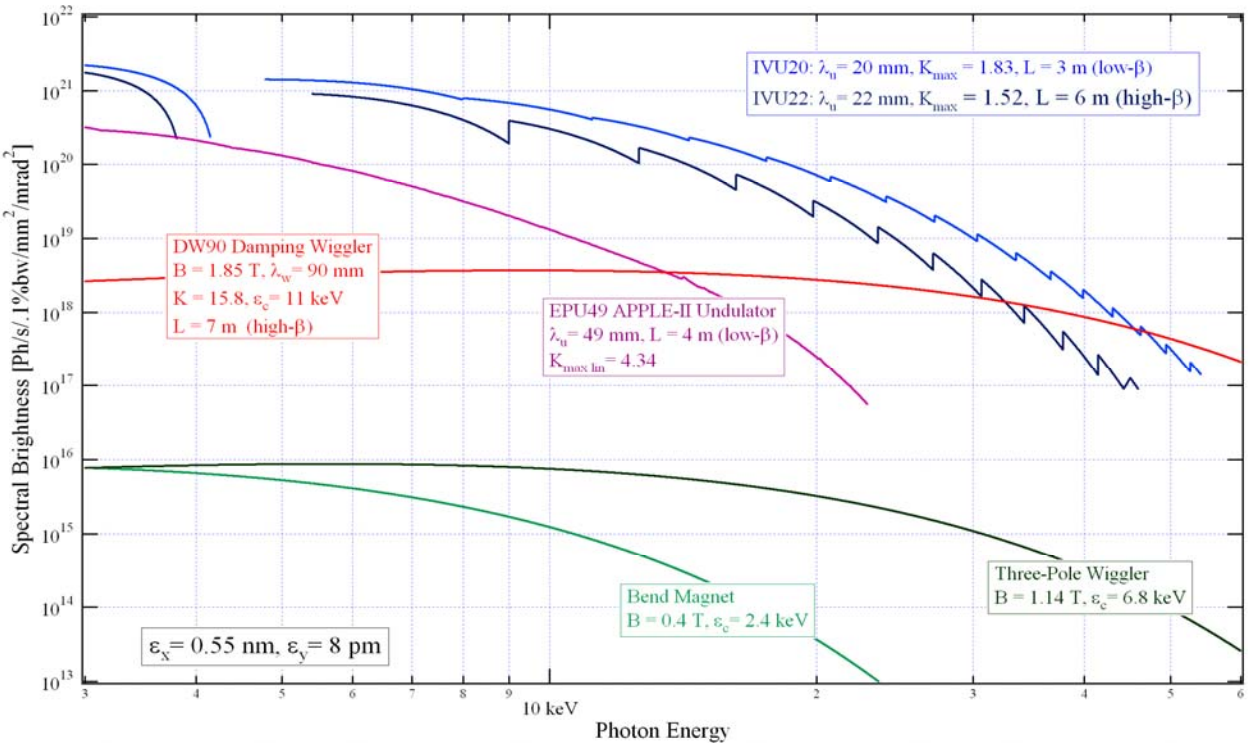

Figure 2.2.1: Brightness vs. photon energy for a number of different NSLS-II radiation sources at 3 GeV and 500 mA.

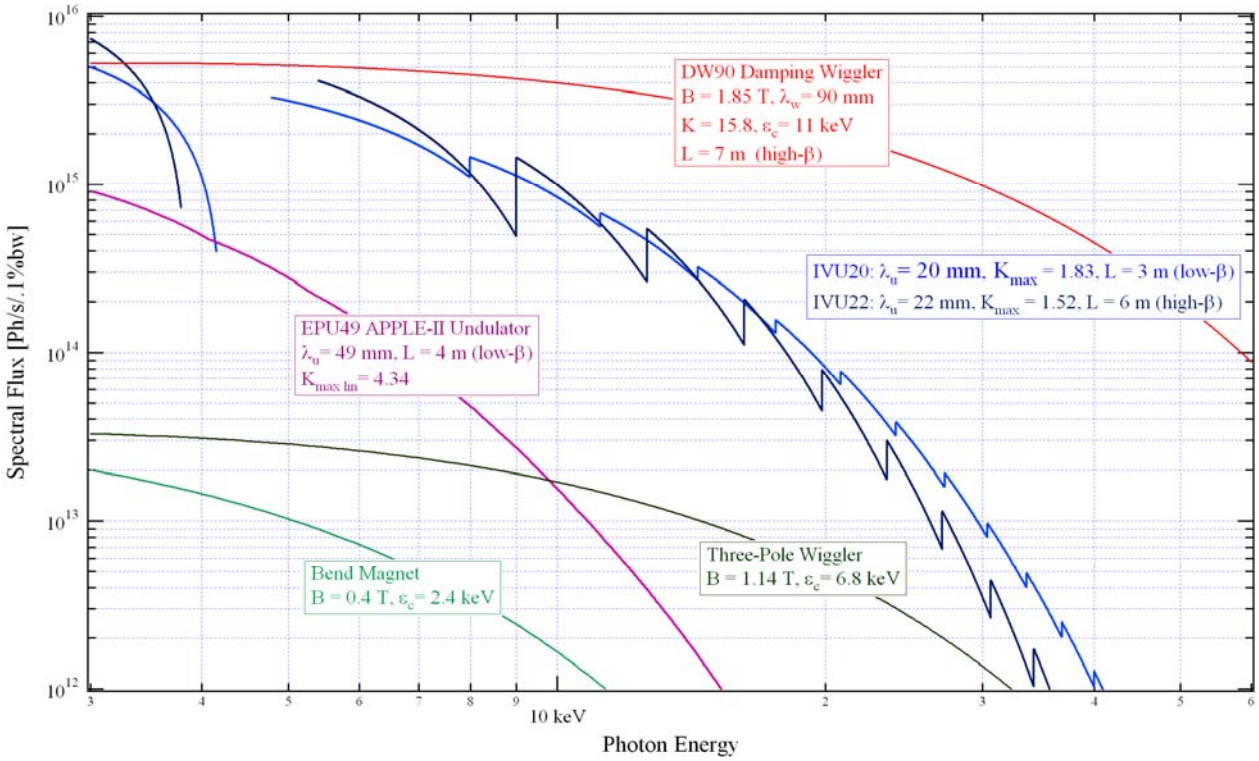

Figure 2.2.2: Flux vs. photon energy for a number of different NSLS-II radiation sources at 3 GeV and 500 mA.

NSLS-II is designed to deliver photons with high average spectral brightness in the 2 keV to 10 keV energy range exceeding 10^{21} ph/s/0.1%BW/mm^2/mrad^2 [2.2.1]. This cutting-edge performance requires the storage ring to support a very high-current electron beam (I = 500 mA) with sub-nm-rad horizontal emittance (down to 0.5 nm-rad) and diffraction-limited vertical emittance at a wavelength of 1 Å (vertical emittance of 8 pm-rad). The electron beam will be stable in its position (<10% of its size), angle (<10% of its divergence), dimensions (<10%), and intensity (±0.5% variation). The one sigma horizontal and vertical electron beam size and divergences in the center of the two types of straights, at the planned location of the 3-pole wigglers, and the range of values in the bend magnets, are given in Table 2.2.1. The brightness and flux curves for the currently planned NSLS-II insertion devices are shown in Figures 2.2.2 and. 2.2.3.

The scientific goal of the HXN beamline demands the highest achievable source brightness over its operating energy range from 6 to 25 keV. The brightness, defined as the flux output per unit bandwidth (0.1%), per unit source area, and per unit solid angular divergence, is the single most important source parameter for x-ray microscopy. The total amount of flux over the diffraction-limited focused spot is limited to the total amount of the coherent flux from a synchrotron source. The coherent flux, F_c, is related to the on-axis source brightness, B, by the following relationship, $F_c = B(\lambda/2)^2$, where λ is the x-ray wavelength. Consequently, higher source brightness gives higher coherent flux and higher integrated flux over a diffraction-limited focused beam spot. Among the currently planned insertion devices, the in-vacuum undulator (IVU20) located at the low-beta straight section is the most logical choice for the HXN beamline based on its highest brightness in the hard x-ray regime. The basic parameters for an IVU20 device are listed in Table 2.2.2 below.

Table 2.2.2: Basic parameters of the IVU20 at NSLS-II.

Parameter	Value
Type of straight section	Low-β ($\beta_H \approx 2$ m, $\beta_V \approx 1$ m)
total device length	3.0 m
Period length	20 mm
number of periods	148
minimum magnetic gap	5 mm
peak field linear mode B	1.03 T
Max K_y	1.83
Minimum fundamental resonance energy	1.6 keV
maximum total power	7.9 kW
on-axis power density	62 kW/mrad^2

The estimated source brightness with 0.5 nm-rad emittance (ε) is 5.5 x10^{20} ph/s/0.1%bw/mm^2/mrad^2 at 10 keV and 7.1x10^{19} ph/s/0.1%bw/mm^2/mrad^2 at 20 keV, with the total coherent flux of 2.1x10^{12} and 6.8x10^{10} ph/s/0.1%bw at the respective energies. Figure 2.2.3 shows the RMS angular and source size of IVU20. This calculation takes into account broadening due to the finite energy spread, emittance of the electron beam and convolution with the x-rays [2.2.1]. The solid curves correspond to the source parameters at the exact resonant photon energies of harmonics. The dotted curves correspond to the source parameters at photon energies slightly lower than the undulator resonance energies, which yield higher flux. The horizontal source size and angle depend on the emittance. The reduction of emittance from its initial operation value of 0.9 nm-rad to the steady state operation value of 0.55 nm-rad will decrease both horizontal source size and angle by ~1.3 times. Whereas, the vertical source size and angle are unaffected. With an assumption that source size and angle can be described by a Gaussian shape, the RMS (root mean square) values can be converted into the "full width at half maximum," FWHM (FWHM = 2.35σ). The FWHM source size and angles at 10 keV with 0.5nm-rad emittance are S_h = 80.1μm, θ_h = 42.3μrad, S_v = 17.6 μm, and θ_V = 18.1 μrad. The subscripts *h* and *v* denote the horizontal and vertical directions. In the vertical direction the distribution of source size and angle deviate considerably from a Gaussian distribution, in particular at photon

energies slightly less than the undulator resonance energy [2.2.2, also read Appendix 6 for more details]. More accurate values of the vertical FWHM source size and angle at 10keV are 12 μm and 21 μrad, respectively. Though it exhibits some discrepancy, the analyses shown in this report are carried out using the Gaussian assumption because of its simplicity.

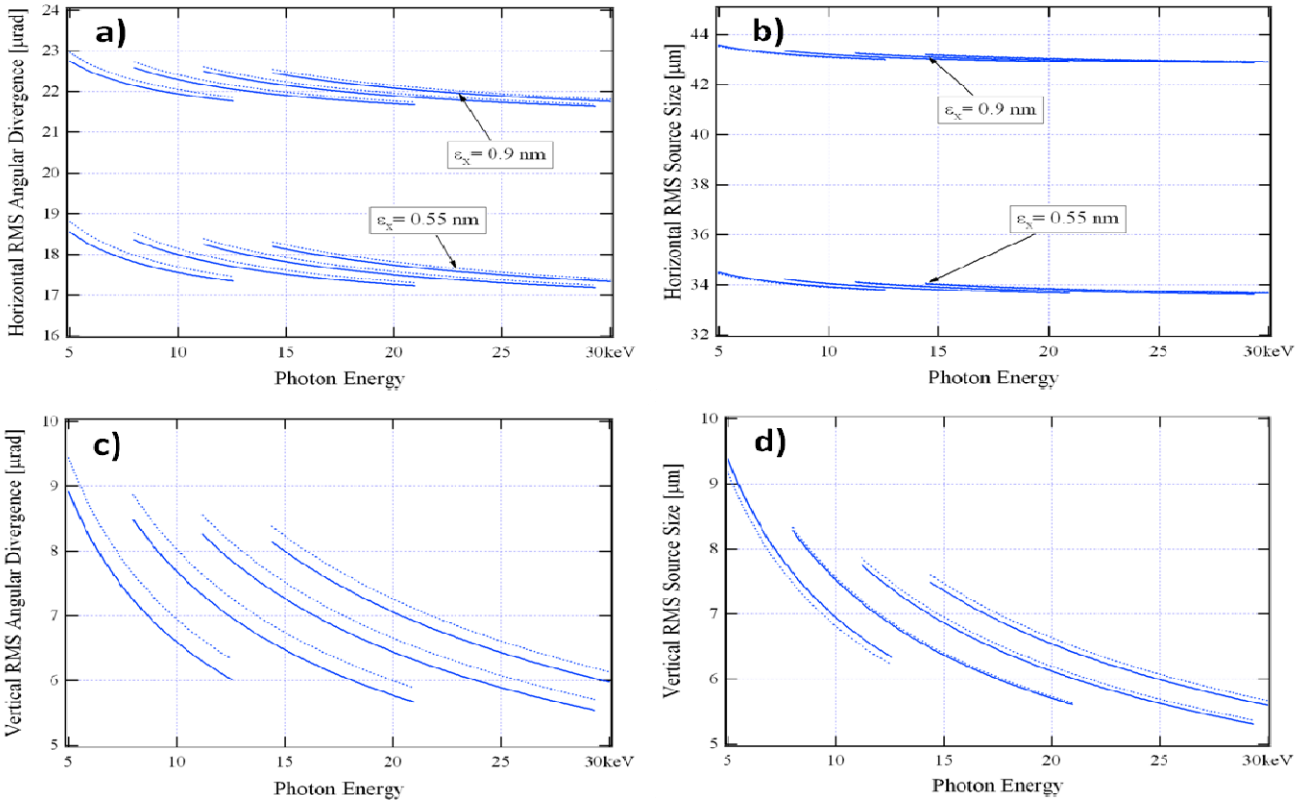

Figure 2.2.3: The RMS x-ray angular and source size of the IVU20. A) Horizontal angular divergence, B) horizontal source size, C) vertical angular divergence, and D) vertical source size. The solid curves show the source parameters at the undulator resonance energy. The dotted curves show the source parameters slightly below the resonance energy, which yield more flux.

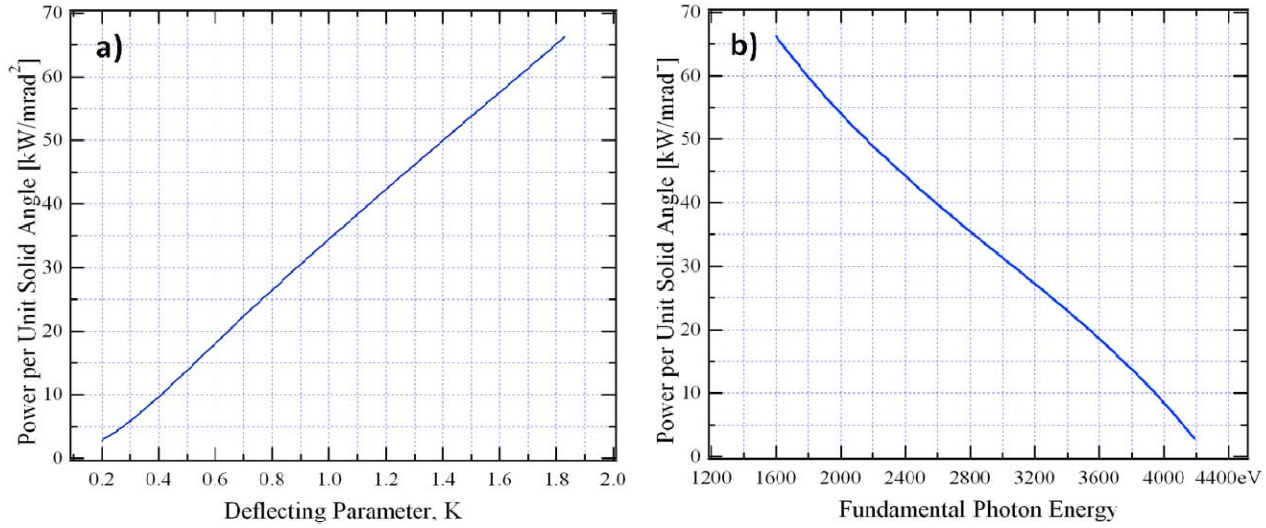

Figure 2.2.4: On-axis power density of the IVU20 at NSLS-II. A) Power density vs. K. B) Power density vs. fundamental photon energy.

One of the important technical considerations for the HXN beamline is how to manage the power delivered by the x-rays onto the high heat load optics for the beamline, so that the thermally induced slope errors results in as little impact on the beamline performance as possible. A brief summary on the estimated power from IVU20 is given here so that the power management strategy implemented in the preliminary design of the HXN beamline can be understood easily. Figure 2.2.4 shows the angular power density from the IVU20 as a function of K (deflecting parameter) and the fundamental photon energy. The angular power density increases almost linearly with K. The maximum angular power density of 66 kW/mrad^2 is produced at the maximum K value of 1.83, corresponding to the minimum gap of 5 mm and the fundamental photon energy of 1.6 keV. The same power density occurs for all the high-order odd harmonics, 4.8keV (3rd), 8 keV (5th), 11.2 keV (7th), 14.4 keV (9th), 17.6 keV (11th), and so on. On the other hand, the power density decreases almost linearly with the fundamental photon energy. For example, at the fundamental photon energy of 2 keV, the power density is reduced by about 30%.

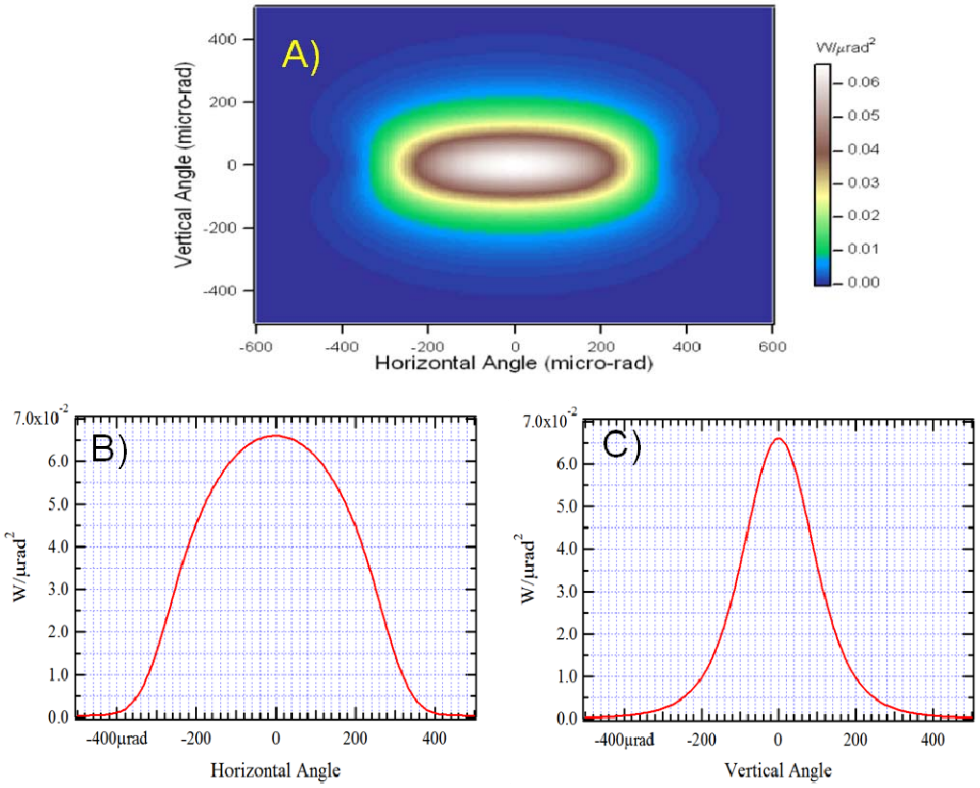

Figure 2.2.5: Angular power distribution emitted by IVU20 at K=1.83. A) 2D angular distribution, B) horizontal cut through the central axis and C) vertical cut through the central axis.

Figure 2.2.5 shows the 2D angular distribution of the power emitted from an IVU20 at K=1.83. The horizontal (Figure 2.2.5A) and vertical cuts (Figure 2.2.5B) through the center show that the FWHM widths of the power distribution are ~500 μrad in the horizontal direction and ~200 μrad in the vertical direction. For an angular aperture considerably smaller than the power distribution fan, the total transmitted power can be estimated by multiplying the on-axis power density by the angular acceptance without significant error. Since the monochromatic central cone, 42.3 μrad (H) x 18.1 μrad (V), is much smaller than the angular size of the power distribution and the HXN nanofocusing optics use a small fraction of the central cone, the HXN power management scheme uses an optimized balance between the amount of accepted monochromatic flux and the accepted power. The details on the HXN power management strategy are described in section 2.5.

[2.2.1] NSLS-II Source Properties and Floor Layout (http://www.bnl.gov/nsls2/docs/PDF/SourceProperties.pdf).
[2.2.2] O. Chubar, Y.S. Chu, K. Kaznatcheeve, H. Yan, "Application of Partially-Coherent Wave Propagation Calculations for Design of Coherence-Preserving Synchrotron Radiation Beamlines", submitted to SRI 2010 Conference Proceedings.

2.3 Front end (FE)

The primary functions of the front end are to provide reliable monitoring of position and angle of the white beam, to reduce the power of the radiation from the undulator by using fixed masks, and to limit the Bremsstrahlung radiation for safe operation of the beamline. The HXN beamline uses a standard front end (FE) design with one minor modification to the X-Y slits. The white beam slits will be modified so that the corners of the L-shaped slits have a radius of curvature smaller than 200 μm, in order to provide a well-defined beam shape. The front end of the HXN beamline is designed by the Front End Group within the Accelerator System Division of NSLS-II, led by Lewis Doom. More complete FE specifications are provided in an NSLS-II technical document, "RSI for the Front-Ends for Six NSLS-II Project beamlines" (LT-XFD-RSI 1.04.06).

2.3.1 General layout of the front end

A layout of the standard NSLS-II front end is shown in Figure 2.3.1.1 and comprises: slow gate valve (SGV); fixed aperture mask (MSK); photon beam position monitor (XBPM); lead collimators (LCO and RCO); fast gate valve (FGV); safety shutters (SSH, BMPS, and PSH); X-Y slits (SLT).

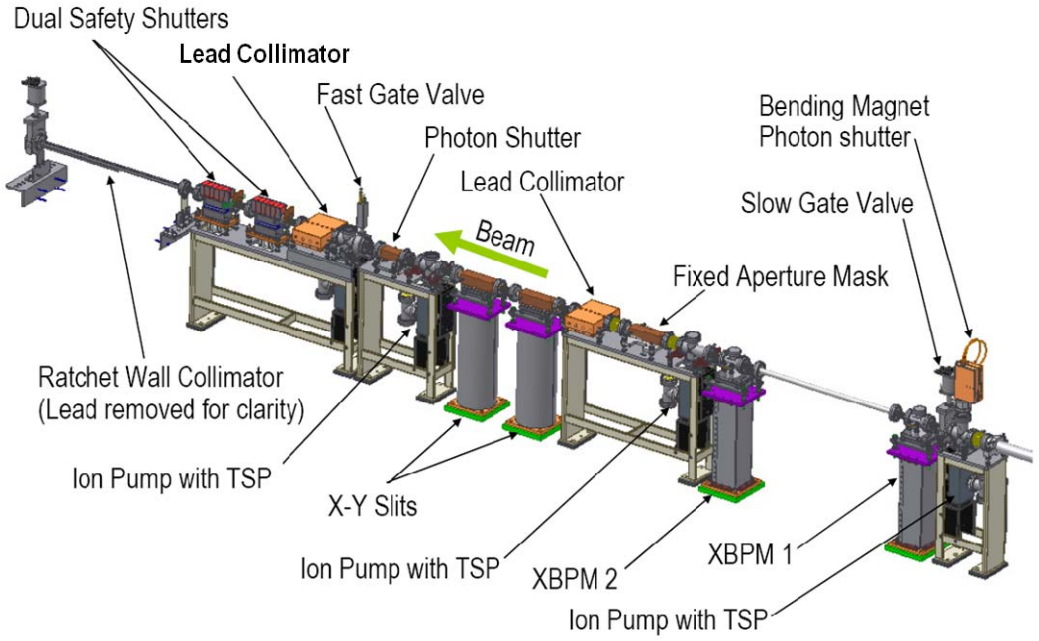

Figure 2.3.1.1: Typical front end configuration at NSLS-II.

2.3.2 Brief description of the major components of the front end

Bending Magnet Photon Shutter (BMPS): The BMPS is part of the storage ring vacuum system and is designed to protect the slow gate valve (SGV) from the nearby bending magnet radiation before the upstream straight is fitted with an insertion device and a complete front end. The BMPS provides complete isolation of the front end from the machine. If it is necessary to close the SGV during machine operation, the insertion device power will first be reduced, followed by closing the BMPS and then the SGV.

Slow Gate Valve (SGV): The SGV is part of the storage ring vacuum system and is included to isolate the machine and FE, but will not withstand white beam from the undulator or bending magnet radiation. The SGV is controlled and monitored by the storage ring vacuum PLC (Programmable Logic Controllers) using a logic scheme with inputs from vacuum sensors at both sides of the valves and position of the BMPS.

Beam Position Monitor 1 (XBPM1): The XBPM is designed to work with the insertion devices. It has water-cooled mountings and tungsten blades, and a will have a pre-mask if design considerations dictate. The device is motorized to allow proper positioning to the beam. The XBPM is mounted on X-Y stages with a position stability of Δx, Δy = 1 μm over any 8-hour period, and a position resolution of x, y = 0.1 μm**.** One design being considered for the XBPMs is shown in Figure 2.3.2.1.

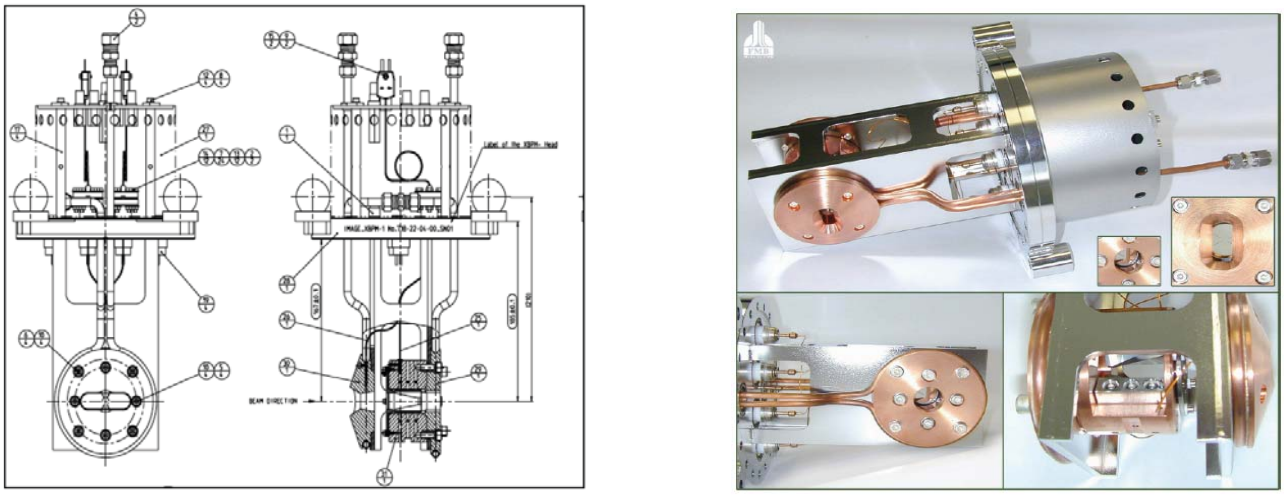

Figure 2.3.2.1: Possible XBPM design.

Beam Position Monitor 2 (XBPM2): The second Beam Position Monitor and X-Y stages are identical to XBPM1, with the exception that the blades are relocated to avoid masking effects. XBPM2 is used to monitor the angle of the beam and also serves as a backup monitor for XBPM1.

Fixed Aperture Mask (MSK): The fixed aperture mask provides radiation fans limited to 0.5 mrad (H) x 0.5 mrad (V) to the first optical enclosure (FOE). No tolerance is added to the mask for mis-positioning. However a manufacturing tolerance of ±0.2 mm for the aperture (at the downstream end of the mask) is specified. Figure 2.3.2.2 shows the design of the fixed mask.

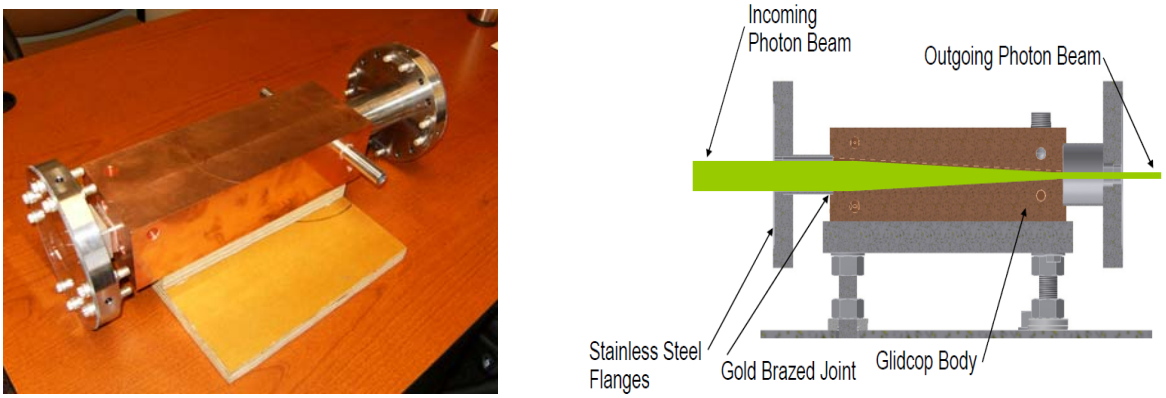

Figure 2.3.2.2: Design of the fixed aperture mask at the FE.

Bremsstrahlung Collimator 1 (CO): The bremsstrahlung collimator restricts the bremsstrahlung radiation fan exiting the shield wall. This is designed to be as tight to the beam as is reasonable without undue mechanical tolerances or alignment difficulty.

X-Y Slits (SLT): A pair of white beam X-Y slits is located immediately downstream of the first lead collimator to further reduce power loads and reduce the angular acceptance. The X-Y slits are based on the SPring8 dual "L" type design, connected with bellows to allow full adjustment of all four "blades" via two X-Y stages. The slits used for HXN will have a minimum corner radius of 200 μm, to provide a well-defined beam. The slits are made of water-cooled Glidcop® with tungsten blocks. The aperture stability is Δx, Δy = 1.5 μm over any 8-hour period. The aperture stability specification is governed by differential movement between the two X-Y slit units. The specification will be met with high stability X-Y stages. For the high stability stages some form of additional coupling between stands may be required to constrain any differential movement.

Photon Shutter (PSH): The photon shutter is designed to stop the full white beam. For insertion devices (IDs), PS design uses water-cooled Glidcop at a grazing incidence angle. The photon shutter length will be 30 cm.

Fast Gate Valve (FGV): The fast gate valve is to shut within a few milliseconds once triggered by FGV sensors located in the FE and beamline, whenever there is a sudden increase of pressure of a few decades. The stored beam has to be dumped prior to FGV closing. The cause is then investigated and mitigated.

Bremsstrahlung Collimator 2 (CO): Bremsstrahlung collimators 1 and 2 and the ratchet wall collimator are made as tight as possible using a combination of in-vacuum tungsten and out-of-vacuum lead designs.

Safety Shutter (SSH): The safety shutter is actually a pair of shutters, required for redundancy, which are air actuated with independent redundant and diverse position sensing. An external lead design is being used, as shown in Figure 2.3.2.3.

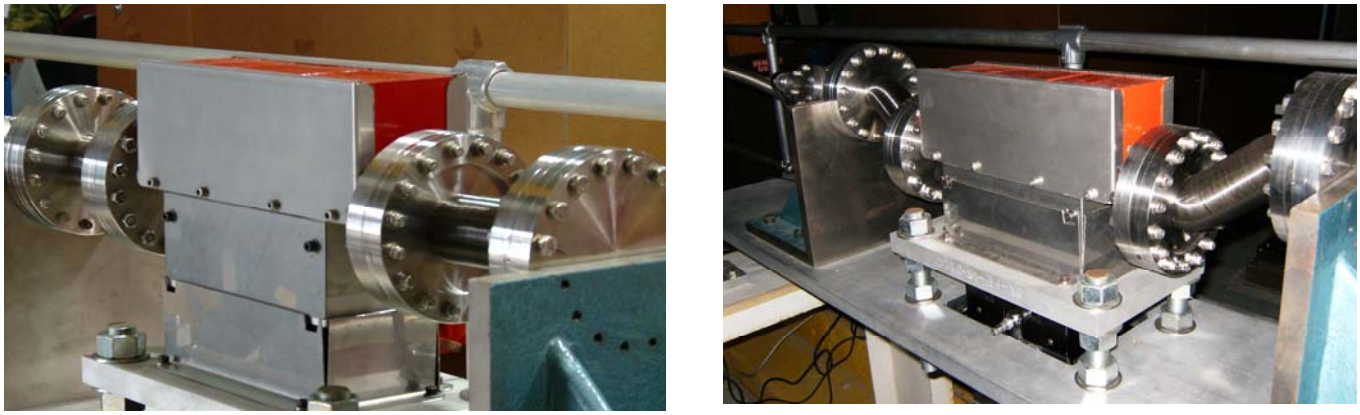

Figure 2.3.2.3: FE Safety shutter

Ratchet Wall Collimator (RCO): The Ratchet Wall Collimator provides the final collimation of bremsstrahlung radiation between the interior and exterior of the ratchet wall. Mounting brackets on the inner and outer faces of the ratchet wall support the beampipe with the lead collimator around it. Final definition of the stacking arrangement of the lead is still in progress.

Gate Valve Downstream of Ratchet Wall (SGV): This slow gate valve, pneumatically actuated with position-sensing switches, is monitored and controlled by the storage ring vacuum programmable logic controller (PLC) using vacuum sensors in the FE and beamlines. The SGV is the last component downstream that is considered part of the FE. This gate valve cannot be removed after commissioning and must be protected from any exposure to beam.

2.4 Optical concept

The optical layout of the HXN beamline is designed to achieve a diffraction-limited focus down to ~1 nm to ensure the technical feasibility of using 1nm nanofocusing optics, as they are being developed actively through NSLS-II's 1nm Spatial Resolution R&D. To ensure a diffraction-limited focus size, the nanofocusing optics must be coherently illuminated. In practice, the condition for coherent illumination is achieved by matching the transverse coherence length of the incident beam to the size of the nanofocusing optics. The FWHM transverse coherence length is defined as $0.44 \cdot L \cdot \lambda / S$, where L is the distance from the source to the nanofocusing optic, λ is the x-ray wavelength, and S is the FWHM source size [2.4.1]. For the multilayer Laue lenses (MLL), focusing in the horizontal and the vertical directions is implemented independently, and the condition for coherent illumination can be met independently for each direction. On the other hand, a circular zone plate (ZP) has more limited freedom for manipulating phase space, in order to avoid stigmatism. Since the goal of the HXN beamline is to use both MLLs and ZPs as the focusing optics, a stigmatism-free optical scheme is implemented, in which the distance from the source to the nanofocusing optics is identical in both directions.

There are two basic optical schemes for the HXN beamline: high-throughput mode and high-resolution mode. Presently, the HXN baseline configuration includes only the high-throughput mode, which is schematically represented in Figure 2.4.1A. A secondary source aperture located at z=94m (SSA2) is used to create an effective source for both horizontal and vertical directions. A focusing mirror (in the horizontal direction) and compound refractive lenses (in the vertical direction) are used to image the primary source in front of SSA2, and the aperture size of SSA2 is selected to match the transverse coherence length to the lateral size of the nanofocusing optics for diffraction-limited focusing.

Figure 2.4.1B shows the range of the achievable transverse coherence lengths as functions of the incident x-ray energy and the secondary source aperture size. At 10 keV, a transverse coherence length up to 164 μm can be achieved with an aperture size of 5 μm, allowing the use of focusing optics with lateral dimension as large as 150 μm with some overfilling of the incident x-ray beam.

Figure 2.4.1C through Figure 2.4.1E shows x-ray intensity distribution at the primary source, at the secondary source and at the nanofocusing optic, respectively, obtained by SHADOW [2.4.2] simulation. The image of the primary source at SSA2 has a Gaussian-like distribution with a FWHM size of 174 μm (H) x 21 μm (V), while the intensity distribution at the plane of the nanofocusing optics (z = 109 m) has a FWHM of 372 μm (H) x 187 μm (V). The size of the beam illuminating the nanofocusing optic is larger than 150 μm and provides sufficient tolerance for misalignment, particularly in the horizontal direction, where the incident beam is actively manipulated by the beamline optics.

The amount of focused flux depends on the following factors:

- Brightness of the primary source
- Amount of flux passed through the secondary source aperture
- Amount of flux accepted by the nanofocusing optics

For a given nanofocusing optic located at a given beamline, the first and the last factor are already determined, and the integrated focus flux is a sole function of the size of the secondary source aperture. In the context of achieving a diffraction limited focus size, the size of the secondary source aperture is not a free parameter but determined by the angular size of the nanofocusing optic and by the condition for coherent illumination as explained above. In the absence of aberration and absorption, the amount of integrated flux for the diffraction-limited focus size is determined only by the brightness of the primary source. Obviously, the diffraction-limited focused flux cannot exceed the total coherent x-ray flux determined by the brightness. For IVU20, the amount of coherent flux is 2.1×10^{12} ph/s/0.1%bw at 10keV and 6.8×10^{10} ph/s/0.1%bw at 20keV.

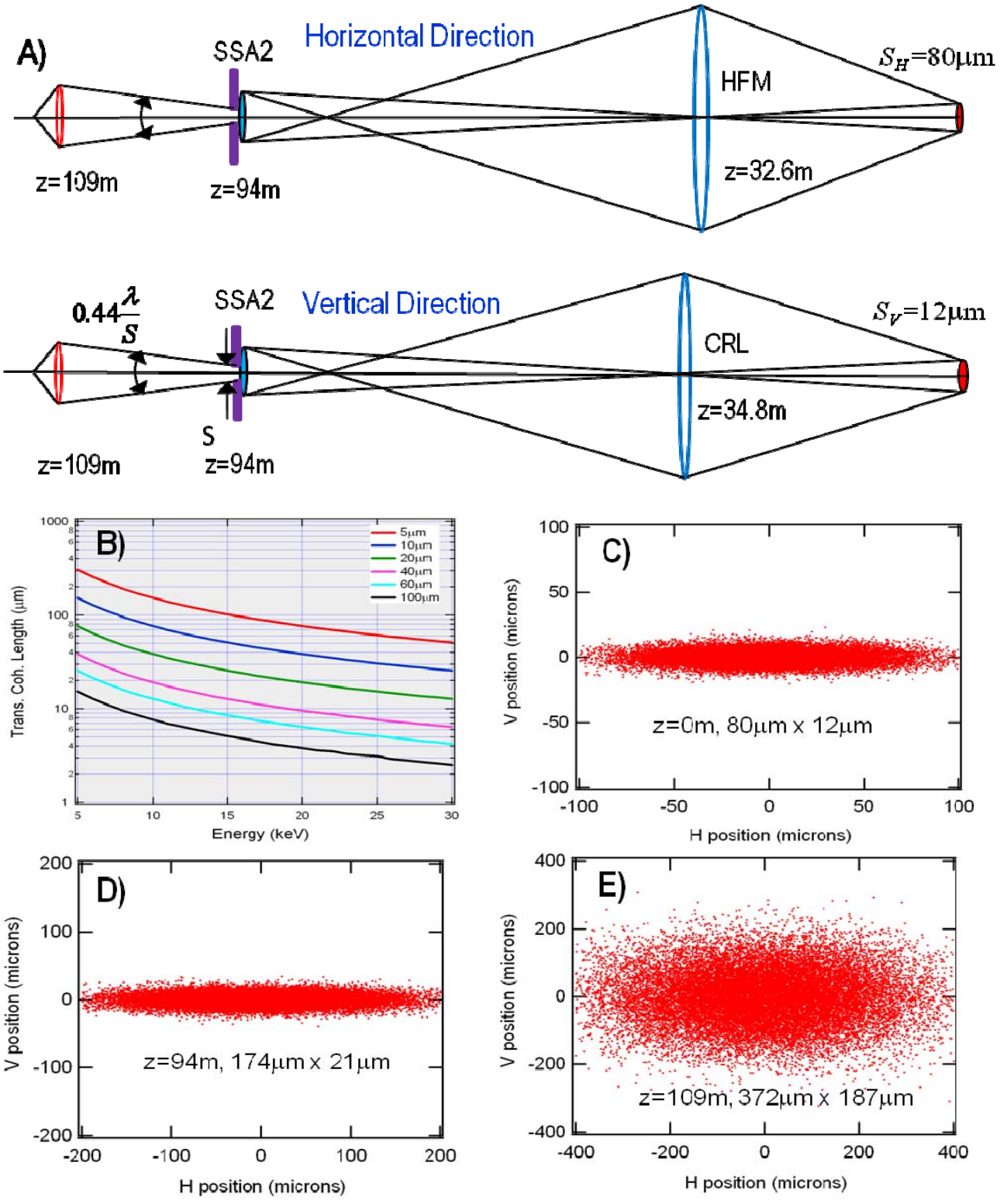

Figure 2.4.1: Baseline optical concept for the HXN beamline (high-throughput mode). A) Optical manipulation scheme using SSA2 at z=94m and the nanofocusing optic at z=109m. The distance from the secondary source to the nanofocusing optic is 15m. For simplicity, the horizontal collimating mirror is omitted. B) Transverse coherence length (FWHM) as a function of secondary source aperture size and x-ray energy. C) X-ray intensity distribution at the primary source. D) X-ray intensity distribution at the secondary source. E) X-ray intensity distribution at the nanofocusing optic. The effective source-to-nanofocusing optic distance is 15 m.

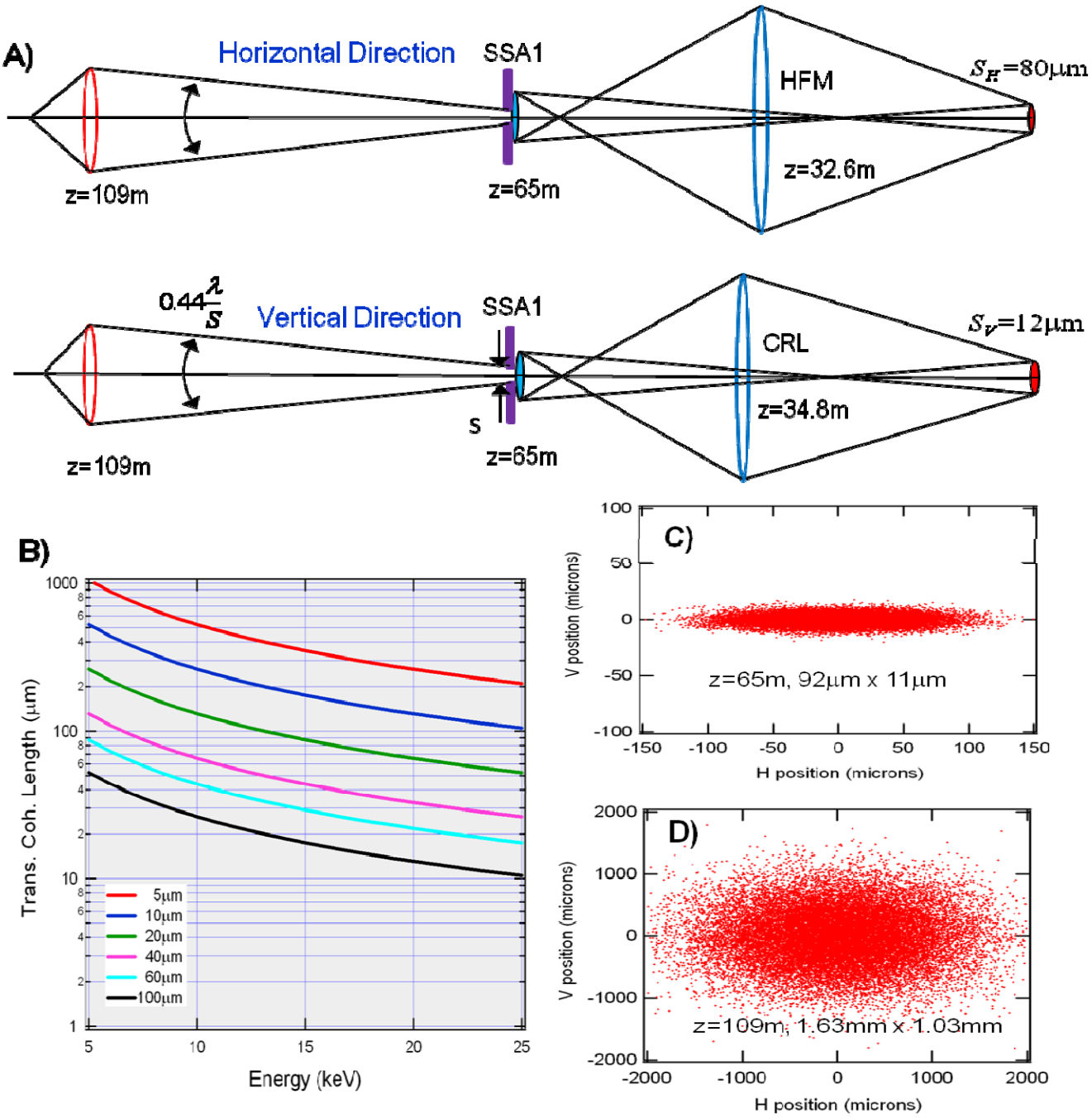

Figure 2.4.2: Mature scope addition to the optical scheme for the HXN beamline (high-resolution mode). A) Schematic view of the optical scheme using SSA1 at z=65 m. The distance from the secondary source to the nanofocusing optic is 44 m. For simplicity, the horizontal collimating mirror is omitted. B) Transverse coherence length (FWHM) as a function of secondary source aperture size and x-ray energy. C) X-ray intensity distribution at the secondary source. D) X-ray Intensity distribution at the nanofocusing optic. The effective source-to-nanofocusing optic distance is 44 m.

An alternative way of estimating the diffraction-limited focused flux is to consider the number of coherent modes, defined as $N_c = S \cdot \theta / 0.44\lambda$, where S is the FWHM source size, θ is the FWHM source angle, and λ is the x-ray wavelength. It is a measure of the coherent fraction of the x-ray source. For the IVU20 source at 10keV, there are approximately 62 coherent modes (for ε=0.5nm-rad) in the horizontal direction and 6 in the vertical direction. Thus, about 0.27% (=1/(62 x 6)) of the total flux are considered coherent. SHADOW analysis indicates that the HXN optical scheme presented in Figure 2.4.1 utilizes 0.2% of the total incident beam (see Appendix 6 for more details).

X-ray microscopy experiments do not always use a diffraction-limited focus. Most of the time, it is more desirable to use a much larger beam in order to perform fast preview scans, in order to survey a large area before acquiring high-resolution images over smaller regions of interest. The HXN optical scheme allows for increasing the integrated flux of the focus by opening up the secondary source aperture. About a 100 fold increase in the focus flux can be achieved. However, as the secondary source aperture is increased, the focus is no longer diffraction-limited and will be equal to the demagnified image of the aperture. As a good approximation, the size of the focused beam is a convolution of the point-spread function of the nanofocusing optics and the geometrically demagnified source size. For example, a nanofocusing optic with a focal length of 4 mm produces a demagnification factor of 2.67 x 10^{-4} (=4mm/15m). In the absence of aberration, a focus size of 47.5 nm (H) x 18 nm (V) is achieved with a fully opened secondary source aperture with MLL optics with dr_N=10 nm. This capability to trade spatial resolution for flux is an important design feature of the HXN beamline. This "zooming" capability allows for adjusting the focus size without disturbing the nanofocusing optics or the sample.

An important limitation for the high-throughput mode is that the source distance of 15 m is not sufficient for the ~1nm focusing goal. Achieving a coherent illumination condition for a nanofocusing optic of ~150μm in size requires narrowing down the secondary source aperture to ~0.5 μm. An aperture size of 0.5 μm is much too small to achieve. For these reasons, the HXN beamline design includes the high-resolution mode with an additional secondary source aperture (SSA1) at z = 65m. Though the high-resolution mode is not in the baseline configuration, it is an integral part of the complete capability of the HXN beamline, offering the feasibility of using nanofocusing optics with a larger lateral dimension for a longer working distance and with a higher resolution.

The high-resolution mode uses a secondary source aperture located at z = 65 m (SSA1) in order to create an effective source distance of 44 m, as shown in Figure 2.4.2. As expected, this mode results in a transverse coherence length about three times larger than the high-throughput mode with the same aperture size of the secondary source. For example, a secondary source aperture size of 5 μm at 10 keV produces a transverse coherence length of 481 μm. At SSA1, the image of the primary source is 92 μm (H) x 11 μm (V) in FWHM. For the vertical direction, opening up the secondary source aperture more than 11 μm does not provide any performance enhancement. Consequently, use of a nanofocusing optic with a size less than ~150 μm will result in a waste of coherent flux. The fraction of incident flux utilized for diffraction-limited focusing for the high-resolution mode is identical to that of the high-throughput mode, provided that the nanofocusing optics are larger than 150 μm. At the plane of the nanofocusing optic (z = 109), the beam size is 1.63 mm (H) x 1.03 mm (V) and provides a uniform intensity sufficiently large for the nanofocusing optics.

The optical scheme implemented for the HXN beamline is not new. Similar methods have been successfully implemented in soft and hard x-ray microscopy beamlines [2.4.3-2.4.5]. The described optical scheme offers a direct and flexible method to adjust the transverse coherence length, so that a range of focus sizes down to the diffraction limit can be achieved. Additionally, the secondary source aperture is positioned downstream of the high heat load optics and provides an effective way for spatially filtering the undesired focusing effects due to imperfections of the beamline optics and thermally induced slope errors.

[2.4.1] Soft X-rays and Extreme Ultraviolet Radiation, David Attwood, Cambridge University Press.
[2.4.2] See website http://www.esrf.fr/computing/scientific/xop/shadowvui/doc for details.
[2.4.3] I. McNulty, et. al., "A beamline for 1-4 keV microscopy and coherence experiments at the Advanced Photon Soruce (APS)", Rev. Sic. Instrum. 67, 3359 (1996).
[2.4.4] B. Winn, et. al., "X1A: Second-generation undulator beamlines serving soft x-ray spectromicroscopy experiments at the NSLS", J. Synchr. Rad. **7**, 395-404 (2000).
[2.4.5] J. Maser, et al., "The Hard X-ray Nanoprobe Beamline at the Advanced Photon Source," Proceedings of the 8th International Conference on X-ray Microscopy, Institute of Pure and Applied Physics, pp 26 - 29. (2006).

2.5 Optical layout

Figure 2.5.1 shows a schematic overview of the HXN beamline with the major optical components, and Figure 2.5.2 shows how the beam path is affected by the major components. The HXN beamline uses an IVU20 undulator in a low-beta straight section. The white beam slits in the FE are used to define the size of the white beam illuminated onto the beamline optical components.

A water-cooled horizontal collimating mirror (HCM), located at z = 28.2 m, is used to collimate the incident x-rays in the horizontal direction. Operating at a fixed incidence angle of 3.0 mrad, the HCM also serves as a low-energy bandpass filter by rejecting high-order harmonics. The HCM has three different reflecting surfaces, Si, Rh, and Pt, corresponding to cut-off energies of ~10.4 keV, ~21.8 keV, and ~28 keV, respectively.

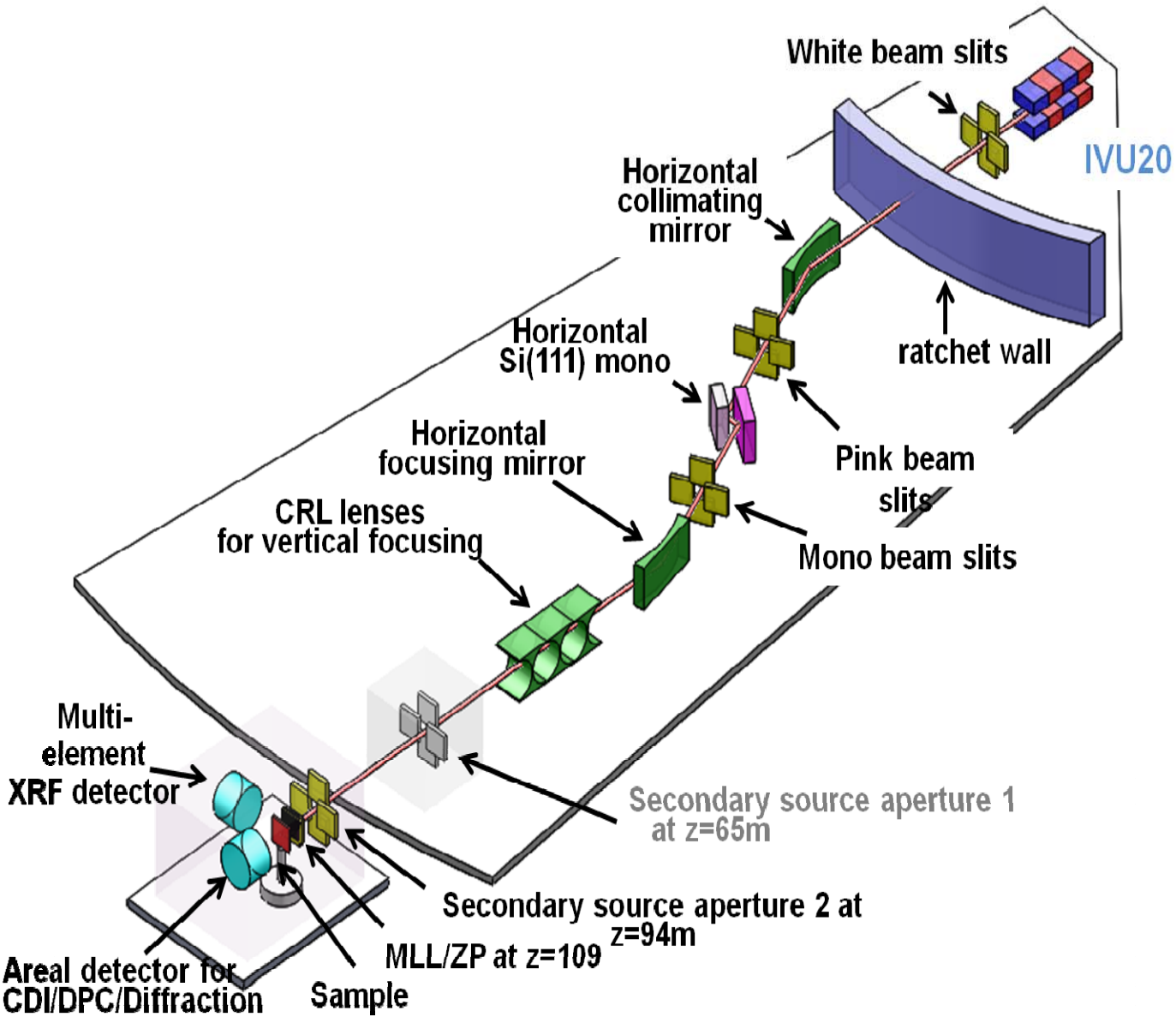

Figure 2.5.1: Schematic overview of the HXN beamline. The First Optical Enclosure (3-ID-A) houses the beam conditioning optics. The HXN endstation (3-ID-C) is outside of the NSLS-II storage ring building, enclosed within a remote satellite building to ensure vibration and temperature stability for the x-ray microscopy experiments. The secondary source aperture 1 and the monochromatic experimental station, 3-ID-B, are planned in the mature scope.

Pink beam slits are used to define the beam footprint on a horizontally diffracting monochromator, DCM, so that the central portion of the beam reflected from the HCM is illuminated on the DCM. The DCM uses double Si(111) crystals to provide a fixed exit condition for a horizontally focusing mirror HFM. A small offset value of 10 mm and high stiffness flexures with reduced degrees of freedom will be used for the DCMH, in order to provide high angular stability.

The DCMH is cryogenically cooled using liquid nitrogen, to minimize the thermally induced figure errors. As demonstrated in section 2.6 and 2.9, implementing a horizontal diffraction geometry minimizes the negative effects of thermally induced slope errors and also helps increase the mechanical stability for the bending and translating mechanisms. The HCM, DCM, and HFM create a combined horizontal offset of 36.6 mm, which is sufficiently large for safety components such as a white beam stop and Bremsstrahlung stop. A horizontal focusing mirror, HFM, is used to focus the incident beam in the horizontal direction in front of the SSA1 at z = 65 m or SSA2 at z = 94 m. The SSA2 is located in the HXN endstation within a dedicated satellite building. Construction of the SSA1 and Experimental Station 3-ID-B housing the SSA1 are not within the HXN baseline scope. In the vertical direction, a set of beryllium compound refractive lenses (CRL) are used to provide a vertical focus at SSA1 or SSA2. The HFM and the CRL focus the incident beam at the same position, providing a stigmatism-free optical scheme for nanofocusing. The HXN microscope is used to position the nanofocusing optics located at z = 109 m. The SSA1 and SSA2 provide an effective source-to-optic distance of 44 m and 15 m, respectively.

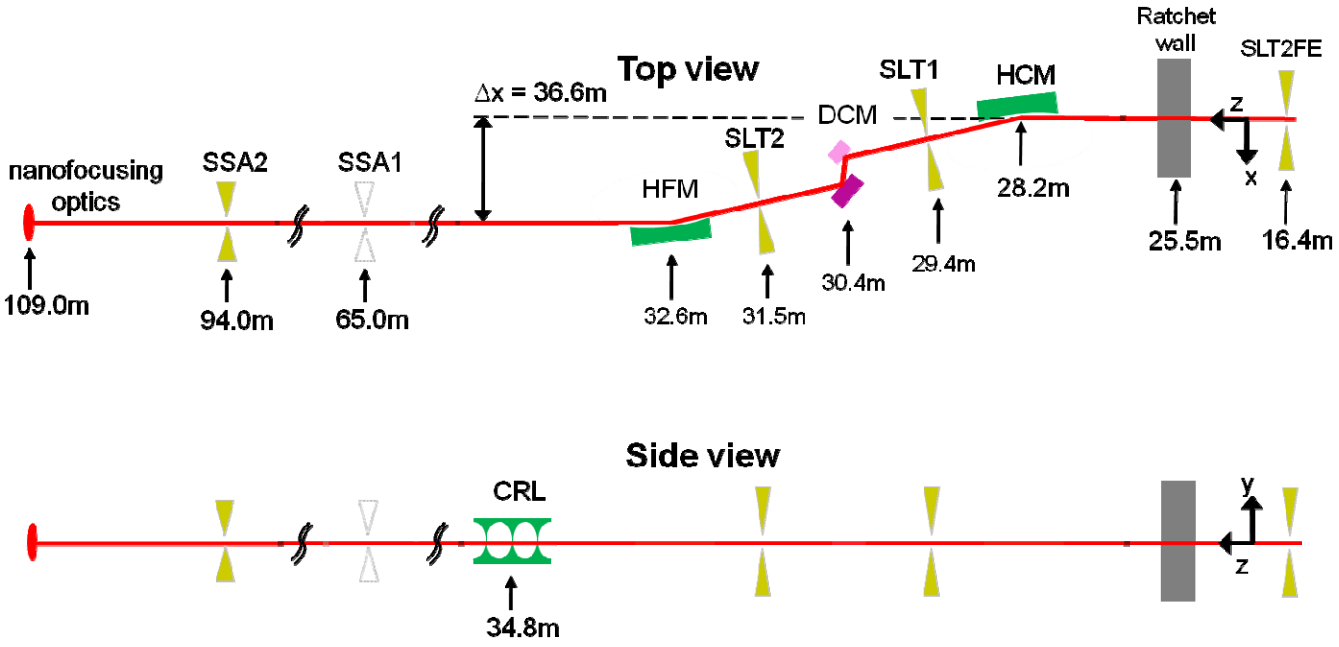

Figure 2.5.2: Schematic overview of the HXN beamline with three experimental stations 3-ID-A, B, and C (from left to right), showing X-ray beam path through the major optical components. “Top view” shows the horizontal direction and “side view” the vertical direction. The coordinates are defined such that z-direction is along the beam, y-direction is up, and x-direction is the outboard direction. All the mirrors have a nominal incidence angle of 3.0 mrad. The nominal offset distance for the double crystal monochromator (DCM) is 10 mm. A combined horizontal offset of 36.6 mm is achieved using horizontally reflecting/diffracting mirrors and a monochromator. Station 3-ID-B and the SSA1 shown in dotted lines are not included in the HXN beamline baseline scope.

2.6 High heatload optics

2.6.1 Power management strategy for the HXM beamline

As described in detail in section 2.2, the IVU20 undulator at NSLS-II delivers substantial power. At its minimum gap of 5 mm, corresponding to K = 1.83 and the fundamental energy of 1.6 keV, the on-axis angular power density is 62 kW/mrad^2 with a total power of ~8 kW in its angular fan of ~500 μrad (H) x ~200 μrad (V). An important observation is that the FWHM source angle of IVU20 is 42.3 μrad (H) and 18.1 μrad (V) at 10 keV. In addition, the angular acceptance of the nanofocusing optics for the HXN beamline cannot use the entire source angle, particularly in the horizontal direction. Consequently, our power management strategy is to minimize the power load on the mirror and monochromator while preserving the monochromatic flux for nanofocusing. The HXN power management strategy can be summarized as below.

- Use of the FE mask and white beam slits to reduce the undulator fan angle down to 70 μrad (H) x 30 μrad (V)
- Use of a modest number of attenuators to reduce the power on the white beam mirror (or Horizontal Collimating Mirror, HCM), while retaining more than 90% of the monochromatic x-rays for the entire operating energy range
- Use of multiple stripes on the white beam mirror (HCM) to lower the transmitted power to the monochromator, while providing effective harmonic rejection
- Tailoring the acceptance of the pink beam onto the monochromator to minimize the accepted power

The incremental power reduction scheme using the fixed mask, white beam slits, filters, and the pink beam slits is summarized in Table 2.6.1.1 and further discussed below.

Table 2.6.1.1: Incremental reduction of the power to the high heatload optics. The estimated power is based on the worst-case scenario, corresponding to K = 1.83.

Beamline component	Aperture H x V (rad)	Power incident	Power absorbed	Power transmitted	Notes
Fixed mask	500 x 300	~8 kW	~2.4 kW	~5.6 kW	In the front end
White beam slits	70 x 30	~5.6 kW	~5.42 kW	139 W	In the front end
White beam filters	70 x 30	139 W	34 W	105 W	A 100μm-thick CVD diamond filter used at 8keV. The thickness of filter varies with energy
White beam mirror (HCM)	70 x 30	105 W	42 W (Si, 8 keV)	63W (Si, 8keV)	3.0mrad incidence angle and Si, Rh, and Pt reflective surfaces. The absorbed and reflected power depends on the mirror surface.
		70 W	11 W (Rh, 14.4 keV)	88 W(Rh, 14.4keV)	
		58 W	8 W(Pt, 24 keV)	50W(Pt, 24keV)	
Pink beam slits	50 x 25	88 W	36 W	52 W	Define the incident beam on the mono and reduce power.
Si(111) mono (DCM1)	50 x 25	52 W	52 W at 14.4 keV	negligible	Horizontal beam size can be further reduced to make a symmetric beam for the nanofocusing optics.

The first critical component for power reduction is the fixed mask located at the FE, which has an angular aperture of 500 μrad (H) x 300 μrad (V) and cuts off the lower energy side lobes of the undulator radiation. The angular size of the FE is sufficiently large to ensure that the central cone of the undulator can make it through even if considerable mis-steering should occur. Most of the undulator power is taken out by the white beam slits in the FE. An x-ray beam with a small solid angle of 70 μrad (H) x 30 μrad (V) delivers a maximum power of 139 W when K=1.83. The solid angle of 70 x 30 μrad corresponds to 3.9 sigma values of the central cone, sufficient to accept about 95% of the source angle in each direction. At 8 keV (the 5th harmonic of 1.6 keV, corresponding to K=1.83),

a 100μ-thick CVD diamond filter absorbs about 25% of the incident power, transmitting 105 W to the HCM. The reason for using the x-ray filter is not to reduce the incidence power on the mirror. Most of the synchrotron white beam mirrors handle a substantially greater power than 105 W and function properly. Instead, the use of the filter is to ensure that the monochromator receives the lowest power possible without sacrificing the useful monochromatic flux. Placing the filter before the white beam mirror gives the benefit of lowering the power on the mirror, as well. The highest power is absorbed in the HCM when the Si surface is used at 8 keV. A total power of 42 W (about 40% of the incidence power) is absorbed in the mirror, in drastic contrast to the Pt surface (used at 24 keV), which reflects most of the incidence power with extremely low power absorption. Though the Pt surface reflects 87% of the incident power, the condition for the highest delivered power to the monochromator occurs at 8 keV, because only small amount of filter can be used at low energies. In the worst-case scenario, 63 W is reflected from the HCM. By reducing the incident beam down to 50 μrad (H) x 25 μrad (V) using the pink beam slits, the highest power delivered to the monochromator is 38 W. Although a solid angle of 50 μrad (H) x 25 μrad (V) sounds quite small, it is sufficient to illuminate the nanofocusing optics with a circular or square aperture. In fact, there is room to reduce the horizontal solid angle by a factor of 2 and still provide sufficient illumination on the nanofocusing optics as can be seen in Figures 2.4.1E and 2.4.2D.

Because the use of an x-ray filter with appropriate thickness is critical to managing the power delivered to the monochromator, a brief discussion on the use of filters is given here. Figure 2.6.1.1A shows the energy dependent x-ray transmission of CVD diamond attenuators with various thicknesses, and Figure 2.6.1.1B shows the effect of the filters on the spectral flux. Even though a 25μm-thick diamond filter attenuates only 0.57% of the 6 keV x-rays, it eliminates almost all the incident power below 3 keV, resulting in a total power reduction of about 17%. On the other hand, a diamond filter that is 1600 μm thick reduces the total power by 58.6%, with less than 8% absorption of the 25keV x-rays. Table 2.6.1.2 summarizes the energy-dependent power reduction scheme using the x-ray filters.

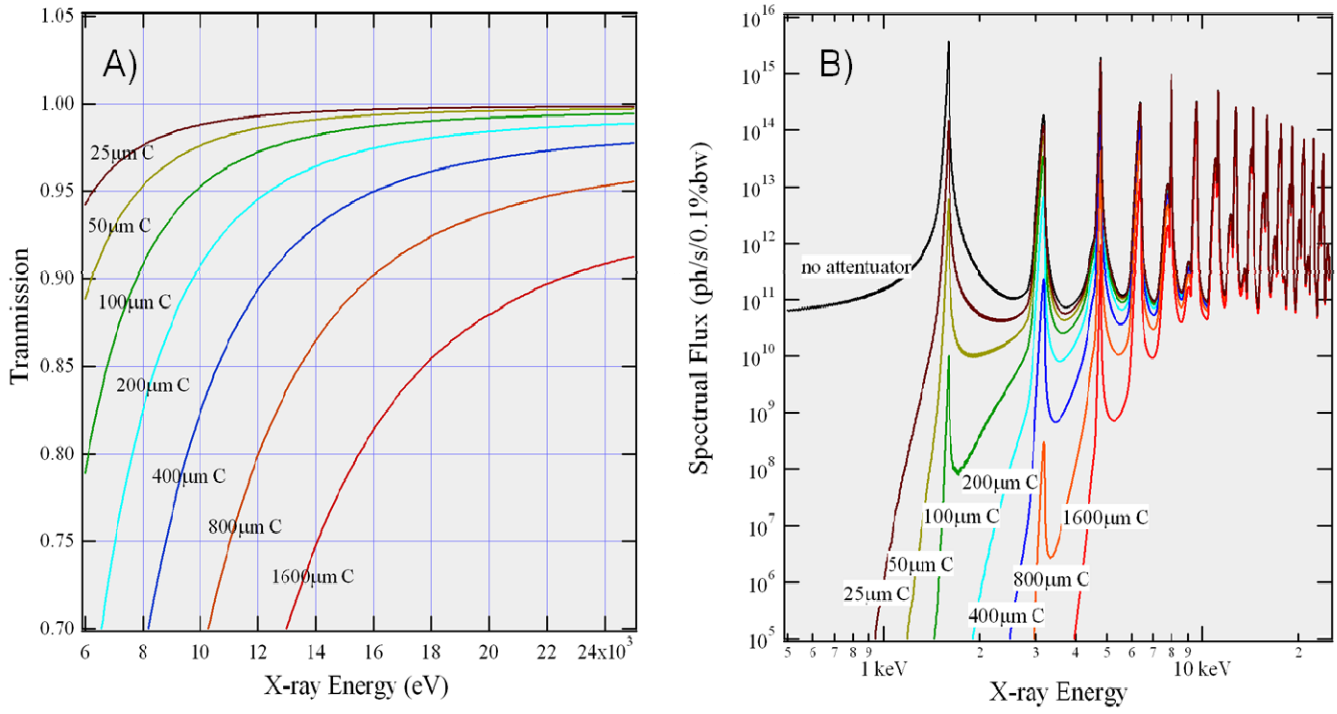

Figure 2.6.1.1: A) x-ray transmission of CVD diamond attenuator with various thicknesses. B) The transmitted spectral flux of IVU20 (at K=1.83) through CVD diamond attenuators with various thicknesses.

Table 2.6.1.2: Reduction of incident power using CVD diamond filters.

Energy	K	Incidence power (W)	Filter thickness (μm)	X-ray attenuation	Absorbed power (W)	Transmitted power (W)
6	1.51	113.6	25	0.943	19.1	94.5
7	1.29	95.9	50	0.930	19.3	76.6
8	1.83	139.0	100	0.908	34.3	104.6
9	1.66	125.6	100	0.936	31.0	94.6
10	1.51	113.6	200	0.907	35.5	78.1
11	1.37	102.7	200	0.930	32.1	70.6
12	1.73	131.2	200	0.946	41.0	90.2
13	1.62	122.1	400	0.915	48.4	73.7
14	1.51	113.6	400	0.930	45.0	68.6
15	1.77	134.4	400	0.942	53.2	81.1
16	1.68	127.0	800	0.902	62.0	65.1
17	1.59	120.1	800	0.915	58.6	61.5
18	1.79	136.4	800	0.924	66.5	69.9
19	1.72	130.3	800	0.932	63.6	66.8
20	1.65	124.5	800	0.938	60.7	63.8
21	1.81	137.9	800	0.943	67.2	70.6
22	1.75	132.6	800	0.947	64.7	67.9
23	1.69	127.6	1600	0.903	74.8	52.8
24	1.82	139.0	1600	0.909	81.5	57.5
25	1.77	134.4	1600	0.913	78.8	55.6

2.6.2 Horizontal collimating mirror (HCM)

The HCM is the first optical component of the HXN beamline, receiving white beam radiation from the source. The HCM has the following three functions:

- To reduce the power of the incident beam to the monochromator
- To reject high order harmonics from the undulator spectrum
- To collimate the incident x-rays well below the Darwin width of a Si(111) monochromator (35 μrad at 6 keV and 11 μrad at 25 keV)

The HXN beamline design uses horizontal reflection geometry because it has the following advantages:

- The IVU20 undulator has a larger source size and angle in the horizontal direction. Thus, given the same mechanical stability and level of thermally induced slope error on the mirror, horizontal reflection leads to better overall optical performance.
- The horizontal geometry provides a more stable mechanical structure. In addition, a large mirror does not bend due to its self-weight, because gravity is acting against the stiffest direction.

Overall specifications for the HCM are listed in Table 2.6.2.1. The horizontal collimating mirror has a fixed grazing incidence angle of 3.0 mrad (or 0.1719°) with an optically active length of 800 mm. The total physical length

depends on the specific bending mechanism. The estimated total length needed is ~1.0 m for symmetric bending (i.e., creating spherical/parabolic focusing) and ~1.2 m for asymmetric bending (i.e., creating elliptical focusing). Since the focal length of the HCM is large, no measurable difference exists between symmetric and asymmetric bending. The focal length of the mirror needed to collimate the incident beam is 28.2 m with a radius of bending curvature of 18.8 km. Due to the finite size of the source (80.1μm FWHM), the collimated x-rays will still have a minimum residual collimation error of 2.84 μrad—substantially smaller than the angular bandpass of Si(111).

The HCM has a stringent figure error requirement of 0.5 μrad or better, in order to avoid considerable source broadening. In addition, the HCM requires angular stability better than 0.25 μrad, in order to keep the position of the focused beam (produced by the HFM, located downstream) to better than 10% of its size. Consequently, the translation and rotation stages used for the HCM must have extremely high mechanical stability. In order to ensure the highest positional and angular stability, the HCM will have a minimum number of motorized motion degrees of freedom, only those which are absolutely critical for robust operation of the mirror. The critical degrees of freedom are the pitch for aligning the mirror to the correct incidence angle, the vertical translation for selecting a desired stripe, the horizontal translation for centering the mirror to the incident beam, and translational motion(s) required for bending. All other motions will be adjusted manually and securely locked after the adjustment, in order to prevent any potential vibration or slow drift. Having a smaller number of motors also helps reduce the number of heat sources near the mirror, resulting in greater temperature stability within the FOE.

Table 2.6.2.1: Specifications for the Horizontal Collimating Mirror

Description		Horizontal Collimating Mirror (HCM)
Substrate material		Single crystal silicon
Surface roughness, RMS		< 3 Å
Slope error, RMS		<0.5 μrad (tangential), <2.0 μrad (sagittal)
Minimum beam acceptance		70 μrad (H) x 30 μrad (V)
Substrate dimensions		1,200 mm long x 80 mm wide x 100 mm thick. The length can be shorter depending on the specific choice of bending mechanism.
Optically active length		800 mm in the center
Reflective coatings		Bare Si, Rh, Pt. Each reflecting region is a 20mm-wide stripe with 5mm gap to the nearby regions.
Coating thickness		~500 Å
Coating roughness		3 Å (RMS)
Bending method		2 points or 4 points bending
Focal lengths	F_1	28.2 m
	F_2	∞ (collimating)
Reflection geometry		Horizontal reflection
Incidence angle	θ	Fixed at 3.0 mrad (0.1719°)
Radius of curvature $R = \frac{2}{\left(\frac{\sin(\theta)}{F_1} + \frac{\sin(\theta)}{F_2}\right)}$		18.8 km
Total power load		56~105 W
Average surface power density		0.10~0.17 W/mm^2
Cooling		Water or liquid-Ga cooling
Angular stability		< 0.25 μrad
Special requirement		Minimum number of motion degrees of freedom for highest mechanical stability. Multiple external reference fiducial marks are needed for manual positioning.

The requirement for the degrees of freedom for the HCM is summarized in Table 2.6.2.2.

Table 2.6.2.2: Requirements for motion degrees of freedom

Motion	Range	Resolution	Drive system
Coarse pitch (incidence angle)	-5mrad to +2mrad from nominal 3.0 mrad	<50 µrad	2 linear stepper motors or single rotation, extremely high mechanical stability required.
Fine pitch (incidence angle)	±200µrad	<0.1 µrad	Piezo actuation
Vertical translation (selecting stripe)	±40 mm	<50µm	3 linear stepper motors, require extremely high mechanical stability and trajectory straightness
Horizontal translation	±5mm	<20 µm	2 linear stepper motors, require extremely high mechanical stability and trajectory straightness
Mirror bending	-10mm/ +30mm	<0.2µm	2 stepper motors
Manual horizontal translation	±25 mm	<250µm	Surveyed using fiducials
Manual yaw alignment	±1°	<0.05°	Surveyed using fiducials
Manual roll alignment	±1°	<0.05°	Surveyed using fiducials

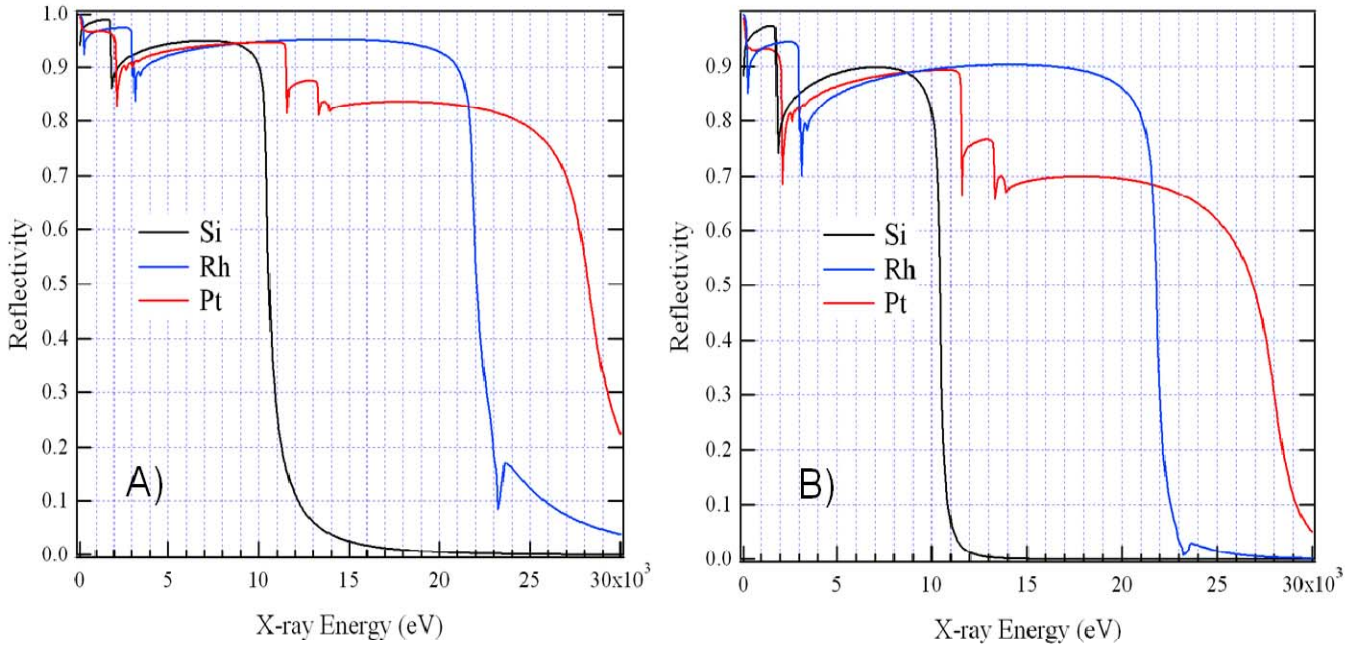

Figure 2.6.2.1: A) Reflectivity of the HCM with three different reflecting surfaces. B) Combined reflectivity from the HCM and HFM. Combined reflectivity from the two mirrors provides enhanced harmonic rejection particular for the Rh surface above 23keV.

To ensure an adequate level of power reduction to the monochromator and effective harmonic rejection required for the x-ray microscopy experiments, the HCM has three reflecting surfaces. They are a bare Si surface of the substrate, Rh coating and Pt coating. Each stripe is 20 mm wide and has the same length as the substrate. Three reflecting regions are separated by a 5 mm gap from the neighboring regions. The reflectivity from the HCM and the combined reflectivity from the HCM and HFM (with identical reflecting surfaces) are shown in Figure 2.6.2.1A and 2.6.2.1B, respectively. The HFM is identical to HCM, except that it requires no cooling (see section 2.7.1).

The cut-off energies (based on 50% intensity reduction) for Si, Rh, and Pt surfaces are, ~10.5, ~21.8 and ~28 keV, respectively. Consequently, the Si surface is used for 6-10keV, the Rh surface for 10-21keV and the Pt surface above 21keV. For the energy range, 6-10keV, the higher order harmonic energies that can be transmitted through

the Si(111) monochromator by exciting the Si (333) reflection are in the range 18-30 keV. The combined reflectivity from both mirrors is $1.0x10^{-4}$ at 18keV and $1.0x10^{-6}$ at 30 keV. For operation at 11keV using the Rh surface, the harmonic rejection for 33 keV is $1x10^{-3}$. However, the NSLS-II flux at 33 keV is about 2.5 orders of magnitude lower than the intensity at 11keV. Thus, the intensity of 33 keV x-rays surviving through two mirrors and a monochromator is about 5.5 orders of magnitude lower than the intensity at 11 keV. The harmonic rejection provided by both the HCM and HFM is sufficient for the technical requirements of the HXN beamline.

Table 2.6.2.3 lists the estimated power delivered to, absorbed in, and transmitted from the HCM based on the geometric parameters shown in Table 2.6.2.1 and the filter setting shown in Table 2.6.1.1. The highest power is delivered at undulator energies corresponding to K=1.83, which are the higher order harmonics for the fundamental energy of 1.6 keV (i.e., 8, 11.2, 14.4, etc.). The maximum estimated incidence power is ~105 W with an average power density of $0.19W/mm^2$ on the mirror surface. The maximum estimated power absorbed on the HCM is ~41W at 8 keV on the Si surface. The highest estimated reflected power is ~63W at 8 keV. The estimated absorbed power of 22~41W is comfortably managed by side water-cooling or liquid Ga-cooling, without resorting to more aggressive cooling methods such as internal cooling or cryogenic cooling.

Table 2.6.2.3: Estimated power on the HCM vs. x-ray energy

Energy (keV)	Deflecting parameter (K)	Reflecting surface	Incidence power (W)	Incidence pwr. den. on mirror surface (W/mm^2)	Absorbed power (W)	Absorbed pwr. den. on mirror surface (W/mm^2)	Reflected power (W)
6	1.51	Si	94.5	0.17	37.3	0.0670	57.2
7	1.29	Si	76.6	0.14	30.2	0.0543	46.4
8	1.83	Si	104.6	0.19	41.3	0.0742	63.3
9	1.66	Si	94.6	0.17	37.3	0.0671	57.2
10	1.51	Si	78.1	0.14	12.4	0.0554	65.6
11	1.37	Rh	70.6	0.13	11.2	0.0500	59.3
12	1.73	Rh	90.2	0.16	14.4	0.0639	75.8
13	1.62	Rh	73.7	0.13	11.7	0.0523	62.0
14	1.51	Rh	68.6	0.12	10.9	0.0486	57.7
15	1.77	Rh	81.1	0.15	12.9	0.0575	68.2
16	1.68	Rh	65.1	0.12	10.4	0.0461	54.7
17	1.59	Rh	61.5	0.11	9.8	0.0436	51.7
18	1.79	Rh	69.9	0.13	11.1	0.0496	58.8
19	1.72	Rh	66.8	0.12	10.6	0.0473	56.1
20	1.65	Rh	63.8	0.11	10.2	0.0452	53.6
21	1.81	Rh	70.6	0.13	11.3	0.0501	59.4
22	1.75	Pt	67.9	0.12	10.8	0.0482	57.1
23	1.69	Pt	52.8	0.09	7.0	0.0374	45.8
24	1.82	Pt	57.5	0.10	7.6	0.0408	49.9
25	1.77	Pt	55.6	0.10	7.3	0.0394	48.3

Finite element analysis (FEA) was performed to investigate the impact of the incidence power on the mirror surface. The analysis used the boundary conditions for a Si mirror with a dimensions, 1m (L) x 80mm (W) x 50mm (H) which was sided cooled with a Cu-In-Si interface. A heat transfer coefficient value of $1W/cm^2/C°$ was used. Two scenarios were investigated; A: incidence power of 159W and B: 120W. Case A corresponds to unfiltered power of an x-ray beam with an angular aperture of 80 μrad (H) x 30 μrad (V). Case B corresponds to filtered power using a 100-μm thick diamond filter. The results of the FEA investigation are shown in Table 2.6.2.4 and Figure 2.6.2.2 (next page).

Table 2.6.2.4: Finite-element analysis for the HCM. The central region corresponds to the region of the mirror corresponding to the angular acceptance of the monochromator (see Figure 2.6.2.2).

Case	Incidence Power [IP] (W)	IP density on surface (W/mm²)	Absorbed P. density on surface (W/mm²)	Bulk temp (C)	Max. temp (C)	Min. temp (K)	Tangential slope error (μrad)	Slope error for central region (rad)	Estimated uncompensated slope error (rad)
A	159	0.250	0.099	25	26.4	25.1	5.0	3.0	< 0.2
B	120	0.189	0.074	25	26.0	25.0	4.0	2.0	< 0.2

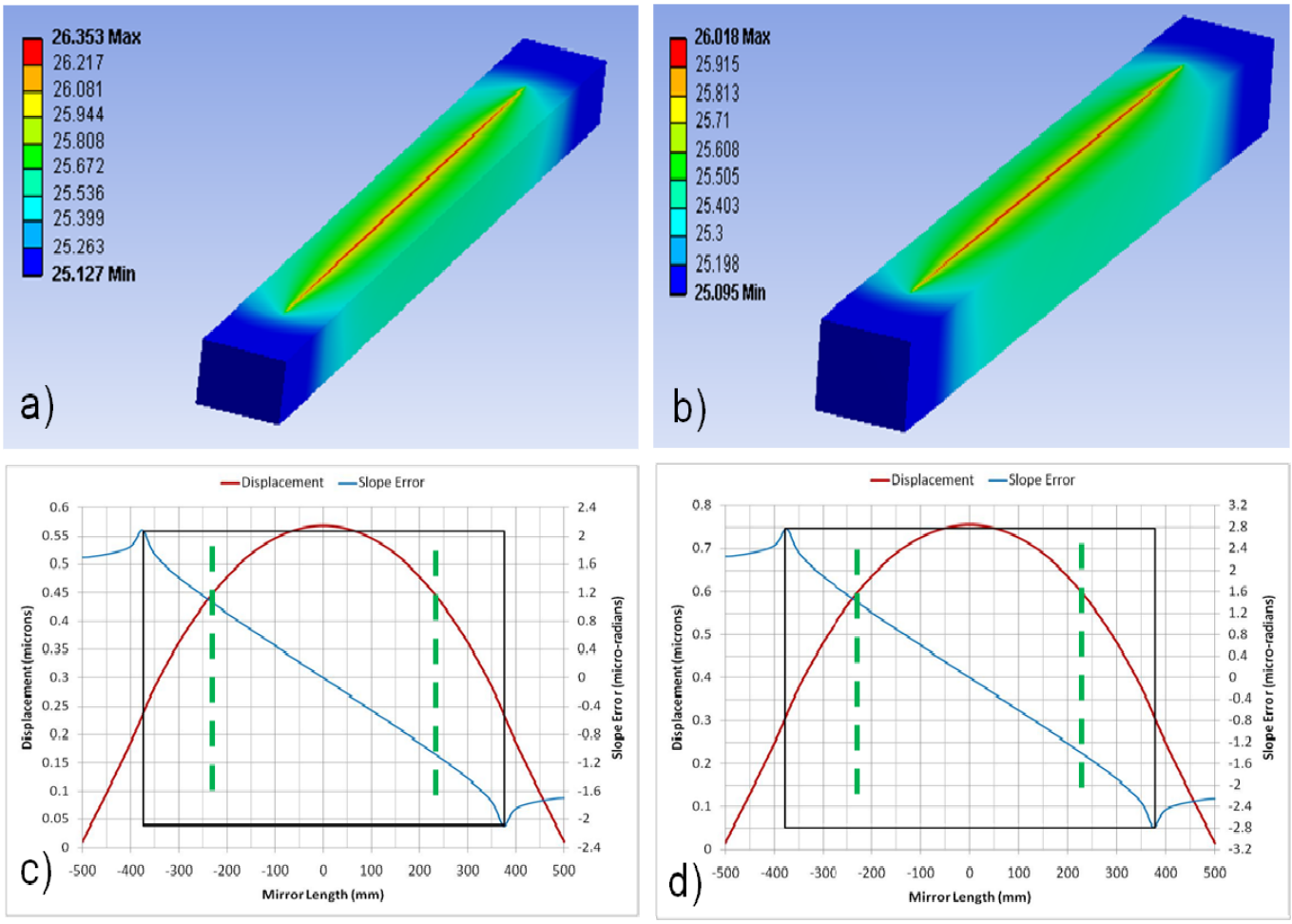

Figure 2.6.2.2: Finite element analysis for the HCM. The temperature is given in C°. The black box indicates the footprint of the beam. The green dotted line indicates the region of the mirror, corresponding to the angular acceptance of the monochromator.

For case A, the maximum temperature is 1.4 C° higher than the outer region in contact with the cooling block and 1.0 C° for case B. Small temperature differences indicate that the absorbed power is well dissipated by the side cooling. A higher temperature cause convex bending of the mirror. The red curves in Figure 2.6.2.2c and 2.6.2.2d show the displacements of the mirror surface. The thermally induced slope error curves (blue line) are computed by taking the derivative of the displacement. The numerical value of the tangential slope errors are shown in Table 2.6.2.4. The slope error for the entire footprint (indicated by black boxes) has contributions from "edge" effects. The monochromator receives the reflected x-rays from the central region of the mirror (indicated by the green dotted lines). The tangential slope error over the central region is 3.0 μrad for an incident power of 159W and 2.0 μrad for 120W. The FEA simulations used a somewhat larger size of the beam than intended, in order to investigate the worst case scenario. As indicated in Table 2.6.2.2, the estimated absorbed power densities on the

mirror surface are all smaller than case A. Therefore, the thermally induced slope error is expected to be less than 2.0 μrad for most of the operating energy range of the HXN beamline. During normal operation of the HXN beamline, the effective thermally induced slope error is expected to be substantially smaller than 2.0 μrad. The induced bending curvature, as shown in Figure 2.6.2.2, is highly symmetric due to the Gaussian-like power distribution and the symmetric dissipation of the incident power. Consequently, the induced bend curvature, which leads to defocusing of the reflected beam, can be corrected if a proper compensation can be made. This concept has been already presented extensively in the CD2 report of the HXN beamline [2.6.2.1]. Because of its importance, a brief summary of this concept is given below.

The red curve in Figure 2.6.2.3 shows a thermally induced displacement of the mirror surface caused by an absorbed total power of 130.6W. The blue line indicates the ideal mirror bend, demanded by the optical condition of the beamline. The black line indicates the curvature of the mirror that is required to compensate for the thermally induced curvature, in order to achieve the ideal mirror bend. The uncompensated residual slope error after the corrective over-bending of the mirror in this particular simulation was 0.16μrad in the 80% of the central region of the mirror. In horizontal reflection geometry, the self-weight of the mirror does not contribute to the final bending curvature. Consequently, implementation of the corrective bending is much more straightforward. Since the HXN beamline has two horizontally bendable mirrors (HCM and HFM) before and after the horizontal monochromator, these mirrors can be used to make corrections for the thermally induced slope error even for the monochromator, as long as the distribution of the slope error is symmetric and well-understood. During the commissioning of the HXN beamline, various corrective schemes will be explored.

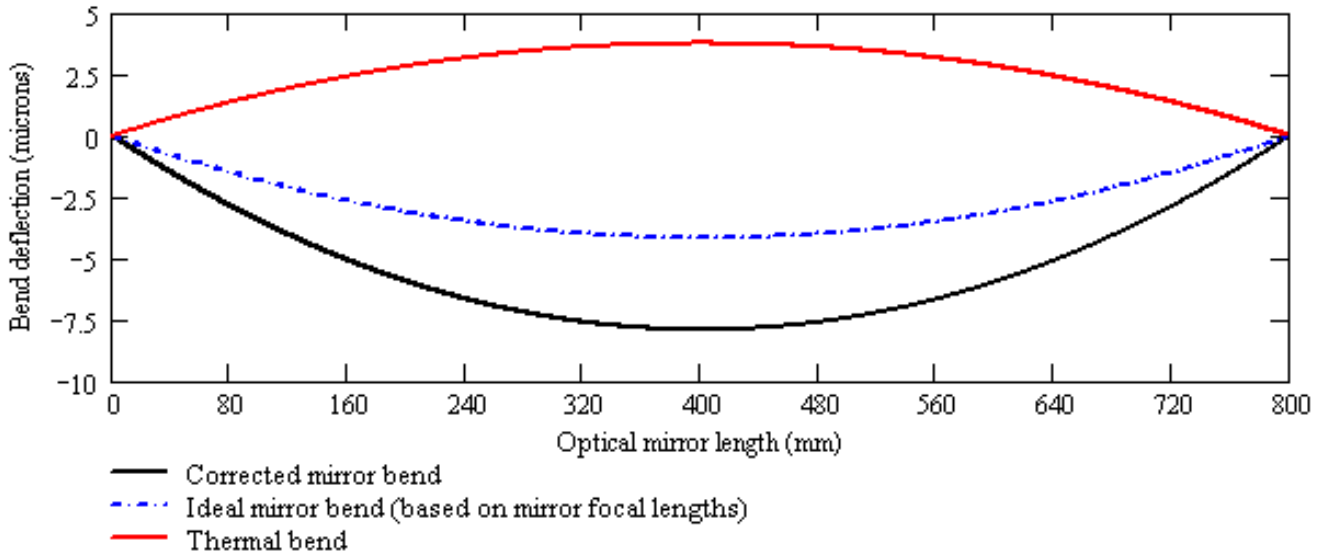

Figure 2.6.2.3: Compensation of the thermally induced slope error by over bending the mirror. The simulation has been performed by IDT.

Horizontally reflecting white beam mirrors with very high stability, and similar capabilities are commercially available through a few well-established synchrotron instrumentation vendors such as Bruker ASC (the former ACCEL), IDT, and FMB-Oxford. For example, the horizontally reflecting white beam mirror (elliptically bendable with side water-cooling) at the Nanoprobe beamline of the APS was produced by ACCEL. This mirror was designed for a much higher total power and a shorter focal length than the HXN requirement. IDT has produced a horizontally reflecting white beam mirror with focusing capability for the XFM beamline (Australian Synchrotron) and has demonstrated a high level of mechanical stability. FMB-Oxford is currently constructing a horizontally reflecting white beam mirror for beamline I13L at the Diamond Light Source, which has mechanical design features developed to meet the specifications for extremely high stability (0.1μrad), fine pitch resolution (50 nrad), a total power of 110W, and a 0.5 μrad slope error.

Figure 2.6.2.4 shows the 3D models of commercially available horizontally focusing mirrors with white beam capability. The FMB-Oxford mirror (Figure 2.6.2.4A) is supported by rods secured on a high-stiffness vertical granite elevator, placed on a granite support. The vacuum chamber (not shown) is supported by a metal frame, mechanically isolated from the granite block supporting the mirror. This mirror is designed to have a minimum number of degrees of freedom to insure high mechanical stability. The IDT mirror (Figure 2.6.2.4B) uses a liquid Ga-cooling method in order to eliminate potential vibration concerns (not shown). The vacuum vessel is supported by three kinematic support jacks mounted on a granite support providing yaw and vertical translation (needed to select the desired stripe on the mirror). The horizontal position and pitch adjustment of the mirror bender (not shown) are provided by two "through-vacuum" linear actuators. A large horizontal track mounted on the raised portion of the granite is used to open the vacuum chamber. The vertical base plate and the mirror assembly are retracted from the vacuum enclosure by the large horizontal track. No further technical details will be given in this document in order to protect the vendor's interests.

The horizontally collimating mirror (HCM) for HXN has stringent mechanical stability and figure error requirements. The power management scheme is designed to minimize the thermally induced slope error. The bending capability will be used to compensate for estimated induced slope errors less than 3 μrad in the central region of the mirror. The design requirements, though stringent, can be met by available commercial products.

[2.6.2.1] NSLS-2 Design study: Nanoprobe beamline, NSL-100-50-01.

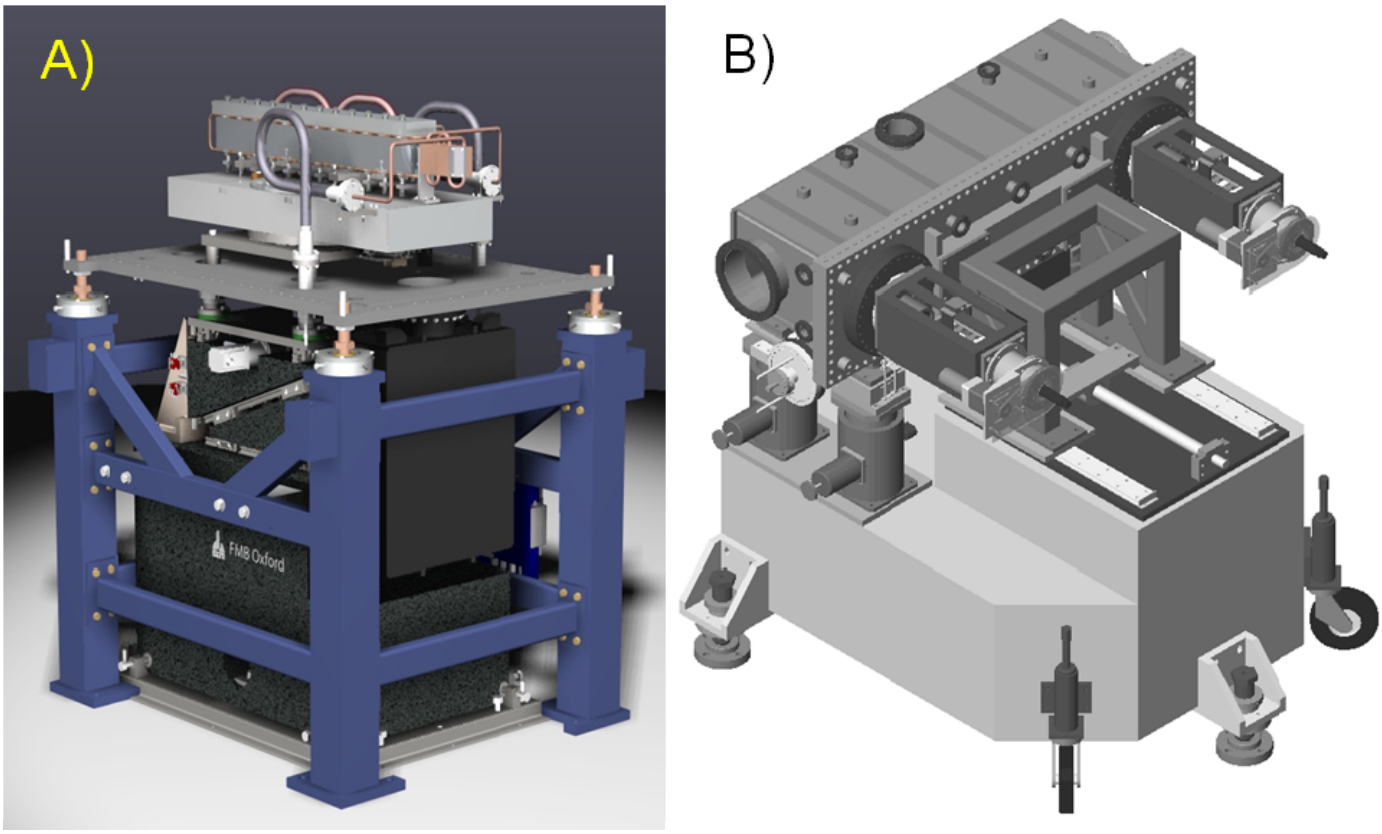

Figure 2.6.2.4: Examples of commercially available horizontally focusing mirrors. A) 3D model of a high-stiffness horizontal mirror with wide water cooling from FMB-Oxford. This mirror is fully developed and is scheduled to be installed at beamline I13L at the Diamond Light Source this year. Courtesy of FMB-Oxford. B) 3D model of a horizontally focusing mirror with a liquid Ga cooling from IDT. This mirror has been commissioned and is used at the XFM beamline of the Australian Synchrotron. Courtesy of IDT.

2.6.3 Horizontally diffracting crystal monochromator (DCM)

The HXN monochromator is designed to diffract the x-rays in the horizontal plane for the following reasons:

- The IVU20 undulator has a larger source size and angle in the horizontal direction. Thus, given the same mechanical stability and level of the thermally induced slope error on the monochromator crystal, horizontal diffraction leads to better overall optical performance.
- The horizontal geometry provides a more stable mechanical structure. In a horizontal geometry, the distance between the crystals and the supporting granite can be significantly reduced, leading to a shorter lever arm by which vibrations from the support system can be amplified. In addition, all the rotations and most of the translations are in the horizontal plane, leading to better mechanical stability.
- Gravity is acting in a direction that is insensitive to the crystal diffraction.
- As will be shown later, the FEA analysis reveals that horizontal diffraction leads to a lower peak temperature on the crystal surface due to the incidence power.

The two major technical concerns for the DCM are:

- To achieve an angular stability of the diffracted beam down to 0.1 μrad or better, by increasing the mechanical stiffness of the crystal cage and the second monochromator crystal and minimizing the vibrations induced by the cryogenic cooling
- To minimize the thermally induced slope error on the first monochromator crystal

Table 2.6.3.1 summarizes the overall specification for the DCM and Table 2.6.3.2 summarize the requirement for the motion degrees of freedom for the DCM.

Table 2.6.3.1: Specifications for the Horizontally Diffracting Monochromator

Description	Horizontally diffracting crystal monochromator
Monochromator crystal	Si (111)
Diffraction geometry	Horizontal double diffraction
Energy range	6-25 keV
Minimum Bragg angle range	4.5° – 20°
Distance from the source	30.4 m
Configuration	Fixed exit for all energy range
Beam offset	10 mm or smaller provided by flexure-based motion
1st Crystal dimensions	40 mm long x 40 mm wide x 50mm high
2nd Crystal dimensions	60 mm long x 40 mm wide x 50 mm high
Maximum absorbed power	52 W
Nominal beam acceptance	50 (H) x 25 (V) μrad
Cooling method for the 1st crystal	Cryogenic cooling with liquid nitrogen
Cooling method for the 2nd crystal	Cooling through Cu braids
Angular stability of the 2nd crystal, θ2	0.1 μrad or better
Special requirement	Pseudo channel-cut configuration for the highest level of angular stability of the exit beam. Minimum number of motion degrees of freedom to ensure the highest level of mechanical stability.

Table 2.6.3.2: Motions for the monochromator crystals

Motorized Motion	Range	Resolution	Drive System
Bragg angle (i.e., energy), rotation of the crystal cage containing both crystals	-5° to 30°	<2 µrad	In vacuum stepper motor driven
Coarse pitch for 2nd crystal ($\theta 2$, about y-axis)	±1°	<5µrad	In vacuum stepper motor driven
Fine pitch for second crystal pitch ($\theta 2$, about y-axis)	200µrad	<0.05µrad	In vacuum piezo driven
Coarse roll for 2nd crystal ($\chi 2$, about z-axis)	±1°	<5µrad	In vacuum stepper motor driven.
Fine roll for 2nd crystal ($\chi 2$, about z-axis)	200µrad	<0.05µrad	In vacuum piezo driven.
Perpendicular translation for 2nd crystal (fixed offset)	±0.5mm	<1µm	Flexure based motion to increase the mechanical stiffness.
Manual Motion			
Pitch for the support system (rotation about y-axis)	±1°	<0.25°	System alignment
Roll for the support system (rotation about z-axis)	±1°	<0.25°	System alignment
Horizontal translation for the support system (x-axis)	±10mm	<250µm	System alignment
Vertical translation for the support system (y-axis)	±10mm	<250µm	System alignment
Longitudinal translation for the support system(z-axis)	±10mm	<250µm	System alignment

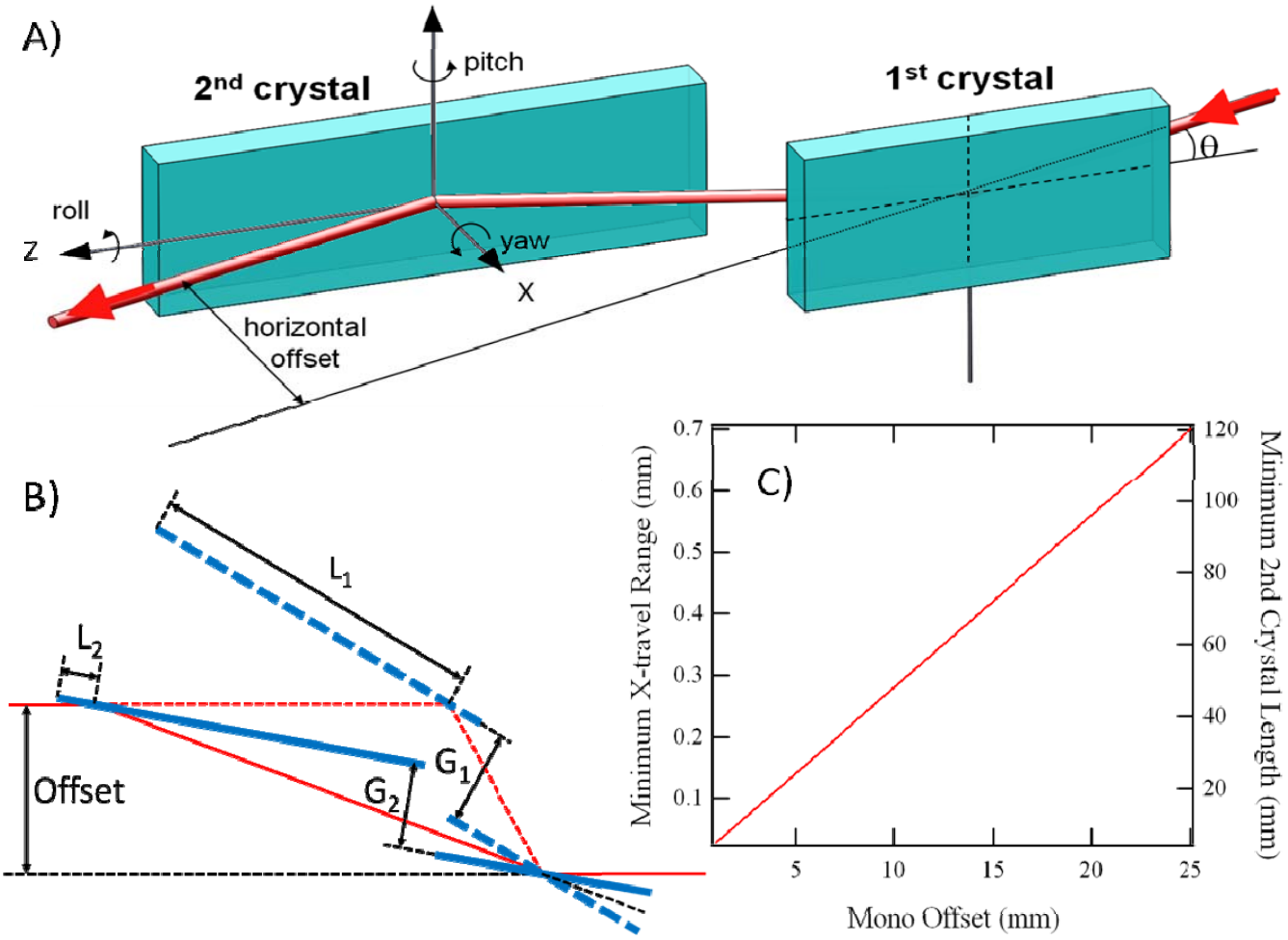

Figure 2.6.3.1 A) Schematic view of the DCM. B) Schematic representation of meeting "the fixed-exit" condition without sliding translation (z-motion) of the second crystal. C) Minimum requirement for the second crystal x-travel range (normal to the surface) and second crystal length as a function of the monochromator offset.

The geometric arrangement of the DCM is shown in Figure 2.6.3.1A. The coordinates shown there are for the reference frame of the second crystal (i.e., Y-Z plane on the surface of the second crystal). When referring to the first crystal, we use a similar coordinate system attached to the surface of the first crystal. In order to ensure the highest stability, the DCM will be designed as a "pseudo channel-cut." That is, the second crystal will have a limited number of degrees of freedom and limited travel range. Such an arrangement will allow the use of high-stability linear flexure-based stages.

Figure 2.6.3.1B shows the "fixed-exit" geometry of the pseudo channel-cut. In the absence of the "sliding" motion of the second crystal (along the z-axis), the condition for achieving the same exit position of the diffracted beam (i.e., fixed-exit condition) requires small translational motions of the second crystal normal to the surface (i.e., along the x-axis). The drawback of this arrangement is that the diffracted beam from the first crystal walks across the second crystal when the energy is changed (represented by L_1 and L_2 in Figure 2.6.3.1B).

Figure 2.6.3.1C shows the minimum requirement of the x-translation for the second crystal and the length of the second crystal, as a function of the monochromator offset. For our target mono offset of 10 mm, the minimum required x-translation range is less than 0.3 mm. With careful pre-positioning of the crystals, a total travel range less than 1 mm will be sufficient. This small travel range provides options for using high-stability flexure-based translational motion that will maximize the mechanical stability of the second crystal. Furthermore, a small monochromator offset decreases the required length of the second crystal, increasing the overall stiffness of the second crystal. Additionally, in a horizontal geometry gravity is acting in a direction transverse to the scattering plane of the crystal. Consequently, any gravity induced mechanical bending or distortion of the crystal, crystal cage, translation and rotation stages, or supporting structure lead to a smaller impact on the stability of the diffracted beam, when compared with a vertical geometry. As listed in Table 2.6.3.2 above, some of the motorized motions present in conventional monochromators are absent for the DCM, and these less critical adjustments will be made manually and locked afterward to ensure the highest level of stability.

The estimated incidence power on the monochromator is shown in Table 2.6.3.3 as a function of the x-ray energy. The calculation accounts for the transmitted power from the filter and the subsequently reflected power from the HCM through an angular aperture size of 50 μrad (H) x 25 μrad (V), set by the pink beam slits. The estimated power ranges from 19 to 52W and the power density on the crystal surface from 10.5 to 2.2 W/mm^2. Although the highest incidence power of 52 W is illuminated on the first crystal at 14.4 keV, corresponding to K=1.83, the highest surface power density of 10.5 W/mm^2 occurs at 6 keV, due to the largest Bragg angle.

To estimate the thermally induced slope error on the first crystal of the monochromator, finite element analysis (FEA) investigation has been performed under several conditions. The FEA investigation was intended to explore the worst-case scenario and uses higher power (and power density) than the actual case. A total of eight different simulations have been performed. The input parameters for the FEA are listed in Table 2.6.3.4, together with the results. Key input parameters for the FEA are:

- Incident power and power density on the crystal surface
- Heat transfer coefficient (h_{cv}).
- Bulk temperature

The FEA simulations used different sizes of the beam. In all cases, the used power densities on the crystal surface were larger than the actual value for the energy (see Table 2.6.3.4). In the FEA investigation, three different values of h_{cv} were used. Based on a published work [2.6.3.1], a coefficient value of 3000 W/K/m_2 corresponds to fair thermal contact between Cu and Si for cryogenic side-cooling. A coefficient value of 5000 W/K/m^2 corresponds to excellent thermal contact. A coefficient value of 2120 W/K/m^2 is based on empirical data from the monochromator produced by IDT, which performed FEA case G and H in the Table 2.6.3.4.

Table 2.6.3.3: Energy dependent power loading on the horizontal diffracting monochromator. The calculation was based on an x-ray beam with a solid angle of 50 μrad (H) x 25 μrad (V).

Energy (keV)	Deflecting parameter (K)	Bragg angle (deg)	Horiz. footprint (mm)	Incidence power (W)	Absorbed power (W)	Absorbed pwr. Density on mono surface (W/mm^2)
6	1.51	19.239	4.28	34.0	34.0	10.47
7	1.29	16.406	4.99	27.6	27.6	7.27
8	1.82	14.308	5.71	37.7	37.7	8.69
9	1.66	12.690	6.42	34.1	34.1	6.99
10	1.51	11.403	7.13	39.1	39.1	7.21
11	1.37	10.354	7.84	35.3	35.3	5.92
12	1.73	9.483	8.56	45.1	45.1	6.94
13	1.62	8.748	9.27	36.9	36.9	5.24
14	1.51	8.118	9.98	34.3	34.3	4.52
15	1.77	7.574	10.70	40.6	40.6	4.99
16	1.68	7.098	11.41	32.6	32.6	3.76
17	1.59	6.678	12.12	30.8	30.8	3.34
18	1.79	6.306	12.84	35.0	35.0	3.59
19	1.72	5.973	13.55	33.4	33.4	3.24
20	1.65	5.673	14.26	31.9	31.9	2.94
21	1.81	5.402	14.98	35.3	35.3	3.11
22	1.75	5.156	15.69	34.0	34.0	2.85
23	1.69	4.931	16.40	27.3	27.3	2.19
24	1.82	4.725	17.12	29.7	29.7	2.28
25	1.77	4.536	17.83	28.7	28.7	2.12

Table 2.6.3.4: Finite-element analysis for the DCM. The power density used is significant higher than the actual case

Case	h_{cv} (W/m^2)	Power	X-ray energy (keV)	Footprint H x V (mm x mm)	Surf. P density (W/mm^2)	Bulk temp (K)	Max. temp (K)	Min. temp (K)	Slope error μrad	Darwin width rad	Mono transmission
A	3000	53 W	8	4.8 x 0.6	17.27	77	98.9	86.5	4.0	34.5	0.89
B	3000	105 W	8	7.2 x 0.9	17.35	77	116.5	95.5	1.2	34.5	0.97
C	3000	201 W	8	9.7 x 1.2	17.27	77	150.0	109.0	36	34.5	0.22
D	5000	53 W	8	4.8 x 0.6	17.27	77	94.0	82.6	4.6	34.5	0.88
E	5000	105 W	8	7.2 x 0.9	17.35	77	105.8	88.1	4.8	34.5	0.87
F	5000	201 W	8	9.7 x 1.2	17.27	77	127.0	96.1	4.8	34.5	0.97
G	2120	94 W	6.5	5.9 x 0.9	17.65	80.5	118.8	94.8	7.1	43.5	0.94
H	2120	94 W	25	22.8 x0.9	4.59	80.5	102.3	94.8	2.9	10.5	0.75

Figure 2.6.3.2A and Figure 2.6.3.2B show the temperature distribution on the first crystal surface for FEA cases A and B in Table 2.6.3.4, corresponding to a total power of 53 W and 105 W. The resulting maximum temperatures are 98.9K and 116.5K, respectively. The simulation used a bulk temperature of 77K. Consequently, the maximum and minimum temperatures are about 21.9K and 39.5K above the temperature of the Cu cooling blocks. The minimum temperature is largely determined by the heat transfer rate between Cu and Si.

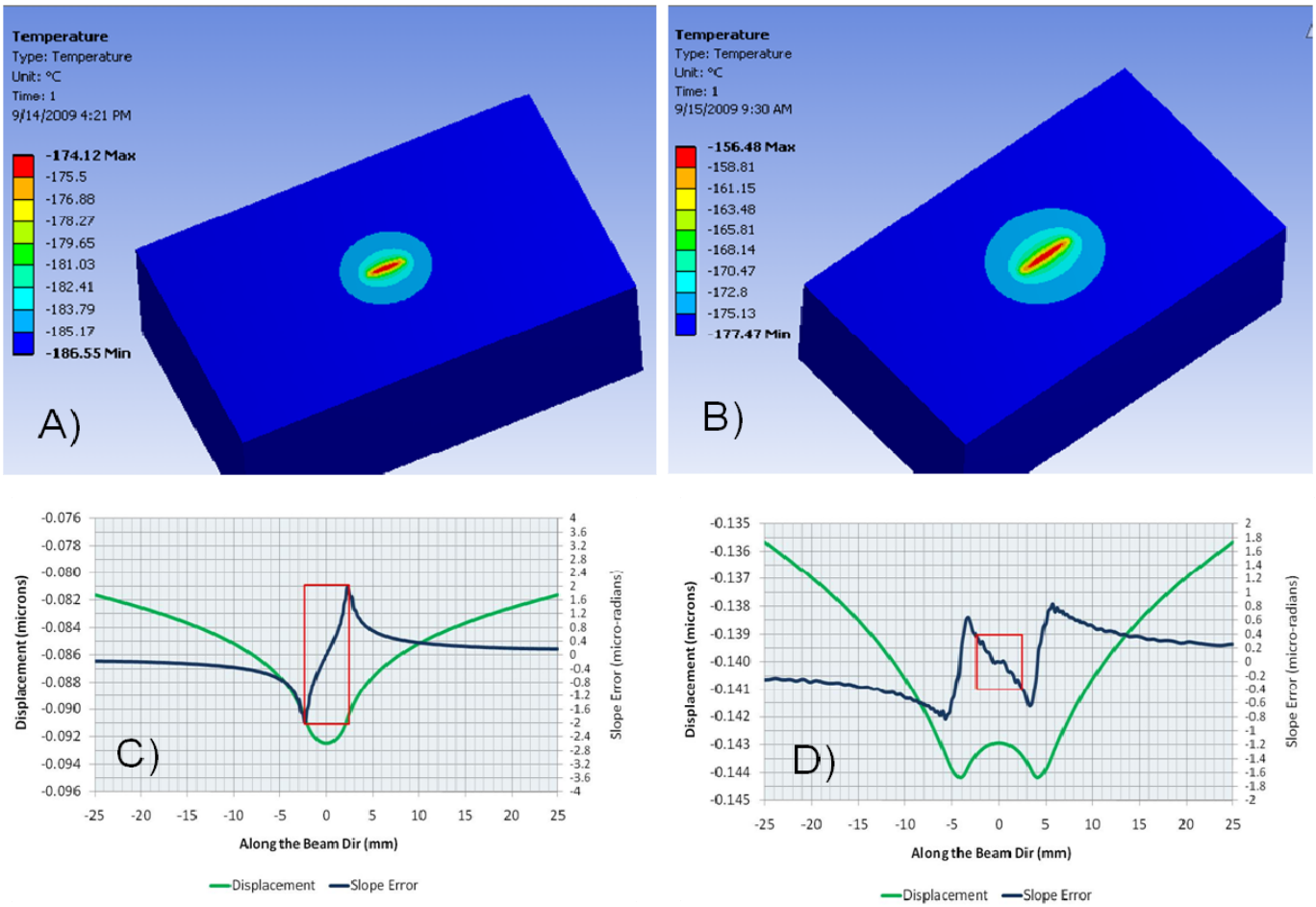

Figure 2.6.3.2: Finite element analysis results. A) Temperature on the first crystal due to an x-ray beam with a footprint of 4.8 mm (H) x 0.6 mm (V) with a total power of 50W. B) Temperature on the first crystal due to an x-ray beam with a footprint of 7.2 mm (H) x 0.6 mm (V). C) The thermally induced displacement and slope error for A). D) The thermally induced displacement and slope error for A). The red box in C) and D) identifies the same region of the crystal.

The resulting slope errors due to the expansion of the Si for both cases are shown in Figure 2.6.3.2C and Figure 2.6.3.2C. An interesting finding is that case B, despite the higher incidence power, produces a lower slope error. This is because the thermal expansion coefficient for Si is nonlinear. A total incidence power of 201 W results in an extremely large value of the slope error. The values contained in the last column of Table 2.6.3.4 were produced by estimating the overlap between the rocking curves of the first and second crystal. In the absence of the slope error, the two rocking curves overlap completely, resulting in 100% transmission through the double crystal monochromator. Thus, the figure of merit is not the absolute size of the thermally induced slope error but its size in comparison to the intrinsic Darwin width of the Si (111) at a specific energy. For example, the thermally induced slope error of 7.1 μrad at 6.5 keV (case G) results in higher transmission through the double crystal monochromator than 4.0 μrad at 8 keV. For the expected HXN incidence power, the transmission through the monochromator is expected to be better than 85% for the entire operation energy range.

Two important conclusions can be drawn from the FEA investigation. First, in all the cases with the exception of case C, the induced slope errors are on an acceptable level. For case C, the total power is too large for the cooling rate and the resulting maximum temperature is quite large. The same power condition with a higher heat transfer coefficient value significantly lowers the maximum temperature, resulting in a smaller slope error. Second, the simulation results suggest that the induced slope error is not a fast function of h_{cv} as long as the total power is not too large, which agrees with the published work by Zhang et al. [2.6.3.1]. According to this work, for a power less than 300 W, the thermally induced slope error is linearly dependent on the total power without a strong dependence

on the value of the h_{cv}. Based on this work, the expected slope error for 100 W is ~2.5 μrad, which is consistent with our FEA investigation.

In the HXN conceptual design, the primary high heat load optics (the mirror and monochromator) are placed in a horizontal reflection/diffraction geometry. The benefits of using a horizontal geometry for the mirror and monochromator are explicitly mentioned in the beginning of sections 2.6.2 and 2.6.3. Here we present the FEA results comparing the temperature distribution on the monochromator crystal between the vertical and horizontal diffraction geometries under the identical incidence power and boundary conditions. The temperature distributions on the monochromator crystal surface for both cases are shown in Figure 2.6.3.3.

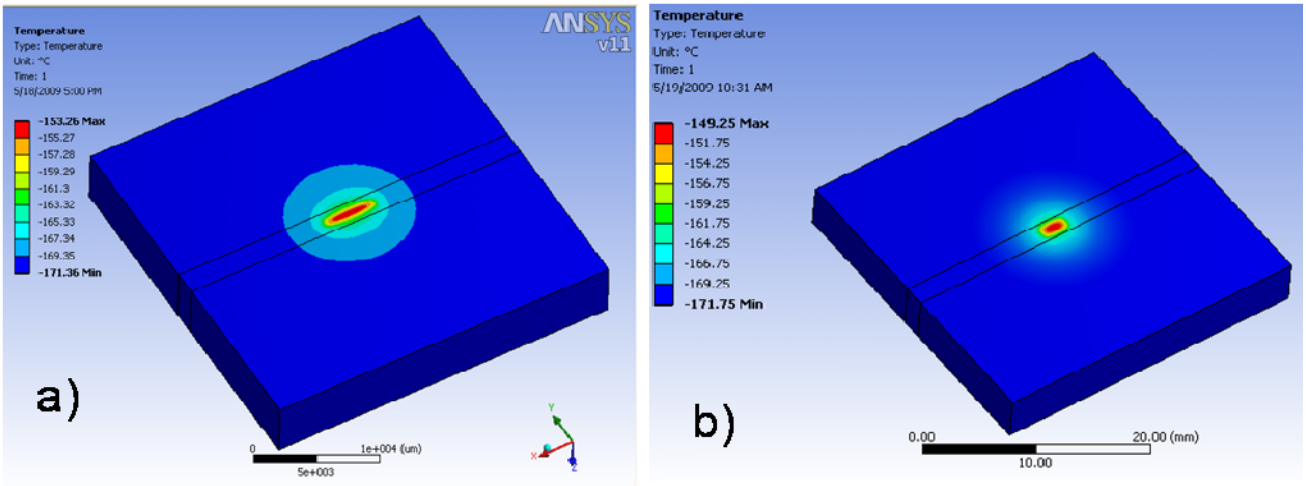

Figure 2.6.3.3: Comparison of the FEA simulated temperature distributions on the Si monochromator crystal placed in a) horizontal diffraction geometry and b) vertical diffraction geometry. With identical power and boundary conditions, horizontal diffraction geometry leads to a lower surface power density and consequently a lower peak temperature. The lines show the tangential direction of the beam.

Because of the inherent asymmetry of the undulator source along the horizontal and vertical directions, the spread of the incident power density in a horizontal diffraction geometry leads to a lower power density on the surface, resulting in a lower peak temperature. For example, the FEA simulations shown in Figure 2.6.3.3 predicted a difference of 4 K in the peak temperature between the two cases. In addition, a larger thermal distribution for the horizontal case leads to a smaller slope error over the region of the crystal, where the x-rays are diffracted. Despite the large on-axis power density of the NSLS-II IVU20, the FEA investigations presented here demonstrate that the proposed incremental power reduction scheme of the HXN beamline taking advantage of a horizontal geometry leads to small amount of thermally induced slope error on the monochromator with better than 85% transmission efficiency through the double crystal monochromator. The low incidence power on the monochromator enables the use of less aggressive cooling methods that will ultimately result in a much lower level of vibration on the monochromator crystals.

Certainly, there are a fewer number of commercial options for horizontal monochromators than horizontal mirrors, because the source properties of most of the existing synchrotron facilities are not favorable for horizontal diffraction. With the development of synchrotron sources with relatively small horizontal source angle sizes, synchrotron instrumentation vendors are allocating more engineering efforts to develop horizontal monochromators. Based on our extensive technical discussion with the engineers from Bruker ACS, the existing design of their vertical monochromator can be easily converted to a horizontal monochromator with much higher stability, without significant engineering work. IDT already has a working horizontal monochromator, which has been commissioned and is being used at the XFM beamline of the Australian Synchrotron. This monochromator has demonstrated excellent mechanical stability and a high degree of energy stability. A schematic of this monochromator is shown in Figure 2.6.3.4A.

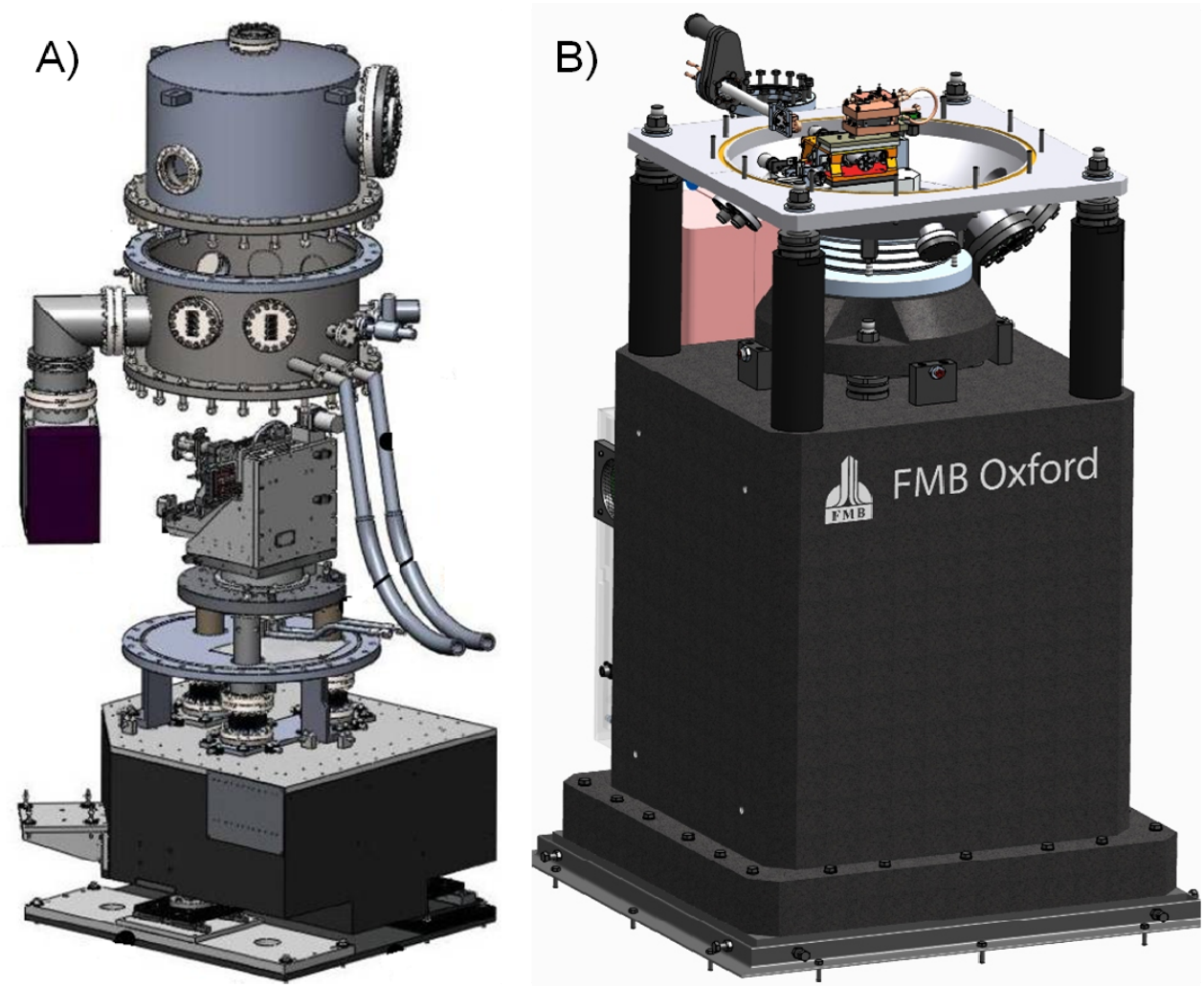

Figure 2.6.3.4: Examples of commercially available horizontally diffraction monochromator with liquid Nitrogen cryo-cooling. A) Horizontal monochromator produced by IDT. It has been commissioned and being used at the FXM beamline of the Australian Synchrotron. B) Prototype horizontal monochromator by FMB-Oxford.

The crystal assembly containing in-vacuum translation and rotation motions for the crystals is supported by three invar shafts through bellows. The supports for the vacuum vessel are mechanically de-coupled to the invar support shafts. The cryo-cooling lines are carefully engineered to eliminate the transmission of vibration from the cryo pump. The position of the granite support table can be manually adjusted and locked afterward. Recently, FMB-Oxford produced a prototype horizontal monochromator shown in Figure 2.6.3.4B. Considerable engineering efforts have been made to minimize the lever arm length from the supporting granite surface to the crystal assembly. The overall crystal assembly is designed to be extremely stiff and compact. The vacuum vessel is supported by four sturdy rods, mechanically de-coupled to the support of the crystal assembly. In this design, a water-cooled white beam stop is mounted behind the monochromator crystal. A massive granite table has manual adjustments, which can be further secured by grouting to the floor, in order to eliminate potential vibration amplification. Both monochromators are designed to provide high angular stability. The stability requirement for the HXN monochromator is extremely high (< 100 nrad, preferably ~50nrad). However, this is not beyond the current vendor capabilities, and viable commercial options exist.

[2.6.3.1] Lin Zhang, et. al., “The performance of a cryogenically cooled monochromator for an in-vacuum undulator beamline”, J. Synchrotron Rad. 10, 313-319 (2003).

2.7 Monochromatic beam optics

2.7.1 Horizontally focusing mirror (HFM)

The horizontally focusing mirror is required to image the primary source at SSA1 at z=65m for the high-resolution mode (mature scope) and SSA2 at z=94 for the high-throughput mode (baseline scope). It has virtually identical specifications and requirements as the horizontal collimating mirror with three exceptions:

- No cooling requirement due to handling of monochromatic x-rays
- Shorter length due to the incremental reduction of the solid angle from the HCM to DCM
- Requires higher pitch resolution (50nrad) in order to perform a beam positioning feedback to keep the horizontal focus at the secondary source aperture.

The specifications and motion requirements are summarized in Table 2.7.1.1 and Table 2.7.1.2. The HFM requires an RMS figure error of less than 0.5μrad in order to avoid considerable focus broadening at the secondary source aperture. In addition, the HFM requires angular stability better than 0.25 μrad, in order to avoid intensity fluctuations of the beam through the secondary source aperture. The commercial option for the HFM is not different from that of the HCM (see section 2.6.2).

Table 2.7.1.1: Specifications for the Horizontal Focusing Mirror

Description		Horizontal Focusing Mirror (HCM)
Substrate material		Single crystal silicon
Surface roughness, rms		< 3 Å
Slope error, rms		< 0.5 μrad (tangential), <2.0 μrad (sagittal)
Minimum beam acceptance		50 μrad (H) x 25 μrad (V)
Substrate dimensions		1000 mm long x 80 mm wide x 100 mm thick. The length can be shorter depending on the specific choice of bending mechanism.
Optically active length		700 mm in the center
Reflective coatings		Bare Si, Rh, Pt. Each reflecting region is a 20mm-wide stripe with 5mm gap to the nearby regions.
Coating thickness		~500 Å
Coating roughness		< 3 Å (rms)
Bending method		2 points or 4 points bending
Distance from the source		32.6 m
Focal lengths	F_1	∞ m
	F_2	32.4 m at SSA1 and 61.4m at SSA2
Reflection geometry		Horizontal reflection
Incidence angle	θ	Fixed at 3.0 mrad (0.1719°)
Radius of curvature $R = \frac{2}{\left(\frac{\sin(\theta)}{F_1} + \frac{\sin(\theta)}{F_2}\right)}$		21.6 km for focusing at SSA1 and 40.9 km for focusing at SSA2
Total power load		Negligible
Cooling		None
Angular stability		< 0.25 μrad
Special requirement		Minimum number of motion degrees of freedom for highest mechanical stability. Multiple external reference fiducial marks are needed for manual positioning.

Table 2.7.1.2: Requirement for motion degrees of freedom

Motion	Range	Resolution	Drive system
Coarse pitch (incidence angle)	-5mrad to +2mrad from nominal 3 mrad	<50 μrad	2 linear stepper motors or single rotation, extremely high mechanical stability required.
Fine pitch (incidence angle)	±200μrad	<0.05 μrad	Piezo actuation. Must enable feeback speed at 4Hz or faster
Vertical translation (selecting stripe)	±40 mm	<50μm	3 linear stepper motors, require extremely high mechanical stability and trajectory straightness
Horizontal translation	±5mm	<20 μm	2 linear stepper motors, require extremely high mechanical stability and trajectory straightness
Mirror bending	-10mm/ +30mm	<0.2μm	2 stepper motors
Manual horizontal translation	±25 mm	<250μm	Surveyed using fiducials
Manual yaw alignment	±1°	<0.05°	Surveyed using fiducials
Manual roll alignment	±1°	<0.05°	Surveyed using fiducials

2.7.2 Vertical focusing using CRL or kinoform (baseline scope)

The figure error requirement for vertical focusing by the HXN beamline optics is ~0.1 μrad (see section 2.9 for details). Fabricating mirrors with 0.1 μrad is now feasible for short mirrors (<300 mm). For longer mirrors, achieving ultra-low figure errors is still a technical challenge. In addition, maintaining a stable intensity of a small focused beam (~20 μm at ~60 m away from the vertical focusing optic) through a small secondary source aperture (~5 μm) requires an angular stability of ~30 nrad. An angular stability of 30 nrad corresponds to a positioning stability of 10% of the focused beam size over 60 m. Use of a double mirror system (focusing plus flat) to maintain such angular stability is a substantial technical challenge. In the baseline scope of the HXN beamline, the vertical focusing will be performed by either compound refractive lenses or kinoform lenses, in order to meet the stability requirements for the beamline.

Refractive optics have the advantage that the focused beam position is completely insensitive to the angular instability of the optics. The only requirement for maintaining the beam stability is to keep the lateral position of the optics constant. Achieving a positional stability of 10% of the beam size (i.e., 2.1 μm) is a trivial engineering task. For the HXN beamline, Be CRLs or Si kinoforms are considered. A major disadvantage is that refractive optics are highly chromatic. Changing the energy shifts the focal length. For the HXN beamline application, the focus will change from the position of the secondary source aperture. Figures 2.7.2.1E and 2.7.2.1F show the blurring of the beam size at the SSA2 and the transmission of x-rays through the SSA2 over a small energy range centered at 10.920 keV and 20.424 keV, respectively. The flat region in the center corresponds to the depth of focus of the Be CRL of 0.984 m at 10.920 keV and 0.526 m at 20.424 keV. A change of energy over 250 eV at 10.920 keV (400 eV at 20.424 keV) results in an intensity loss of less than 50% without measurable effects on the nanofocused beam size.

Table 2.7.2.1: Scheme for using Be CRLs with R = 0.5 mm to meet the optical requirement of the HXN beamline for both high-throughput and high-resolution modes. D_{eff} is the effective aperture size.

	SSA @ 94 m			SSA @ 65 m		
N	Energy (keV)	Transmission	D_{eff} (mm)	Energy (ev)	Transmission	D_{eff} (mm)
1	5.465	0.893	0.859	4.697	0.838	0.846
2	7.724	0.918	0.865	6.638	0.879	0.856
3	9.458	0.925	0.867	8.128	0.894	0.860
4	10.920	0.927	0.867	9.384	0.900	0.861
5	12.208	0.927	0.867	10.491	0.903	0.862
6	13.373	0.925	0.867	11.491	0.903	0.862
7	14.444	0.922	0.866	12.412	0.902	0.862

(Table 2.7.2.1 Continuing)

	SSA @ 94 m			SSA @ 65 m		
N	Energy (keV)	Transmission	D_{eff} (mm)	Energy (ev)	Transmission	D_{eff} (mm)
8	15.440	0.918	0.865	13.268	0.900	0.861
9	16.377	0.915	0.865	14.073	0.897	0.861
10	17.262	0.911	0.864	14.834	0.894	0.860
11	18.105	0.906	0.863	15.557	0.891	0.859
12	18.909	0.902	0.862	16.249	0.887	0.858
13	19.681	0.898	0.861	16.912	0.884	0.857
14	20.424	0.893	0.860	17.550	0.880	0.856
15	21.141	0.889	0.859	18.166	0.876	0.855
16	21.834	0.884	0.858	18.762	0.872	0.854
17	22.506	0.880	0.856	19.339	0.867	0.853
18	23.158	0.875	0.855	19.900	0.863	0.852
19	23.793	0.871	0.854	20.445	0.859	0.851
20	24.411	0.866	0.853	20.976	0.855	0.850
21	25.014	0.862	0.852	21.494	0.850	0.849
22	25.602	0.857	0.851	21.999	0.846	0.848
23	26.177	0.853	0.850	22.494	0.842	0.847
24	26.740	0.848	0.849	22.977	0.838	0.846
25	27.292	0.844	0.848	23.451	0.833	0.845
26	27.832	0.840	0.847	23.916	0.829	0.844
27	28.362	0.835	0.846	24.371	0.825	0.843
28	28.883	0.831	0.845	24.818	0.821	0.842
29	29.394	0.827	0.844	25.257	0.817	0.841
30	29.896	0.822	0.842	25.689	0.812	0.840
31	30.390	0.818	0.841	26.114	0.808	0.839

Be CRL

Be compound refractive lenses (CRL) have been used widely as an effective focusing and imaging optic [2.7.2.1, 2.7.2.2]. Recently, one dimensional Be CRLs have become commercially available (see Figure 2.7.2.1). The focal length of a CRL is determined by a simple relationship, $f = R/2fN\delta$, where f is the focal length, N is the number of lenses, δ is the real part of the index of refraction deviating from unity for the lens material, and R is the radius of curvature for the lens. A factor of 2 is due to the fact that each lens can be made with two parabolic interfaces. Table 2.7.2.1 summarizes a scheme that can provide vertical focusing at the SSA1 at z=65m and SSA2 at 94 m over an energy range from 6 to 25 keV, using 1 through 31 Be CRL lenses with R=500 μm. Be CRL lenses with R=500 μm are commercially available. Two important parameters in Table 2.7.2.1 are the transmission through the lenses and the effective aperture (D_{eff}), which defines the effective aperture size of the Be CRL. The operation scheme of the Be CRL lenses is developed with a specific requirement that the effective aperture is large enough to capture the available beam in the vertical direction, without significant absorption. Since the focal length requirement associated with SSA1 and SSA2 are quite different, the operation energies for two different modes are not the same. However, the proposed scheme ensures a large number of operation energies within 6-25keV.

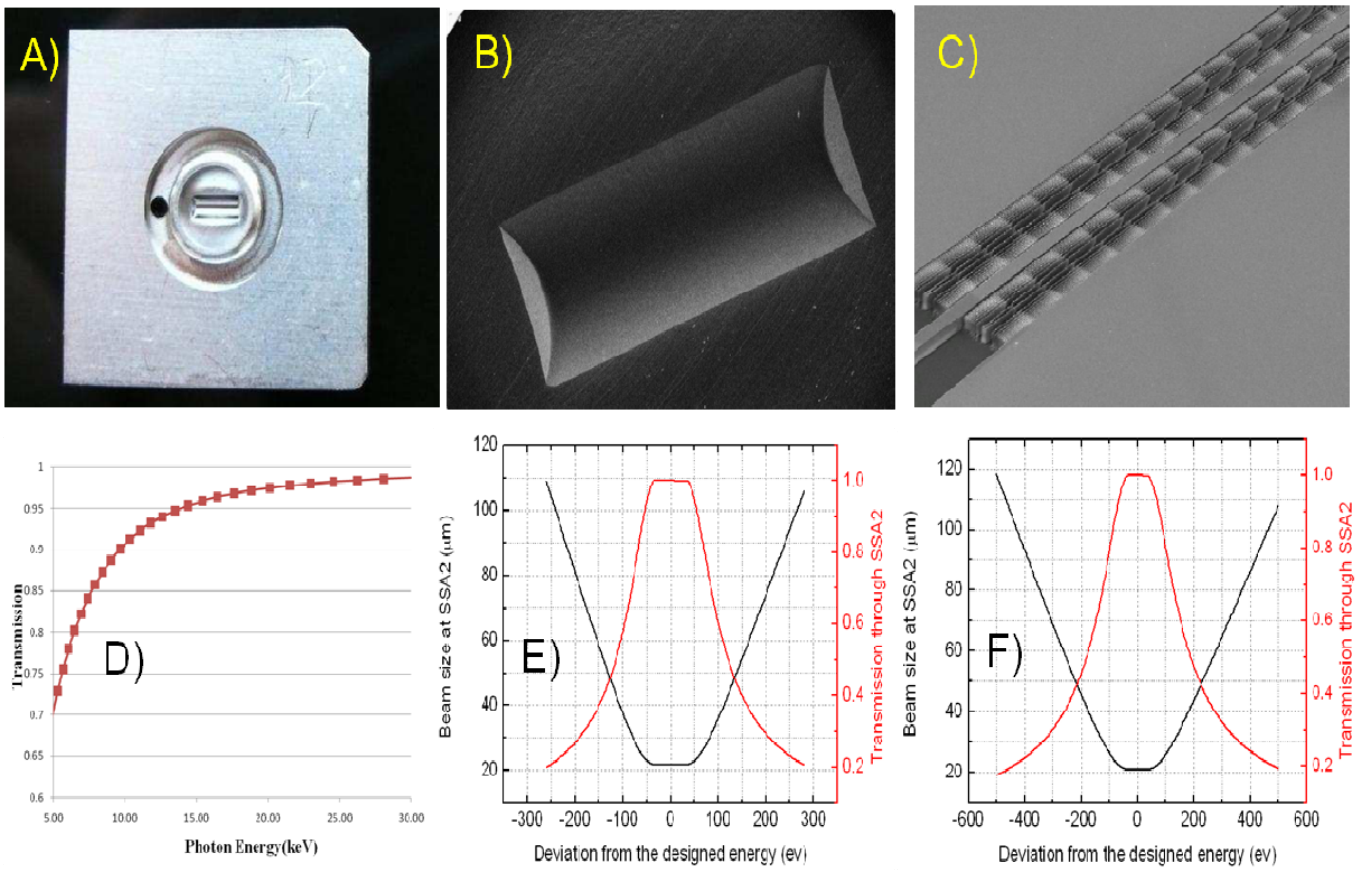

Figure 2.7.2.1: A) Photograph of a 1D parabolic Be CRL, Curtsey, B. Lengeler B) SEM Image of the Be CRL, Curtsey, B. Lengeler. C) Photograph of Si Kinoform lenses, Curtsey of K. Evans-Lutterodt. D) Transmission of the Si Kinoform lense discussed in the text. Beam size at SSA2 and transmission through SSA2 vs. energy centered at the designed value for Be CRLs. E) centered at 10.920 keV and F) centered at 20.424keV.

Si Kinoform

Use of single crystal Si rather than polycrystalline materials for fabricating x-ray lens eliminates possible diffuse scattering or unwanted phase contrast due to internal defects such as voids or large grain boundaries. Development of Si kinoforms at BNL has made significant progress over the last several years, spear-headed by Ken Evans-Lutterodt [2.7.2.3].

Here we discuss the possibility of using a silicon kinoform optic in order to vertically focus the source onto SSA1 at z=65 m and SSA2 at z=94 m, using a kinoform at z= 34.8 m. In order to integrate a 3-sigma source angle in the vertical direction, the effective aperture of the kinoform must be larger than ~800 μm. We propose a design with an aperture of 1 mm, which is larger than the required aperture. In fact, such a lens with a focal length of 30m has already been demonstrated at APS 32-ID with a similar focal length and apertures that exceeded 1 mm.

For this size aperture, the number of segments required for a kinoform implementation can be estimated. If the number of segments is 1 or fewer, then a refractive lens would be adequate. However, absorption of Si is considerably larger than that of Be and a simple Si CRL is not attractive. The size of a kinoform segment is set by the ratio of the wavelength λ to the refractive index decrement δ, and is the thickness required to give a 2π phase shift. At a typical value of 10 keV, the length of a kinoform segment $t_{2\pi} = \lambda/\delta = 26$ μm. Using the 1mm estimate of the total aperture, the distance from the optical axis to the thickest part of the refractive lens is half that, i.e., 500 μm. In a parabolic approximation for this estimate, T = $(\text{aperture})^2/(2.0\times\delta\times\text{focal length})$ ~700 μm. Consequently, the number of segments ($=T/t_{2\pi}$) is 20. Clearly using a kinoform would result in considerable gain.

Transmission through a Si kinoform lens over the operation energy range of the HXN beamline is shown in Figure 2.7.2.1D. The transmission of a single lens exceeds 90% at photon energies above 10 keV. Lenses with these parameters can be fabricated today. However the transmission at energies below 10 keV cannot be improved upon without going to a different material, namely single crystal diamond. A final consideration that could affect the transmission is the depth of the lens in the direction transverse to the focusing direction (i.e., the horizontal direction). As the depth of the lens increases, one may be required to use thicker segments than $t_{2\pi}$, but this would depend on mechanical design issues such as the curvature of the lens and the support on the two ends of the curve, and the mechanical continuity between all of the segments. Currently, considerable efforts are being made to increase the depth of the lens, in order to maximize the integrated flux in the horizontal direction for the HXN beamline.

CRL Transfocator

In order to maximize the utility of the CRLs over a wide energy range, a mechanism that can vary the number of lenses in the beam with a high level of positioning accuracy and stability is needed. This mechanical device is called a Transfocator, first developed at the ESRF ID11. Since the initial development, different engineering designs have been developed to meet the specific requirements of the hosting beamlines. The scheme presented in Table 2.7.2.1 can be implemented by a transfocator with 5 actuators that carry, 1, 2, 4, 8 and 16 pre-aligned lenses. Different permutation of the five actuators can provide a focusing capability using 0 to 31 lenses.

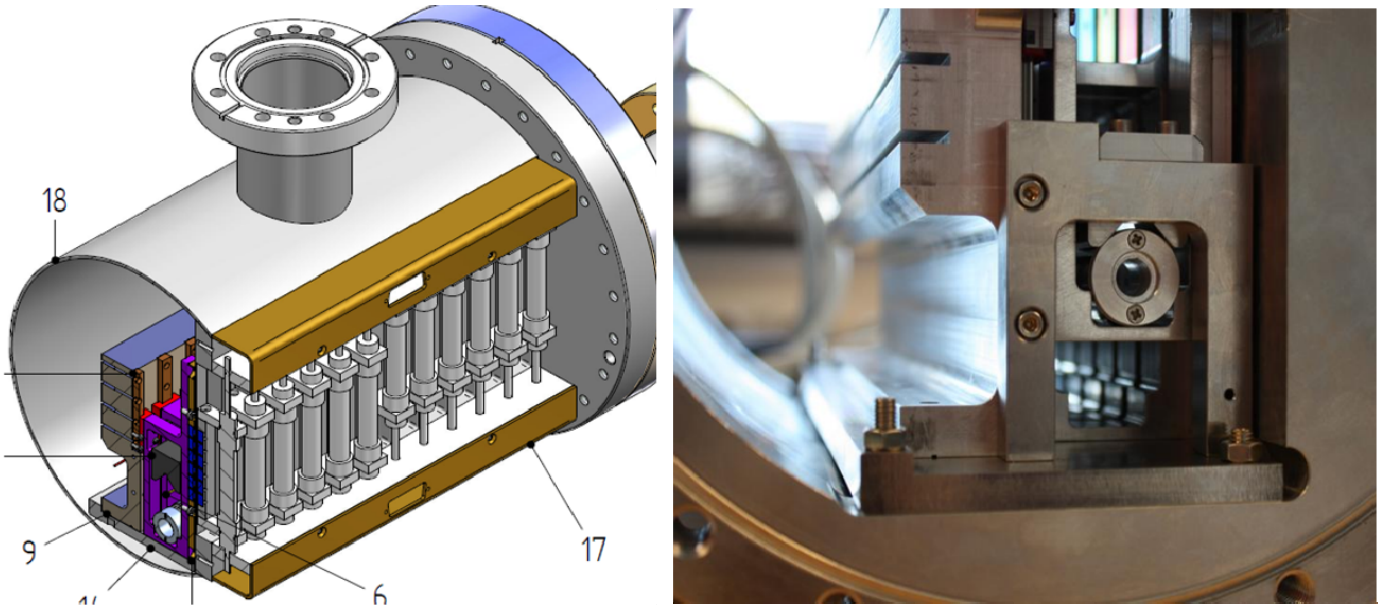

Figure 2.7.2.2: Transfocator developed at the Petra III and currently being used at beamline P08. A) 3D model of the actuation mechanism. B) Photograph showing the inside of the transfocator vacuum chamber. Curtsey of Dr. Oliver Seeck at Petra III.

For the HXN beamline, the transfocator must meet the following requirements:

- Operation in UHV.
- With the absence of aberration, the vertical focus size at SSA1 and SSA2 is 15 μm and 33 μm, respectively. In order to avoid a focus broadening of more than 25%, all the actuators must be aligned to better than 4μm accuracy, and each actuator must have a positioning repeatability better than 4 μm.
- In order to avoid intensity fluctuations of the x-ray beam transmitted through the secondary source, the transfocator and its support system must have a mechanical stability and RMS vibration better than ~2.1 μm, corresponding to 10% of the focused beam size.
- The transfocator is the only vertical optical component of the HXN beamline. To guard against any potential beam drift in the vertical direction (i.e., due to physical source motion from the undulator), the transfocator must provide sufficiently fast vertical translation motion, in order to enable efficient beam

position feedback. The vertical translation motion of the transfocator must have a positioning accuracy and repeatability better than ~0.5 μm.

The transfocator developed at Petra III by Oliver Seeck, Alexander Liehr, Tom Schubert, and Kathrin Pflaum is very close to meeting the HXN requirements. This instrument is installed and operating at beamline P08, already meeting the first three requirements listed above. Figure 2.7.2.2 shows a 3D model of the transfocator actuation system and a photograph showing the inside of the transfocator vacuum chamber. In order to meet the last requirement for the HXN beamline, we plan to reduce the total weight of the transfocator system by 1) reducing the total number of the actuators 2) reducing the size of the vacuum chamber and c) use of a high accuracy vertical stage. Development of the transfocator for the HXN beamline will be carried out in collaboration with Oliver Seeck and Kathrin Pflaum at Petra III.

[2.7.2.1] B. Lengeler, C.G. Schroer, M. Richwin, et al., "A microscope for hard x rays based on parabolic compound refractive lenses," *Applied Physics Letters* **74** (26), 3924-3926 (1999).

[2.7.2.2] Bruno Lengeler, Christian Schroer, Johannes Tummler, et al., "Imaging by parabolic refractive lenses in the hard x-ray range," *Journal of Synchrotron Radiation* **6** (6), 1153-1167 (1999).

[2.7.2.3] K. Evans-Lutterodt, A. Stein, J.M. Ablett, et al., "Using compound kinoform hard-x-ray lenses to exceed the critical angle limit," *Physical Review Letters* **99** (13), 134801-134804 (2007).

2.7.3 Vertical focusing using mirror system (mature scope)

In the baseline scope of the HXN beamline, Be CRL or Si kinoform is proposed because of the stringent angular stability and the figure error requirements for vertical focusing. As shown in sections 2.9 and 2.10, the figure error must be 0.1 μrad, if x-ray mirrors were to be used without causing significant flux loss for the nanofocused beam. Recently, mirror polishing capabilities have been dramatically improved and will continually improve with higher performance demands for x-ray mirrors. In the mature scope of the HXN beamline, we plan to use x-ray mirrors, in order to carry out x-ray microscopy experiments over a continuous energy range. In order to keep the x-ray beam position leveled, a mirror system with focusing and flat mirrors must be used. The technical specifications for the vertical mirror system are summarized in Table 2.7.3.1.

Table 2.7.3.1: Specifications for the vertical mirror system

Description		Vertical Mirror System
Number of mirrors		2; focusing mirror (reflecting up) and flat mirror (reflecting down)
Substrate material		Single crystal silicon
Surface roughness, RMS		< 3 Å
Slope error, RMS		~0.1 μrad (tangential), <0.5 μrad (sagittal)
Minimum beam acceptance		50 μrad (H) x 25 μrad (V)
Substrate dimensions		500 mm long x 80 mm wide x 50 mm thick. The length can be shorter depending on the specific choice of bending mechanism.
Optically active length		300 mm in the center
Reflective coatings		Pt
Coating thickness		~500 Å
Coating roughness		< 3 Å (rms)
Bending method		2 points or 4 points bending
Distance from the source		34.8 m
Focal lengths	F_1	∞ m
	F_2	30.2 m at SSA1 and 59.2 m at SSA2
Reflection geometry		vertical reflection with a fixed exit.

Table 2.7.3.1 continuing

Incidence angle θ	Fixed at 3.0 mrad (0.1719°)
Radius of curvature $R = \frac{2}{\left(\frac{\sin(\theta)}{F_1} + \frac{\sin(\theta)}{F_2}\right)}$	20.1 km for focusing at SSA1 and 39.4 km for focusing at SSA2
Total power load	Negligible
Cooling	None
Angular stability	< 35 nrad, 10% of the expected beam size (=2.1μm) 59.2 m away.
Special requirement	Minimum number of motion degrees of freedom for highest mechanical stability. Multiple external reference fiducial marks are needed for manual positioning. Beam position feedback is carried out using the pitch adjustment for the flat mirror located downstream. The angular resolution of the pitch must be better than 10nrad.

2.8 List of major components

2.8.1 Tabular list of components

Table 2.8.1.1 contains a list of all HXN Beamline components. Minor components and lengths of beampipe are included to account for all lengths along the beamline. Positions of hutch and building walls are also noted.

Table 2.8.1.1: List of HXN Beamline Components

Item	Description	Acronym	Length (m)	Position (m)	Station
	Fixed Mask	MSK1FE	0.30	19.26	FE
	White Beam Slits	SLT1FE	0.30	20.20	FE
	White Beam Slits	SLT2FE	0.30	20.74	FE
	Storage Ring Wall (downstream end)		1.45	25.47	A
1	Gate Valve	GV1	0.07	25.59	A
2	Bellows	BLW1	0.15	25.70	A
3	Diagnostic Chamber	BPM1	0.18	25.87	A
4	Bellows	BLW2	0.15	26.03	A
5	Mask	MSK	0.25	26.23	A
6	Collimator	CO	0.40	26.55	A
7	Bellows	BLW3	0.15	26.83	A
8	White Beam Filters	FLT	0.31	27.06	A
9	Be Window (cooled)	WIN1	0.11	27.26	A
10	Bellows	BLW4	0.15	27.39	A
11	Horizontal Collimating Mirror	HCM	1.40	28.17	A
12	Bellows	BLW5	0.15	28.94	A
13	Gate Valve	GV2	0.07	29.05	A
14	Pink Beam Slits	SLT1	0.60	29.39	A
15	Pink Beam Screen Monitor	FLSW	0.18	29.78	A
16	Gate Valve	GV3	0.07	29.90	A

Table 2.8.1.1: List of HXN Beamline Components *(concluded)*

Item	Description	Acronym	Length (m)	Position (m)	Station
17	Bellows	BLW6	0.15	30.01	A
18	Monochromator, Horizontal Double Crystal	DCM	0.57	30.37	A
19	Bellows	BLW7	0.15	30.73	A
20	White Beam Stop	WBS	0.42	31.02	A
21	Mono Slits & Florescent Screen	SLT2,FLSM	0.55	31.50	A
22	Gate Valve	GV4	0.07	31.81	A
23	Bellows	BLW8	0.15	31.92	A
24	Horizontal Focusing Mirror	HFM	1.20	32.60	A
25	Bellows	BLW9	0.15	33.27	A
26	Gate Valve	GV5	0.07	33.38	A
27	Bremsstrahlung Stop	BRS	0.40	33.62	A
28	Mono Beam Position Monitor (BPM) / Screen	BPM2	0.40	34.01	A
29	Gate Valve	GV6	0.07	34.25	A
25	Bellows	BLW9	0.15	33.27	A
26	Gate Valve	GV5	0.07	33.38	A
27	Bremsstrahlung Stop	BRS	0.40	33.62	A
28	Mono Beam Position Monitor (BPM) / Screen	BPM2	0.40	34.01	A
29	Gate Valve	GV6	0.07	34.25	A
30	Bellows	BLW10	0.31	34.44	A
31	Compound Refractive Lens (Transfocator)	CRL	0.44	34.81	A
32	Bellows	BLW11	0.31	35.18	A
33	Beampipe	BP1	3.37	37.02	A
34	Gate Valve	GV7	0.07	38.74	A
35	Bellows	BLW12	0.15	38.85	A
36	Diagnostic Chamber (BPM)	BPM3	0.18	39.01	A
37	Bellows	BLW13	0.15	39.18	A
38	Mono Beam Shutter	SSH1	0.25	39.38	A
30	Bellows	BLW10	0.31	34.44	A
31	Compound Refractive Lens (Transfocator)	CRL	0.44	34.81	A
32	Bellows	BLW11	0.31	35.18	A
33	Beampipe	BP1	3.37	37.02	A
34	Gate Valve	GV7	0.07	38.74	A
35	Bellows	BLW12	0.15	38.85	A
36	Diagnostic Chamber (BPM)	BPM3	0.18	39.01	A
37	Bellows	BLW13	0.15	39.18	A
38	Mono Beam Shutter	SSH1	0.25	39.38	A
39	Gate Valve	GV8	0.07	39.53	A
	Hutch A Downstream Wall (upstream end)		0.10	39.91	A
	Mature Scope Configuration for Hutch B				
	Hutch B Upstream Wall (downstream end)		0.10	60.80	B
40	*Gate Valve w/ X-ray Window*	WIN2	0.07	61.02	B
41	*Beampipe, Removable*	BP2	3.15	62.73	B
42	*Gate Valve w/ X-ray Window*	WIN3	0.07	64.35	B

43	*Quad Diode and Screen Monitor*	QBPM1	0.31	64.56	B
44	*Secondary Source Aperture*	SSA1	0.57	65.00	B
45	*Beampipe*	BP3	0.61	65.59	B
46	*Gate Valve*	GV9	0.07	65.93	B
47	*Mono Beam Shutter*	SSH2	0.25	66.09	B
	Hutch 2 Downstream Wall (upstream end)		0.10	66.44	B
	End of Experimental Floor			73.41	
	Ring Building Outer Wall			80.54	
	Satellite Building Upstream Wall (upstream end)		0.11	90.10	
	Hutch 3 Upstream Wall (downstream end)		0.25	93.05	C
48	Gate Valve	GV10	0.07	93.68	C
49	Secondary Source Aperture	SSA2	0.57	94.00	C
50	Quad Diode and Screen Monitor	QBPM2	0.31	94.44	C
51	Be Window	WIN3	0.11	94.65	C
52	Beampipe, Removable	BP4	13.64	101.52	C
53	HXN Microscope		3.30	109.00	C
	Hutch 3 Downstream Wall (upstream end)		0.25	113.06	C
	Satellite Building Downstream Wall (downstream end)		0.11	115.45	

2.8.2 Detailed description of all beamline components

Detailed views of the components for the three experimental stations are shown in Figures 2.8.2.3–2.8.2.5. The descriptions of the components are given below.

Gate valves
Gate values are used to isolate the vacuum in case of a vacuum failure or to enable venting optical components for repair or upgrade. Gate values are installed around each major optical component.

Mask
The FOE mask (item 5 in Table 2.8.1.1) is used to limit the angular size of the white beam. It has an aperture size of 4.0 x 4.0 mm. It has an identical design as the FE fixed aperture mask (see section 2.3.1 and Figure 2.3.2.2), except for the length. The length of the FOE mask is shorter because the incident solid angle of the white beam is already reduced by the FE fixed aperture mask. During normal operation of the HXN beamline, the incident beam into the FE is defined by the white beam slits in the FE. The nominal size of the beam defined by the white beam slits is smaller than the aperture of the FOE mask. The FOE mask is required for safe operation of the beamline because the personal safety system cannot rely on a beamline component that can be moved by the users or beamline scientists.

Collimator
A FOE collimator is used to reduce the bremsstrahlung fan, in order to operate the HXN beamline safely.

Diagnostic chamber
The purpose of installing diagnostic chambers is to provide designated places where different types of BPMs can be installed. In other locations in the HXN beamline, a specific type of beam position monitor such as “quad diode” or “screen monitor” has been identified.

Screen monitor
The screen monitor consists of a scintillation screen such as YAG and a high resolution camera. The size and the position of the beam can be monitored. For monochromatic x-rays, the screen monitor completely blocks the beam and cannot be used as an "in-situ" or "parasitic" monitor. Screen monitors are useful for aligning beamline optics such as focusing mirrors or monochromator. Different types of screen monitors are commercially available.

Quad diode BPM
This monitor consists of four diode detectors measuring either fluorescence or the scattered beam from a thin metal foil. Typically a few different metal foils are used to select an appropriate intensity level. A few different commercial options are available.

High-resolution x-ray BPM developed at BNL
The beam position monitor R&D, led by Peter Siddons, produced a novel prototype XBPM [2.8.2.1, 2.8.2.2]. This new compact design uses Si PIN-junction photodiodes for detecting fluorescence x-rays produced by an x-ray beam impinging on a thin metal foil. Recent measurements at NSLS demonstrated a beam position sensitivity of 0.6 μm. Further refining is expected to produce beam position sensitivity below 0.1 μm. This prototype XBPM can easily fit in the diagnostic chamber of the HXN beamline.

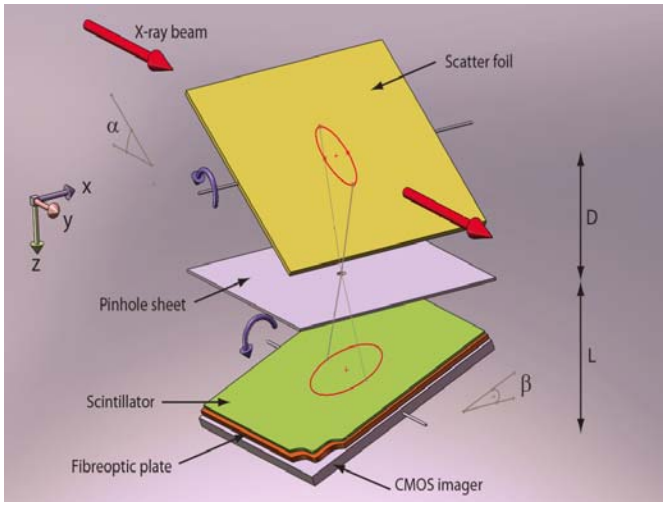

Figure 2.8.2.1: Schematic of NanoBPM. Courtesy of FMB-Oxford

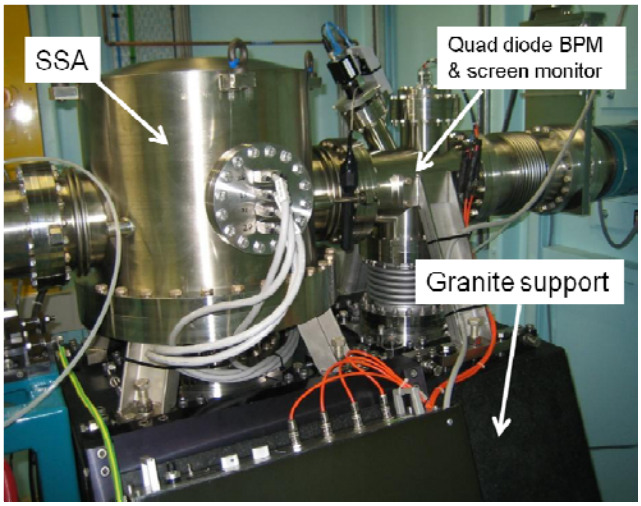

Figure 2.8.2.2: Photograph of a secondary source aperture produced by ID. Courtesy of IDT.

White Beam Position Monitor
A drawback of the Quad Diode BPM is that it is designed for monochromatic x-rays. With the lack of cooling, the metal foil will instantly vaporize in the NSLS-II's undulator white beam. Monitoring accurate position of the white beam position is extremely important, because this capability will determine where beam instability problems actually exist (e.g., undulator or monochromator). In addition, there are fewer commercial options for "in-situ" white beam position monitors.

One candidate beam position monitor for BPM1 in the HXN beamline (to be housed in the diagnostic chamber) is NanoBPM, which has been exclusively licensed by FMB-Oxford from the University of Manchester. Figure 2.8.2.1 shows how it works. A thin foil of diamond (shown in yellow) is placed in the beam. A pinhole camera is used to image the shape of the beam illuminated on the diamond foil with a magnification determined by the ratio of D and L. Because of the use of a thin low Z screen, this particular beam position monitor allows "in-situ" or "parasitic" operation.

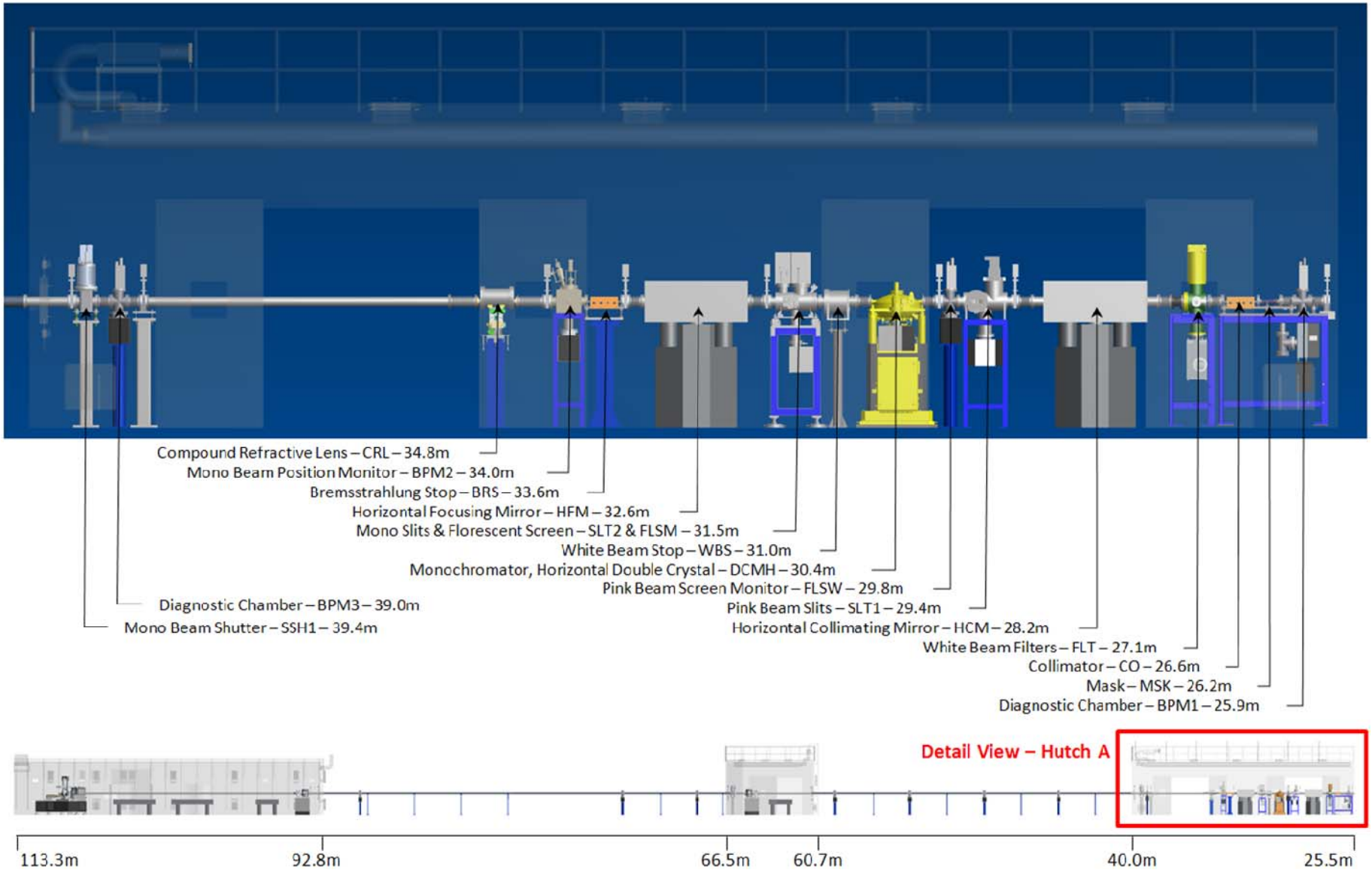

Figure 2.8.2.3: Detail view of HXN Beamline showing components in station A. The enclosure, doors and labyrinths are also shown together in translucent colors.

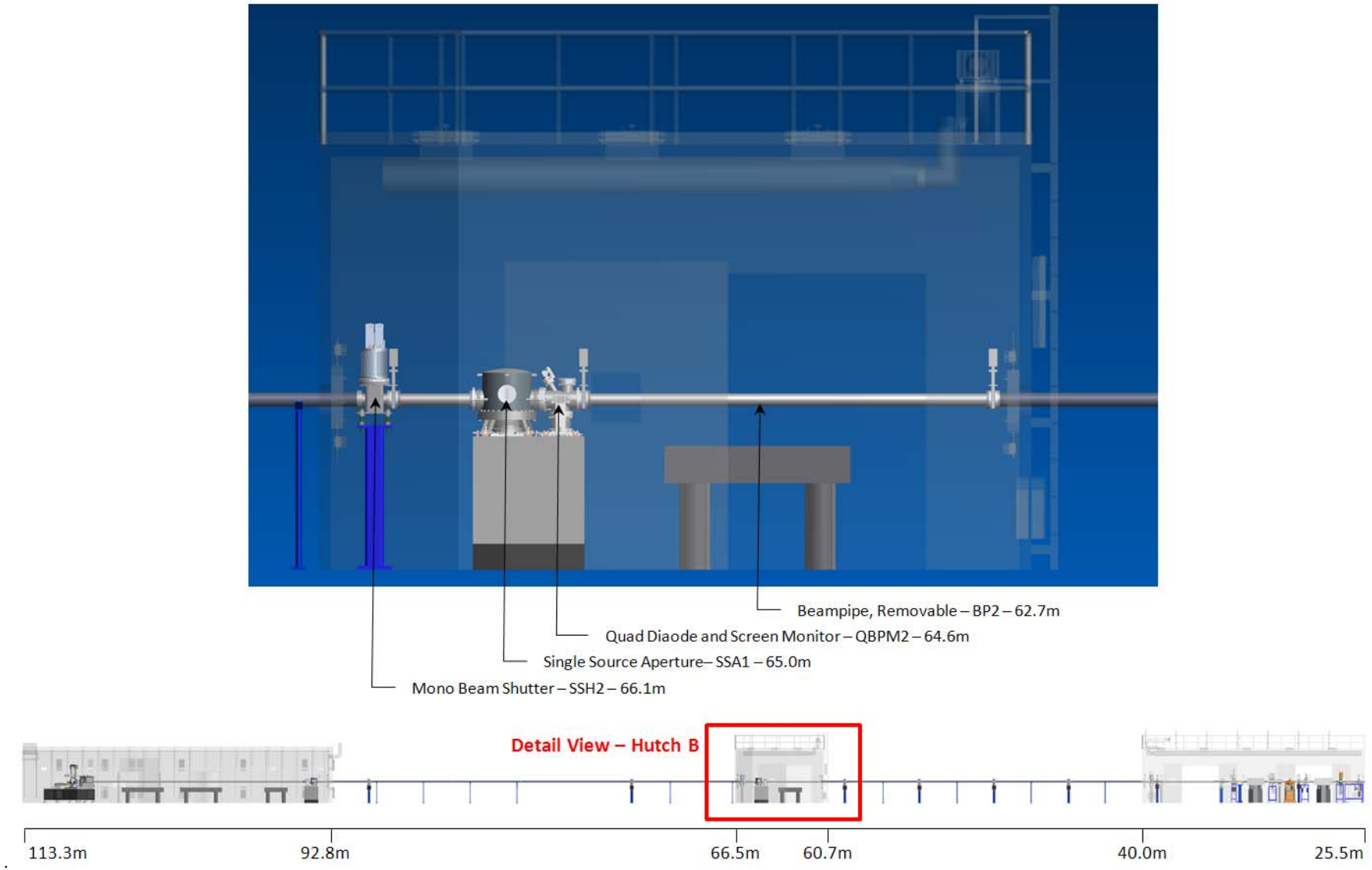

Figure 2.8.2.4: Detail view of HXN Beamline showing components in station B. The enclosure, door and labyrinths are also shown together in translucent colors.

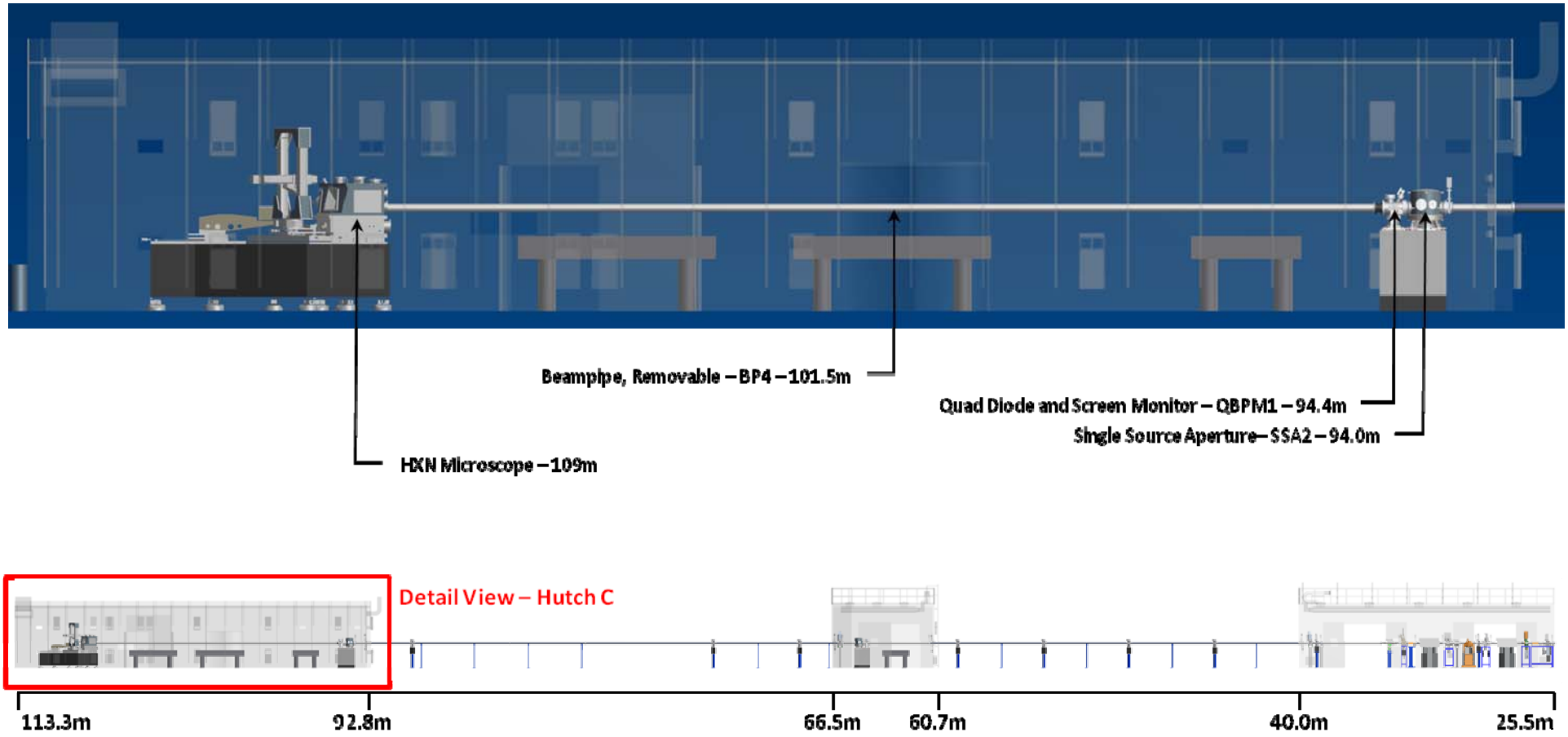

Figure 2.8.2.5: Detail view of HXN Beamline showing components in station C. The enclosure, door and labyrinths are also shown together in translucent colors. The hutch is sufficiently large and can accommodate two more dedicated experiment setups. The table immediate right of the HXN microscope will be used for developing ~1nm prototype instrument (see section 8 for details).

Secondary Source Aperture (SSA)
A secondary source aperture is a critical instrument for the HXN beamline. The specifications of a secondary source aperture for the HXN beamline are summarized in Table 2.8.2.1.

Table 2.8.2.1: Specifications for a secondary source aperture.

Positional stability	<1 μm (2 sigma)
Gap accuracy	< 0.2 μm, vertically < 0.5 μm, horizontally
Repeatability (center position)	< 1 μm, both directions
Repeatability (gap size)	< 0.2 μm, vertically < 0.5 μm, vertically
Parallelism of slits	< 0.01°
Slit surface roughness	< 0.1μm
Minimum gap size	-0.1 mm, both directions
Maximum gap size	4 mm, horizontal 1mm, vertical

In the past, high-precision slits have been developed at a number of synchrotron beamlines by beamline scientists or engineers. Currently, IDT produces a secondary source aperture that is very close to meeting the HXN specifications. Figure 2.8.2.2 shows a photograph of the secondary source aperture installed at the FXM beamline of the Australian Synchrotron.

[2.8.2.1] P.S. Yoon and D.P. Siddons, "Photodiode-based X-ray Beam-position Monitor with High-Spatial Resolution for the NSLS-II Beamlines," *Proceedings of Beam Diagnostics and Instrumentation for Particle Accelerators* (DIPAC) 2009, Basel, Switzerland; BNL-90364-2009-CP

[2.8.2.2] P.S. Yoon and D.P. Siddons, "Fluorescence-type Monochromatic X-ray Beam-Position Monitor with High-spatial Resolution for the NSLS-II Beamlines," *Synchrotron Radiation Instrumentation* (SRI 2009), AIP Conference Proceedings, 1234, 853

2.8.3 Comparison with optical configuration proposed by vendors

The preliminary design of the HXN beamline has been developed through detailed communication with major vendors providing synchrotron instrumentation. In fact, the 3D model of the HXN beamline contains actual individual models that are either supplied directly by the vendors or taken from the NSLS-II instrument data base, which has been compiled over the last few years. Close communication with the vendors has been a critical aspect of the HXN beamline design because moving the z-position of the focusing optics more than ~0.5m from the designed values can result in a considerable change to the optical scheme. In addition, close communication with the vendors has made it possible that the preliminary design of the HXN beamline can be directly translated into immediate procurement of most of the beamline components, without further technical evaluation. For those components that require some development or further technical evaluation, namely the CRL transfocator and beam position monitors, appropriate provision for the space has been allocated. In order to eliminate any potential risks three major vendors, Bruker ACS (the former ACCEL), IDT and FMB-Oxford, were asked to provide a 3D model of the HXN beamline using their own instrument designs. All three vendors provided detailed technical inputs that ensure the fabrication capability of the components in accordance with the preliminary design of the HXN beamline. In particular, FMB-Oxford has graciously provided a complete 3D model of the HXN beamline within the first optical enclosure, which is being compared with the 3D model of the HXN preliminary design in Figure

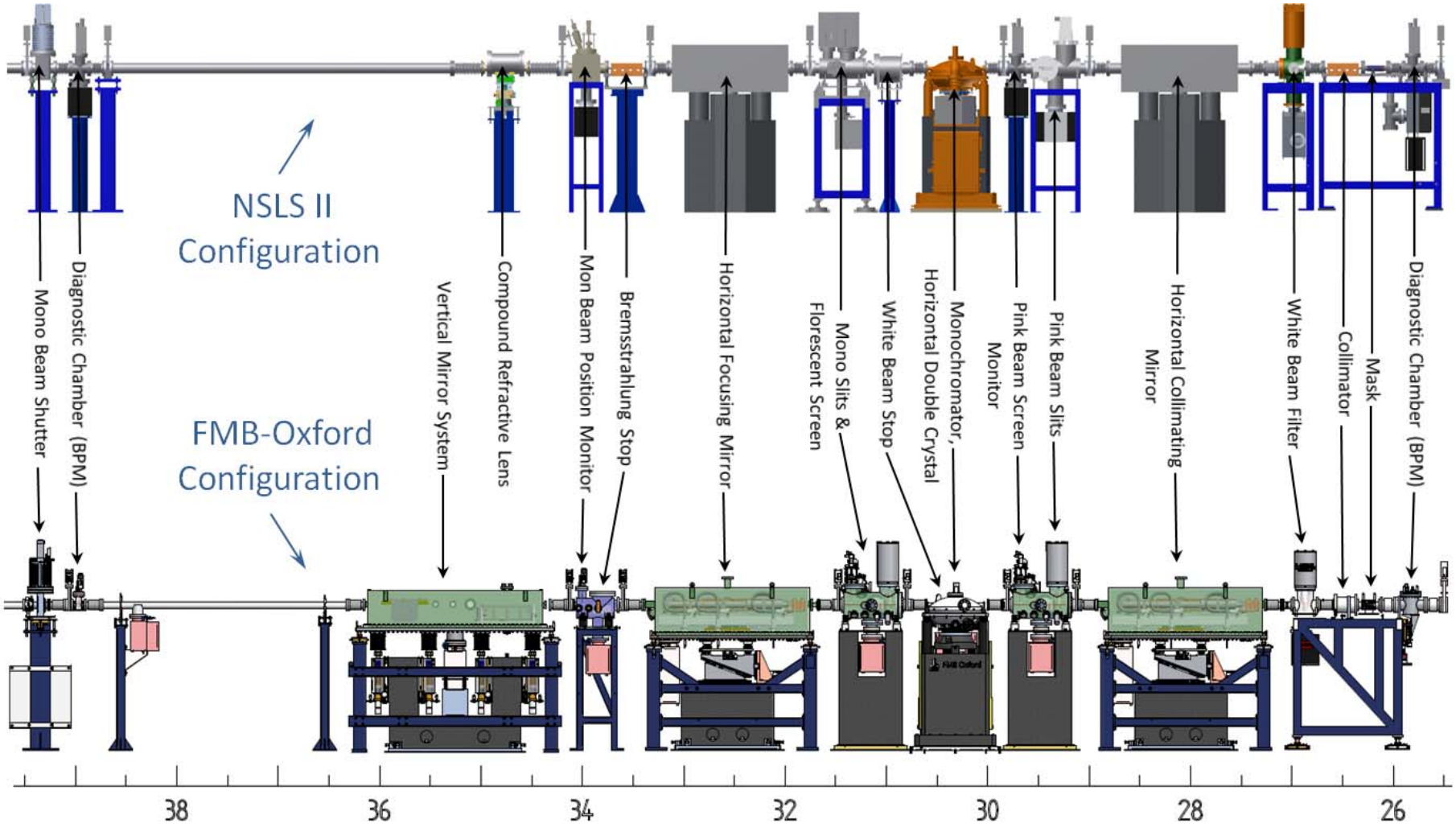

Figure 2.8.3.1: Comparison of HXN Beamline Configurations by NSLS-II and FMB-Oxford (Elevation View).

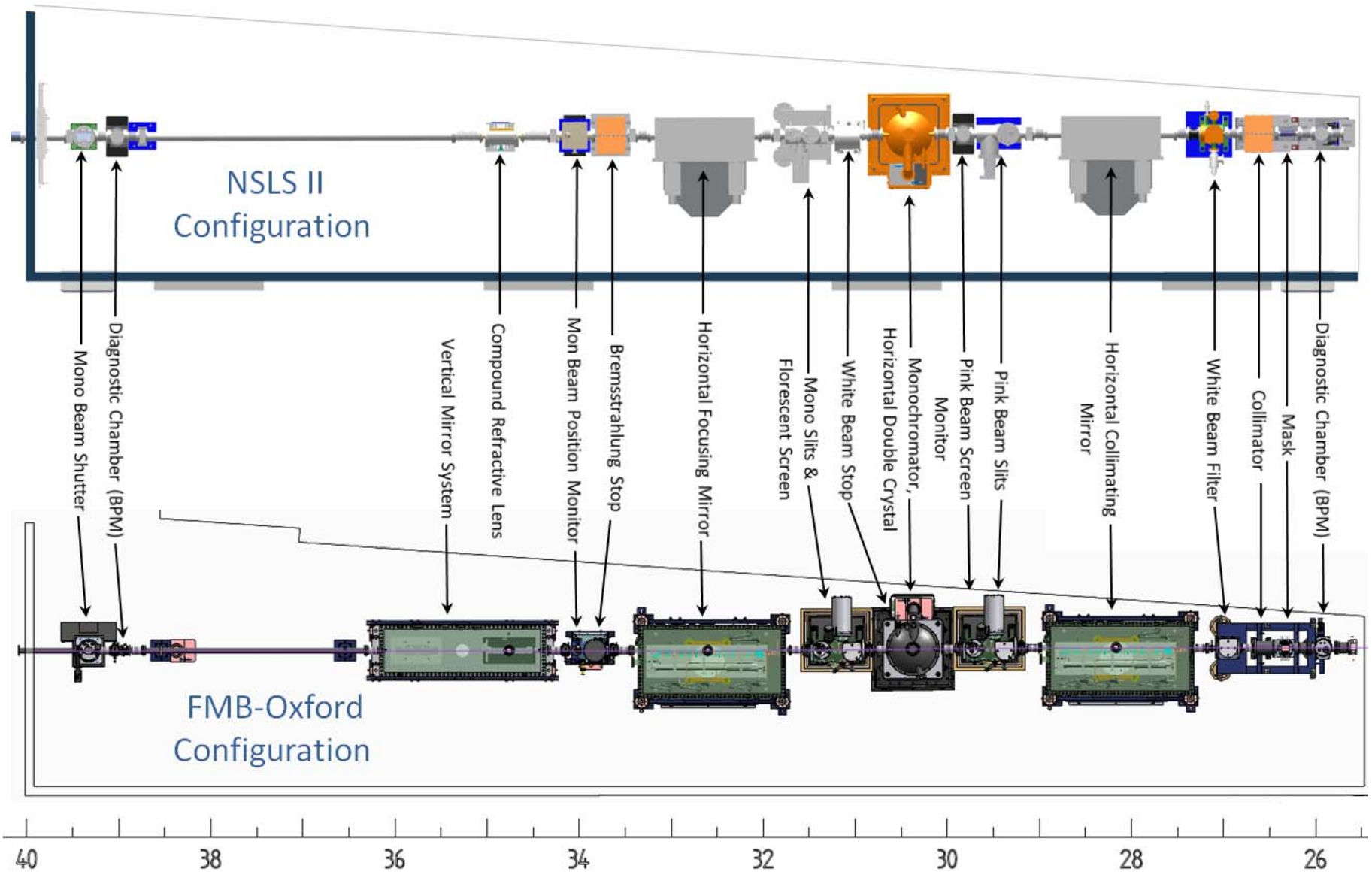

Figure 2.8.3.2: Comparison of HXN Beamline Configurations by NSLS-II and FMB-Oxford (Plan View).

2.8.3.1 and Figure 2.8.3.2. The only major difference is that the FMB-Oxford configuration shows a vertical mirror system, which demonstrates that the space in the first optical enclosure is sufficiently large for the future upgrade of the Be CRLs to the mature scope mirror system.

It is important to point out that this comparison does not imply any preference of FMB-Oxford over other vendors. The procurement decision will be strictly based the vendor capabilities and the policy governing the open bidding procedure for the procurement.

2.9 Shadow ray tracing

Shadow ray tracing was performed in order to carry out simple performance evaluations of the optical scheme presented in this report. Shadow ray tracing uses geometric calculation combined with random numbers generated according to the input probability density describing the source size and angle. Consequently, effects due to phase interference from diffraction from slits, mirrors and monochromator crystals are not included. Nevertheless, Shadow tracing provides a simple diagnostic of the beamline optics. In this section, the ray tracing resulting from beamline optics without figures is presented first, in order to illustrate the evolution of the beam size and beam angle through each major optical component. Then, the effects due to figure errors are discussed. In the ray tracing presented here, vertical focusing was provided by a vertical mirror system (consisting of the first mirror for focusing and the second flat mirror for keeping the beam horizontal) as an alternative to the Be CRL lenses, because the current version of Shadow does not handle the Be CRL. The Shadow simulations shown below are for the high-throughput mode using the SSA2.

2.9.1 At the x-ray source, z=0 m

A Gaussian source with the following FWHM size and angle was used: S_h = 80.1μm, θ_h = 42.3μrad, S_v = 12.0 μm, θ_V = 21.0 μrad. Figure 2.9.1 shows beam position and angles at the source. At the source, the position and the angles are not correlated. Consequently, the phase space (angle vs. position) is an upright ellipse for both the horizontal and vertical directions.

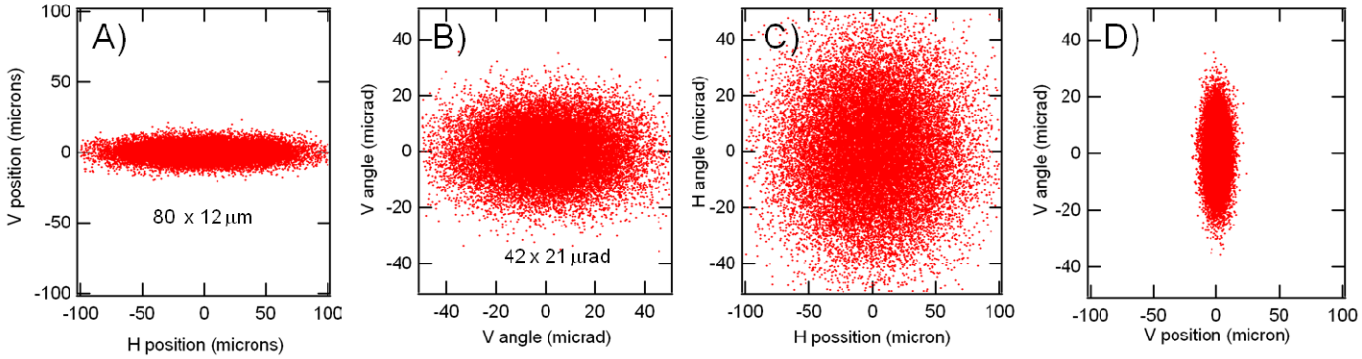

Figure 2.9.1: Beam position and angle at the source: A) Vertical position vs. horizontal position, B) Vertical angle vs. horizontal angle. C) Horizontal angle vs. Horizontal position, and D) Vertical angle vs. vertical position.

2.9.2 At the horizontal collimating mirror (HCM), z=28.2m

Before the x-ray beam reaches the HCM, it is apertured down to 70 μrad (H) × 30 μrad (V) by the white beam slits. The position and angle of the beam at the HCM (just before getting reflected) is shown in Figure 2.9.2. The x-rays stopped by the white beam slits are shown in black. About 86% of the x-rays (from the central cone) are transmitted through the white beam slits. The phase space (angle vs. position) is rotated because the beam size increases due to propagation while the angle remains constant. The angle of the beam is highly correlated with the size of the beam. The effect of slits as an angular aperture is clearly seen in Figures 2.9.2C and 2.9.2D.

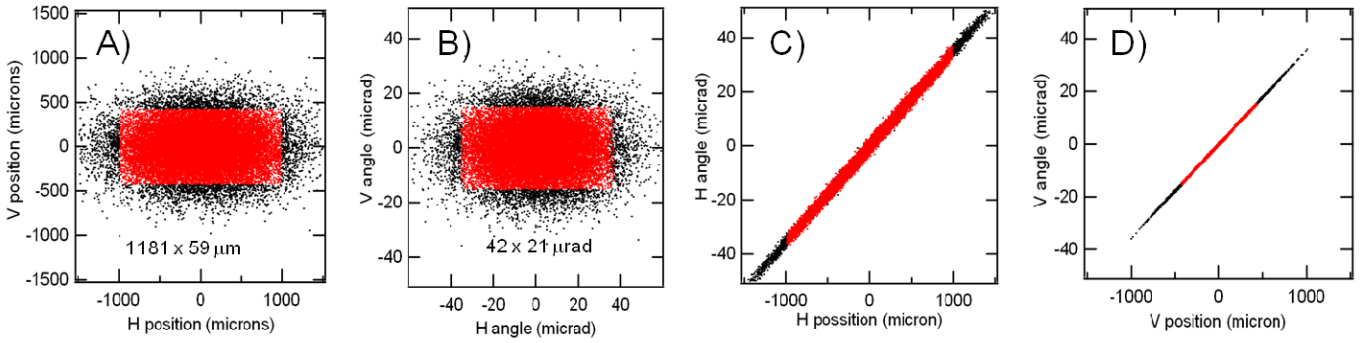

Figure 2.9.2: Beam size and angle immediately before the HCM. A) Vertical position vs. horizontal position. B) Vertical angle vs. horizontal angle. C) Horizontal angle vs. Horizontal position. D) Vertical angle vs. vertical position. The black dots represent the x-rays stopped by the white beam slits.

2.9.3 At the horizontal focusing mirror (HFM), z=32.6m

Before the beam is incident on the monochromator, the size of the beam is further reduced by the pink beam slit down to 50 μrad (H) to 25 μrad, resulting in the transmission of about 75% of the central cone. Thus, Figure 2.9.3 shows a greater number of black dots, representing the stopped x-rays. The angular distribution of the beam in the horizontal direction is greatly narrowed by the HCM. Due to the finite source size, the angular collimation cannot be perfect (i.e., a delta-function). The horizontal angular distribution has a FWHM size equal to the horizontal source size divided by the distance from the source to the HCM. Due to the collimation, the horizontal angle is uncorrelated with the horizontal size, causing the horizontal phase ellipse to lie flat. In the vertical direction, the angle is still well correlated with the size. The horizontal monochromator does not change the beam angle, or perturb the trajectory of the x-rays other than in a horizontal offset.

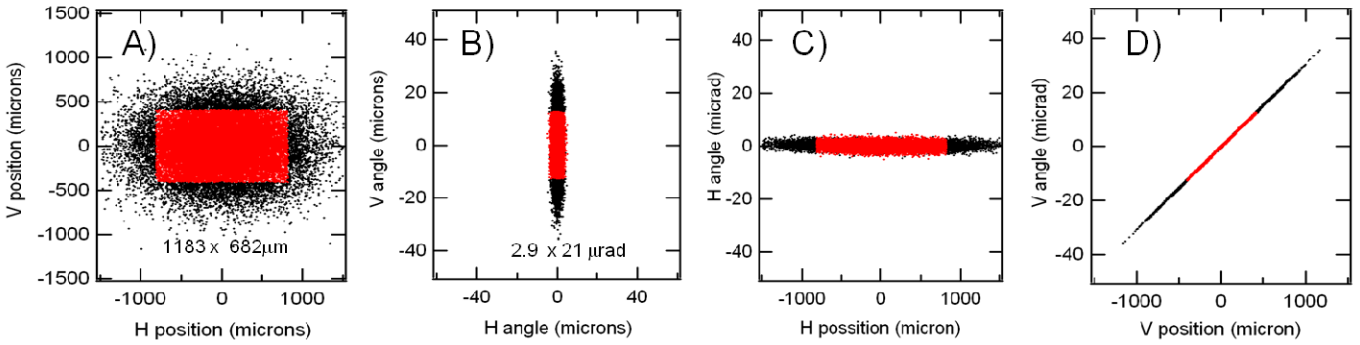

Figure 2.9.3: Beam position and angle immediately before the HFM. A) Vertical position vs. horizontal position. B) Vertical angle vs. horizontal angle. C) Horizontal angle vs. Horizontal position. D) Vertical angle vs. vertical position. The black dots represent the x-rays stopped by the pink beam slits with an angular aperture of 50 μrad (H) by 25 μrad (V).

2.9.4 At the Be CRL, z=34.8m

Figure 2.9.4 shows the beam position and angles immediately before the Be CRL. The effect of the horizontal focusing by the HFM is modest due to a short distance from the HFM of only 2.2 m. Due to the horizontal convergence, the horizontal angle is well correlated with the horizontal size. The FWHM vertical size of the beam is 717 μm. The vertical beam size transmitted from the pink beam slits (shown in red) corresponds to 870 μm. Consequently, the vertical aperture of the Be CRL should be larger than 900 μm.

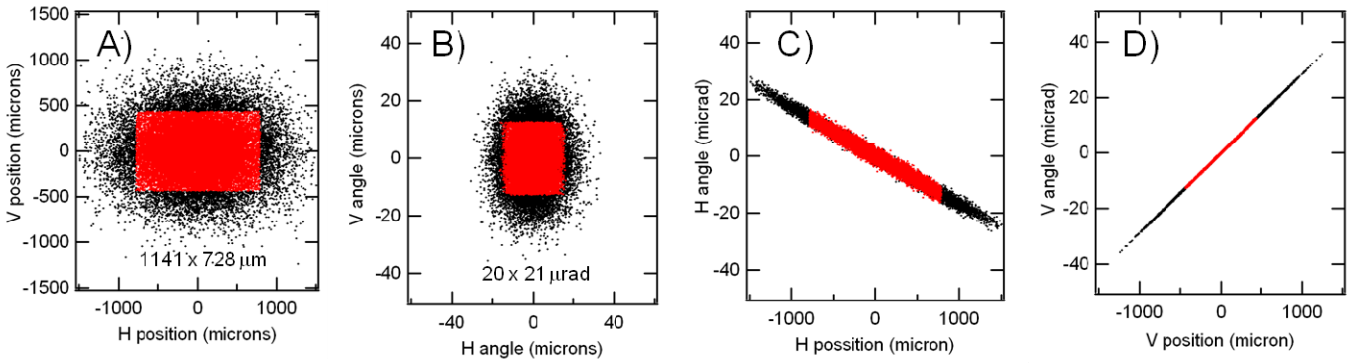

Figure 2.9.4: Beam position and angle immediately before the Be CRL. A) Vertical position vs. horizontal position. B) Vertical angle vs. horizontal angle. C) Horizontal angle vs. Horizontal position. D) Vertical angle vs. vertical position. The red dots corresponds to the x-rays transmitted through the pink beam slits, 50 μrad (H) by 25 μrad (V).

2.9.5 At the SSA2, z=94m

At the SSA2, the x-ray beam is focused in both directions, forming an image of the primary source. The focusing in the vertical direction was simulated using a set of vertical mirrors (the first mirror to focus (reflecting up) and the second mirror to reflect down, maintaining the horizontal exit beam) rather than using the CRL. Shadow yielded a FWHM beam size of 174.8 μm (H) x 20.5 μm (V) as shown in Figure 2.9.5. This is in good agreement with an estimated FWHM image size of 174.2 μm (H) x 20.4 μm (V), based on the respective demagnification factors of 2.17 and 1.70 for the horizontal and vertical directions. Since the primary beam forms a secondary source at SSA2, the horizontal and vertical angles do not show a correlation with the beam size. Consequently, the x-rays transmitted through the pink beam slits and stopped by the pink beam slits are no longer separated spatially. In other words, the x-ray intensity at a given point is an integral over the entire source angle. When using the SSA1 at z=65m, the demagnification factors are changed to 1.15 in the horizontal direction and 0.87 in the vertical direction, resulting in a FWHM beam size of 92 μm (H) x 11 μm (V) as shown in Figure 2.4.2C.

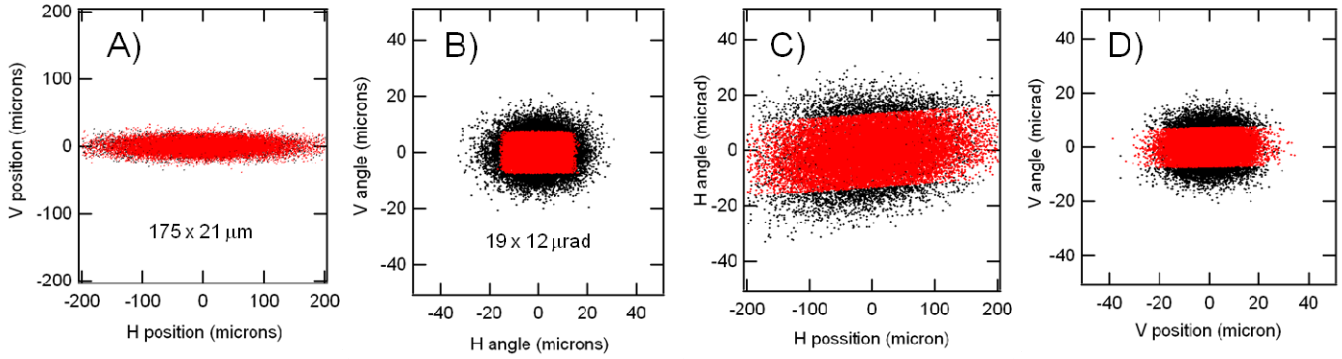

Figure 2.9.5: Beam position and angle at the SSA2. A) Vertical position vs. horizontal position, B) Vertical angle vs. horizontal angle. C) Horizontal angle vs. Horizontal position, and D) Vertical angle vs. vertical position. The red dots corresponds to the x-rays transmitted through the pink beam slits, 50 μrad (H) by 25 μrad (V).

2.9.6 At the nanofocusing optics, z=109m

The beam position and angle at the nanofocusing optics (z=109 m) is shown in Figure 2.9.6. The FWHM beam size is 372 μm(H) x 187 μm(V). In the vertical direction, the definition of the pink beam slits (boundary between the red and black dots) is clearly visible. On the other hand, the horizontal boundary due to the pink slits is much more diffuse. The reason for this diffuseness is that the beam angle is larger in the horizontal direction and the slits are far away. The vertical FWHM size of the beam transmitted through the pink beam slits is 133 μm. This size is still

fine for a nanofocusing aperture up to 100μm. For a larger aperture size, the pink beam slits should be opened up by a small amount (~30μrad). This will increase the power on the monochromator by about 17%.

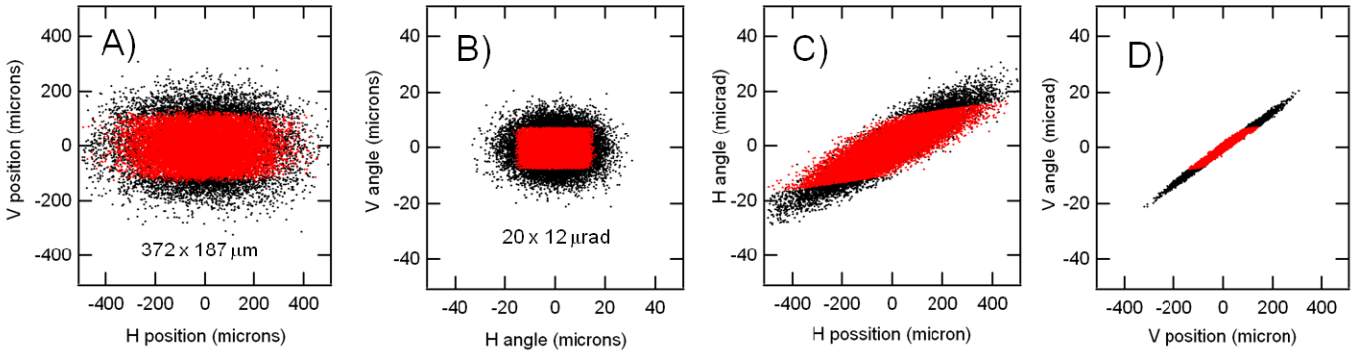

Figure 2.9.6: Beam position and angle at the nanofocusing optics. A) Vertical position vs. horizontal position. B) Vertical angle vs. horizontal angle. C) Horizontal angle vs. Horizontal position. D) Vertical angle vs. vertical position. The red dots correspond to the x-rays transmitted through the pink beam slits, 50 μrad (H) by 25 μrad (V).

2.9.7 Effect of figure errors

The Shadow simulations shown until this point were carried out using perfect x-ray optics. In reality, all x-ray optics have figure errors or aberrations. Aberrations due to slope error cause distortion of the image of the primary source formed at the plane of the secondary source aperture. In other words, the intensity distribution at the plane of the secondary source aperture is no longer Gaussian-like or symmetric. The Shadow simulation results are shown in Figure 2.9.7 for both high-throughput mode (shown in red) and high-resolution mode (shown in blue). In both cases, an RMS figure error of 0.9 μrad was used for the horizontal mirrors (HCM and HFM) and an RMS figure error of 0.3 μrad was used for the two vertical mirrors. The simulations used actual metrology data supplied by Zeiss.

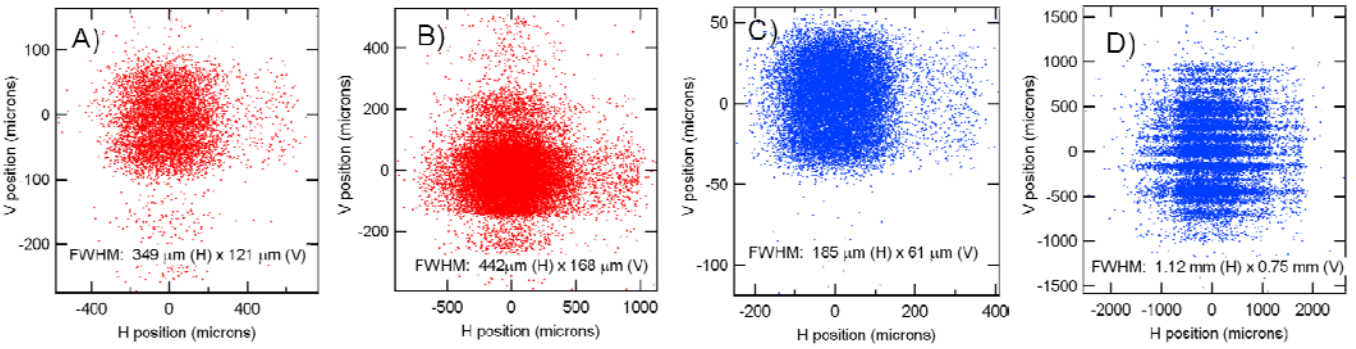

Figure 2.9.7: Intensity distribution at the secondary source and the nanofocusing optics. A) Intensity distribution at SSA2, z=94m. B) Intensity distribution at nanofocusing optics, z=109m. A) and B) are for the high-throughput mode. C) Intensity distribution at SSA2, z=94m. D) Intensity distribution at nanofocusing optics, z=109m. C) and D) are for high-resolution mode.

In high-throughput mode, the beam size at the SSA2 is 2.0 times larger in the horizontal direction (349 μm vs. 174.8 μm) and 5.9 times in the vertical direction (121 μm vs. 20.5 μm). Despite the fact that a smaller figure error was used in the vertical direction, the broadening of the beam is much more severe. This is because the primary source size in the vertical direction is only 12 μm, so even a small figure error can have a significant impact. The beam size at the nanofocusing optics is 422 μm (H) x 168 μm (H), which is not so different from the beam size of 372 μm (H) x 187 μm (V) in the absence of figure errors. Instead, the intensity distribution is no longer symmetric.

However, the central region appears to be more or less uniform and can provide adequate illumination over the nanofocusing optics.

In high-resolution mode, the beam size at the secondary source aperture is 185 μm (H) x 61 μm (H) vs. 92 μm (H) x 11 μm (V) in the absence of figure errors. The image of the primary source is broadened by 2.0 times in the horizontal direction and 5.5 times in the vertical direction. The amount of the broadening is comparable to the high-throughput mode. However, the intensity distribution at the nanofocusing optics shows significant undulation in the vertical direction. This is because the distance from the SSA1 to the nanofocusing optics is about 3 times larger and the intensity fluctuations become more visible.

Smaller values for the figures will decrease broadening of the beam at the secondary source aperture. For example, if figure error values of 0.5 μrad (RMS) (H) and 0.2 μrad (RMS) (V) were used; the estimated beam size at SSA2 would be 236 μm (H) x 81 μm (V). The broadening would be about 1.4 times in the horizontal direction and 4.0 times in the vertical direction. To keep the broadening less than a factor of 2 in the vertical direction, the RMS figure error for the vertical mirrors must be less than 0.1 μrad. Such a low level of figure error is difficult to achieve with a mirror ~0.5m long. Broadening of the image size of the primary source at the plane of the secondary source aperture can be easily modeled using a Gaussian assumption that 1) the figure errors on the mirror surface are random and 2) the figure errors on the two mirrors in each direction are not correlated. The result of this simple calculation is plotted in Figure 2.9.8. In the horizontal direction, an RMS figure error of ~0.8 μrad results in broadening of the primary source image by a factor of two. In drastic contrast, only 0.1 μrad figure error results in doubling of the source broadening in the vertical direction. For a mirror length of ~0.5 m, RMS figure errors of 0.3 or better are feasible. However, even at such a small level of figure error, the broadening in the vertical direction is about six times the broadening in the horizontal direction.

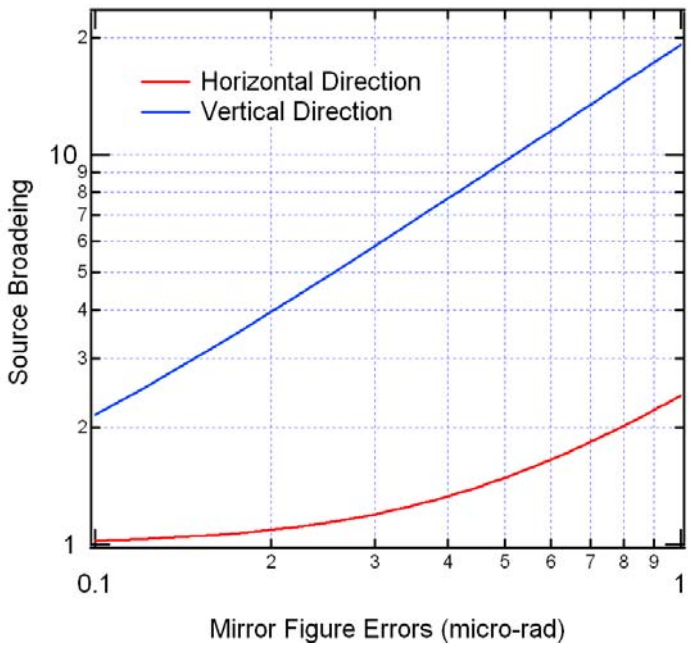

Figure 2.9.8: Broadening of the image of the primary source at the secondary source due to the mirror figure errors. The calculation assumes identical figure errors for the two mirrors in the horizontal and the vertical direction. The amount of the broadening is given as the fold increase in the size of the beam in comparison with the case for the absence of figure errors.

The analysis shown here provides good reason that an alternative solution to a focusing mirror should be considered in the vertical direction. For the baseline scope of the HXN beamline, instead of mirrors we plan to use Be compound refractive lenses (CRL) or Si kinoform. Refractive optics work in a transmission geometry and do not exhibit high sensitivity to figure errors on surface curvature, because the expected roughness (<1 μm) on the surface is a small fraction of the thickness of the lens in the direction of the x-rays. The error of the phase shift of the x-ray due to the thickness variation is negligible. Consequently, the amount of source broadening would be less severe for the CRLs.

2.10 Performance estimate

As shown in the previous section, the optical quality of the beamline optics, particularly in the vertical direction, makes significant impact on the size of the primary source image formed at the secondary source aperture. We refer this effect as "source broadening." Consequently, the amount of x-rays transmitted through a given aperture size critically depends on the level of source broadening. In this section, we present comprehensive performance estimates leading to the integrated flux of the nanoprobe. This calculation is summarized as follows:

- The estimated parameters of the beamline optics and the angular aperture of the slits are used to calculate the integrated flux at the plane of the secondary source aperture.
- The x-ray flux transmitted through the secondary source aperture is calculated as a function of the source broadening.
- The accepted flux at the plane of the nanofocusing optics is calculated based on the aperture size of the nanofocusing optics.
- The calculation is performed based on an assumption that the 2D intensity distribution at the secondary source and the nanofocusing optics is Gaussian. The flux is integrated using a Gaussian integral.

2.10.1 From the primary source to the secondary source aperture

Total flux at the plane of the secondary source aperture is estimated by accounting for the expected transmittance from each beamline component that impacts the flux. Table 2.10.1 summarizes the transmittance from different types of optical components, estimated at 10 keV. In the table, only the pink beam slits are used because the total solid angle is determined by the pink beam slits, which provide the smallest angular aperture before the SSA. The estimated flux at the SSA2 is 4.45 x 10^{13} ph/s at 10 keV and 3.06 x10^{12} ph/s at 20 keV. The estimated flux at the SSA1 is about 3% smaller due to the use of the Be CRL (see estimated energy-dependent transmission for Be CRL Table 2.7.2.1).

Table 2.10.1: Estimated transmittance of the beamline optical components and transmitted flux. The estimate given in the table is for 10 keV. For 20 keV, the flux from the source is 5.40 x 10^{13} ph/s/0.1% bw, and the flux at SSA2 is 3.06 x10^{12} ph/s.

Optical Components	Individual transmittance	Transmitted flux (accumulative)	Note
		7.68 x 10^{14} ph/s/0.1% bw	IVU20 source
Pink beam slits	0.700	5.38 x 10^{14} ph/s/0.1% bw	An angular aperture of 50 x 25 μrad. The smallest aperture for the beamline before the secondary source aperture
Be Window	0.901	4.85 x 10^{14} ph/s/0.1% bw	Accumulative thickness of 1mm
HCM	0.949	4.60 x 10^{14} ph/s/0.1% bw	Reflectivity from Rh coating at 3.0 mrad incidence angle
Monochromator			Overall reflectivity through two crystals
(dE/E)/0.1%	0.144	6.60 x 10^{13} ph/s	For Si (111), 0.144 is the additional energy bw factor.
reflectivity	0.903	5.96 x 10^{13} ph/s	For accounting for small absorption factor for dynamical reflection
slope error	0.850	5.07 x 10^{13} ph/s	Reduced transmission due to the slope error (see section 2.6.3)
HFM	0.949	4.81 x 10^{13} ph/s	Reflectivity from Rh coating at 3.0 mrad incidence angle
Be CRL	0.926	4.45 x 10^{13} ph/s	For focusing at SSA2 (see section 2.7.2)
Total flux at SSA2		4.45 x 10^{13} ph/s	The flux at SSA1 is ~3% less due the CRL (see section 2.7.2)

2.10.2 Flux accepted by the nanofocusing optics

The flux accepted by the nanofocusing optics depends critically on the image size of the primary source formed at the secondary source aperture, by the beamline focusing optics. As explained in section 2.4, the size of the SSA is not a free parameter but set by the coherence illumination condition for the nanofocusing optics. For a given

aperture size of the nanofocusing optics and coherence requirement, the used fraction of the available flux is determined by the observed source broadening at the SSA or equivalently the flux density at the SSA. As explained in section 2.9, an RMS figure error value of 0.5 μrad for the HCM and HFM results in a source broadening of only 1.4. In the vertical direction, a source broadening of 2 is estimated for the mirrors with an RMS figure error value of only 0.1 μrad. As mentioned before, the use of a Be CRL will get around the figure error problem. Rather than specifying the type of the beamline focusing optics, the calculation uses an amount of source broadening as an input parameter. The fraction of the available flux transmitted through the SSA and accepted by the MLL optics with the lateral dimension D=124μm is calculated for four different values of the FWHM transverse coherence length: ξ =D, D/2, D/4, and D/10. The condition ξ =D corresponds to the coherence illumination condition for the diffraction-limited focusing.

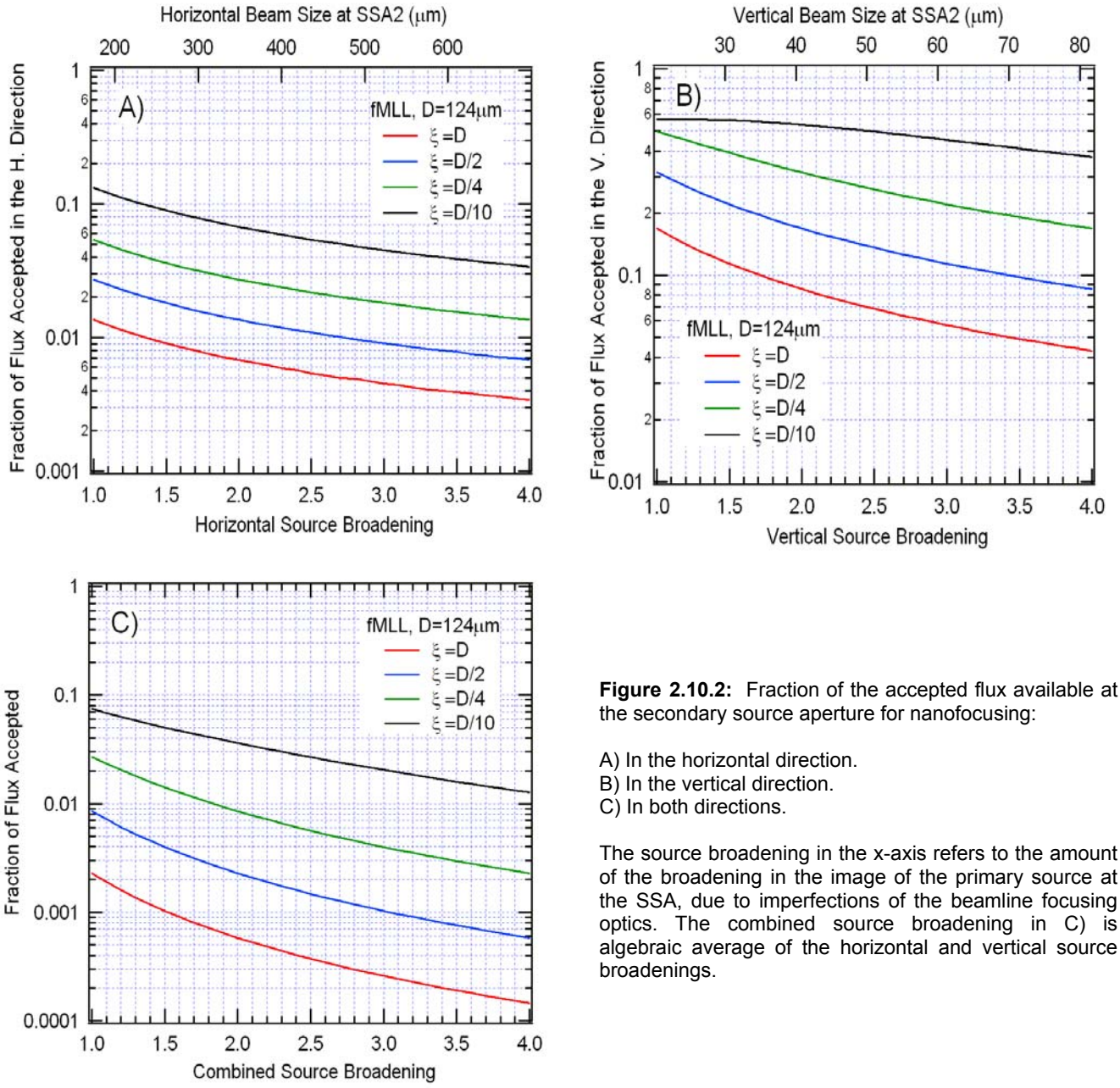

Figure 2.10.2: Fraction of the accepted flux available at the secondary source aperture for nanofocusing:

A) In the horizontal direction.
B) In the vertical direction.
C) In both directions.

The source broadening in the x-axis refers to the amount of the broadening in the image of the primary source at the SSA, due to imperfections of the beamline focusing optics. The combined source broadening in C) is algebraic average of the horizontal and vertical source broadenings.

Figure 2.10.2A shows the accepted fraction of the available flux in the horizontal direction. In the absence of source broadening (i.e., ideal beamline focusing optics), which corresponds to a horizontal source broadening equal to unity, 36% of the total flux at the SSA is used to achieve the diffraction-limited illumination condition. With a highly relaxed coherence illumination condition, ξ =D/10, 10 times more flux is collected by the nanofocusing optics. As mentioned before, the expected horizontal source broadening is less than 1.5, leading to better than 0.1% utilization of the available flux. The x-rays in the vertical directions are more coherent due to a much smaller source size and angle. Consequently, up to 16.8% of the available flux can be used to achieve diffraction-limited focusing, in the absence of source broadening. If we assume that a vertically focusing beamline optic can achieve a vertical source broadening less than 3, about 5.7% of the available flux can be used for achieving diffraction-limited focusing as shown in Figure 2.10.2B. Again, relaxing the coherence illumination condition by 10 times, 10 times more flux can be used. The black curve in 2.10.1b does not increase much with decreasing values of the source broadening because the SSA is already wide open under this condition.

Figure 2.10.2C shows the calculation performed over both directions. The source broadening shown in the x-axis indicates the source broadening in each direction. Mathematically, a horizontal broadening of 1 and vertical broadening of 4 is equivalent to the "combined" source broadening of 2. Or, the combined source broadening can be considered as the algebraic average of the horizontal and vertical broadening. The instrumentation goal for the HXN beamline is to achieve a combined beam broadening less than 2. With the broadening factor of 2, the fraction of the accepted flux is about 0.06%, which corresponds to 25% of the maximum achievable fraction.

It is worthwhile to point out that the fraction of the accepted flux does not depend on the size of the optics. As explained in section 2.4, the size of the secondary source aperture and the desired coherence length at the nanofocusing optics are not independent parameters but constrained by the diffraction condition. For a fixed coherence illumination condition, a smaller MLL requires a smaller transverse coherence length and consequently a larger secondary source size. However, this increase in the transmitted flux through the secondary source aperture is exactly cancelled by the fact that a smaller MLL has a smaller angular acceptance, leading to an identical utilization of the available flux as long as the size of the nanofocusing optic is not too large or too small (see section 2.4).

2.10.3 Flux of the nanofocused beam

Having calculated the fraction of the available flux that is accepted by the nanofocusing optics, the focused flux can be estimated by multiplying this fraction by the total flux at the secondary source aperture and the efficiency of the nanofocusing optics. In this calculation, we assumed the following efficiencies:

- 50% of the theoretical efficiencies for the flat and wedge MLLs. The 2D efficiencies used for the calculation are: 1.45% for fMLL at 10keV, 2.20% for fMLL at 20keV, 22% for wMLL at 10 and 20keV.
- 2% for the zone plate at 10keV with dr_N=24nm (which will result a 30 nm diffraction-limited focusing). 2% efficiency at 10keV is somewhat optimistic but still within the current and near future fabrication capabilities.

The results are presented in Figure 2.10.3. In the absence of source broadening, the focused flux for a flat MLL is $1.5x10^9$ ph/s at 10 keV when ξ =D. Under this condition, the resulting focus size still has a tiny contribution from the source demagnification. Convolution of the point spread function of the nanofocusing optics with the contribution from the source demagnification results in a focus size of 10.9 nm for MLL optics with dr_N=10nm. With a source broadening of 2, the estimated flux is 3.7 $x10^8$ ph/s. A conservative flux estimate is $3.7\sim6.6x10^8$ ph/s, where $6.6x10^8$ ph/s corresponds to a source broadening of 1.5. Under a highly relaxed coherence illumination condition (ξ =D/10), leading to a focus size of 45.1 nm, a conservative flux estimate is $0.2\sim3.2$ $x10^{10}$ ph/s. The illumination condition for the green curve (ξ =D/4) produces a 20.2 nm focus with an estimated flux of $5.5\sim9.1x10^9$ ph/s. The condition for the blue curve (ξ =D/2) produces a focus size of 13.2 nm, resulting in an estimated flux of $1.5\sim2.6x10^9$ ph/s. Under this condition, the beam size increases by only about 30% in comparison with the case, ξ =D, while the focused flux has increased by four times.

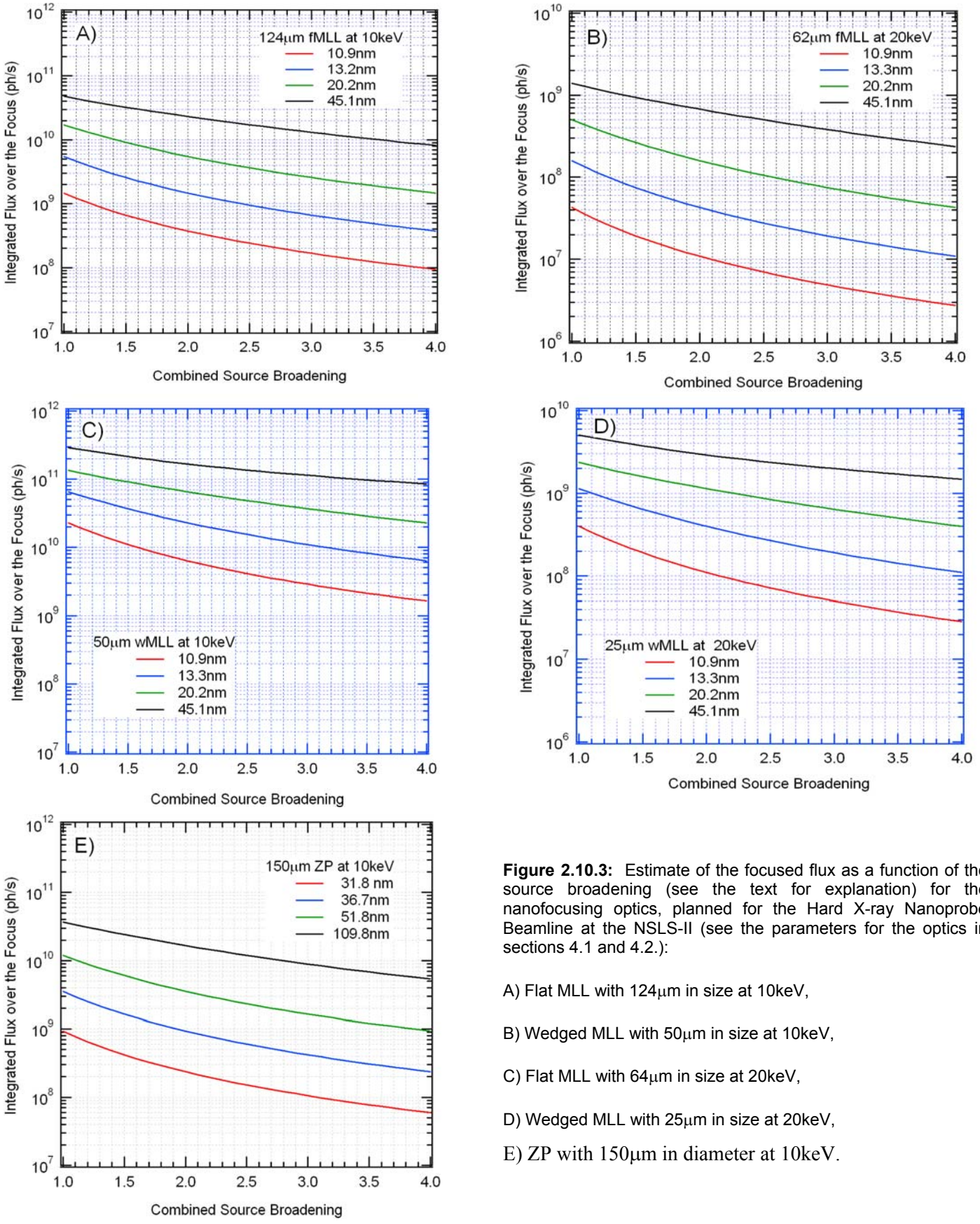

Figure 2.10.3: Estimate of the focused flux as a function of the source broadening (see the text for explanation) for the nanofocusing optics, planned for the Hard X-ray Nanoprobe Beamline at the NSLS-II (see the parameters for the optics in sections 4.1 and 4.2.):

A) Flat MLL with 124μm in size at 10keV,

B) Wedged MLL with 50μm in size at 10keV,

C) Flat MLL with 64μm in size at 20keV,

D) Wedged MLL with 25μm in size at 20keV,

E) ZP with 150μm in diameter at 10keV.

At 20 keV, the focused flux for flat MLLs is about 35 times lower, not because of the efficiency but because of the lower source flux. The estimated focus flux of a 10nm focus is 1.1~1.9 $x10^7$ ph/s assuming a beam broadening of 1.5 to 2.0. The estimated flux for a 44nm focus is 6.8~8.7$x10^8$ ph/s.

The focus flux of wedged MLLs is much higher for comparable conditions. The reason for the enhanced efficiency of the wedged MLLs is explained in Appendix 4. In the absence of source broadening, the integrated flux over a 10.9 nm spot size produced by the wedged MLLs is 2.3$x10^{10}$ ph/s at 10 keV. This estimate, assuming a source broadening of 1.5 to 2.0, is 0.6~1.1$x10^{10}$ ph/s. For a 45.1 nm focus, the estimated flux is 1.7~2.1$x10^{11}$ ph/s. At 20 keV, the flux of the wedge MLLs is lower. For a 10.9 nm focus, the estimated flux is 1.1~1.9$x10^8$ ph/s, and for a 45.1 nm focus, the estimated flux is 2.9~3.7$x10^9$ ph/s.

The flux estimate for a ZP producing a much longer working distance (see section 4.1) but a larger spot size in comparison with the MLLs, is given in Figure 2.10.3E. Based on similar criterion, the estimated flux for a 31.8 nm focus by a ZP is 2.4~4.2 $x10^8$ ph/s at 10 keV. The estimated flux for a 51.8 nm focus is 3.6~6.0 $x10^9$ ph/s. At the 6 keV range, the performance of the zone plate would be more than 5 times higher because of the higher source brightness and ZP efficiency. Table 2.10.1 summarizes the flux estimates discussed in this section.

It is important to point out that the optical scheme presented in this report assumes that the secondary source is completely incoherent and the size of the aperture determines the coherence properties of the x-rays emitted by the secondary source. This assumption is not true particularly in the vertical direction. Consequently, the flux estimate given here should be considered as "conservative" estimate. In-depth discussion on the partial-coherence of the IVU20 source and its impact on the flux estimate on the HXN beamline is given in Appendix 6.

Table 2.10.1: Flux estimate for three different types of nanofocusing optics planned to be used at the HXN beamline. See text for the detailed explanation. See also Table 3.1.1 and Table 3.2.1 for the detailed parameters for the following nanofocusing optics.

Nanofocusing optics	Focus Size (nm)	Flux at 10keV (ph/s)	Flux at 20keV (ph/s)
flat MLLs, dr_N=10nm	10.9	3.7~6.6 $x10^8$	1.1~1.9 $x10^7$
	13.2	1.4~2.6 $x10^9$	4.3~7.9 $x10^7$
	20.2	5.5~9.1$x10^9$	1.6~2.6$x10^8$
	45.1	2.3~3.2 $x10^{10}$	6.8~8.7$x10^8$
wedged MLLs, dr_N= 10 nm	10.9	0.6~1.1 $x10^{10}$	1.1~1.9$x10^8$
	13.2	2.3~3.7 $x10^{10}$	4.0~6.4$x10^8$
	20.2	6.5~9.1 $x10^{10}$	1.1~1.6$x10^9$
	45.1	1.7~2.1$x10^{11}$	2.9~3.7$x10^9$
zone plate, drN=24nm	31.8	2.4~4.2 $x10^8$	
	36.7	0.9~1.6 $x10^9$	
	51.8	3.6~6.0 $x10^9$	
	109.8	1.7~2.4 $x10^{10}$	

3 ENDSTATION INSTRUMENTATION

3.1 Overview

The most important endstation instrument is the x-ray microscope that is capable of maintaining a diffraction-limited focal spot onto the sample and enable scientific investigations. The primary functionalities of the HXN microscope are listed below.

- Capable of achieving 10 nm spatial resolution using MLL optics
- Capable of achieving 30 nm spatial resolution using zone plate optics
- Compatible with both MLL and ZP optics
- Capable of providing x-ray fluorescence and diffraction capabilities as primary techniques
- Capable of providing Ptychography and differential phase contrast imaging as supporting techniques, to increase efficiency of the primary techniques and/or to provide complementary measurements that can be beneficial for analyzing the measurement results obtained by the primary techniques
- Able to achieve positioning and scanning capability of ~1nm, providing a solid development platform for sub-10 nm focusing during the operation phase
- Able to provide high vibration and temperature stability around the focusing optics and the sample
- Able to operate in vacuum or in He

The parameters for the MLL and ZP optics targeted for the HXN microscope are listed in Table 3.1.1. Flat and wedged MLL optics will be used for producing a 10-nm focus at energy ranges from 10 to 25 keV. The target working distance for the MLL optics is 2 mm for all energy ranges (detailed discussion on MLL optics are found in section 3.2 and Appendix 3-4). A small working distance of 2 mm adds instrument challenges in addition to meeting the stability requirement for maintaining a 10 nm focus. ZPs will be used for the energy range from 6-12 keV for x-ray microscopy applications at 30 nm spatial resolution. The target working distance for the ZP is much larger due to the lower target spatial resolution and a larger target size than the MLLs. The depth of focus for both types of nanofocusing optic is larger than 3 μm for all energies.

Table 3.1.1: Target parameters of the MLL and ZP optics for the HXN microscope.

Optic type	Target resolution (nm)	Operation energy range (keV)	Target size/ diameter (m)	Depth of focus (m)	Target focal length (mm)	Target working distance (mm)	Target 2D efficiency
flat MLLs	10	10~25	124 at 10keV 62 at 20keV	3.2 at 10keV 6.4 at 20keV	10	2	2.9% at 10keV 4.4% at 20keV
wedged MLL	10	10~25	50 at10keV 25 at 20keV	3.2 at 10keV 6.4 at 20keV	4	2	45% at 10keV 45% at 10keV
ZPs	30	6~12	150	17.4 at 6keV 34.8 at 12keV	21.8 at 6keV 43.5 at 12keV	~7 at 6keV ~14 at 12keV	~2% at 10keV

An x-ray microscope offering the above capabilities and requirements has not been constructed to date, and there is no commercially available microscope or proven technical design with guaranteed performance at 10 nm spatial resolution. The HXN microscope will be designed and constructed through the Nanopositioning R&D at NSLS-II and close collaboration with Dr. Deming Shu at Argonne National Laboratory, who has prototyped the Nanoprobe Instrument at the APS beamline 26-ID [3.1.1] and the first MLL-based microscope currently being used at the same beamline [3.1.2]. The initial conceptual design of the HXN microscope is completed and the performance test of the critical components is ongoing. Our conceptual design utilizes a “modular” concept. Each module is designed

for a specific functionality while ensuring mutual compatibility with well-defined common coordinates. Different types of microscopy measurements, such as x-ray fluorescence using MLLs or x-ray diffraction using a ZP, will be carried out using a different set of modules. A similar modular approach has been successfully implemented at the Nanoprobe Instrument at APS. Individual modules for the HXN microscope are listed below:

- MLL Optic Module (MOM): positions two cross-linear MLLs and produces a focused beam. The MLL OSA is integrated into the MLL optic module:
- ZP Optic Module (ZOM): positions a ZP and produces a focused beam. The ZP OSA is integrated into the ZP optic module:
- SAmple Module for XRF (SAMF): positions the sample using three translation motions (X, Y, Z). This module is designed for the highest stiffness.
- SAmple Module for 1-axis Diffraction (SAM1D): provides XYZ translation and a single rotational degree of freedom for the sample. This module is designed for single-rotation diffraction or fluorescence imaging.
- SAmple Module for 3-axis Diffraction (SAM3D): provides XYZ translation, two limited tilts and a single rotation. This module is designed to provide a versatile sample alignment for diffraction.

The MLL optic module is the most technically challenging component of the HXN microscope since it requires up to 8 degrees of freedom for translation and rotation motions. A prototype MLL microscope has already been constructed and is used for microscopy experiment at APS 26-ID yielding a 2D spatial resolution of 25x27 nm^2 [3.1.3]. The HXN team is actively engaged in this collaborative effort with APS [3.1.2, 3.1.4]. However, the MLL prototype does not offer compatibility with the existing design of the ZP-based microscope and cannot be used as an MLL module for the HXN microscope. Bearing this in mind we have developed a conceptually different approach taking advantage of the principles used at the Nanoprobe Instrument at APS 26-ID but significantly increasing the overall mechanical stiffness and stability of the instrument. In this section of the PDR we describe the instrument development approach and conceptual designs, and present a comprehensive perspective for the HXN microscope.

[3.1.1] D. Shu, J. Maser, B. Lai, and S. Vogt, *SRI 2003 Conf. Proc., 705, AIP (2004) 1287-1290.*
[3.1.2] D. Shu, H. Yan, and J. Maser, in Proceedings of SRI-2008 (to be published in *Nucl. Instrum. Methods* A, Saskatoon, Canada, 2008).
[3.1.3] H. Yan, V. Rose, D. Shu, et al., submitted to *Appl. Phys. Letts*.
[3.1.4] D. Shu, H. Yan, and J. M. Maser, USA Patent 7597475.

3.2 Optimized use of MLL optics

There have been numerous publications on theoretical modeling [3.2.1, 3.2.2], fabrication [3.2.3-3.2.5], and x-ray experiments on MLL optics [3.2.6, 3.2.7]. However, little has been published on an optimized strategy for implementing MLLs in an x-ray microscope for real scientific applications. Unlike reflective or refractive optics, MLLs produces multiple foci. In order to use MLLs in general x-ray microscopy experiments, a beamstop and order-sorting aperture (OSA) must be implemented for filtering out the unfocused incident x-rays and higher-order diffracted x-rays. Presence of the OSA significantly reduces the working space available around the sample, needed for placing energy-dispersive detectors for x-ray fluorescence measurements. The working distance (the distance from the OSA to the focal plane) is proportional to the ratio of the beamstop size to the lateral dimension of the lens. For a given pair of MLLs, increasing the working distance consequently creates a significant apodization effect, resulting in increased intensity for the side lobes around the focus. The optimized use of MLLs in an x-ray microscope therefore requires careful attention to various MLL-specific considerations. Since a complete discussion will be presented elsewhere [3.2.8], only a brief discussion is presented here.

The physical aperture of a MLL is determined by the total thickness of the MLL multilayers deposited on a substrate. The total MLL multilayer thickness is ultimately limited by 1) the interfacial stress accumulated during the film growth, and 2) the maximum deposition allowed by the consumable sputtering target. Consequently, a half-

structure and a full-structure MLL have an identical numerical aperture limit, provided that their focal lengths are the same. The half-structure does not suffer from the apodization effect resulting from the wave interference between two separated apertures. However, it requires the deposition of 200% more zones with a 50% smaller outmost zone width to achieve the same NA as a full-structure MLL. Since the layer-positioning capability of a multilayer is better than 1 nm, an effective trade-off can be made by using the half-structure with a smaller outmost zone width. For flat MLLs, the half-structure is much easier to work with and it can be tilted to meet the local Bragg condition for the outer zones of the MLL [3.2.2]. Until now, the instrumentation development work and x-ray microscopy experiments have carried out using only the half-structure. Thus, it is natural to continue this approach for the HXN microscope.

A more compelling reason to use the half-structure is due to the fact that the half-structure produces much smaller apodization effects, as mentioned earlier. Figure 3.2.1A shows the intensity profiles through 1D focus for three different cases: the full-structure with no beamstop (ε=0), the full-structure with ε=0.2, and the-half structure with ε=0.2, where ε is the ratio between the beamstop size, D_s, and the MLL aperture, D. The geometric configuration of the MLL optic, together with the beamstop and OSA, is schematically represented in Figure 3.2.1B. The simulation shows that the half-structure MLL optic shows no apodization effect. An intuitive explanation can be given in the following way. For the full structure, the obstruction of the central portion of the MLL produces coherent interference between the resulting two partial structures, producing the higher intensity in the side lobes. For the half structure, the interference cannot be produced due to the absence of the counterpart.

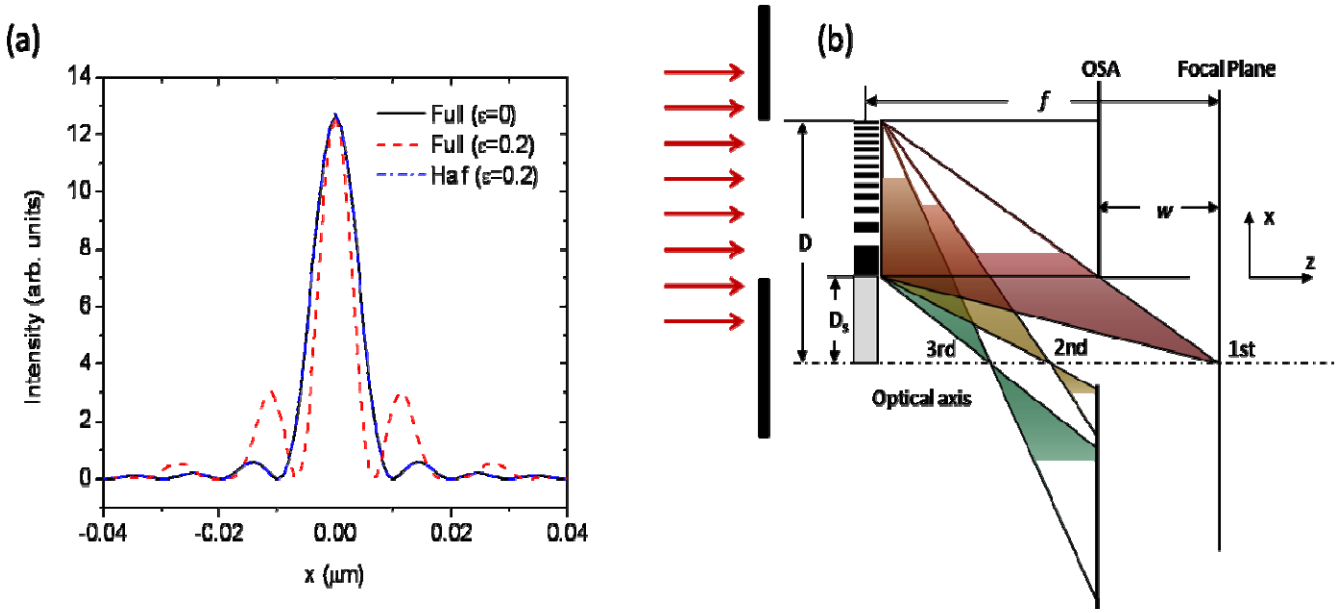

Figure 3.2.1: A) Apodization effect, The black and blue curves overlap completely. (B) Schematic view of a half-structure MLL optic together with a beamstop and an OSA.

However, there is a price to pay for using the half-structure. As shown in Figure 3.2.1B increasing the working distance requires both pushing the OSA closer toward the MLL and increasing the value of ε. In order to maintain the same numerical aperture as the full-structure, the zone width must be decreased. For ε=0.2 (corresponding to the effective use of 40% of the full-structure), the outmost zone width must decrease by 2.5 (=1/40%) times and the inner zones larger than 20 nm do not contribute to the focusing due to the beamstop. As the zone width decreases, the dynamical effect becomes stronger, resulting in broadening of the focus size (see Appendix 3 for an explanation). To reduce the dynamical effect, the lens thickness must be reduced, reducing the focusing efficiency.

For the ideal thickness, 10 nm focusing at 10 keV, increasing the working distance equivalent to ε=0.4 results only a 6.4% 1D focusing efficiency. The resulting 2D focusing efficiency is 0.4%

There are two possible strategies to tackle this challenge. The first is to fabricate a large size MLL optic, so that the working distance can be increased without using a large beamstop. Fabricating MLLs with an aperture size of 100~150 microns is an important R&D goal for the 1nm Spatial Resolution R&D, and considerable efforts are being made in this direction. The second is to use the wedged MLL, in which the dynamical effects can be used for increasing the efficiency without broadening the focus (see Appendix 3). Successful fabrication of high-resolution wedged MLLs is an important milestone for the 1nm Spatial Resolution R&D, and a specialized deposition system has been developed and is in operation (see Appendix 4).

Table 3.2.1 lists the parameters for the MLLs that are targeted to produce 10nm focusing at the HXN beamline. These parameters are produced with two constraints: 1) to produce 10nm focusing and 2) to produce a 2 mm working distance at both 10 and 20 keV [3.2.9]. The wedged MLL can tolerate a much larger value of ε than the flat MLL while producing higher efficiency, because the wedge MLL interface takes advantage of dynamical effects (see Appendix 4). Note that the number of zones required for fabricating such MLL optics is extremely large. Despite the large number of zones, the monochromaticity required of the incident beam for a half-structure can still be satisfied by a Si (111) monochromator. Consequently, achieving a 10nm focus using a MLL aperture of 124 μm does not require a higher resolution monochromator. In fact, if the fabrication of MLLs is not the limitation, a conventional Si (111) monochromator can still be used for a MLL with an aperture size of ~300 μm.

Table 3.2.1: The parameters for MLLs for delivering 10nm focusing at the HXN beamline as an initial goal. Effective innermost zone width is the width of the innermost zone that is illuminated by the incident beam due to the beamstop. Monochromaticity refers to the monochromaticity requirement of the incident beam to avoid the broadening of the focus. Tilting angle is the angle of the MLL with respect to the incident beam. fMLL = flat MLL, wMLL = wedged MLL.

Energy/ type	Focal length (mm)	ε	Working distance (mm)	Aperture size (m)	Outermost zone width (nm)	Effective Innermost zone width (nm)	Number of zones	Mono-chromaticy ($x10^{-4}$)	Thickness (m)	Efficiency/ tilting angle
fMLL/ 10keV	10	0.2	2	124	4	20	14,877	3.2	4	17% 0.35°
wMLL/ 10keV	4	0.5	2	50	2.5	5	18,599	8.1	10	67% 0.00°
fMLL/ 20keV	10	0.2	2	62	4	20	7,440	6.5	8	21% 0.17°
wMLL/ 20keV	4	0.5	2	25	2.5	5	9,300	16.1	16	67% 0°

[3.2.1] J. Maser and G. Schmahl, *Optics Communications* 89, 355 (1992).
[3.2.2] H.F. Yan, J. Maser, A. Macrander, et al., *Physical Review B* 76, 115438 (2007).
[3.2.3] R. Conley, C. Liu, J. Qian, et al., *Review of Scientific Instruments* 79, 053104 (2008).
[3.2.4] C. Liu, R. Conley, A.T. Macrander, et al., *Journal of Applied Physics* 98, 113519 (2005).
[3.2.5] C.A. Liu, R. Conley, J. Qian, et al., *Nuclear Instruments & Methods in Physics Research, Section A, Accelerators, Spectrometers, Detectors, and Associated Equipment,* 582, 123 (2007).
[3.2.6] H.C. Kang, J. Maser, G.B. Stephenson, et al., *Physical Review Letters* 96, 127401 (2006).
[3.2.7] H.C. Kang, H.F. Yan, R.P. Winarski, et al., *Applied Physics Letters* 92, 221114 (2008).
[3.2.8] H.F. Yan, et al., manuscript in preparation.

3.3 Preliminary design of the microscope

To enable the functionalities described in section 3.1, the microscope design has to satisfy a number of strict technical requirements. The instrument must provide the capability to align both MLL and ZP optics and adjust the range for focal distances up to 10 mm for the MLL focusing optics and up to 45 mm for the ZP optics. To enable high spatial resolution and stability, the influence of ambient conditions has to be minimized. In other words, all components of the instrument, including focusing optics and the sample environment, must be designed as a vacuum-compatible system. From a design stand point, due to fundamental differences in alignment requirements for the MLL and ZP optics, it is not possible to build a single instrument where both MLL and ZP optics will be incorporated. Instead, we use a modular approach to accommodate different types of focusing elements. In Figure 3.3.1 we show the schematic of the MLL and ZP modules respectively with the required degrees of motion. In Tables 3.3.1 - 3.3.5 we list the specifications for individual modules.

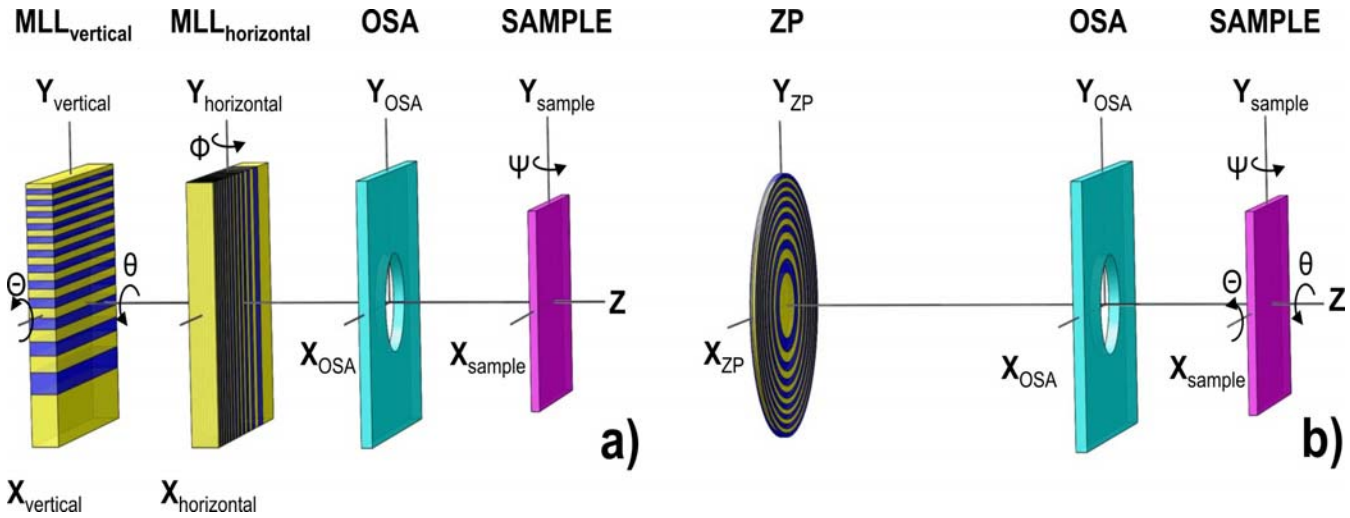

Figure 3.3.1: Schematic representation of the modules for the HXN microscope. a) The MLL module together with the sample module for a 1-axis diffraction (SAM1D). b) The ZP module together with the sample module for a 3-axis diffraction (SAM3D).

Table 3.3.1: Specifications for the MLL module.

	Coarse Travel Range (X, Y, Z) [mm]	Resolution Coarse (min. motion) (X, Y, Z) (m)	Fine Travel Range (X, Y, Z) (m)	Resolution Fine (min. motion) (X, Y, Z) (nm)	Rotation (Θ,θ,Φ,Ψ)	Angular resolution (Θ,θ,Φ,Ψ)	Max. Load (g)
Vertical MLL	10	0.1	7	<1	≤ 3^0	0.002^0	<200
	10	0.1	7	<1	≤ 3^0	0.002^0	
	10	0.1	7	<1	N/A	N/A	
					N/A	N/A	
Horizontal MLL	10	0.1	7	<1	≤ 5^0	0.002^0	<200
	10	0.1	7	<1	N/A	N/A	
	10	0.1	7	<1	N/A	N/A	
					N/A	N/A	
OSA	10	0.1	N/A	N/A	N/A	N/A	<200
	10	0.1					
	10	0.1					

Table 3.3.2: Specifications for the ZP module.

	Coarse Travel Range (X, Y, Z) [mm]	Resolution Coarse (min. motion) (X, Y, Z) (m)	Fine Travel Range (X, Y, Z) (m)	Resolution Fine (min. motion) (X, Y, Z) (nm)	Rotation (Θ,θ,Φ,Ψ)	Angular resolution (Θ,θ,Φ,Ψ)	Max. Load (g)
ZP	23	0.05	15	<1	N/A	N/A	<2000
	3	0.05	15	<1			
	45	0.05	0	N/A			

Table 3.3.3: Specifications for the sample module for fluorescence.

	Coarse Travel Range (X, Y, Z) [mm]	Resolution Coarse (min. motion) (X, Y, Z) (m)	Fine Travel Range (X, Y, Z) (m)	Resolution Fine (min. motion) (X, Y, Z) (nm)	Rotation (Θ,θ,Φ,Ψ)	Angular resolution (Θ,θ,Φ,Ψ)	Max. Load (g)
SAMF	3	<0.1	5	<1	N/A	N/A	<200
	3	<0.1	5	<1			
	15	<0.1	5	<1			

Table 3.3.4: Specifications for the sample module for 1-axis diffraction

	Coarse Travel Range (X, Y, Z) [mm]	Resolution Coarse (min. motion) (X, Y, Z) (nm)	Fine Travel Range (X, Y, Z) (m)	Resolution Fine (min. motion) (X, Y, Z) (nm)	Rotation (Θ,θ,Φ,Ψ)	Angular resolution (Θ,θ,Φ,Ψ)	Max. Load (g)
SAM1D	3	50	15	<1	N/A	N/A	<500
	3	50	15	<1	N/A	N/A	
	20	50	0	N/A	N/A	N/A	
					360°	≤0.0001⁰	

Table 3.3.5: Specifications for the sample module for 3-axis diffraction

	Coarse Travel Range (X, Y, Z) [mm]	Resolution Coarse (min. motion) (X, Y, Z) (nm)	Fine Travel Range (X, Y, Z) (m)	Resolution Fine (min. motion) (X, Y, Z) (nm)	Rotation (Θ,θ,Φ,Ψ)	Angular resolution (Θ,θ,Φ,Ψ)	Max. Load (g)
SAM3D	3	50	15	<1	10	≤ 0.0001⁰	<500
	3	50	15	<1	10	≤ 0.0001⁰	
	20	50	0	N/A	N/A	N/A	
					360	≤ 0.0001⁰	

The preliminary design of the HXN microscope is shown in Figures 3.3.2 and 3.3.3. Much of the preliminary design of the HXN microscope is motivated by the design concept for the Nanoprobe Instrument at APS 26-ID [3.3.1], with some important modifications. As the design matures, the differences will increase because of the HXN-specific requirements. For the HXN microscope, the detectors outside of the vacuum enclosure are placed on a separate support system, in order to isolate potential vibrations or load shifting generated by positioning the external detectors or the detector cooling mechanisms. On the other hand, the multi-element energy dispersive detector for fluorescence measurement will be integrated around the sample module and will be placed on the same support system for the vacuum enclosure. Specific technical details on integrating the XRF detector around the sample have not been fully developed yet.

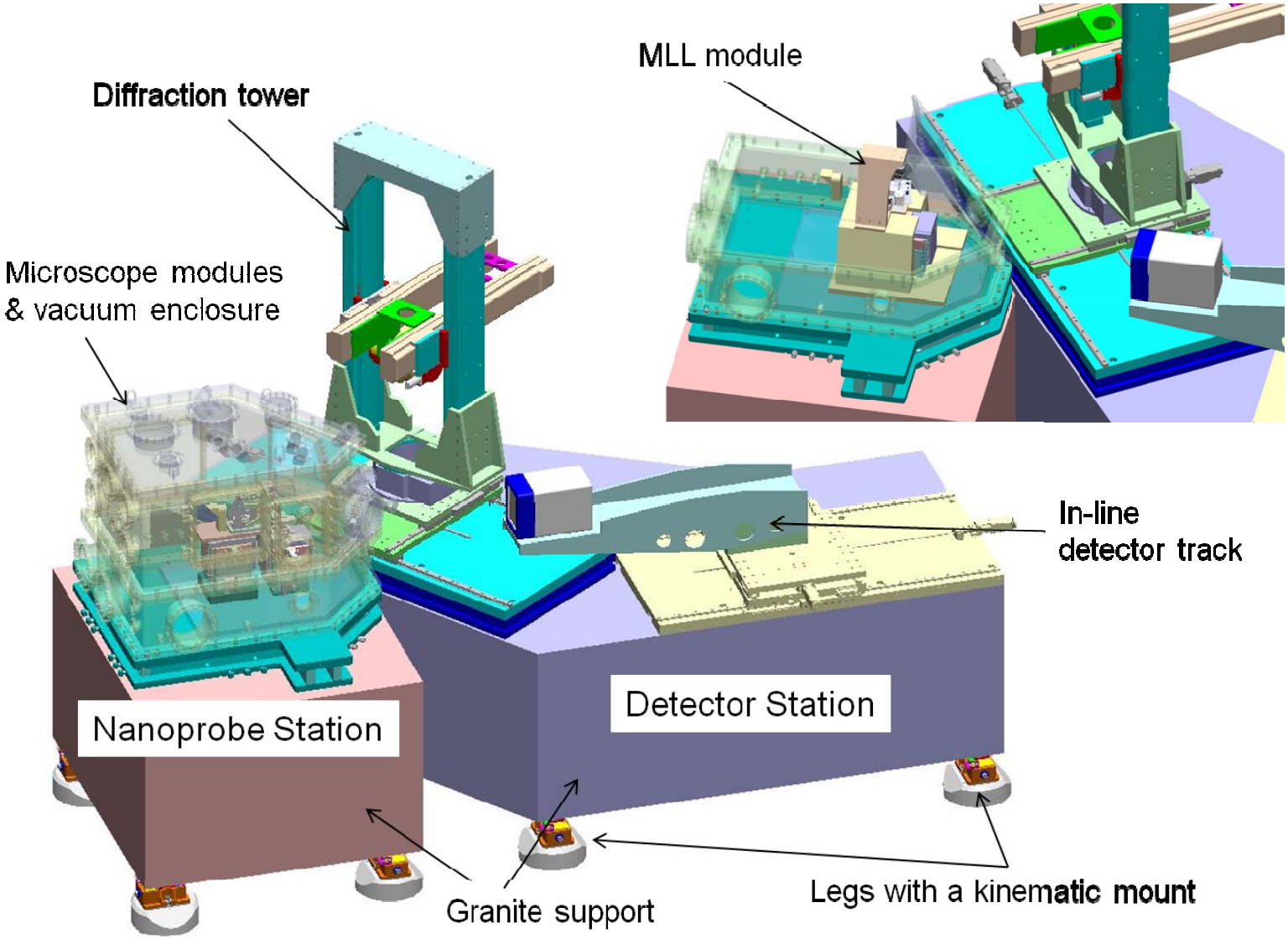

Figure 3.3.2: Preliminary design of the HXN microscope. The HXN microscope has the nanoprobe station containing of the microscope modules within a vacuum enclosure and the detector station consisting of a diffraction tower for nanodiffraction and an in-line detector track for positioning in-line detectors. The granite supports have legs with kinematic mounts allowing manual positioning adjustment. The insert in the upper right corner shows one of the modules without the top cover of the vacuum enclosure.

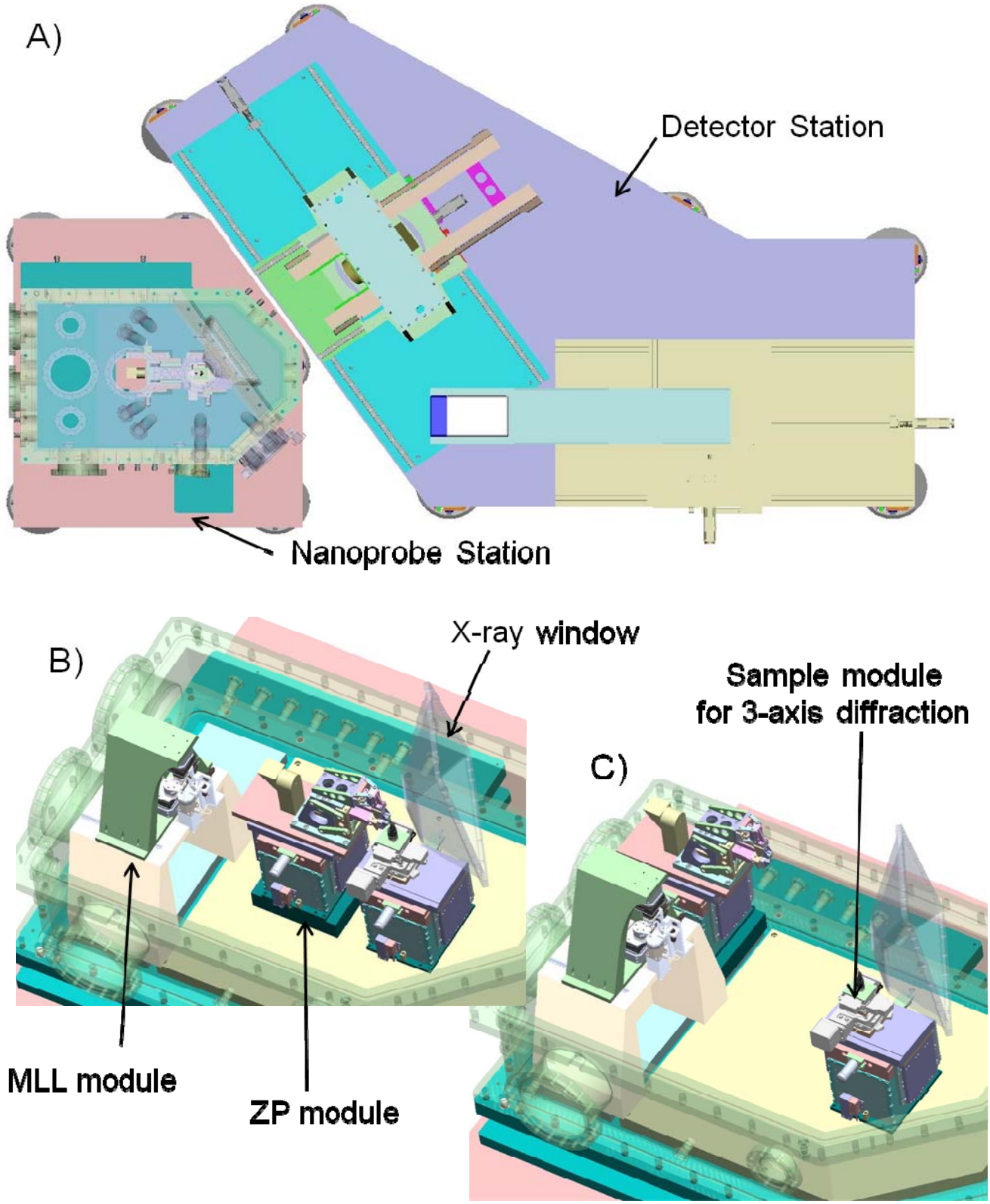

Figure 3.3.3: Preliminary Design of the HXN microscope: A) Top view of the HXN microscope. The modular concept of the HXN microscope is shown in B) and C), where B) shows the ZP module being used while the MLL module is in its "parking" position, and C) shows both modules are in their parking positions. See the text for explanation.

The detector station provides positioning capabilities for three different detectors: a nanodiffraction CCD (which will be upgraded to a pixel-array detector in the mature operation phase of the HXN beamline), a pixel-array CDI/DCP detector, and an optically-coupled high-resolution imaging CCD. The nanodiffraction CCD is positioned by a diffraction tower. The diffraction tower provides 5 degrees of motion freedom, 2 angular and 3 translational motions [3.3.2]. Together, the diffraction tower can align the nanodiffraction detector surface to an arbitrary diffraction vector from the sample with a ~0.4 m adjustment range for the distance to the sample. The diffraction tower will be constructed with a load capacity of ~12 kg, sufficient to hold a significantly heavy detector. A long linear track next to the diffraction tower will be used to position both a pixel-array detector for CDI/DCP and a high-resolution CCD. This in-line detector track will have common kinematic mounts for both detectors, allowing a straightforward swapping capability with highly repeatable positioning accuracy.

[3.3.1] D. Shu et al., *Proc. 8th Int. Conf. X-ray Microscopy*, IPAP Conf. Series 7 (July 2006) 56-58.
[3.3.2] D. Shu, J. Maser, M. Holt, R. Winarski, C. Preissner, B. Lai, S. Vogt, and G.B. Stephenson, *Nucl. Instrum. and Methods A* 582 (2007) 159-161.

3.4 Laser encoder system

Accurate readout or encoding of the positions of the optics and the sample is a critical challenge for high-resolution x-ray microscopes. Design of the microscope is aimed to minimize thermal drifts of sample stages and focusing optics with respect to each other. However, to insure compensation for possible long term drifts due to temperature gradients, vibrations or trajectory errors, we implement a laser interferometer system mounted in the instrument. Furthermore, the goal of the laser interferometer feedback is to keep the relative position between the optics and the sample constant. Differential feedback, which has been implemented in x-ray microscopes [3.4.1], reduces the number of high-resolution stages for the microscope and provides more options for nanopositioning control feedback. Optimization of the differential feedback scheme, specific for the HXN microscope, is one of the critical tasks for the Nanopositioning R&D. Laser interferometer heads will be mounted on an invar reference frame which has a linear thermal expansion coefficient of 1.2×10^{-6} m/m K. The position of focusing lenses and the sample holder will be measured with respect to the reference frame. In addition, a laser interferometer system will be used for encoding of the sample position during scanning. We implement fiber-optic based Fabry-Perot interferometers developed through collaboration with Attocube AG. Advantages of these interferometers include:

- Compact design (measuring head has a diameter of 12 mm and length of 15 mm)
- Vacuum compatibility
- Ability to split the laser beam into 10 channels, so that possible drifts of laser wavelength cannot lead to errors for differential positioning (i.e., systematic errors will cancel each other).
- Low dissipated power per channel (< 100 μW)
- High bandwidth (up to 1 MHz)
- High spatial resolution (better than 1 nm at distances less than 40 mm)
- High long term stability (2σ drifts of less than 1 nm over a 3 hours time period)
- Ability to disconnect fibers from collimating heads and connect to different microscope modules, essential to the HXN microscope requirement.

Disadvantages of this interferometric system include degradation of resolution with increasing working distance and the lack of data which describes behaviour of interferometers in the presence of hard x-rays. These two questions will be explored and addressed within the Nanopositioning R&D program at NSLS-II. In Figure 3.4.2 we show preliminary results for stability evaluation of fiber-optic interferometers. We expect to achieve even better stability within the Nanopositioning R&D program.

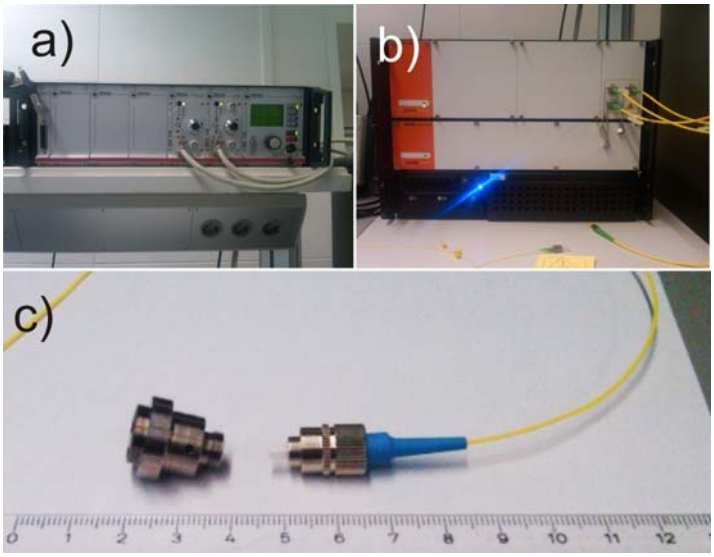

Figure 3.4.1: A) & B) Laser and laser control units. C) Interferometer head with the FC fiber connector

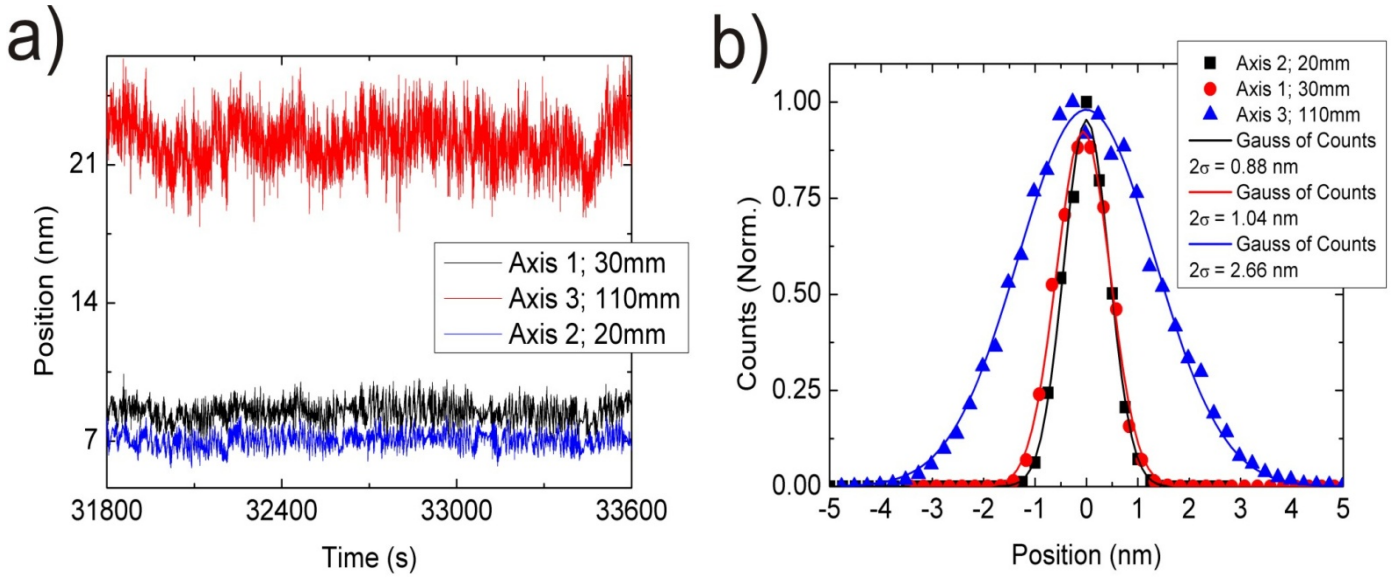

Figure 3.4.2: Preliminary results for stability evaluation. Interferometric cavities of different lengths (20, 30 and 110 mm) were cooled to liquid He temperatures and the signal was recorded as a function of time, see panel a). 2-sigma distribution is plotted in b) for half an hour time period, the measurement drift is on the order of 1 nm for 20 and 30 nm cavities.

As an alternative solution, homodyne interferometers manufactured by SIOS Messtechnik GmbH [3.4.2] may be considered for the HXN microscope. Triple-beam plane mirror interferometers combine three interferometers into a single unit and are capable of simultaneous nanometer precision tri-axial distance measurements. The major disadvantage of these interferometers is vacuum incompatibility which requires installation of optical windows in the microscope vacuum enclosure and an increased optical path from the laser source to the reflector. Recently, a new heterodyne laser Doppler displacement meter with fiber optics output was developed by Optidyne, Inc [3.4.3], offering a much more enhanced sensitivity. The performance of these interferometers will be evaluated within the Nanopositioning R&D at NSLS-II.

[3.4.1] D. Shu et al., Proc. 8th Int. Conf. X-ray Microscopy, *IPAP Conf. Series* **7** pp.56-58
[3.4.2] http://www.sios.de/ENGLISCH/PRODUKTE/SP-TR_E.HTM
[3.4.3] http://www.optodyne.com

3.5 High-stiffness weak-link base stages

Precision ball-bearing- or roller-bearing-based positioning stage systems provide a large travel range. However, it is not possible to meet requirements in sub-nanometer positioning resolution, high tilting stiffness, and sub-microradian straightness of trajectory repeatability with a single guiding system. Traditional flexure linear mechanisms can provide large travel range, however they usually lack a high tilting stiffness and microradian-level straightness of trajectory. Based on the design experiences of precision linear and tilting stages using high-stiffness laminar over-constrained weak-link mechanisms [3.5.1] for high precision monochromators and other experimental instruments at the APS [3.5.2, 3.5.3], we have developed a new two-dimensional (2-D) weak-link stage system for nanopositioning of a specimen holder for the HXN microscope. With a new weak-link linear guiding structure, this system provides sub-nanometer resolution, coupled to sub-nanometer metrology, and a travel range of several millimeters. As shown in Figure 3.5.1, the 2mm-thick 118 mm x 116 mm weak-link module is a "fishbone"-shaped multiple parallelogram weak-link structure [8]. It is a bounded laminar structure with eight thin-metal weak-link sheets. There are two groups of mounting terminals on the weak-link module: terminals on frame 1 are mounted on a carriage, terminals 2-7 are terminals for a mounting base. The finite-element simulation for a 1.61-mm displacement of the carriage shows that, when a 17-N force is applied to the carriage, the maximum Von Mises stress is 974 MPa, which is about 81% of the tensile yield strength of the stainless steel 17-7 PH. The simulation shows that, if the carriage is driven by the same level of push-pull force, the weak-link linear stage will have a travel range of 3.22 mm.

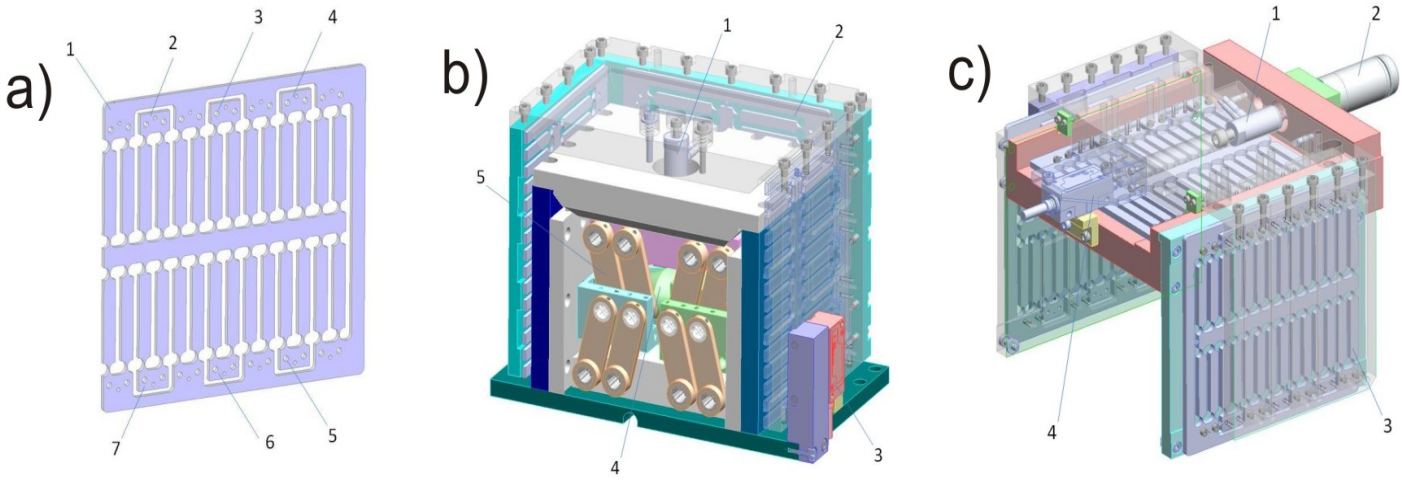

Figure 3.5.1: A) A 3-D model of the fishbone-shaped multiple parallelogram weak-link structure. Item (1) is the moving part, items (2) to (7) are terminals mounted to the fixed base. B) A 3-D model of the vertical weak-link stage T8-41. (1) PZT actuator PI P-841.10. (2) Weak-link guiding structure. (3) Optical encoder. (4) Newport PZA-12 actuator. (5) Linear motion reduction flexure mechanism. C) A 3-D model of the A 3-D model of the T8-42 horizontal weak-link stage. (1) PZT actuator PI P-841.10. (2) Newport PZA-12 actuator. (3) Weak-link guiding structure. (4) Optical encoder.

Using four fishbone-shaped laminar weak-link modules to construct a vertical linear motion guiding structure, we have designed a vertical weak-link stage guiding structure as shown in Figure 3.5.1B. The vertical stage T8-41 is driven by a customized driving mechanism combining a Newport PZA-12 actuator [3.5.4] with a PI P-841.10 PZT actuator [3.5.5], which will provide a 10 kg driving force for a 3 mm travel range with 10 nm open-loop resolution and sub-nanometer-resolution within the PI PZT 15-μm travel range. Figure 3.5.1C shows a 3-D model of the horizontal stage T8-42.

With an external laser encoder, both T8-41 and T8-42 weak-link stages have sub-nanometer closed-loop resolution in the entire 3 mm travel range. Preliminary tests of the vertical weak-link linear stage have demonstrated high tilting stiffness and high straightness of trajectory with nanometer-level positioning sensitivity. The tilting stiffness is better than many commercial motor-driven linear bearing-guiding vertical stages with a similar structure size.

According to a motion straightness-of-trajectory test result, the amount of the tilt is repeatable within 1 μrad throughout the stage's full travel range [3.5.6].

In our current design, the weak-link XYZ stage stack is an integral component for the HXN microscope, providing high-stability base translations for all the HXN modules. For example, the compact MLL module (described in section 3.6.1) is specifically designed for easy attachment and detachment from the SAMF (the sample module for x-ray fluorescence). The flexure-based MLL module (described in section 3.6.2) and the ZP module (described in section 3.7) use a common weak-link XYZ stack as their base support.

[3.5.1] U.S. Patent granted No. 6,984,335, D. Shu, T. S. Toellner, and E. E. Alp, 2006.
[3.5.2] D. Shu et al., SRI 2006, AIP CP879, (2007) 1073-1076.
[3.5.3] S. Narayanan, A. Sandy, D. Shu, M. Sprung, C. Preissner and J. Sullivan, *J. Synchrotron Rad*. (2008) 15, 12-18.
[3.5.4] Newport is a trademark of the Newport Co. USA.
[3.5.5] Physik Instrumente (PI) is a trademark of the Physik Instrumente GmbH & Co. Germany.
[3.5.6] D. Shu and J. Maser, *Proceedings of the 6th International Conference on Mechanical Engineering Design of Synchrotron Radiation Equipment and Instrumentation*, July 2010, Oxford, UK.

3.6 MLL module

A pair of MLL optics requires a total of eight degrees of freedom, five linear and three angular. The horizontal MLL is designed to have a shorter focal distance, corresponding to a higher source demagnification, because the horizontal source size is typically larger for synchrotron x-rays. This arrangement gives a better aspect ratio of the focused beam than the reversed case. For the vertical MLL, the vertical translation motion moves the focused beam vertically. Consequently, the vertical motion must have the highest resolution and stiffness. On the other hand, the horizontal translation motion for the vertical MLL does not have a direct impact on the position of the line focus and is used to select the location of the MLL optic to avoid possible bad spots. For a vertical MLL, prepared to have a horizontal thickness gradient, the horizontal translation can be used to select the optimal thickness for a given fixed energy for the flat MLLs. Consequently, a single MLL with a thickness wedge from 4~20 μm can be used for an energy range of 10-25keV. For the vertical MLL, the rotation about the x-axis is used to optimize the focal intensity. For the flat half-structure MLL, this rotation corresponds to "tilting", which is used to satisfy the local Bragg condition for the outer zones. The same description holds true for the horizontal MLL. The remaining two degrees of freedom are the z-translation of the vertical MLL, to be used for bringing the two linear foci to a common z-position and the azimuthal rotation of the vertical MLL about the incident beam, to be used for ensuring the orthogonality of the two linear foci, to avoid focus broadening.

During the design process of the microscope we will develop two different MLL modules. The first design is based on a new approach of implementing "stick and slip-based" piezo scanning devices, which are optimized for highest stiffness with a compact form factor. The second design is based on implementing stiff mechanical flexures, described in section 3.5, which is a mature concept that has been used successfully for several synchrotron instruments including the MLL prototype installed at APS 26-ID. Both of these modules will be optimized and evaluated within the Nanopositioning R&D and the best parts of both approaches will be merged into a final design installed at the HXN microscope.

3.6.1 Compact MLL module

To provide maximum stability and stiffness for the microscope using MLL optics, we are developing a MLL module based on the stick-and-slip stages shown in Figure 3.6.1.1. Stick-and-slip positioning stages require a minimal amount of power reducing possible thermal drifts, have a compact form factor, and extended travel ranges, as indicated in Table 3.3.1. Stick-and-slip stages have been successfully installed in scanning-probe microscopes and are used for coarse positioning even at low temperatures [3.6.1.1, 3.6.1.2]. In terms of heat dissipation, if we assume the typical holding force of 5 N along the movement axis and the positioning generates a 100 nm step, this

yields an energy dissipation of 500 nJ. If the positioning is performed with a frequency f of 10 Hz then the overall power dissipated is equal to 5 μW. In addition to mechanical friction, there are losses in the piezo element, $P = C \cdot U^2 \cdot f \cdot \tan(\delta)$, where C = 200 nF (typical piezo capacitance), f = 10 Hz (stepping frequency), U = 70 V (driving voltage), $\delta = 5^{\circ}$ (the loss angle of a piezo element at room temperature), yielding a power of 8.5 μW. When combined, both losses generate the heat on the order of 10 – 15 μW, a miniscule number compared to stepper motors. Moreover, after initial positioning stick-and-slip stages can be grounded eliminating any possible heat dissipations. Vertical MLL lens will be mounted on a positioning stage providing three lateral and two rotational degrees of motion, the horizontal MLL stage has three lateral and one rotational degrees of motion, sufficient to perform MLL lens alignment. The OSA stage provides three lateral degrees of motion. X and Y positions of the vertical and horizontal MLLs and also the X and Y positions of the sample stage are monitored using interferometers. Relative distances between interferometer heads and reflecting surfaces of the microscope components do not exceed 20 mm thus maximizing the interferometers spatial resolution, better than 1 nm. The scanning of the sample will be performed using a high stiffness (9.8 kHz resonance frequency) XYZ scanner PI-363 mounted on top of a high-stiffness flexure based mechanical stage developed by Dr. D. Shu at APS, described in section 3.5 (SAMF module). The design of the SAMF module targets maximum stiffness and stability in the XYZ translational motions.

[3.6.1.1] C. Meyer, O. Sqalli, H. Lorenz, K. Karrai, *Rev. Sci. Instr*., **76**, 063706 (2005).
[3.6.1.2] E. Nazaretski, et al., *Appl. Phys. Lett*. **90**, 234105 (2007).

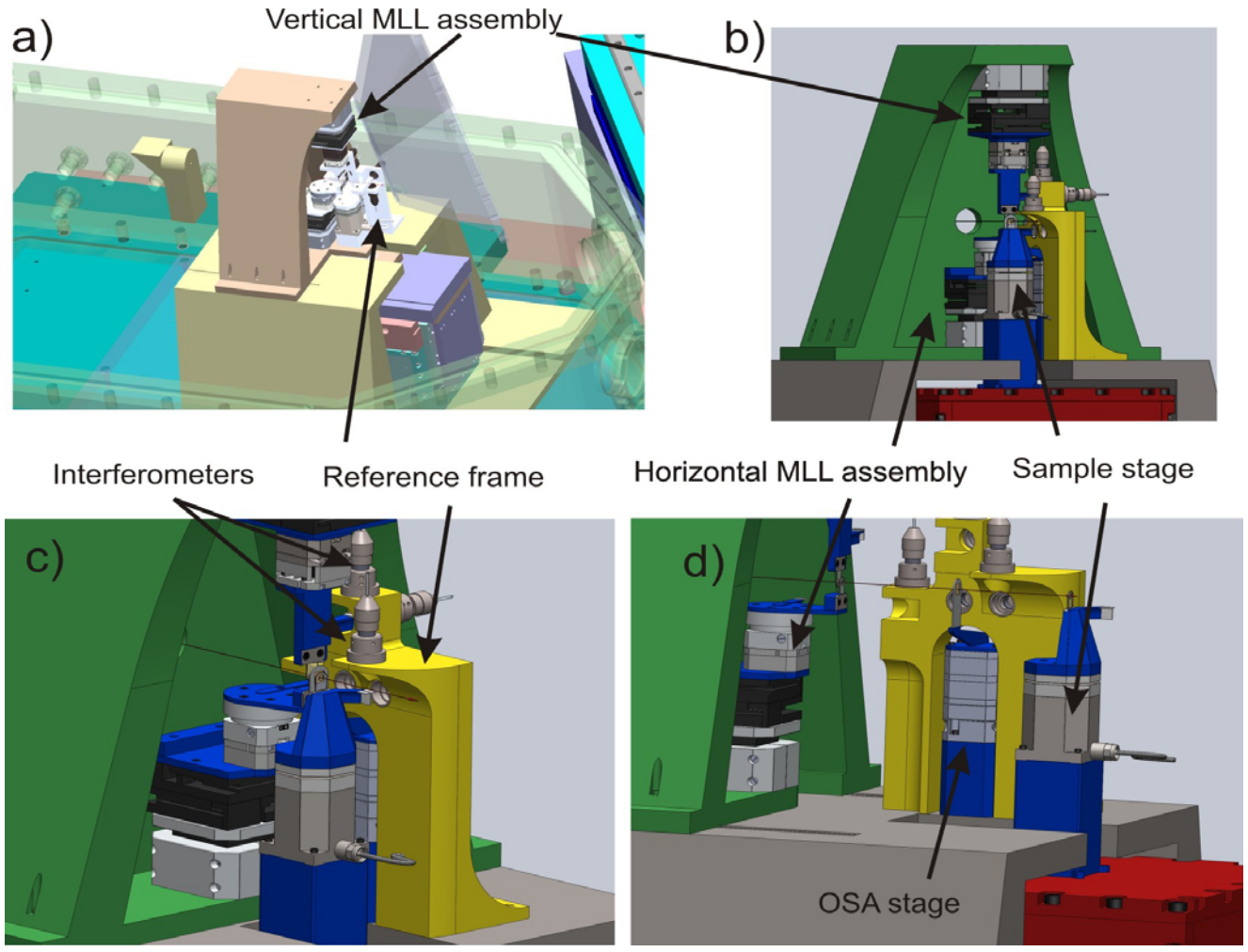

Figure 3.6.1.1: Compact MLL module based on stick-and-slip piezo stages.

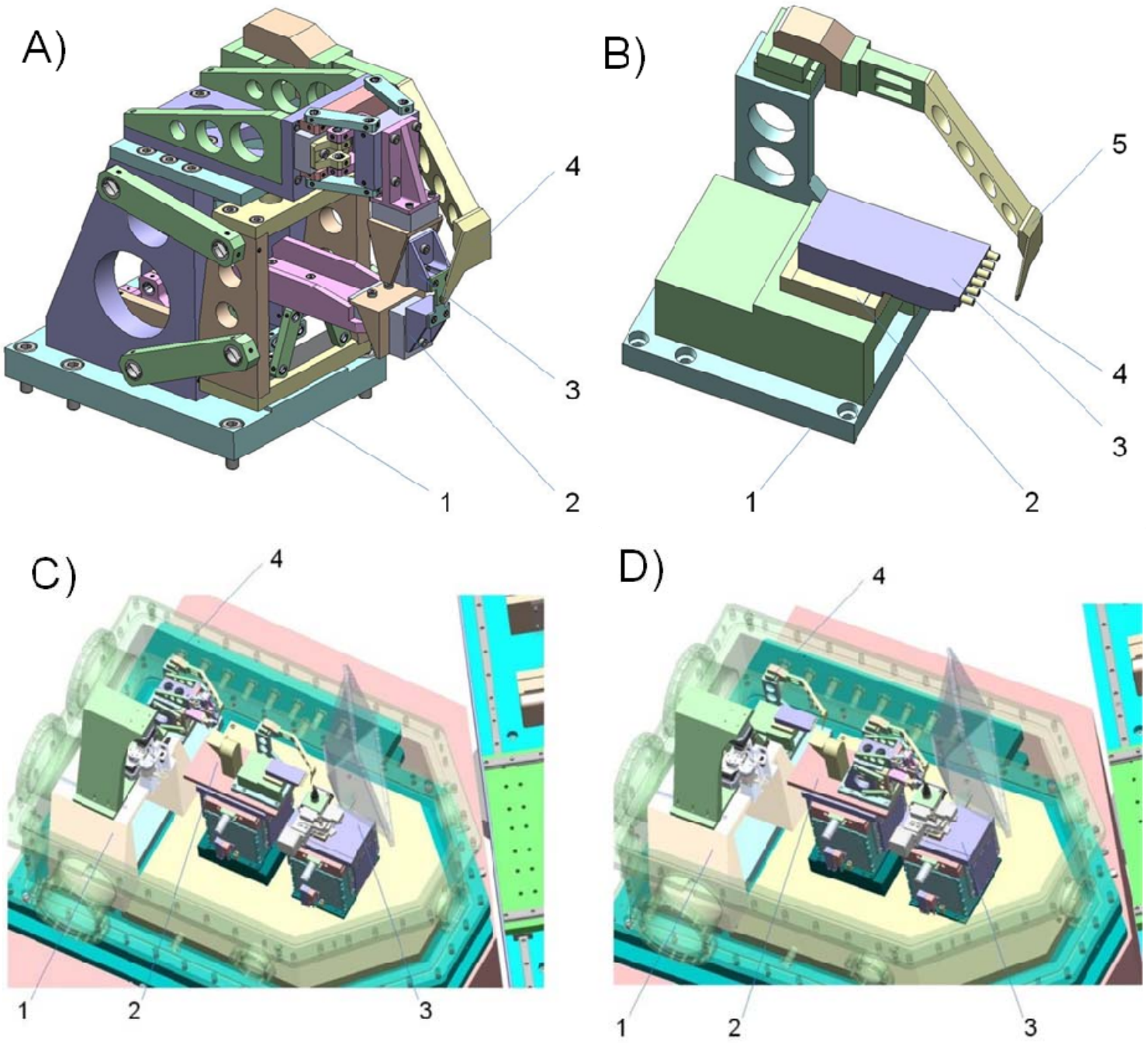

Figure 3.7.1: 3D models of ZP/MLL sub-modules.

A) Flexure-base MLL sub-mod.
1: Base plate
2: Stage group, upstream MLL
3: Stage group, downstream
4: Stage group for OSA

B) ZP sub-module:
1:Base plate
2: Linear stage for ZP on X-axis
3: ZP magazine
4: ZP holder
5: stage group for OSA

C) ZP/MLL diffraction module with ZP configuration
1: MLL fluorescence module
2: ZP/MLL diffraction optics with ZP sub-module
3: sample stage system for diffraction module
4: MLL sub-module

D) ZP/MLL diffraction module with MLL configuration.

1: MLL fluorescence module
2: ZP/MLL diffraction optics with MLL sub-module;
3: sample stage system for diffraction module;
4: ZP sub-module. The flexure-based MLL sub-module and ZP module are designed to use a common base stage stack with high-stiffness weak-link flexures (see section 3.5).

3.6.2 Flexure-based MLL module

Based on the design experiences of the precision flexure stages for an MLL test bed at the APS sector 26, a new precision flexure stage system has been designed to satisfy the MLL positioning requirements for the HXN microscope. The flexure-based MLL sub-module consists of a base plate (1) and three stage groups: a stage group for the upstream (horizontal) MLL (2), a stage group for the downstream MLL (vertical) (3), and a stage group for the Order Sorting Aperture as shown in Figure 3.7.1A (see the next page). The flexure-based MLL sub-module is designed to be supported by a high-stiffness weak-link linear base stage described in section 3.5

The stage group for the upstream MLL provides two tip-tilting motions around the X and Z axes and two linear motions along the X and Y axes. The stage group for the downstream MLL provides one tip-tilting motion around the Y axis and two linear motions along the Y and Z axes. The stage group for the OSA provides three linear motions along the X, Y, and Z axes. All of the stages are driven by commercial PZT-driven stick-and-slip stages with cross roller bearings and grating optical encoders. All of the tip-tilting motions are tilted around the center of the MLL. The base of the MLL sub-module will be encoded with a laser encoder system described in section 3.4. The design of the reference frame of the laser encoders for the MLL sub-module is currently in progress.

3.7 ZP module

As shown in Figure 3.7.1B, the ZP module consists of a base plate (1), ZP magazine (3), ZP holders (4), and two stage groups: a stage group (2) for the ZP magazine; and a stage group (5) for the OSA. The stage group for the ZP provides two linear motions along the X and Y axes sufficient for a 12-ZP configuration (two rows of six ZPs). The Y-axis motion may not be needed for a 6-ZP configuration (a single row of six ZPs). The stage group for the OSA provides three linear motions, along the X, Y, and Z axes. All of the stages are driven by commercial PZT-driven stick-and-slip stages with cross roller bearings and a grating optical encoder. The ZP sub-module will be encoded with the laser encoder system described in section 3.4. The design work for the reference frame of the laser encoders for the ZP sub-module is currently in progress. The ZP module and the flexure-based MLL module are designed to share a common base stage, which is already described in detail in section 3.5. Figures 3.7.1C and 3.7.1D show two possible configurations.

3.8 Sample modules

The HXN microscope will use three different types of sample modules as described in section 3.1 and 3.3. They are SAMF (sample module for x-ray fluorescence), SAM1D (sample module for 1-axis diffraction), and SAM3D (sample module for 3-axis diffraction). SAMF is shown in Figure 3.6.1.1, together with the compact MLL module, providing XYZ high-stiffness translation motions.

Figure 3.8.1 shows the 3D model of SAM3D. The SAM3D consists of two stage groups: a XYZ weak-link flexure base stage stack and a 3-axis rotary/tip-tilt stage system. The XYZ weak-link flexure stage system is already described in section 3.5. A customized PZT-driven stick-and-slip positioning stage (3) is used for linear motion along for the Z-axis. The rotary stage (4) is a commercial stepping-motor-driven high-precision stage. A pair of customized PZT-driven stick-and-slip tip-tilt stages (5) will be mounted on the top of the rotary stage. All six positioning stages in the sample stage system are integrated with grating optical encoders. The 3-axis linear stage system is also encoded with the laser encoder system described in the section 3.4. The SAM1D (sample module for 1-axis diffraction) consists of identical components as the SAM3D without the stick-and-slip tip-tilt stages.

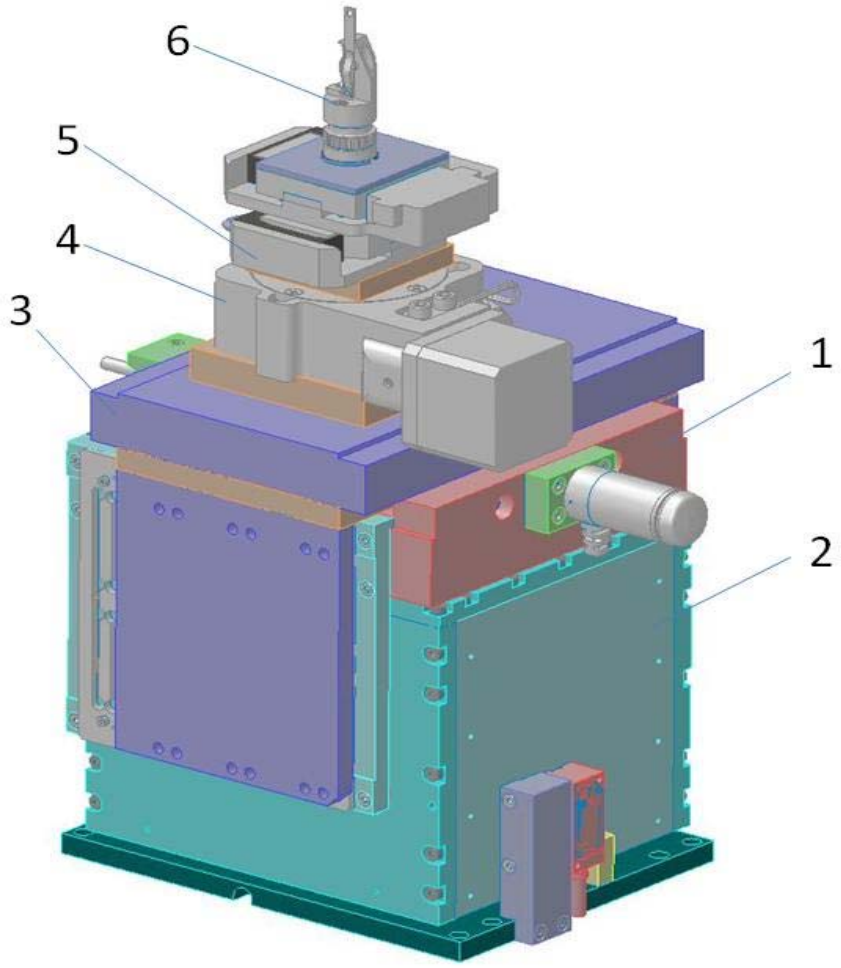

Figure 3.8.1: A 3-D model of the sample module for 3-axis diffraction (SAM3D):

1) T8-42 horizontal high-stiffness weak-link stage
2) T8-41 vertical high-stiffness weak-link stage
3) Customized PZT-driven stick-and-slip positioning stage for Z-axis
4) Stepping-motor-driven high-precision rotary stage
5) Customized PZT-driven stick-and-slip tip-tilt stage
6) Sample holder and adaptor

3.9 Summary and timeline for the development of the HXN microscope

Upon completion of the design and validating of critical components, the HXN microscope will be optimized to provide enhanced functionalities and superior characteristics as opposed to existing systems. Major distinctions include but are not limited to:

- Modular approach (MOM, ZOM, SAMF, SAM1D, SAM3D modules), ease of access to the modules, and ability to interchange modules within the vacuum enclosure
- Implementation of compact, low power stick-and-slip stages minimizing thermal drifts
- Implementation of high-stiffness, flexure based stages for enhanced stability
- Integrating state-of-the art fiber-optic based interferometry used for differential feedback
- High bandwidth (due to the high stiffness of components) yielding high scanning rates

The projected timeline for the development of the microscope is listed below:

- October 2011 - critical decision on microscope configuration and components to be implemented
- January 2012 – final design of the HXN endstation, start manufacturing
- February 2014 – HXN microscope installation and testing

3.10 Detectors

This section discusses the potential detectors for the HXN beamline.

3.10.1 Multi-element SDD (Si drift diode) energy-dispersive detector

This is the main detector for x-ray fluorescence measurement. Initially, a MAIA detector [3.10.1] was considered. However, the extremely small working distance (~2 mm) of the Hard X-ray Nanoprobe and risk of the temperature gradient around the sample and nanofocusing optics made it difficult to incorporate this phenomenal detector. In the baseline scope, we plan to use a multi-element SDD. Two major manufacturers of multi-element SDD are SII [3.10.2] and Ketek [3.10.3]. We have communicated with these companies about designing a custom multi-element SDD detector. Details on geometric configuration around the sample will be worked out as the detailed design of the HXN microscope progresses. Due to the limited working distance, the most likely arrangement of the multi-element detector will be an arc-shape positioned perpendicular to the incident beam with a solid angle of 90~120° in the vertical direction and 20~30° in the horizontal direction, with 3~11 elements. No new technology needs to be developed for this detector.

3.10.2 Single-element SDD energy-dispersive detector

There are two purposes for this detector. One, it can be used as a secondary detector for fluorescence measurements on the HXN microscope. When performing nanodiffraction measurements, the sample geometry is not always ideal with respect to the primary fluorescence detector because the sample needs to be rotated. The microscope will be designed to house a secondary fluorescence detector, so that fluorescence measurements can be performed even when the sample is rotated out of the ideal angle for the primary fluorescence detector. Its second purpose is to support the 1nm prototype development (see section 8 for details). This detector is an off-the-shelf item.

3.10.3 Pixel-array detector for Ptychography/differential phase contrast imaging:

The requirement for the pixel size is relaxed for Ptychography experiments in comparison with CDI experiments because a small size beam is used. The angular size of the pixel determines the reconstructed field of view. On the other hand, the total solid angle of the detector defines the highest possible resolution, assuming that measurable scattering intensity extends over the solid angle. These relationships are summarized in Table 3.10.1. A pixel-array detector of 512 x 512 with a 200 μm pixel size is suitable for Ptychography measurements using a 100nm-size beam. A pixel-array detector (PAD) with a single photon counting capability and with a dynamic range larger than 10^5 is ideal. The pixel array detector currently being developed by Peter Siddons' group at BNL [3.10.4] is an ideal choice for the HXN beamline. Since the detector will be positioned outside the vacuum chamber (see section 3.3), heat generated by the detector is not an issue. We have been communicating with Peter Siddons about using this detector at the HXN beamline. A commercial alternative is the Pilatus 300K with 487 x 619 pixels with a pixel size of 172 μm [3.10.5]. The requirements for differential phase contrast imaging are much more relaxed than those for Ptychography.

Table 3.10.1: Expected resolution and field of view vs. size and number of pixels. The calculation assumes: detector-sample distance=1 m, energy=10 keV, beam size for Ptychography measurement =100 nm. Maximum resolution is based on the total acceptance of the detector.

Pixel size (m)	No. of pixels	Max. resolution (nm)	Max. field of view (m)	1D over-sampling ratio
100	1024 x 1024	1.2	1.2	12
200	512 x 512	1.2	0.6	6
300	256 x 256	1.2	0.4	4
400	128 x 128	1.2	0.3	3

3.10.4 Optically-coupled high-resolution CCD

This imaging detector uses a scintillation screen, converting the x-rays into visible light photons. Conventional optical lenses are used to magnify the intensity distribution on the scintillation screen onto a CCD. This is a standard imaging detector for high-resolution imaging or microtomography at synchrotron sources. The highest achievable resolution is about 0.5 μm or better, depending on the type of scintillation screen and the objective lens. The purpose of this imaging detector is to carry out simple diagnostic measurements to visualize the intensity distribution of the beam and to support alignment of the nanofocusing optics and the sample. There are many commercial options for this detector.

3.10.5 Ion chambers and NaI scintillation detectors

Ion chambers are used for normalizing the incident x-ray intensity. A scintillation detector will be used for single-photon counting for nanodiffraction whenever necessary.

3.10.6 CCD for nanodiffraction

In the baseline scope, we will use a Quad-RO CCD manufactured by Princeton Instruments [3.10.6]. This CCD has been purchased already, to support the R&D experiments. During the initial phase, we will be developing data collection and analysis methods for nanodiffraction. Although the CCD detector is relatively slow, this is not likely to impede development. This CCD has 4096 x 4096 pixels (15μm/pixel), 16-bit dynamic range, a readout time of 4.8s (at 1 MHz ADC speed), and a low dark current of 0.06 electron/pixel/s at a CCD temperature of -45°C. Complete technical details can be found in reference 3.10.6.

3.10.7 Pixel array detector for nanodiffraction (mature scope)

In the mature scope, we will use a much faster area detector in order to take full advantage of the highly focused flux of the HXN beamline. The pixel-array detector being developed at BNL by Peter Siddons' group is a potential candidate for a high-speed area detector with a point spread function equal to the pixel size. On the other hand, there are two commercial alternatives. The first is a Pilatus detector with 2M or 6M pixels (172 μm pixel size), which provides a single-photon counting capability based on the newly developed CMOS hybrid-pixel technology [3.10.5]. The Pilatus detectors provide a high frame rate up to 30Hz. A drawback for these detectors is the weight (~42 kg for Pilatus 2M and 95 kg for Pilatus 6M). The current detector station design (see section 3.3) needs to be modified to accommodate such weight. The second commercial alternative is an amorphous silicon flat panel detector, known as the PerkinElmer detector [3.10.7]. A detector with 2048 x 2048 pixels (pixel size of 200 μm) with 15 frames per second is available. Though the off-the-shelf models are designed for high energy applications (40 keV-15MeV), the detector can be configured for lower energy applications at 10~20 keV. The manufacturer is planning R&D to reduce the pixel size to 100 μm. We believe that additional options will be available before the year 2014.

Table 3.10.2: Estimated data rate for the HXN detectors

Detector	Data production	Data rate (MB/s)
Multi-element SDD for XRF	12 bit, 2 k, ~100 Hz (maximum speed), ~11 elements	3.3
Single-element SDD for XRF	12 bit, 2k, ~100 Hz (maximum speed)	0.3
Pixel-array detector for Ptychography/DPC	20 bit, 0.3M pixels, 200 Hz (Pilatus 300 k) or equivalent.	150
Optically-coupled Hi-res CCD	12 bit, 2 k x 2 k, 4 Hz	24
CCD for XRD	16 bit, 4 k x 4 k, 0.2 Hz	6.4
Point detectors	Depending on the trigger time.	negligible
Pixel-array detector for XRD (mature scope)	20 bit, 6M pixels, 12 Hz frame rate (Pilatus 6M), or 16 bit, 4M pixels, 15 Hz (PerkinElmer)	180 120

[3.10.1] C.G. Ryan, et al. "Elemental X-ray imaging using the MAIA detector array: The benefits and challenges of large solid-angle," *Nuclear Instruments and Methods in Physic Research A* 619, p 37 (2010). Also see the references in this article.
[3.10.2] http://www.siintusa.com/x-ray_detectors.html
[3.10.3] http://www.ketek.net/
[3.10.4] Carnie et al., "The XAMPS detector for the X-ray Pump-Probe instrument at LCLS," 2009 IEEE *Nuclear Science Symposium Conference Record*, N38-4, p 2151-2153 (2009).
[3.10.5] http://dectris.com/sites/pilatus300k.html, http://dectris.com/sites/pilatus6m.html
[3.10.6] http://www.princetoninstruments.com/Uploads/Princeton/Documents/Datasheets/Princeton_Instruments Quad-RO_4096_M1_6.09.pdf
[3.10.7] http://www.shawinspectionsystems.com/products/pe/flat%20panels.htm

4 SATELLITE BUILDING FOR THE HXN BEAMLINE

4.1 Overview

The HXN Satellite Building is designed to meet stringent technical requirements for vibration isolation and temperature stability, which are critical to operating the Hard X-ray Nanoprobe Beamline at a 1~10 nm spatial resolution. The technical requirements and conceptual design of the satellite building have been developed through several planning meetings. In particular, a workshop was held in June, 2009 at NSLS-II, to identify the critical vibration and temperature stability requirements for the HXN Satellite Building. In addition, extensive measurements and computer simulations have been performed to investigate and validate the ideal site for the satellite building, the specific arrangement of the potential noise sources (i.e., air-handlers for the nearby laboratory office building, see Appendix 5), and structural details (i.e., analysis of potential vibrational paths through load-bearing columns, see Appendix 5). The architectural and engineering design of the satellite building has been finalized through a series of design reviews including architects, engineers, facility planners, and scientists. Currently, the architectural and engineering design of the satellite building is 100% complete. The detailed requirements, specifications, and architectural design can be found in the NSLS-II RSI document, "Experimental Facilities Requirements, Specification and Interfaces for the Hard X-ray Nanoprobe Beamline Satellite Building," and "100% Review Submittal Project Manual for Hard X-ray Nanoprobe Satellite Building." The goal of this section is to provide a brief summary of the technical requirements and specifications for the HXN Satellite Building and to present several critical design features.

4.2 Technical requirements and specifications

4.2.1 Functionality for the HXN endstation

In order to deliver the design features of the HXN beamline, the satellite building is required to provide:

- A long beamline site for a low-beta section
- Endstation location at 100~120 m from the source, usable for nanofocusing optics. A distance farther than 120 m causes significant loss of flux.
- Endstation dimensions of 20 m (long) x 5 m (wide) x 3.5 m (high): the length requirement of 20 m is critical to ensure a minimum distance of 15 m from SSA2 to the nanofocusing optics. In addition, a minimum distance of 3 m after the nanofocusing optics is needed to provide sufficient space for the microscope and detectors.
- Adequate space for the user area: needed for experiment control and sample preparation/visualization
- Access to the storage ring building and nearby LOB
- Access to the loading dock for receiving equipment
- Access to utilities including electricity, HVAC, water, and gas
- Access to toilet/bathroom
- Radiation safety for the endstation
- Compliance to building codes and regulations

4.2.2 Vibration isolation

Vibration isolation is a critical functionality of the HXN Satellite Building. Ensuring the desired performance of the HXN beamline, the HXN Satellite Building must provide:

- Vibration isolation of the endstation floor from the other support structures such as external walls and the roof of the satellite building and the nearby buildings
- Sufficient filtering or suppression of the vibrations and noise from natural (i.e., wind) and cultural noise (i.e., air-conditioning, fork-lift, noise generated by the HXN users).
- Sufficiently thick concrete floor for the endstation: Electron microscopy facilities have validated the effectiveness of an isolated thick concrete floor for filtering out vibrations [4.1, 4.2, 4.3]; the simulation investigations (see Appendix 5) have also confirmed the effectiveness of ~1m-thick concrete floor.
- Vibration criterion requirement of VC-F with a goal of achieving VC-G: Vibration criterion is defined to provide a generic identification of the level of vibration. Vibration criteria are used extensively in vibration-sensitive facilities and adopted by various suppliers of sensitive systems (i.e., microelectronics, nano-technologies, electron microscopes). The criteria are based on the RMS velocity of the experimental floor rather than acceleration or displacement, and are expressed in terms of one-third octave band (proportional rather than fixed bandwidth) spectra. As shown in Figure A5.1.1, VC-F and VG-G correspond to RMS velocities of 1.56 and 0.76 μm/s at 1 to 80 Hz. VG-G is considered to be the most stringent stability criterion. The vibration requirement for the experimental floor of the storage ring building is to meet VC-E (3.12 μm/s at 1 to 80 Hz).

4.2.2 Temperature stability

Temperature stability is an extremely important requirement for a nanoprobe instrument. The linear thermal expansion coefficient of invar is 1.3 $x10^{-6}$°C^{-1}. A 100mm-long invar reference frame will change its length by 130 nm with a temperature change of 1 °C. Achieving a stability of better than 10nm requires a temperature stability of ~0.08°C. The temperature stability around the sample and the nanofocusing optics is ~0.01°C. In order to achieve such a high level of temperature stability, the environment outside of the x-ray microscope must provide an adequate level of temperature stability. The temperature requirements within the HXN Satellite Building are summarized in Table 1. Temperature stability is most important over a period of 12 hours, and is more important than the absolute temperature at a specific point within the experimental enclosure. In Section 4.3.3 specific engineering solutions to implement temperature stability are elucidated.

Table 4.2.2.1: Temperature specifications for the HXN Satellite Building.

Normal ambient conditions in the User Area	
Temperature	Long term: 24 ± 1.0°C (75 ± 1.8°F), ±1.0°C is peak-to-valley range not RMS. Over an 1 hour period: 24 ± 0.5°C (75 ± 0.9°F), ±0.5°C, peak-to-valley
Relative humidity	50% or lower
Normal ambient conditions within the Hutch	
Temperature	Long term: 24 ± 0.1°C (75 ± 0.18°F) Over a 4 hour period: 24 ± 0.05°C (75 ± 0.09°F)
Time to reach an equilibrium temperature after the hutch door is closed.	Less than 30 minutes.

4.3 Architectural and engineering design of the satellite building

4.3.1 Contributors

At present, design of the satellite building is 100% complete. The specifications and requirements have been developed through several planning meetings internal to NSLS-II and a workshop soliciting recommendations from scientists and engineers in electron and scanning probe microscopy. The initial conceptual design was developed by the HXN beamline and NSLS-II scientists. Architectural and engineering design was carried out by HDR and approved through preliminary, 25%, 50% and 100% complete design reviews. Vibration simulation and analysis were performed by Dr. N. Simos at NSLS-II. Construction of the satellite building and financial responsibilities will be monitored by the conventional facilities division at NSLS-II.

4.3.2 Location and size of the satellite building

Various options have been evaluated in order to satisfy the requirements specified in 4.2.1 plus the following additional considerations:

- Minimum modification to the structural design of the storage ring building and the nearby LOB.
- Ensuring adequate square footage of the Satellite Building.
- Comparing the benefit of taking advantage of the existing utility infrastructures from the nearby LOB (i.e., air conditioning, electricity, water, etc.) and building dedicated utility infrastructure only for the satellite building.
- Developing cost-effective architectural design without sacrificing the critical requirements.

A total of eight different possible configurations were investigated before the final design was chosen. The detailed descriptions of these different configurations and their "pros vs. cons" can be found in the "Hard X-ray Nanoprobe Beamline Satellite Building Final Design Report." The location of the satellite building with respect to the storage ring building, the nearby LOB (LOB 3), and the perspective view of the HXN endstation (3-ID-C) together with the rest of the HXN beamline, are shown in Figures 4.1–4.3.

4.3.2 Structural design for vibration stability

To ensure the highest level of vibration stability for the HXN Satellite Building, a significant number of specific structural details have been explored. The following are some of the key design features:

- **Total mass:** Rather than implementing a conventional "house-in-house" scheme [4.2.2.1], a modified version of this scheme was implemented, to maximize the total mass of the concrete structure supporting the endstation and the x-ray microscope inside. In the conventional "house-in-house" scheme, the floor supporting the microscope is separated from the enclosing internal walls/ceiling. As shown in Figures 4.4 and 4.5, the 1m-thick concrete floor extends outside the hutch wall (shown as dashed lines) and supports the entire hutch. The cross-sectional views clearly show the extent of the thick concrete floor. Our approach maximizes the benefit of the large mass, providing the highest level of filtering of ambient vibrations, particularly at low frequencies (<5Hz). Comparative vibration simulations validated our modified house-in-house over the conventional house-in-house scheme.
- **Vibration isolation by structural de-coupling:** The hutch and the supporting floor are isolated from the rest of the interior floor around the "quiet" floor. The surrounding floor has the same thickness as the NSLS-II experimental floor, which is 0.35 m. This thinner floor supports the control equipment (electronics, computers, etc.), storage cabinets, work benches, and user activity, so that the "cultural" noise is isolated from the x-ray microscope. As shown in Figure 4.5, the structural isolation extends from the top surface down to the compacted soil, with a gap of 2″. The external walls supporting the ceiling are supported by their own footings, separated also from the thinner floor. The entire satellite building is completely isolated from the storage ring building. However, the satellite building is weakly coupled to LOB 3, by sharing a few load-bearing columns at the boundary between the two buildings, which was necessary to maintain an integrated building structure. Vibration simulations validated that the weak coupling does not compromise the vibration-damping property of

the thick floor. Particular care was taken in designing the vibration isolation joint around the load-bearing columns supporting the ceiling and the cross I-beams. In addition, the bottom of the HXN floor and the top of the column footing are separated by 36 inches, to provide sufficient vibration isolation. The details are shown in the insert of Figure 4.5.

- **Minimizing vibration transmission:** There are five different types of vibration sources, which required attention during the design phase.

  1. **Cultural noise from the storage ring:** sufficient distance from the ring to the thick hutch floor ensures effective isolation. Some vibrations can be transmitted to the thinner floor surrounding the thick floor. However, significant damping will occur, limiting the effective transmission.
  2. **Cultural nose from LOB 3:** The dominant noise sources in LOB 3, such as its loading dock and machine shop, are quite far away. The adjacent LOB room is the conference room and a few offices. Consequently, there will be no significant noise.
  3. **Noise from HVAC:** The most critical source is the air-handler. The noise can be transmitted to the horizontal support beams and travel down to the load-bearing column adjacent to the thick hutch floor. Comprehensive simulation investigation has determined that the transmitted noise is negligible. In order to eliminate noise travelling in the HVAC ducts, all ventilation ducts will have appropriate vibration isolation joints.
  4. **Noise from the users and control equipment:** The entire surface of the thinner floor surrounding the thick hutch floor will be covered with Concredamp® (see Figure 4.5). Concredamp is a concrete mix with additives, resulting in effective vibration damping properties (http://www.concredamp.com). The effectiveness of this substance has been proven in the electron microscopy lab at the CFN [4.3]. In addition, most of the control equipment will be housed in a water-cooled instrument rack that also provides good acoustic damping.
  5. **Noise induced by winds:** Long Island has frequent winds due to its geographic location. Extensive modelling has been performed (see Appendix 5). A particular concern is high speed gusts that will give sudden impulses to the roof structure of the satellite building and LOB 3. Fortunately, the impulse is short-lived, and its energy dissipates quickly. Some impact will be felt by the nanoprobe over a short period of time.

The HXN hutch is made of concrete, which has acoustic damping properties superior to those of conventional metal hutches. Though not part of the construction plan, there is a provision for adding acoustic damping foam in the interior of the hutch. This additional implementation of acoustic damping will be guided by vibration measurements within the hutch after most of the equipment is installed.

4.3.3 Design for temperature stability

The following design considerations have been taken into account to enable temperature stability requirements listed in Table 4.1. Figures 4.6 and 4.7 show the details of the ventilation system that support the required temperature stability.

- The concept of the "house-in-house" is implemented to provide maximum temperature stability. The building's external shell including walls, roof, structural steel, and external metal cladding will have a generous amount of insulation (the target R-value for the external wall system is R-24 and R-30 for the roofing system).
- Users will enter the hutch through an "airlock door," to minimize temperature disturbances. The airlock door with glass walls will be built around a single shielded door (¼″ steel lined and 3′ wide x 7′ high). To ensure the effective use of the airlock door, the PPS (personal protection system) panel will be located outside the airlock vestibule.
- Large equipment will be moved in the hutch using large double doors (¼″ steel lined and 6′ wide x 7′ high). This door will not be used during the normal operation and its interior side will be insulated.
- The ventilation system will be designed for rapid air exchange after the hutch is closed, enabling fast equilibrium of the hutch temperature. After reaching a steady state, the air flow will be reduced.

- The air exchange inside the hutch will be performed through an array of low-pressure (laminar flow) ducts, which will be insulated to minimize sound transmissions and heat dissipation.
- The thermal mass of equipment within the hutch is insignificant compared to the thermal mass of the walls and roof, thus minimizing temperature fluctuations.
- LED lights in the experimental enclosure will be used to minimize heating effects. Normal lighting will also be available for periods when greater visibility is needed at the expense of a longer time to reach temperature stability.
- Most of the electronics equipment that may dissipate heat will be installed inside water cooled instrument racks. Some electronic equipment that must stay in the hutch will be installed inside water instrument racks.

It is important to point out that the temperature stability requirements for the HXN Satellite Building are very much different from those for electron microscopy labs [4.1, 4.3]. For instance, at the electron microscopy facility at the CFN, the air floor requirement is 0 m/min in the horizontal direction and 0 to 0.3/min in the vertical direction [4.3], in order to avoid disturbance of the electron beam column. The ability to reach temperature equilibrium within a short time (required for the HXN endstation) is not sought by electron microscopy facilities because such a requirement cannot be fulfilled together with the slow air floor requirement. The HXN endstation also uses low-pressure laminar flow to maintain quiet and effective air exchange. In addition, the ventilation system has high flow rate capacity to reach a fast equilibrium temperature.

4.3.4 Utilities

The following utilities will be available inside the satellite HXN building; the electrical diagram for lights and power available is shown in Figures 4.8 and 4.9.

- 120V single-phase outlets
- 208V high-capacity socket for vacuum pump in the equipment area
- Chilled water distribution to enable cooling of water-cooled racks for electronics
- Compressed air lines connected to the LOB infrastructure

4.3.5 Design considerations for the users

When designing the User Area, we have taken the following considerations into account:

- User area can accommodate up to six users with desks for workstations and a small conference table
- Non-hazardous sample preparation area is available
- Glass windows will be installed along the experimental hall to give a sense of openness and to avoid any unnecessary need to open the door to the User Area by visitors
- Glass vestibule for airlock entry
- User area will be equipped with an emergency exit, sprinkler system, and card key lock for entry
- Communication infrastructure including phone, wireless web access, Ethernet lines, etc.

[4.1] "Laboratory Design for High-Performance Electron Microscopy, Michael A. O'Keefe et al., *Microscopy Today*, May 2004, pp 8-14.
[4.2] "The Triebenberg laboratory—designed for highest resolution electron microscopy and holography," Hanners Lichte et al., *Microscopy & Microanalysis* 7, supplement 2, 894-895 (2001).
[4.3] Y. Zhu and J. Wall, chapter in: *Aberration-corrected electron microscopy*, ed. Hawkes P.W. (Elsevier/Academic Press), p 481-523 (2008).

Figure 4.1: Location of the Hard X-ray Nanoprobe Satellite Building with respect to the NSLS-II storage ring building and the laboratory and office buildings (LOB). The facility is planned as a one-story building of approximately 4,200 gross square feet wedged between LOB-3 and the storage ring building. Extensive efforts have been made in choosing the site for the satellite building by considering the various nearby noise sources (see Appendix 5 for the details).

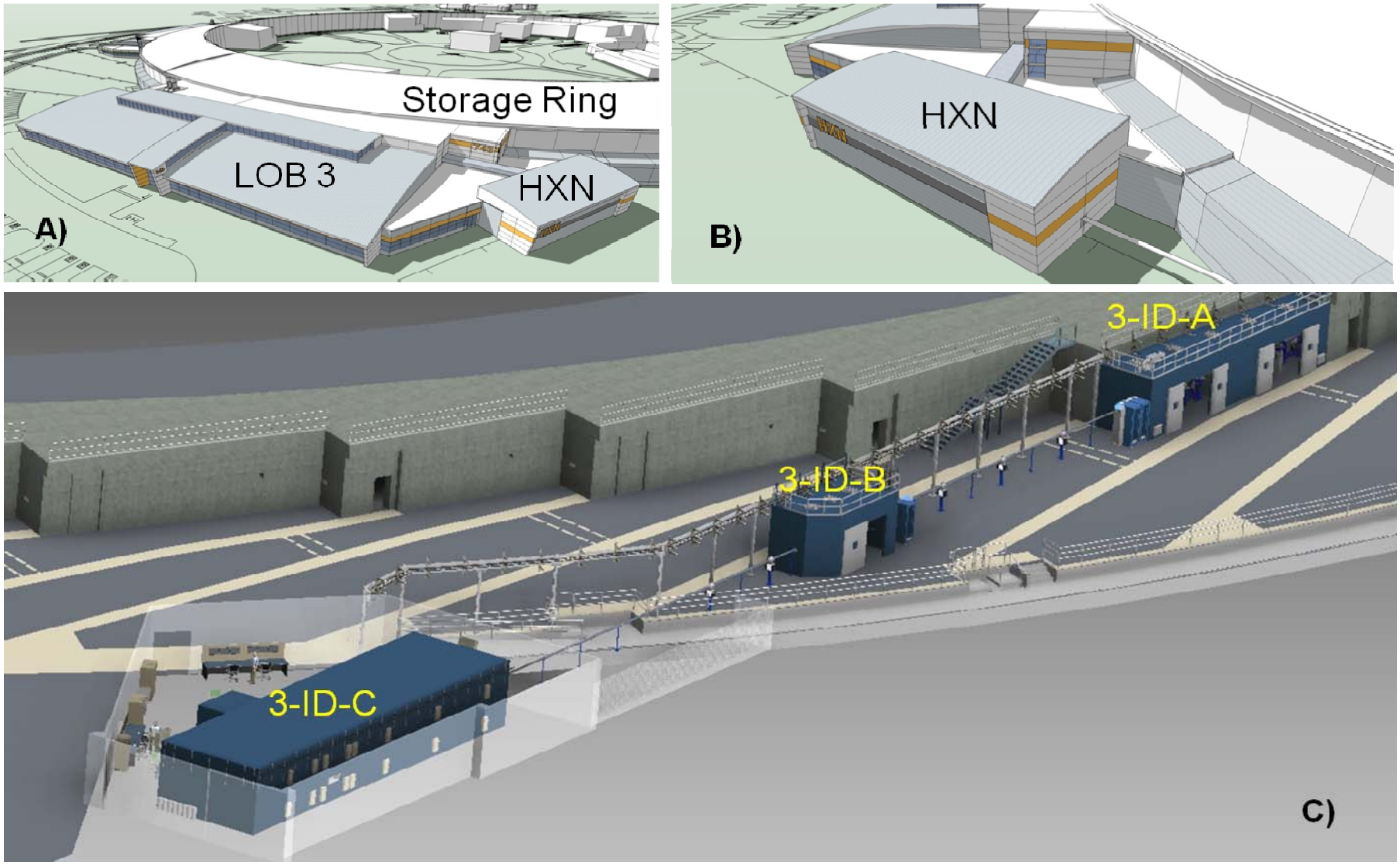

Figure 4.2: A) Aerial view of the HXN Satellite Building B) Side view of the HXN Satellite Building showing the beam transport pipe from the storage ring to the satellite building. C) 3D model of the HXN beamline, showing three experimental stations, 3-ID-A (first optical enclosure), 3-ID-B (monochromatic hutch) and 3-ID-C (endstation). The downstream external wall of the HXN Satellite Building is 115 m from the synchrotron source.

Figure 4.3: 3D side view of the satellite building. The cross section view on the roof shows the supporting structure. The beam transport pipe from the storage ring is ~10 m-long. The vacuum pumps near the two ends are sufficient to maintain a sufficient level of vacuum. The transport pipe will have radiation shielding and weather-proof protection. The access to the transport pipe is secured by a metal wire fence.

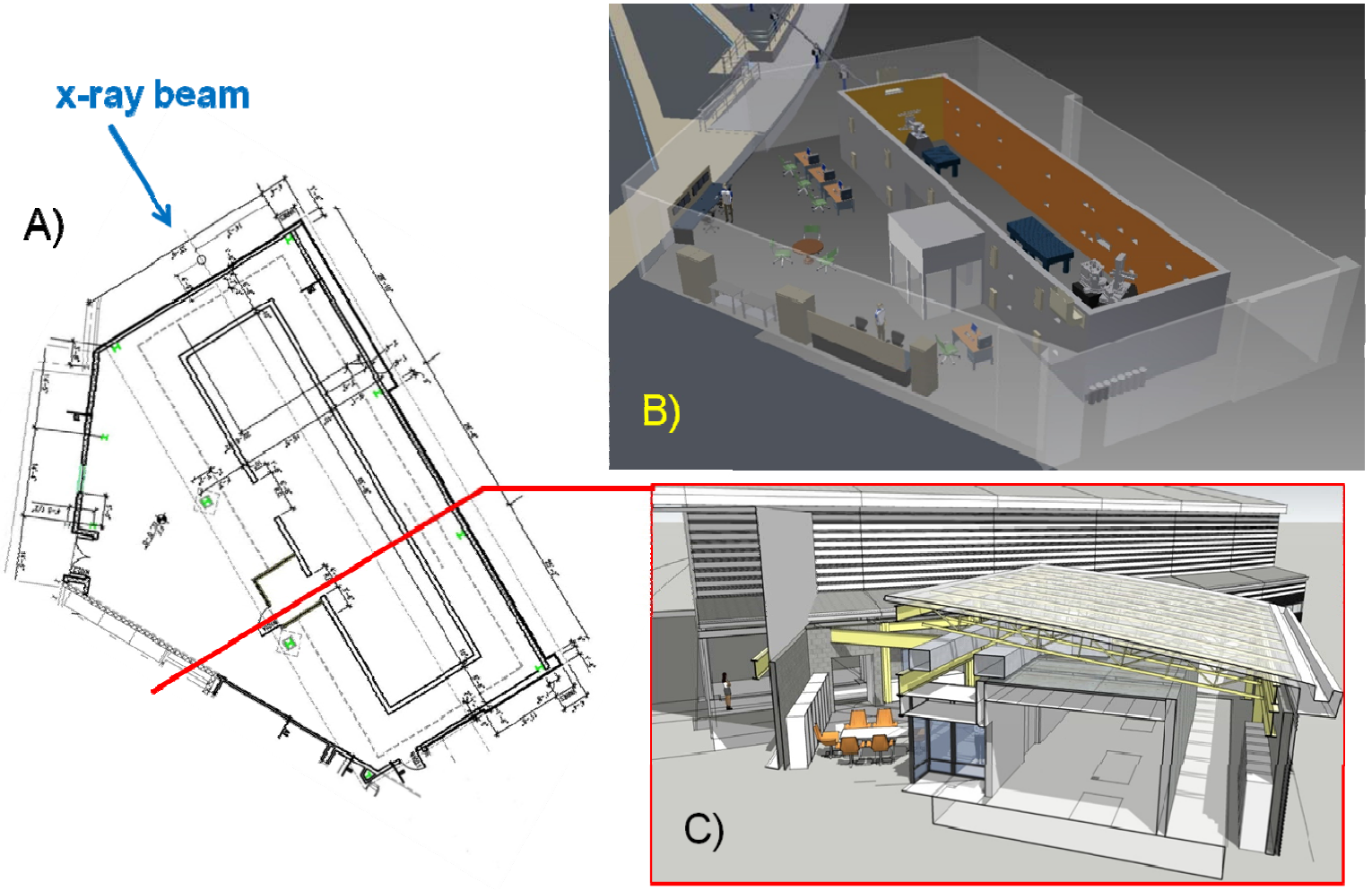

Figure 4.4: Cross sections of the HXN satellite building. The "house-in-house" concept, widely used in the electron microscopy facilities, is implemented for the HXN satellite building. A) Horizontal cross section of the satellite building showing the external walls of the satellite building (i.e., "outer house") and the endstation hutch walls (i.e., "inner house"). The hutch is 20m-long, 5m-wide and 3.5-m high. The entrance to the hutch is protected by an airlock door, minimizing temperature fluctuations inside the hutch. The airlock enclosure is made of clear plastic allowing monitoring of personnel entering/exiting the hutch. The access door to the hutch is a single shielded door, ¼" steel lined and 3' wide x 7' high. To move large equipment inside the hutch there is a shielded double door, ¼" steel lined, 6' wide x 7' high. The user area outside of the hutch accommodates experiment control stations, non-hazardous sample preparation and a mini conference table. B) Vertical cross section along the red line in C) plan view. The hutch resides on top of a vibration-isolated, 1m-thick, concrete slab to damp ambient vibrations. The floor surface of the user area will be covered by Concredamp®, a concrete mixture with vibration damping properties, in order to suppress vibrations induced by user activity.

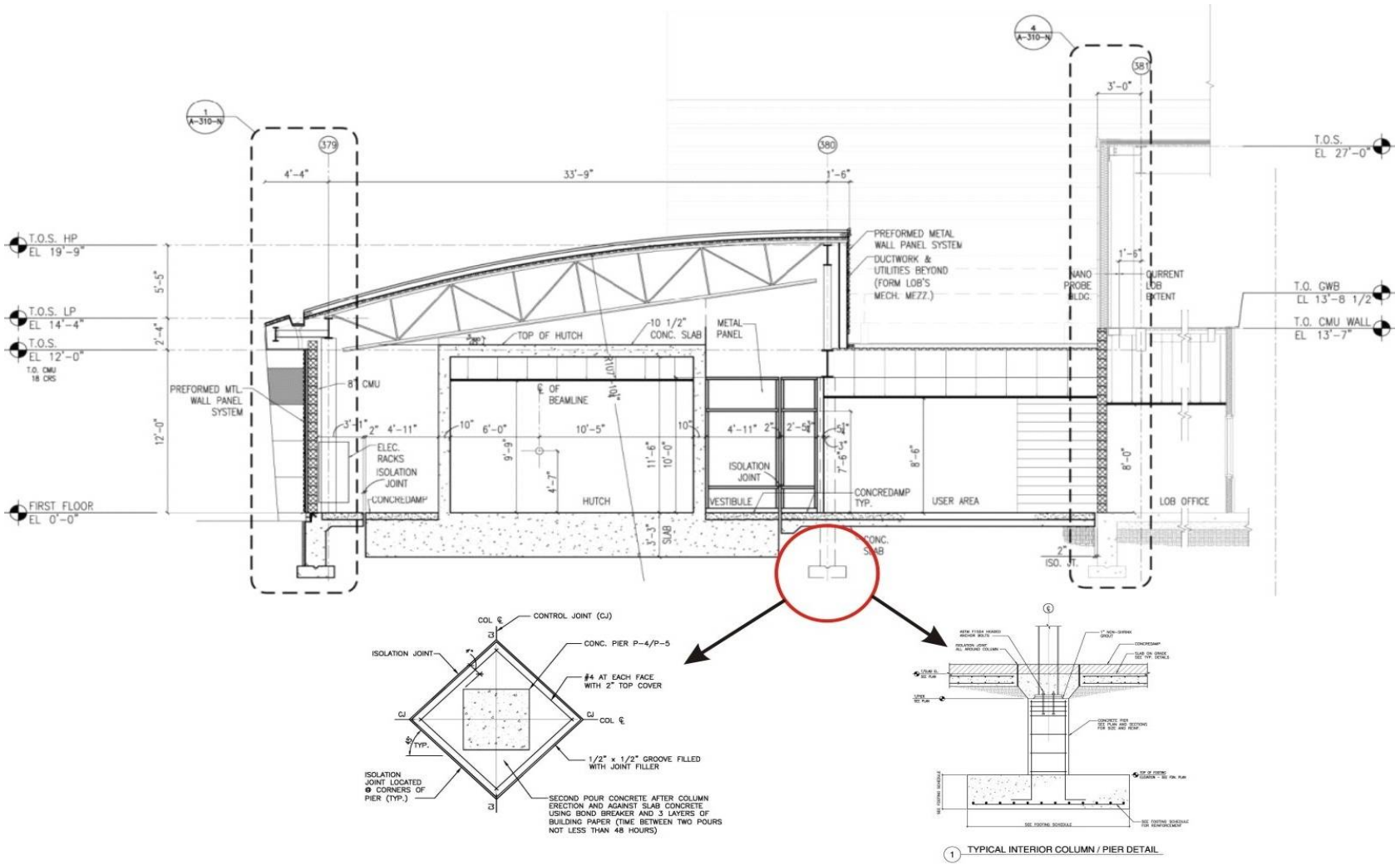

Figure 4.5. Vertical cross section of the satellite building, showing the support structures and floor partitions of the building. The external structure ("the outer house") including the external wall, roof, and load-bearing columns are completely isolated from the concrete hutch ("the inner house) supported by a 1m-thick, vibration-isolated, concrete floor. The hutch will be constructed with concrete with 10"-thick side walls and 10.5"-thick roof, in order to provide sufficient radiation shielding and mechanical strength to support its own weight. Particular care was taken for structural isolation around the load bearing columns (shown in the insets), in order to prevent possible transmission of vibrations through the support columns.

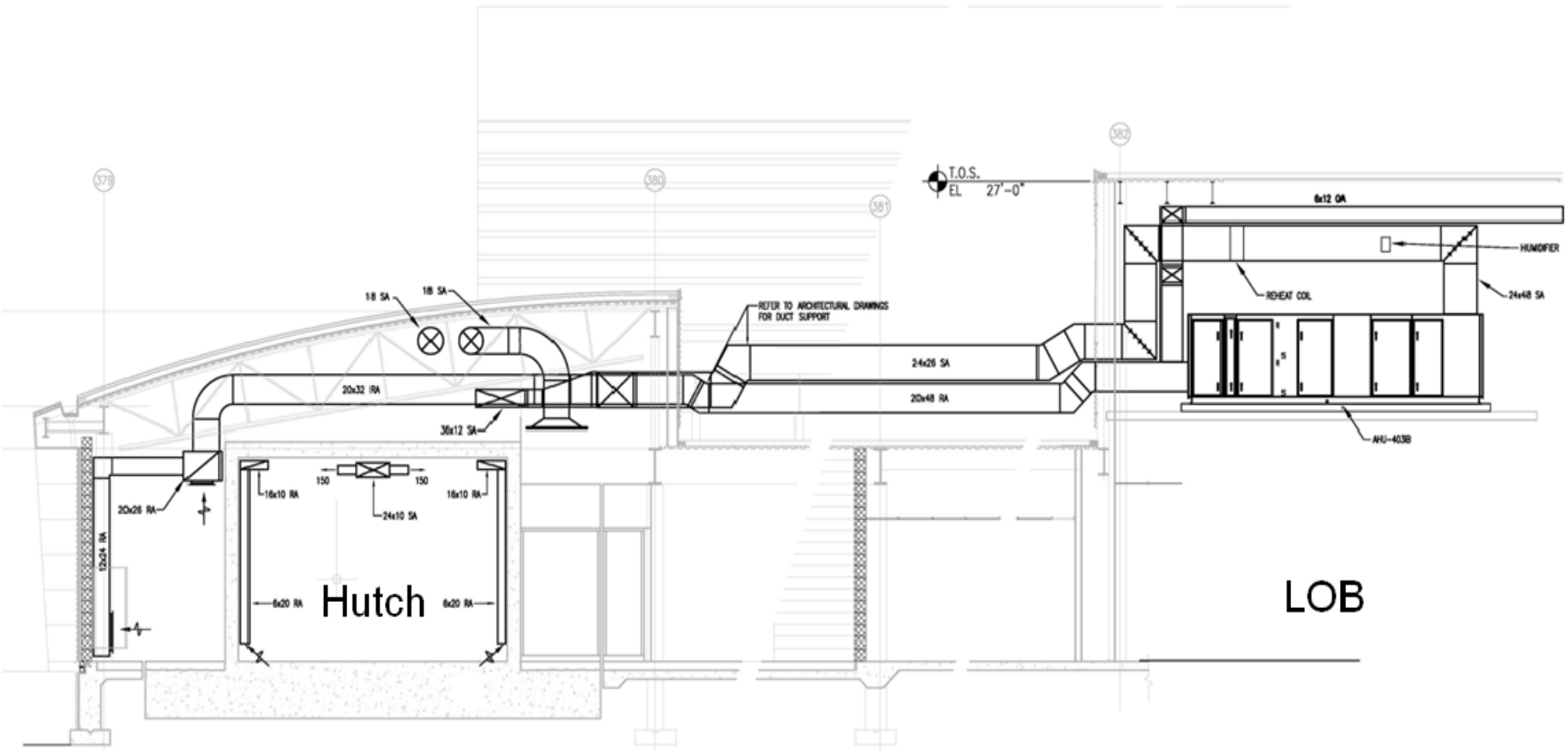

Figure 4.6: Side view of the ventilation system in the HXN Satellite Building. Air handlers and humidifiers are located in the LOB to minimize vibrations transmitted to the Satellite Building. The supply duct system is split into a User Area Zone and a Hutch Zone. In each zone, the supply air temperature will be increased to the desired temperature to meet the cooling requirements of the individual spaces. As seen in the diagram, the air in the hutch will be distributed vertically from a ceiling plenum with perforated panels and air will be returned through low wall open end ducts. In the User Area, the air will be distributed through supply diffusers and return air will be pulled through branch duct mounted registers around the space perimeter, some near the floor and some near the ceiling / roof. In order to provide the lowest possible noise and vibration in the space, the air velocity in the branch ducts will be kept below 500 FPM.

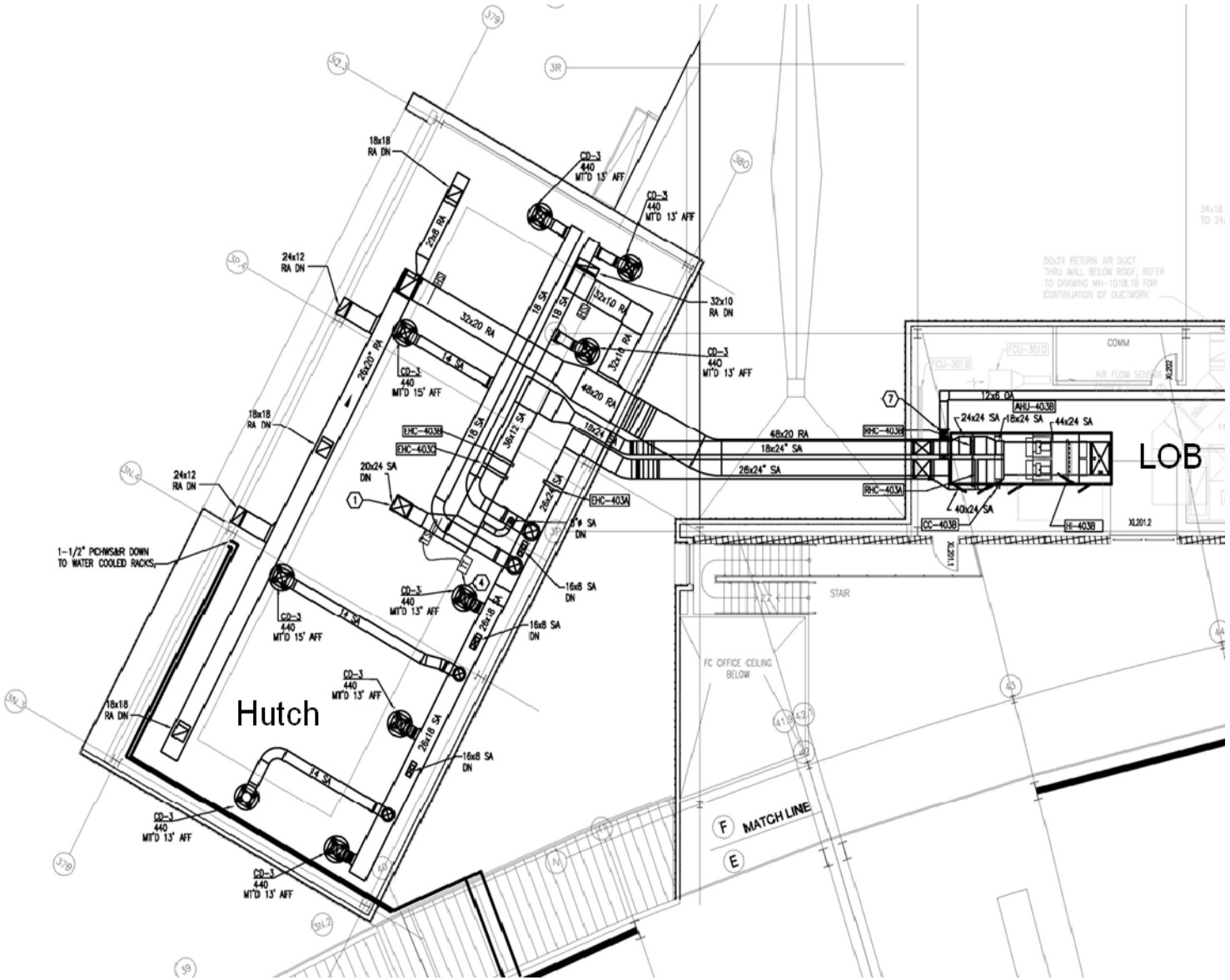

Figure 4.7: Top view of the ventilation system in the HXN Satellite Building. The air handlers and humidifier are located in the LOB building to minimize vibrations transmitted to the Satellite Building. Air flow is distributed through an array of low-pressure, laminar flow, distribution system. Cooling lines to the water-cooled equipment racks are also shown in the diagram.

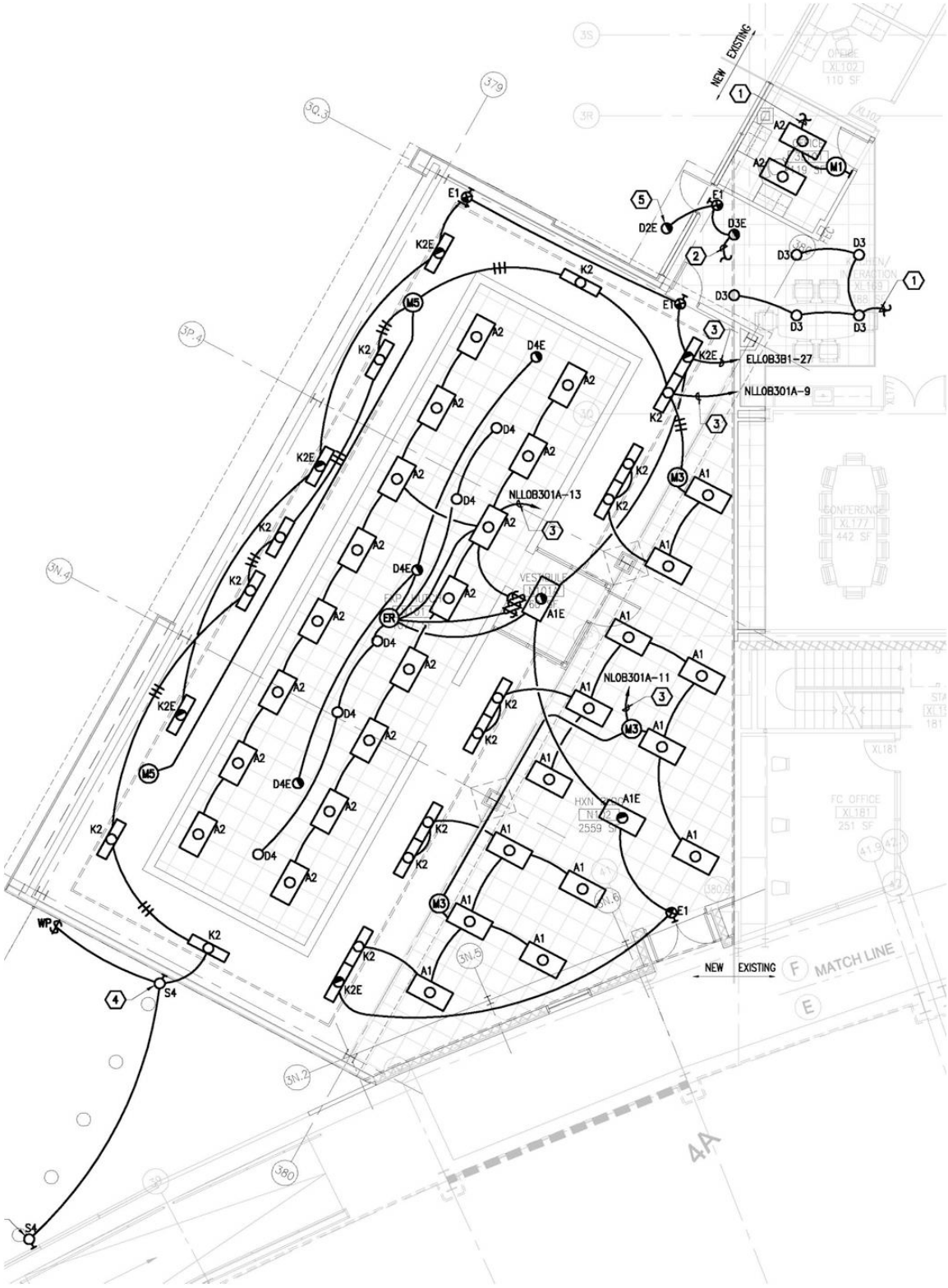

Figure 4.8 Electrical light installations inside the HXN Satellite Building. In the hutch, LED lights provide a minimum level of light during data collection. Fluorescent lights are used for working in the hutch. A1, A1E, A2, A2E – 2x4 2 lamp grid troffer, D2, D2E – 18 Watt triple tube 8” round lamps, K2, K2E – 4’ 2 lamp turret industrial lights, D4, D4E – 36 Watt LED 8” round lights

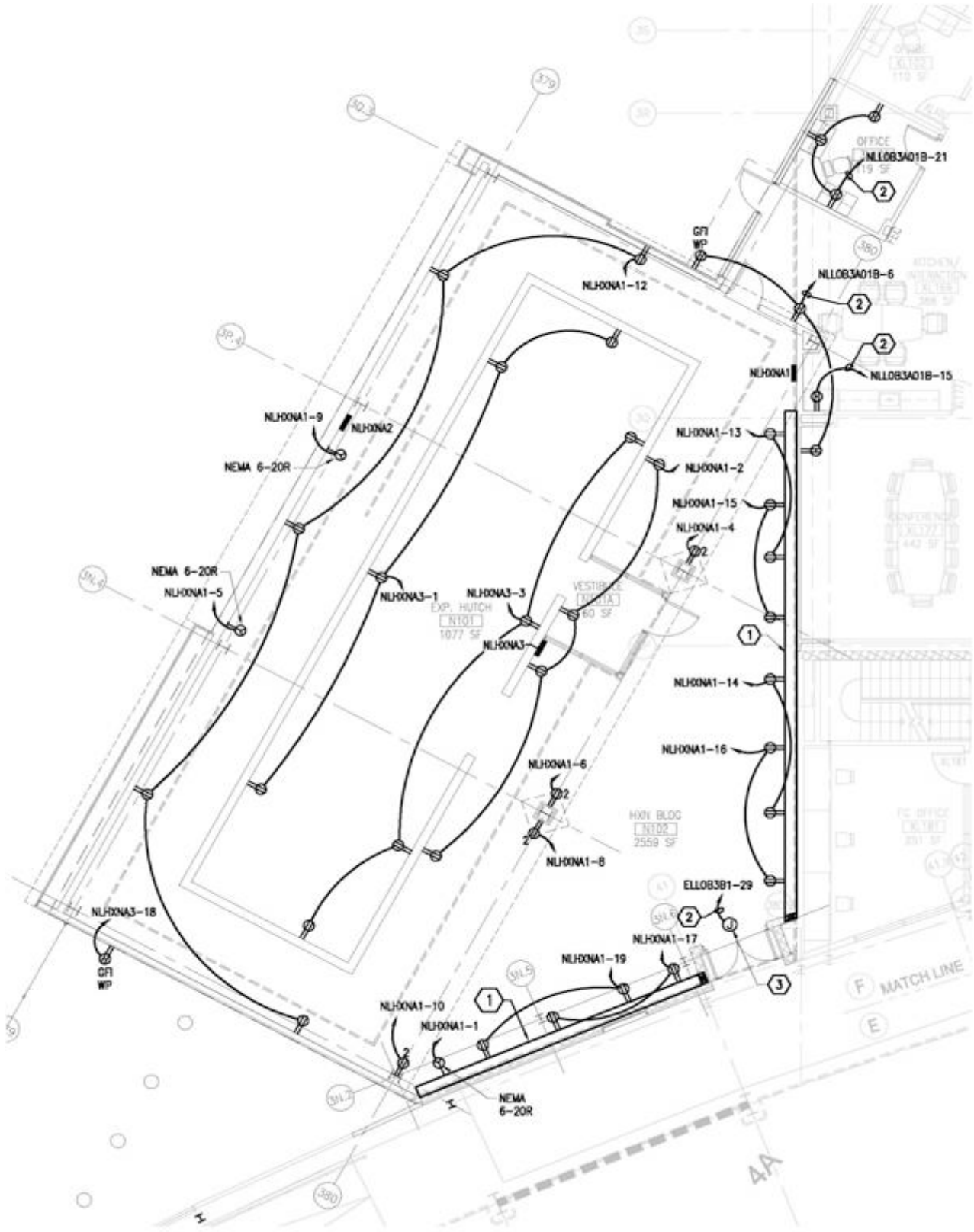

Figure 4.9 Electrical power installations/distribution inside the HXN Satellite Building. 20A, 125V, 2-pole, 3-wire ground receptacles locations are shown inside the hutch and outside in the User area. Keynotes in the diagram: 1- provide two compartment receptacles, 2 – connected to the circuit breakers, 3 – connected to the security system power supply. ▬ indicates location of 208V panel boards.

5 INFRASTRUCTURE FOR BEAMLINE AND USER SUPPORT

5.1 Enclosures

The HXN beamline has three enclosures: the first optical enclosure (3-ID-A, see Figure 5.1.2), the second optical enclosure for monochromatic x-rays (3-ID-B, see Figure 5.1.2) and the endstation located in the HXN Satellite Building for monochromatic x-rays (3-ID-C). A detailed list of the components in each enclosure is given in section 2.8. Extensive technical specifications and 3D models for the endstation are given in section 4. Table 5.1.1 summarizes the specifications for 3-ID-A and 3-ID-B. Radiation shielding analysis can be found in "Guidelines for NSLS-II Beamlines and Front End Radiation Shielding Design", #LT-ESHDES-08-003-rev001 written by P.K. Job and W.R. Casey.

Table 5.1.1: Specifications and Shielding Requirements for 3-ID-A and 3-ID-B

Enclosure Designation	3-ID-A	3-ID-B
Construction Scope	baseline	mature
Shielding material	Lead	Lead
Dimensions (m)	14.5 (L) × 3.3 (W) × 3.5 (H)	5.8 (L) × 3.2 (W) × 3.5 (H)
Temperature Stability	± 0.1°C	± 1°C
Shielding	white beam, IVU20	mono beam, from 6keV to 25 keV
side panels	18 mm-thick lead	6 mm-thick steel
roof panels	6 mm-thick lead	3 mm-thick steel
downstream wall panels	50 mm-thick lead	6 mm-thick steel
add'l downstream wall panel	50 mm-thick lead (1×1 m)	6 mm-thick steel (1×1 m)
guillotine	downstream wall	downstream wall
Door 1	yes	yes
position	upstream outboard	outboard
size (m)	2.4 (H) × 2.4 (W)	2.4 (H) × 1.6 (W)
type	sliding double	sliding double
floor groove	yes	yes
PSS Interfaces	Mounting plates for magnetic lock & dual position switches.	Mounting plates for magnetic lock & dual position switches.
Door 2	yes	no
position	downstream outboard	
size (m)	2.4 (H) × 2.4 (W)	
type	sliding double	
floor groove	yes	
PSS Interfaces	Mounting plates for magnetic lock & dual position switches.	
Hoist	Manual 1000 kg (double sliding rail)	none
Roof Labyrinths		
fluids (roof)	1, low conductivity water	1, low conductivity water
electrical (roof)	3	2
LN_2 labyrinth (roof)	1	Not needed for this hutch
air inlet with fan & filter (roof)	1	1
air outlet (sidewall)	2	1
user access	none	1
Bridge for non-adjacent hutches	utility bridge only (3.5m high)	Utility bridge only (3.5m high)

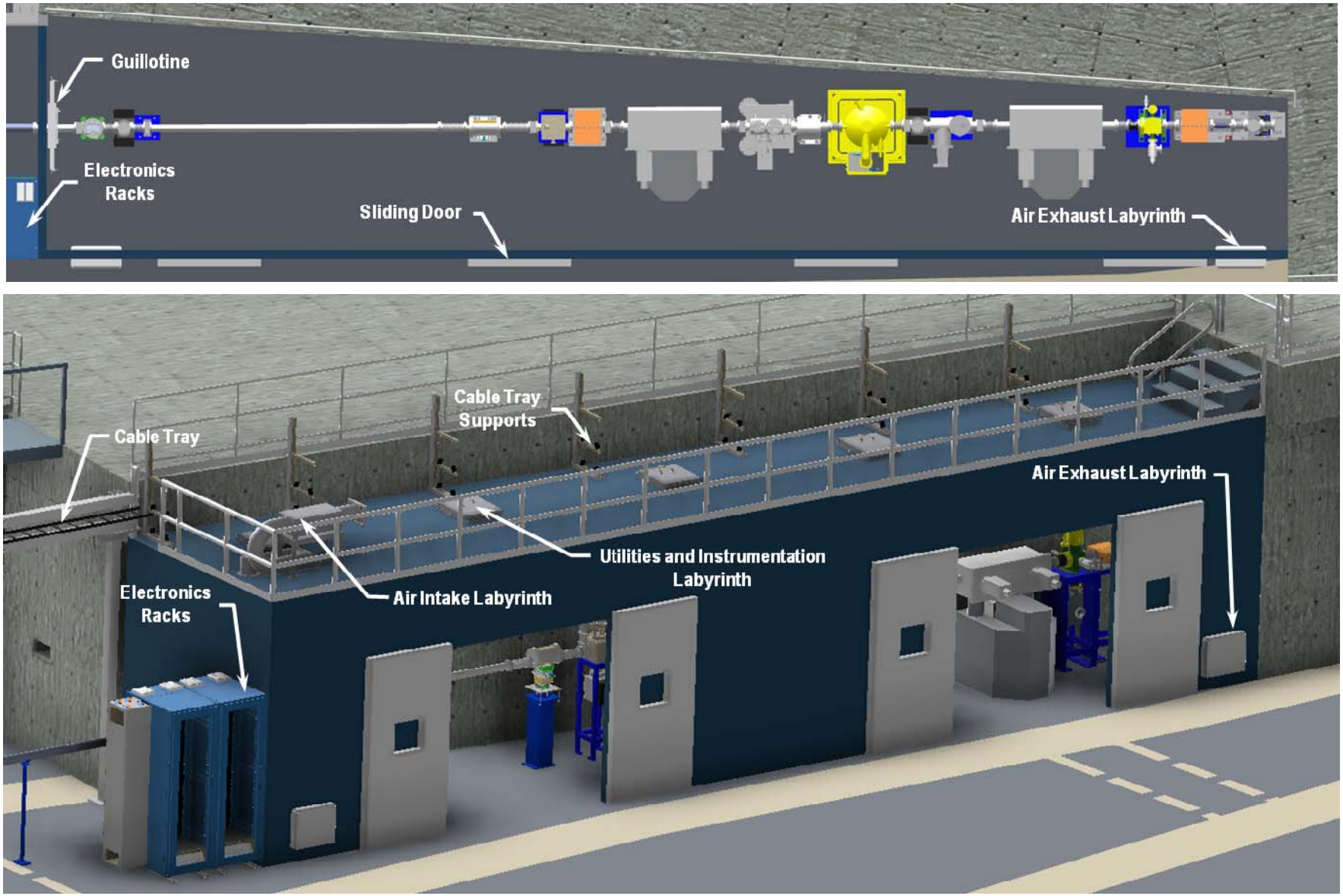

Figure 5.1.1: Experimental station, ID-3-A. Plan view (top) and ISO view (bottom)

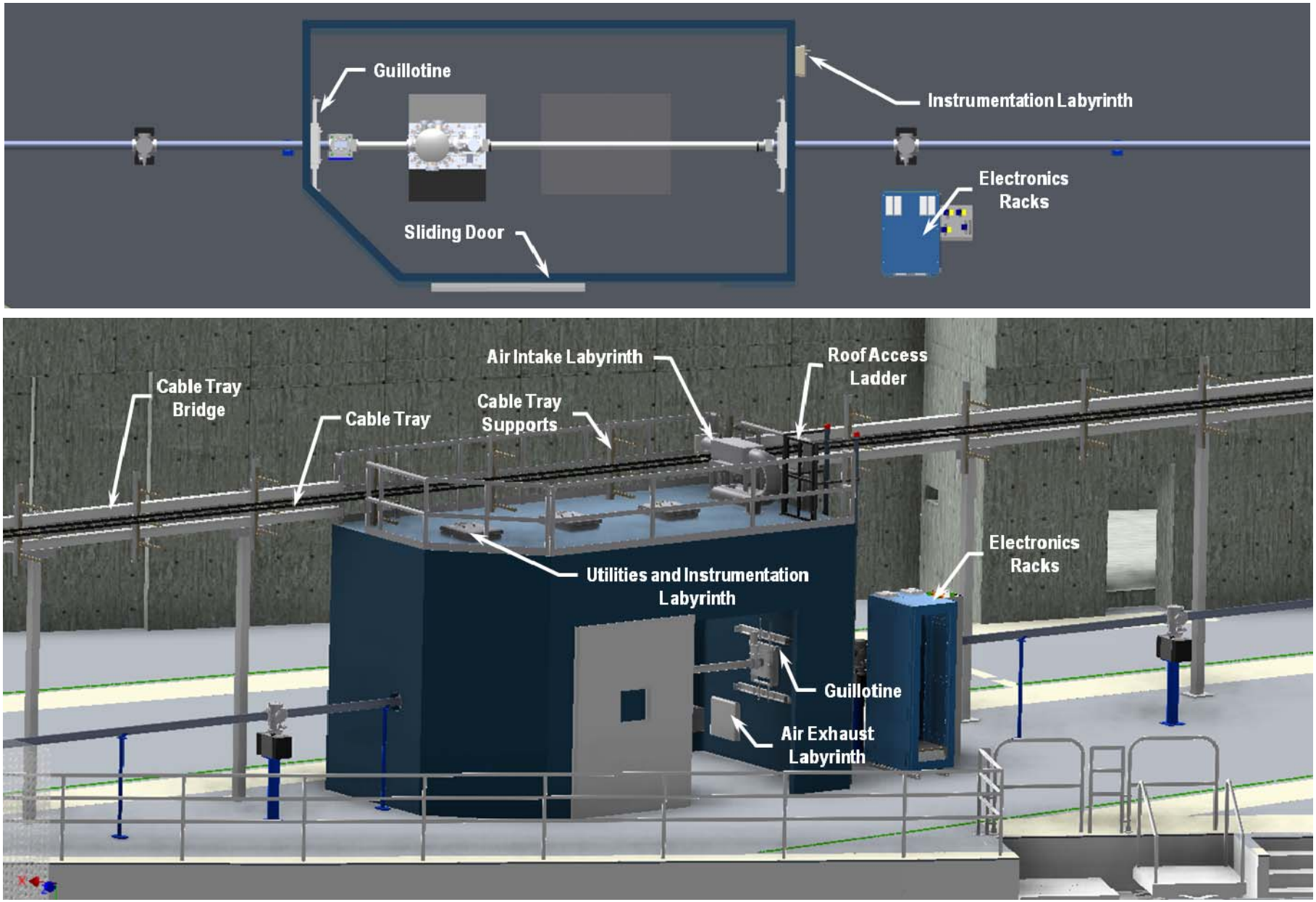

Figure 5.1.2: Experimental station ID-3-B. Plan view (top) and ISO view (bottom)

5.2 Environmental considerations

Vibration and temperature stability requirements for the HXN endstation have been extensively discussed in section 4.1. The temperature stability within the first optical enclosure (FOE, 3-ID-A) is also important because the HXN beamline requires angular stability of the x-ray beam which is heavily influenced by the temperature stability within the FOE. A temperature stability of 0.1 °C must be maintained in the FOE. Because of extremely infrequent entry into the FOE, maintaining a temperature stability of ±0.1°C (peak-to-valley fluctuation over a 24-hour period) is expected to be feasible.

5.3 Surveying requirements

The monochromator and mirrors for the HXN beamline are designed to have the minimum degrees of freedom, in order to maximize the mechanical stability described in section 2. In addition, the ranges of the motorized motions are limited for the same reason. Consequently, the beam position in the first optical enclosure must be surveyed and marked to a high level of accuracy. The required survey accuracy is better than 200 microns in the vertical direction and 400 microns in the horizontal direction. All the optical components in the HXN beamline will be designed to have more than one high-precision fiducial marks, enabling accurate positioning of the optics, crystal, or other internal components that cannot be directly surveyed.

The NSLS-II facility, including the storage ring tunnel and experimental floor, is fitted with a network of survey monuments referenced to a pair of monuments in the center of the ring. This network will be regularly surveyed with a laser tracker to create a robust and accurate network of arbitrarily positioned monuments. Monuments can be added as required, including inside hutches and on the storage ring wall. etc. Positioning a laser tracker on a tripod such that it can view more than three monuments allows it to calculate its position and the position of any new monuments.

Precision machined holes in components are surveyed prior to installation, relative to the component aperture, crystal, mirror or grating surface etc. Fitting a reflector into the precision-drilled hole allows the laser tracker to survey the absolute reflector position so that the aperture or optic position can be accurately calculated. This system of surveying is extremely accurate. Globally (within the NSLS-II complex), components may be positioned to within 100 microns, and where components are close to one another (within a few meters and without sighting restrictions), the accuracy improves to ~30 microns. The accuracy for surveying is sufficient to allow manual alignment of the high stability optics for the HXN beamline.

5.4 Vacuum System

Standard beamline vacuum requirements are applicable to the HXN Beamline, with the exception of a long beam transport pipe section between the experimental floor and the satellite building. As shown in Figure 5.5.1, the length of the beam transport pipe between the two buildings is ~10 m. However, installing a vacuum pump over the bypass corridor (~7m wide) is not practical. Calculations were performed which show that by placing a turbo pump at the last possible location on the experimental floor, and an ion pump immediately inside the satellite building, pressures much better than 10^{-5} Torr can be maintained with a 6″-diameter beampipe.

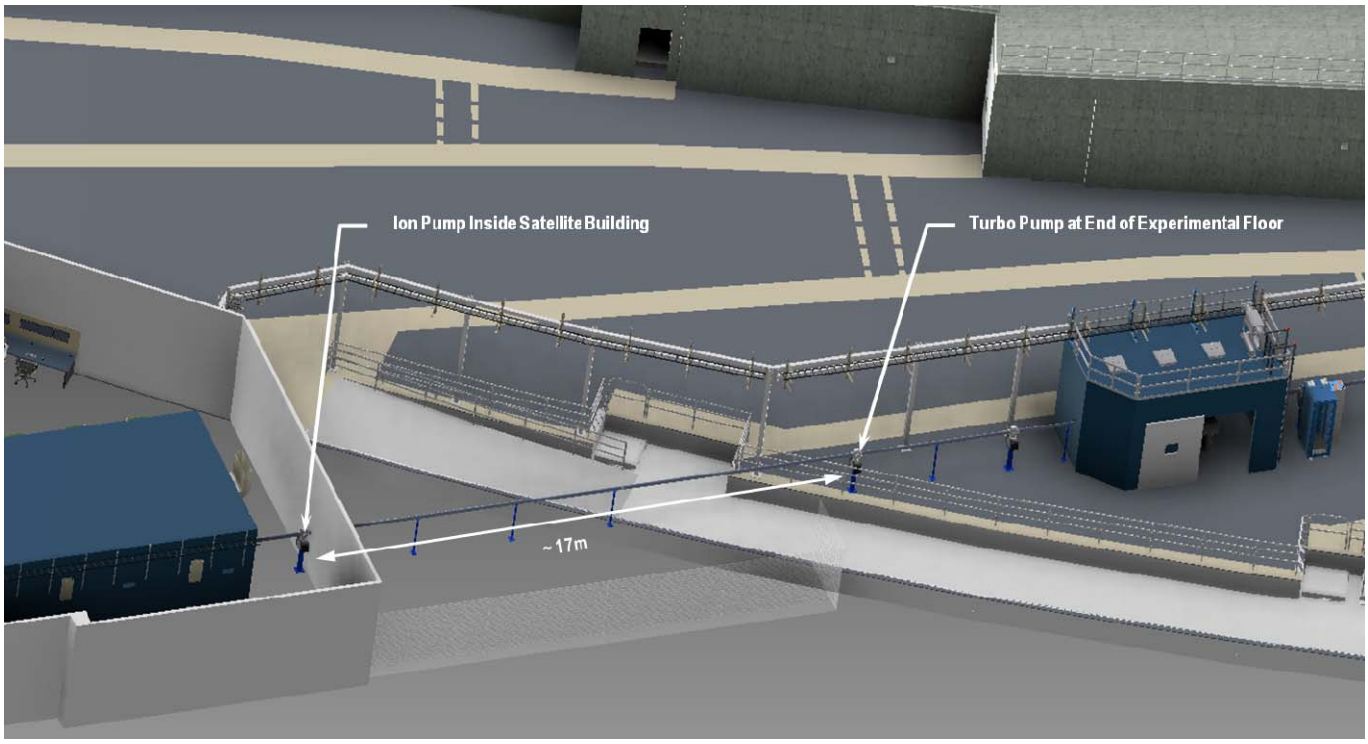

Figure 5.4.1: HXN Beamline detail showing the long beampipe section and associated vacuum pumps.

5.5 Utilities Requirements

Table 5.6.1: Utilities requirements for HXN beamline components.

Description	Acronym	Hutch	Compressed N2	Compressed Air	DI (Process) Water	Chilled Water	Liquid N2	Cylinder Gas	Liquid Ga Cooling
Fixed Mask	MSK1FE	FE			x				
White Beam Slits	SLT1FE	FE			x				
White Beam Slits	SLT2FE	FE			x				
Gate Valve	GV1	A		x					
Diagnostic Chamber	BPM1	A			x				
Mask	MSK	A			x				
Collimator	CO	A			x				
White Beam Filters	FLT	A			x				
Be Window (cooled)	WIN1	A			x				

Description	Acronym	Hutch	Compressed N2	Compressed Air	DI (Process) Water	Chilled Water	Liquid N2	Cylinder Gas	Liquid Ga Cooling
Horizontal Collimating Mirror	HCM	A			x				x *
Gate Valve	GV2	A		x					
Pink Beam Slits	SLT1	A			x				
Pink Beam Screen Monitor	FLSW	A			x				
Gate Valve	GV3	A		x					
Monochromator, Horizontal Double Crystal	DCM	A					x		
White Beam Stop	WBS	A			x				
Mono Slits & Florescent Screen	SLT2 & FLSM	A							
Gate Valve	GV4	A		x					
Horizontal Focusing Mirror	HFM	A							
Gate Valve	GV5	A		x					
Bremsstrahlung Stop	BRS	A			x				
Mono Beam Position Monitor (BPM) / Screen	BPM2	A			x				
Gate Valve	GV6	A		x					
Compound Refractive Lens (Transfocator)	CRL	A		x					
Gate Valve	GV7	A		x					
Diagnostic Chamber (BPM)	BPM3	A							
Mono Beam Shutter	SSH1	A		x					
Gate Valve	GV8	A		x					
Other Hutch Utilities		A				x	x	x	
Gate Valve w/ X-ray Window	WIN2	B		x					
Gate Valve w/ X-ray Window	WIN3	B		x					
Quad Diode and Screen Monitor	QBPM1	B							
Secondary Source Aperture	SSA1	B							
Gate Valve	GV9	B		x					
Mono Beam Shutter	SSH2	B		x					
Other Hutch Utilities		B				x		x	
Gate Valve	GV10	C		x					
Secondary Source Aperture	SSA2	C							
Quad Diode and Screen Monitor	QBPM2	C							
Be Window	WIN3	C							
Endstation Instruments		C			x	x	x	x	
Other Hutch Utilities		C				x	x	x	

* Possible requirement

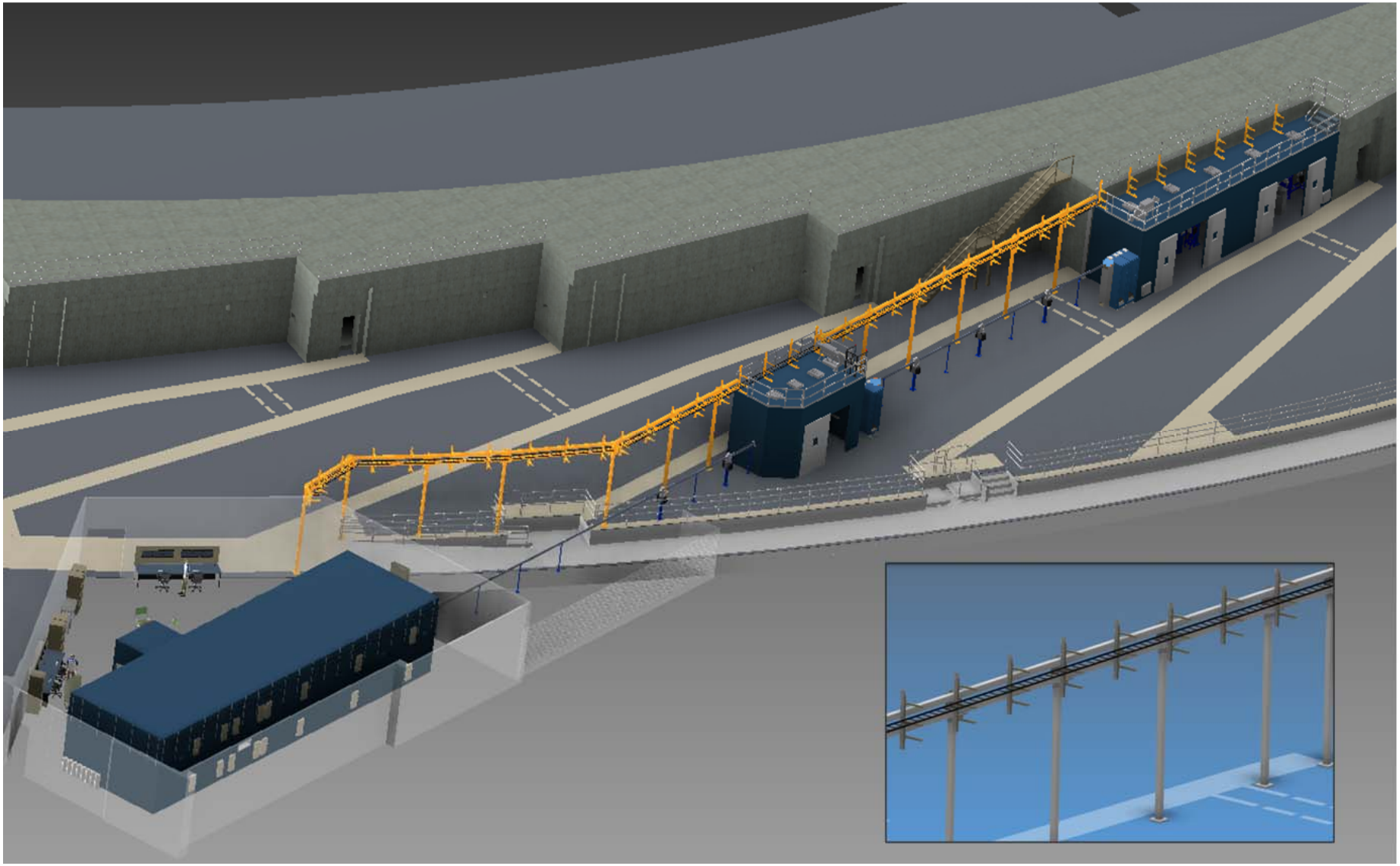

Figure 5.6.1: Transport of the utilities for the three experimental stations of the Hard X-ray Nanoprobe beamline. For the endstation, electricity and HVAC are routed from LOB 3. The insert on the bottom right shows the details on the utility tray and the support structures.

5.6 Control Requirements

Table 5.6.1 summarizes the control requirements for the HXN beamline.

Table 5.6.1: Control Requirements The requirements for the endstation instruments are still not completely finalized and subject to changes.

Item	Component	Stepper motor	Piezo	Temp sensor	Flow sensor	Vacuum sensor	Tilt Sensor	Actuator control	Photon Induced current
1	Gate Valve							1	
2	Bellows								
3	Diagnostic Chamber	1		4		1			4
4	Bellows								
5	Mask			2	1	1			
6	Collimator			1					
7	Bellows								
8	White Beam Filters	2		6	1	1			
9	Be Window (cooled)			1	1				
10	Bellows								
11	Horizontal Collimating Mirror	10	2	4	1	1	2		
12	Bellows								
13	Gate Valve							1	
14	Pink Beam Slits	4		4	1	1			4
15	Pink Beam Screen Monitor	1		1	1				
16	Gate Valve							1	
17	Bellows								
18	Monochromator, Horizontal Double Crystal	10	4	4	2	1	2		
19	Bellows								
20	White Beam Stop			2	1				
21	Mono Slits & Florescent Screen	5							4
22	Gate Valve							1	
23	Bellows								
24	Horizontal Focusing Mirror	10	2			1	2		
25	Bellows								
26	Gate Valve							1	
27	Bremsstrahlung Stop								
28	Mono Beam Position Monitor (BPM) / Screen	2				1			4

Table 5.6.1: Continued

Item	Component	Stepper motor	Piezo	Temp sensor	Flow sensor	Vacuum sensor	Tilt Sensor	Actuator control	Photon Induced current
29	Gate Valve							1	
30	Bellows								
31	Compound Refractive Lens (Transfocator)	4				1	2	8	
32	Bellows								
33	Beampipe					1			
34	Gate Valve							1	
35	Bellows								
36	Diagnostic Chamber (BPM)	1				1			4
37	Bellows								
38	Mono Beam Shutter							1	
39	Gate Valve							1	
40	Gate Valve w/ X-ray Window							1	
41	Beampipe, Removable								
42	Gate Valve w/ X-ray Window							1	
43	Quad Diode and Screen Monitor	2				1			4
44	Secondary Source Aperture	4	2			1	2		
45	Beampipe								
46	Gate Valve							1	
47	Mono Beam Shutter							1	
48	Gate Valve							1	
49	Secondary Source Aperture	4	2			1	2		4
50	Quad Diode and Screen Monitor	2							4
51	Be Window								
52	Beampipe, Removable								
53	Fast Detector Shutter	1						1	
54	HXN Microscope	9	43	12		1	4		
	Other Instruments in the Endstation (tentative)								
55	Optical Table1	6					2		
56	Optical Table2	6					2		
57	HXN prototype	3	12	8			2		
58	X-ray attenuators							12	
59	Mono Slits	4							
60	High-res mono	8	2				2		

6 SPECIAL BEAMLINE REQUIREMENTS

The special requirements for the HXN Satellite Building are extensively described in section 4. The temperature stability requirement for the first optical hutch, ±0.1°C over a 24 hour period, is described in section 5.2. There are no other special requirements.

7 SAFETY

The design, construction and operation of the HXN beamline will be in accordance with the laboratory policies, regulations, and the recommendation of the various review committees that will be evaluating many aspects of safety concerns. The radiation shielding requirements for the enclosures have been completed and are described in section 5.1. The radiation safety reviews have been performed on the conceptual and preliminary design of the HXN beamline. The Bremsstrahlung and synchrotron ray tracings for the preliminary design have been performed, and the results are shown in Figures A2.5 through A2.8 in Appendix 2. The Personnel Protection System (PPS) scheme for the HXN beamline is developed and presented in Figure A2.9 in Appendix 2.

8 FUTURE UPGRADE OPTIONS

The mission of the Hard X-ray Nanoprobe Beamline is to explore the new frontier of hard x-ray microscopy by achieving the highest achievable spatial resolution and measurement sensitivity. The technical design of the beamline optics, x-ray microscope, and satellite building are aimed at x-ray microscopy capabilities beyond the baseline scope. The optical scheme of the HXN beamline is developed to support ~ 1nm focusing. The construction of the HXN Satellite Building with extremely high vibration and temperature stability is an important infrastructure investment that will certainly pave a solid path toward the ultimate goal of ~1nm. The ongoing R&D programs for developing MLL optics and nanopositioning capabilities will lay down a secure foundation for building up technical capabilities toward this ultimate goal. In this section, we specify the details of the mature scope instrument configurations and their performance enhancements.

8.1 High-resolution mode

The optical scheme for the HXN beamline consists of a high throughput mode and a high resolution mode. These two modes are designed to complement each other and to ensure the broadest optical capabilities for the HXN beamline. The high throughput mode is selected in the baseline scope because it is specifically designed to achieve high flux for relatively small to moderate size nanofocusing optics up to 150μm. As the fabrication capabilities for MLLs and ZP are advancing, we expect that high resolution nanofocusing optics with larger sizes will become available. Currently, our target size for the flat MLL optics is ~124μm before year 2014. The fabrication capabilities for zone plates are progressing steadily, and it is feasible to fabricate zone plates with a diameter larger than 150μm and offering a spatial resolution of 30~50nm. Larger nanofocusing optics enable a larger working distance, which is critical in ensuring a greater detection solid angle for fluorescence and flexibility in designing in-situ environment cells around the sample. Implementing the high resolution mode by installing SSA1 at z=65m within the experimental station, 3-ID-B, ensures that the beamline is capable of taking advantage of anticipated advances for both MLLs and ZPs.

8.2 Vertical focusing using x-ray mirrors

In the baseline scope, we choose to use refractive optics for vertical focusing in order to ensure the highest level of beam stability and avoid substantial flux loss, as explained in section 2.7. The desired specifications for the vertical

mirrors are at the limits of the current capabilities for mirror fabrication and mechanical devices. We anticipate that the quality of mirror polishing for ~0.5m-long mirrors will be significantly improved as more advanced metrology instruments are used to close the feedback loop. In addition, vendor capabilities for high stability mirrors are rapidly progressing. In the mature scope, we plan to implement a vertical mirror system, in order access all energies over 6-25keV.

8.3 Pixel array detector for nanodiffraction

Developing robust data acquisition and analysis methods for nanodiffraction at 10 nm is still an open problem. Implementing an ideal detector for nanodiffraction depends considerably on the technical details of implementing sample rotation, methods for establishing the sample coordinate system (after rotating), and the types of crystalline samples. During the initial phase of the HXN beamline, considerable effort will be concentrated on nanofluorescence. Full development of nanodiffraction capabilities will require 1~2 years of development time, before the HXN-specific instrumentation challenges have been sorted out. In the baseline scope, we plan to use a 4k x 4k CCD, which is already purchased for carrying out R&D experiments. During the initial phase, this CCD is adequate for developing nanodiffraction techniques at 10 nm. To implement the developed techniques for high-throughput measurements, an area detector with faster readout and larger dynamic range is required. A 4k x 4k pixel array detector with a 75~100 μm pixel size and dynamic range of ~10^5 can significantly improve the nanodiffraction throughput.

8.4 Development of x-ray microscopy capability at 1~10 nm

The HXN microscope presented in this report is designed for high scientific productivity and robust applications, offering compatibility for both MLLs and ZP optics and fluorescence/diffraction capabilities. Though the HXN microscope will have high mechanical stability and a sub-nm laser encoding capability, it is not an ideal instrument to explore spatial resolutions at 1~10 nm. Achieving x-ray microscopy at 1~10 nm requires a much more simplified, compact and stiffer design, with more focused measurement capabilities. The following are important technical requirements for a 1nm microscope:

- X-ray fluorescence and differential phase-contrast (DCP) capability
- Laser interferometer detection level better than 0.2 nm
- Substantially compact and high mechanical stiffness (i.e., integrated piezo stacks)
- In-vacuum operation
- High temperature stability, better than 0.01°±C
- No amplification of the floor vibration
- Temperature gradients less than 0.01°±C within the vacuum enclosure of the microscope
- Addition of a narrower energy bandpass monochromator
- Implementation of SSA1 in the HXN beamline

The first requirement enables a simplified design of the microscope. Ideally, the position detection sensitivity should be 10~20% of the spatial resolution. Currently, the position detection sensitivity of the interferometer being developed for the HXN microscope is 0.88 nm (2 σ). Reaching a detection level of 0.2 nm within 1~2 years is technically feasible. We are already exploring various options for compact and high stiffness designs for the HXN microscope and potential applications for a 1nm microscope. To achieve 1 nm focusing, it is necessary to implement the SSA1 so that sufficient source demagnification can be achieved. Based on the calculations shown in Table 3.2.1, the monochromaticity requirement will not become a problem until the spatial resolution is down to ~2 nm for wedged MLLs at 10 keV. In addition, the size of the MLLs can be used to balance the need for the

monochromaticity. Thus, the need for the additional monochromator must be evaluated as the nanofocusing development progresses.

As mentioned earlier, development of 1~10nm resolution is not an isolated effort. Rather, this development requires significant coordination to leverage the investment and efforts that are either already made or ongoing. The following resources need to be secured and provided, in order to achieve the ultimate goal:

- Continuing development of MLL optics
- Continuing development of in-house nanopositioning capabilities
- Allocation of resources for developing a prototype instrument for 1nm focusing
- Allocation of 1~2 weeks of beamtime per cycle at the HXN beamline for developing the 1nm prototype instrument

8.5 Development of variable temperature control for the HXN microscope

The capability of regulating the temperature of the sample from ~10 K to 550 K while achieving 10nm spatial resolution will significantly broaden the range of scientific applications for the HXN beamline. Due to the short working distance (<2 mm) required for 10nm focusing, implementing commercially available cryogenic or high temperature options is not feasible without a focused R&D effort. The current design of the HXN microscope requires implementation of a "cold finger" in the vicinity of the sample without cooling the sample stages and the focusing optics. Achieving higher temperatures requires a similar approach without creating a severe temperature gradient around the sample and nanofocusing stages. Incorporating temperature control capabilities in the design of the HXN microscope is an ideal development path. However, due to the considerable technical risks, the initial scope of the HXN microscope focuses on achieving the required spatial resolution. Incorporating temperature control capabilities will be carried out in the mature scope.

APPENDIX 1: SCHEDULE

September 30	2010	Preliminary Design Report
October 19-20	2010	PDR Technical Review
November 15-17	2010	DOE review
January 11	2011	Start Lead Time Procurements (monochromators, mirrors, enclosures,…)
April 14	2011	Complete Final Design of Beamline Major Components
February	2012	Complete Final Design Report
February	2012	Start Installation
May	2012	Start Sub-System Testing
August	2013	Start Integrated Testing
January	2014	Complete Installation
February	**2014**	**Beam-ready**

APPENDIX 2: REFERENCE DRAWINGS

The following drawings are provided here for reference:

Figure A2.1: Sector layout for the Hard X-ray Nanoprobe Beamline
Figure A2.2: Shielding enclosure layout for the Hard X-ray Nanoprobe Beamline: 3-ID-A
Figure A2.3: Shielding enclosure layout for the Hard X-ray Nanoprobe Beamline: 3-ID-B
Figure A2.4A: Shielding enclosure layout for the Hard X-ray Nanoprobe Beamline: 3-ID-C
Figure A2.4B: Shielding enclosure layout for the Hard X-ray Nanoprobe Beamline: air-lock entry
Figure A2.5: Horizontal Bremsstrahlung ray tracings for the Hard X-ray Nanoprobe Beamline.
Figure A2.6: Vertical Bremsstrahlung ray tracings for the Hard X-ray Nanoprobe Beamline.
Figure A2.7: Horizontal synchrotron ray tracings for the Hard X-ray Nanoprobe Beamline.
Figure A2.8: Vertical synchrotron ray tracings for the Hard X-ray Nanoprobe Beamline.
Figure A2.9: Personnel Protection System schematic layout for the Hard X-ray Nanoprobe Beamline
Figure A2.10: Preliminary front end component layout
Figure A2.11: Beamline Layout – Experimental Station 3-ID-A
Figure A2.12: Beamline Layout – Experimental Station 3-ID-B
Figure A2.13: Beamline Layout – Experimental Station 3-ID-C

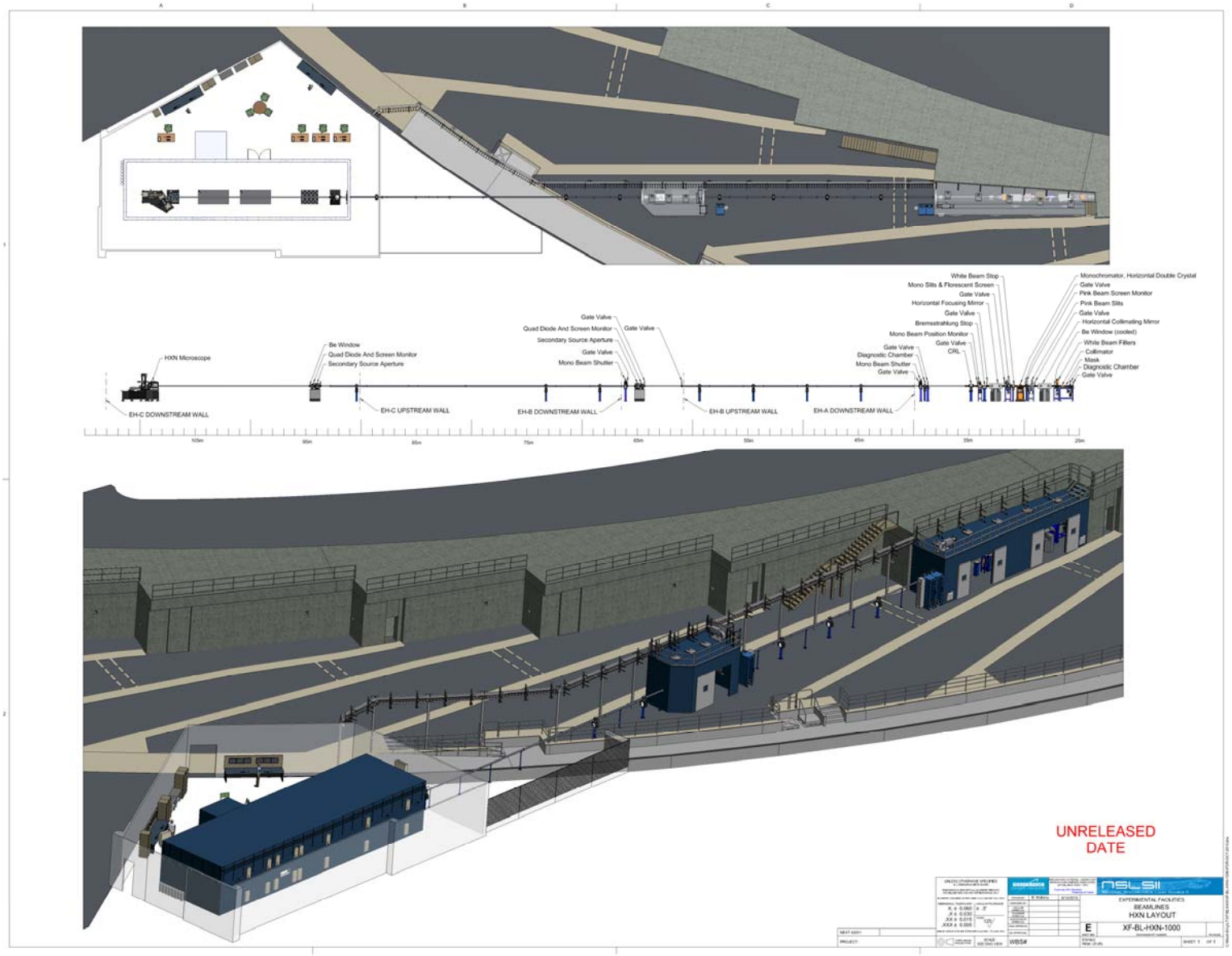

Figure A2.1: Sector layout for the Hard X-ray Nanoprobe Beamline

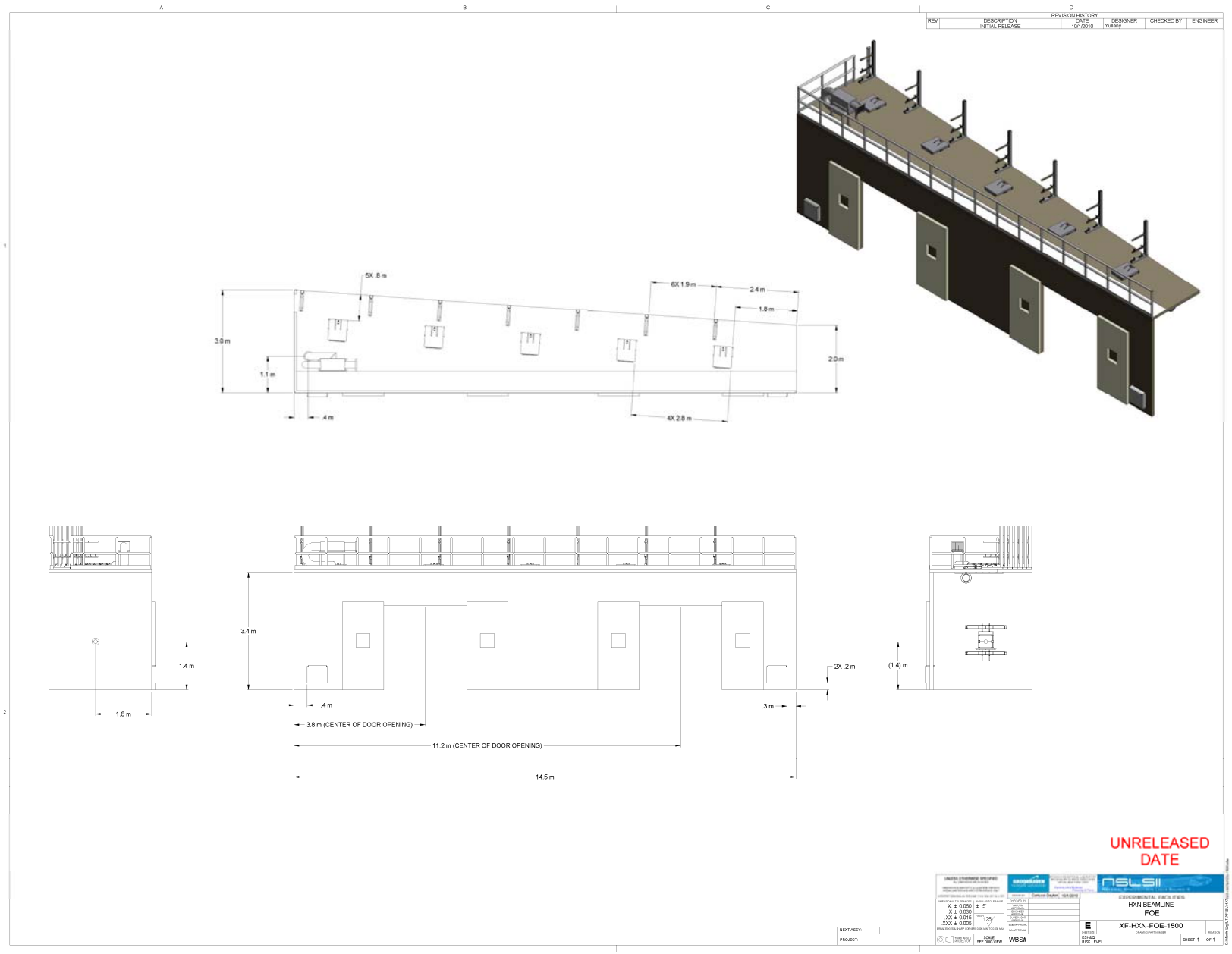

Figure A2.2: Shielding enclosure layout for the Hard X-ray Nanoprobe Beamline: 3-ID-A

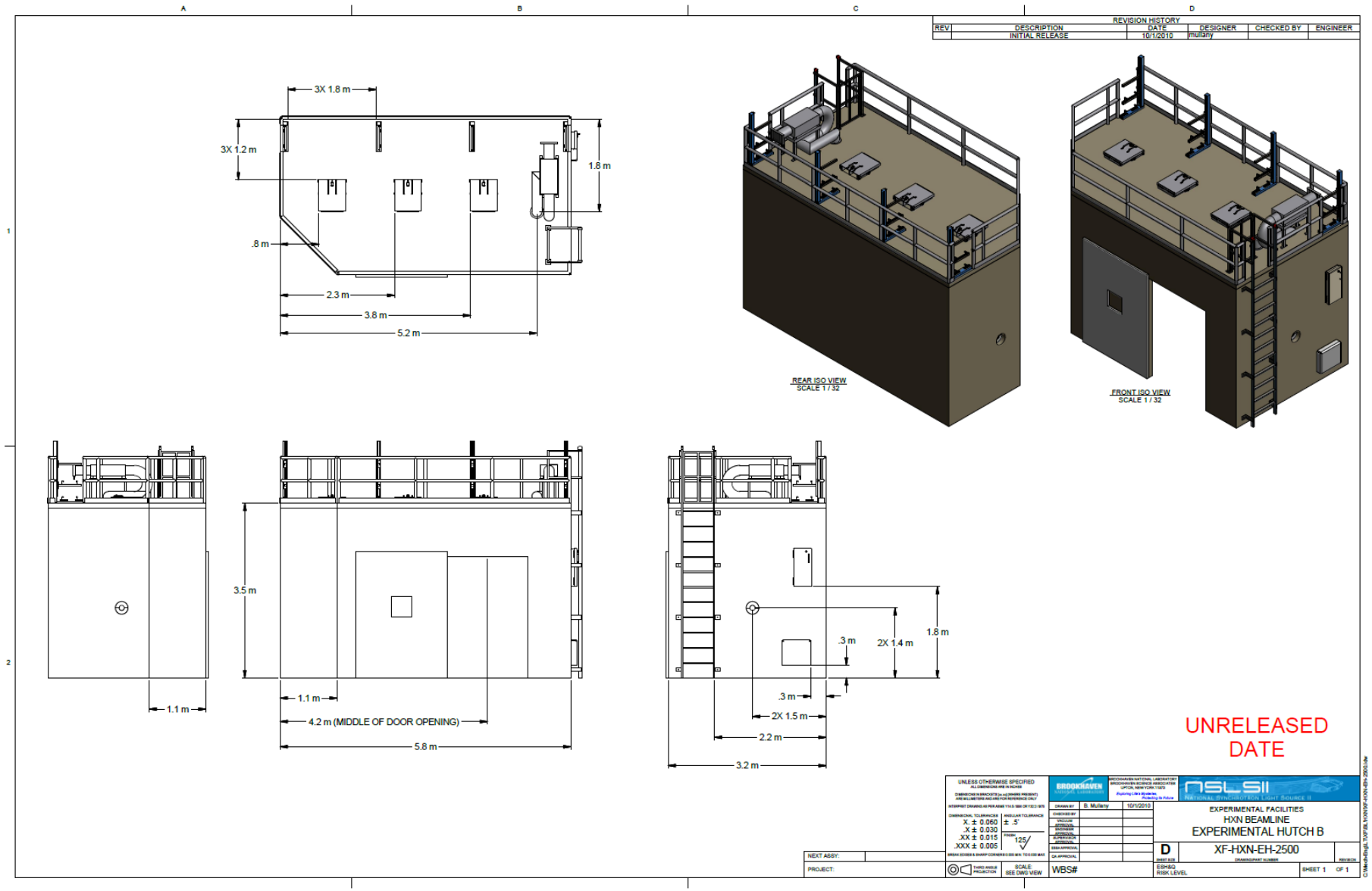

Figure A2.3: Shielding enclosure layout for the Hard X-ray Nanoprobe Beamline: 3-ID-B

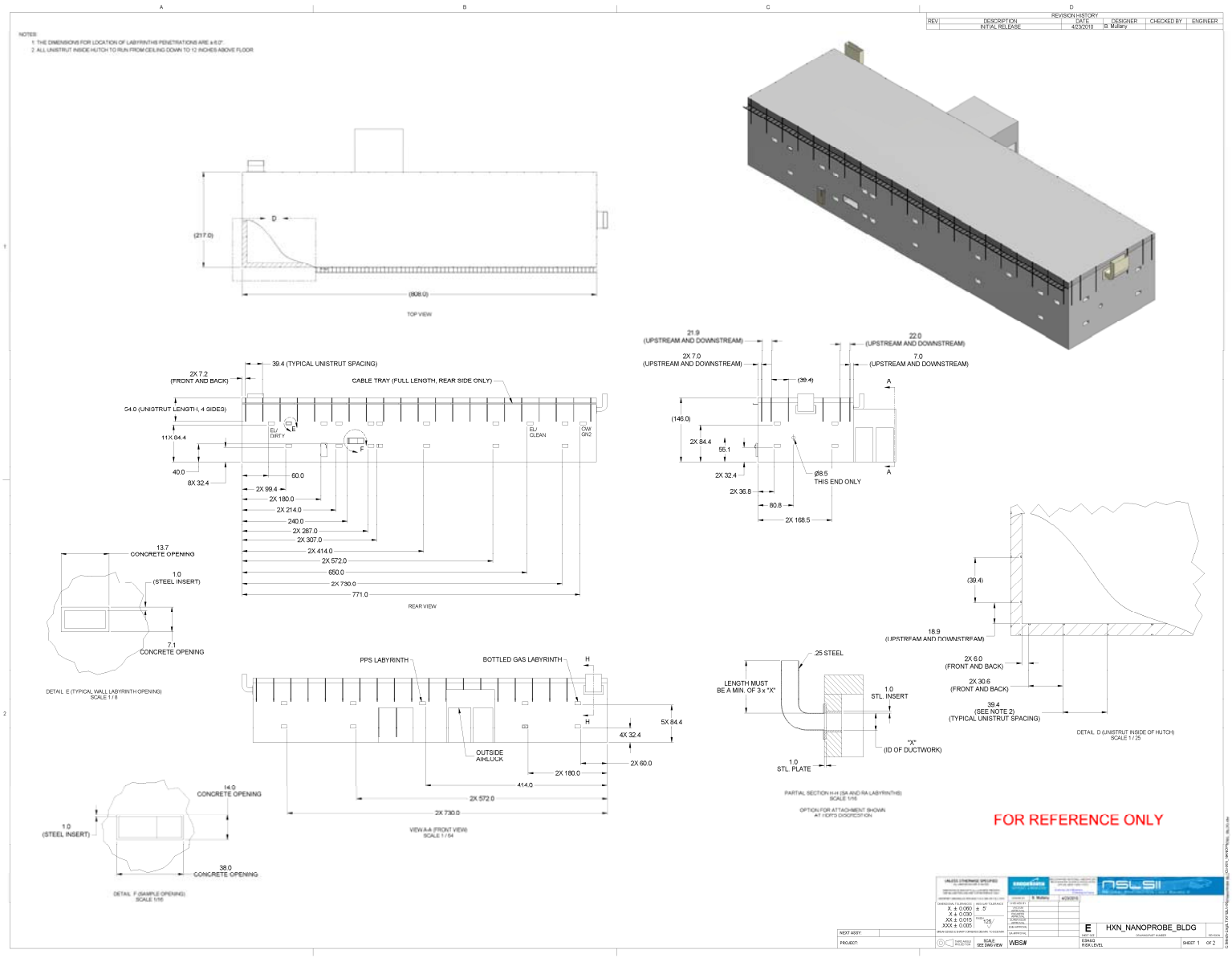

Figure A2.4A: Shielding enclosure layout for the Hard X-ray Nanoprobe Beamline: 3-ID-C

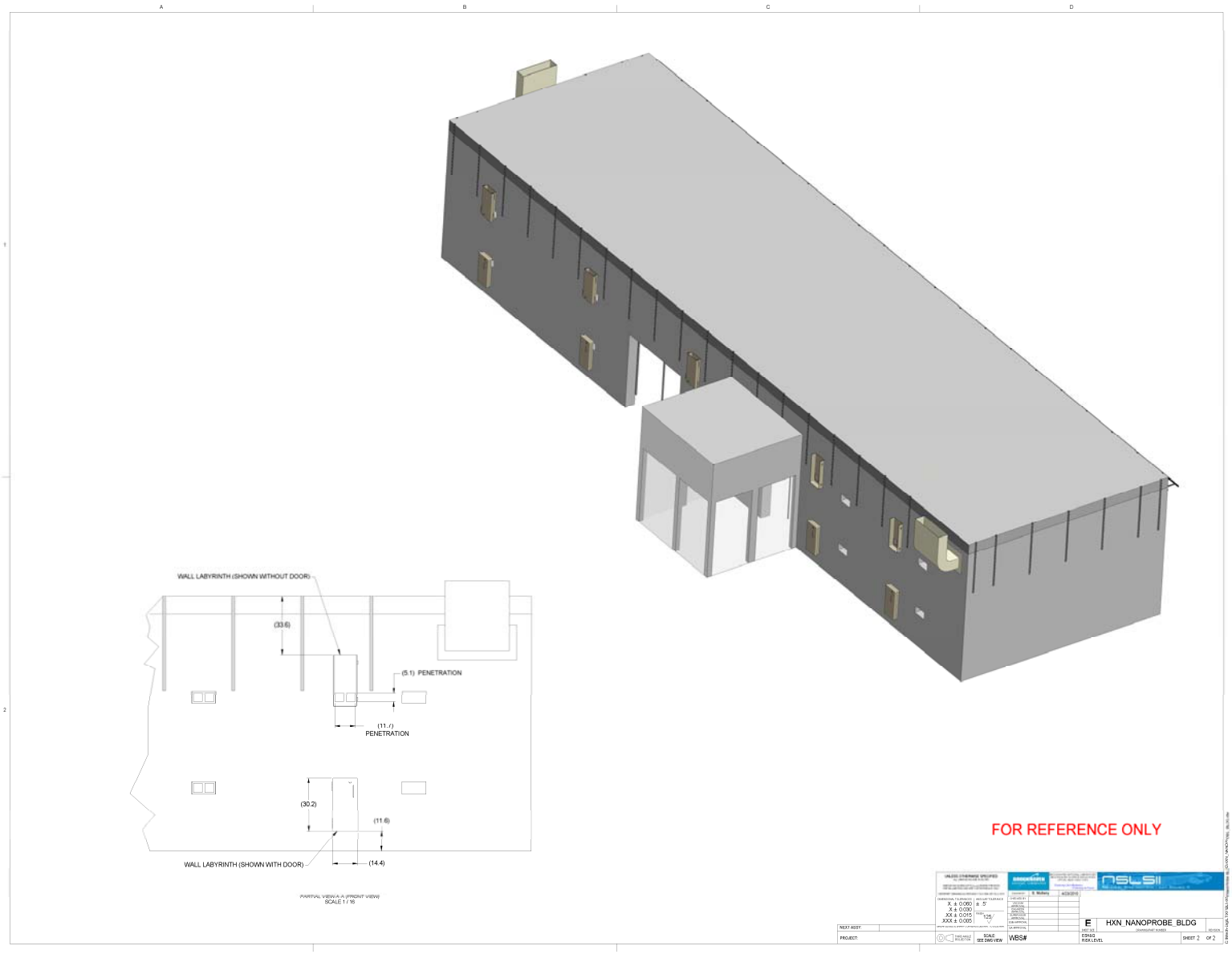

Figure A2.4B: Shielding enclosure layout for the Hard X-ray Nanoprobe Beamline: air-lock entry

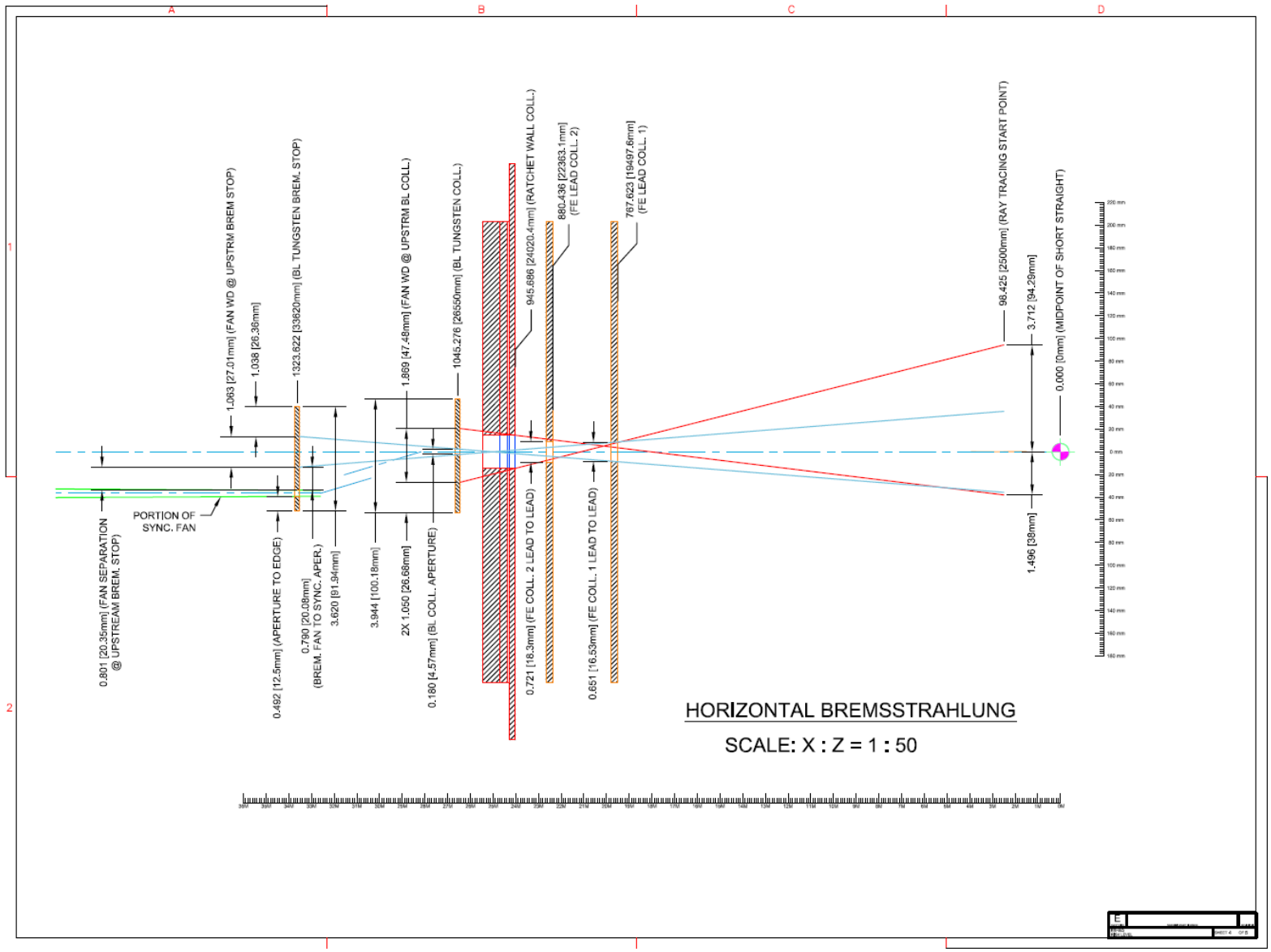

Figure A2.5: Horizontal Bremsstrahlung ray tracings for the Hard X-ray Nanoprobe Beamline.

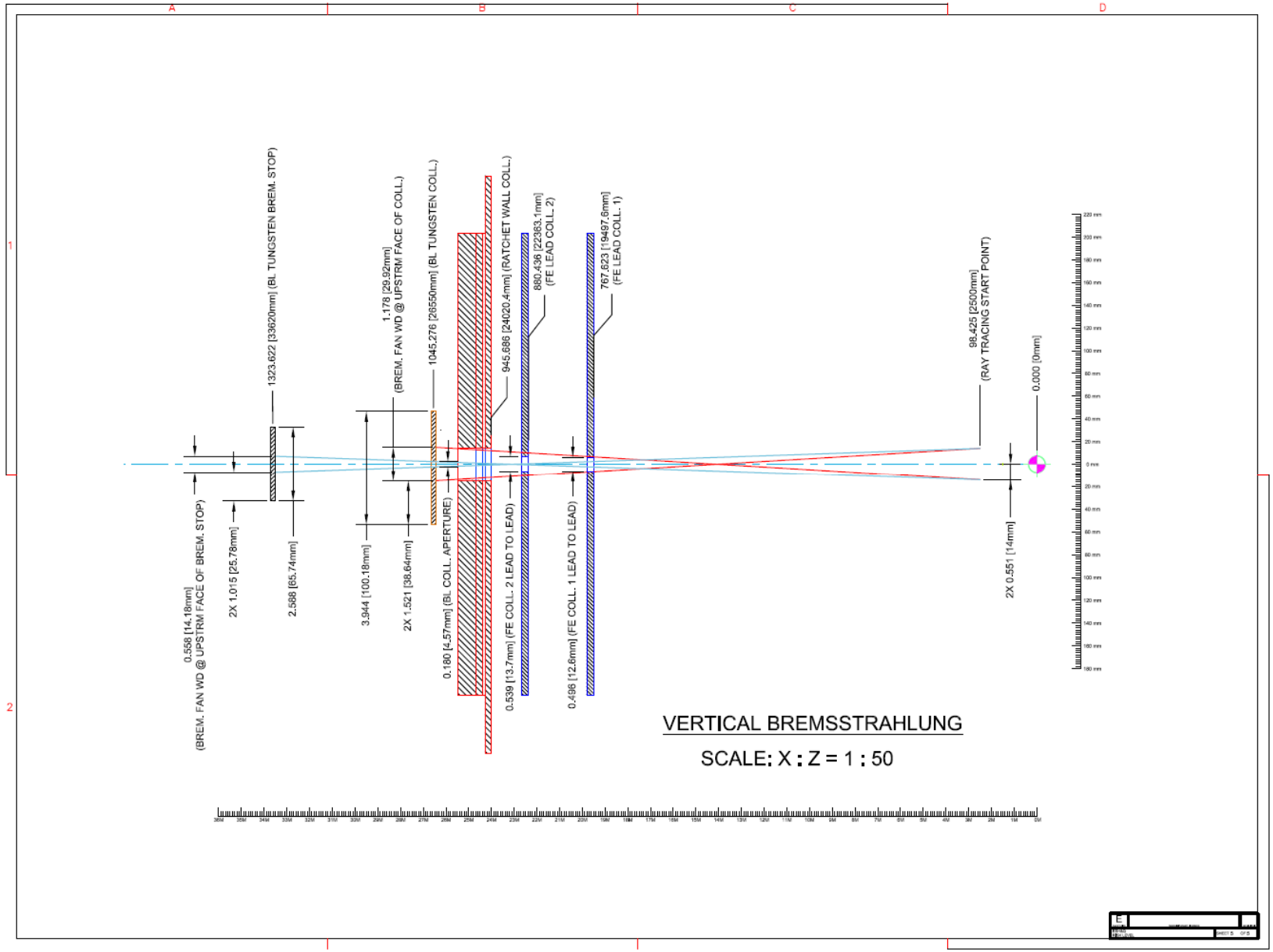

Figure A2.6: Vertical Bremsstrahlung ray tracings for the Hard X-ray Nanoprobe Beamline.

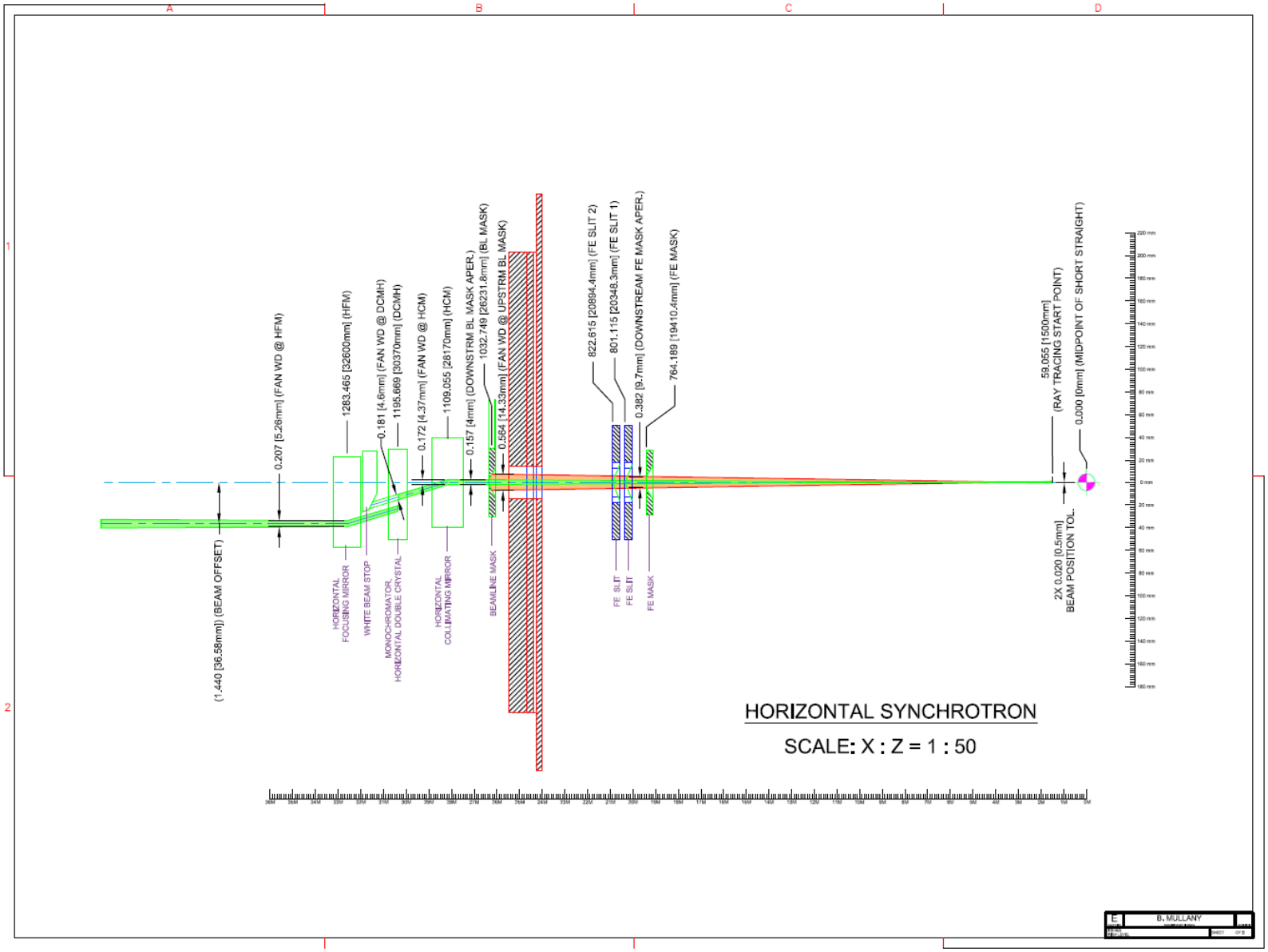

Figure A2.7: Horizontal synchrotron ray tracings for the Hard X-ray Nanoprobe Beamline.

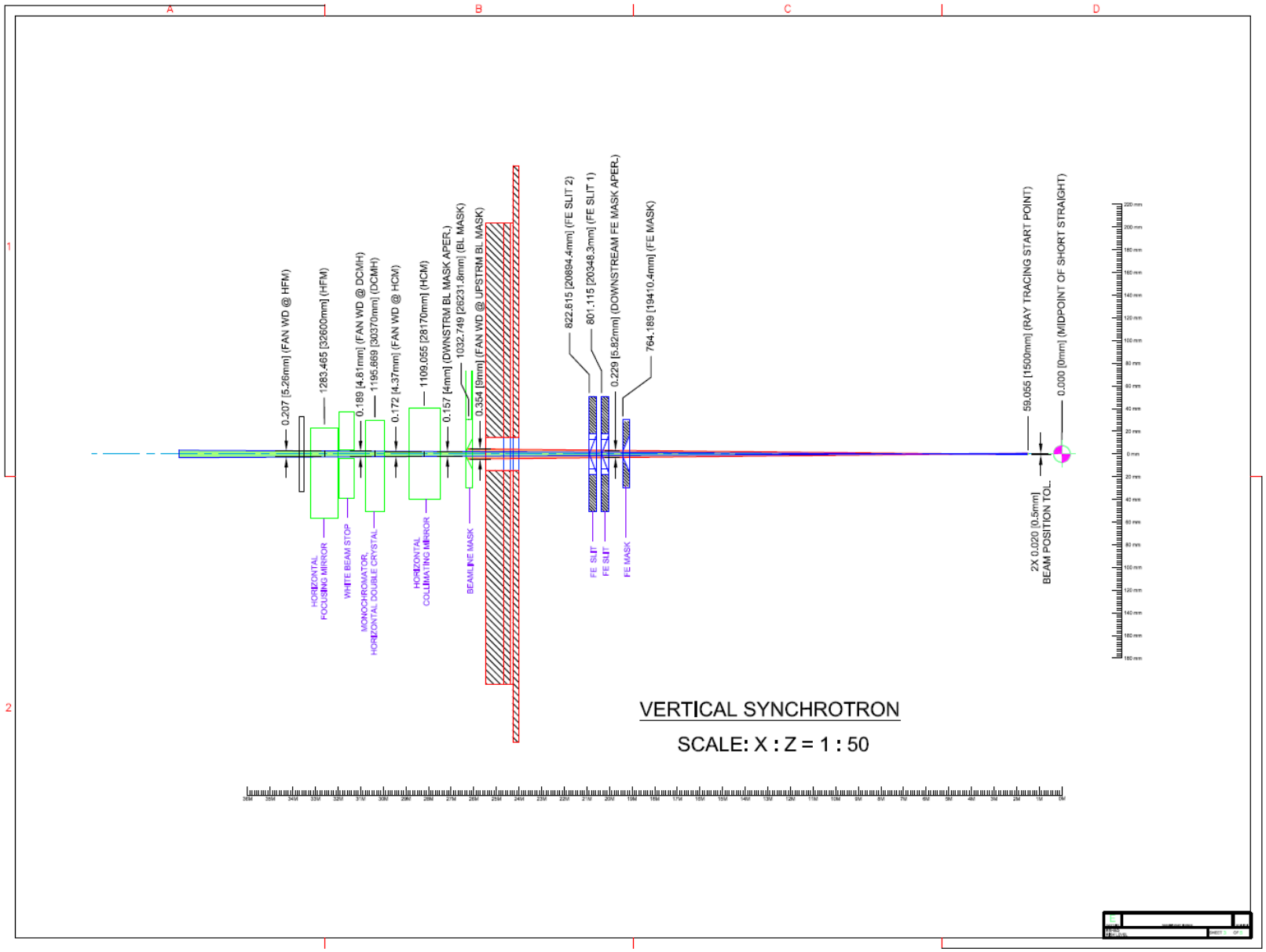

Figure A2.8: Vertical synchrotron ray tracings for the Hard X-ray Nanoprobe Beamline.

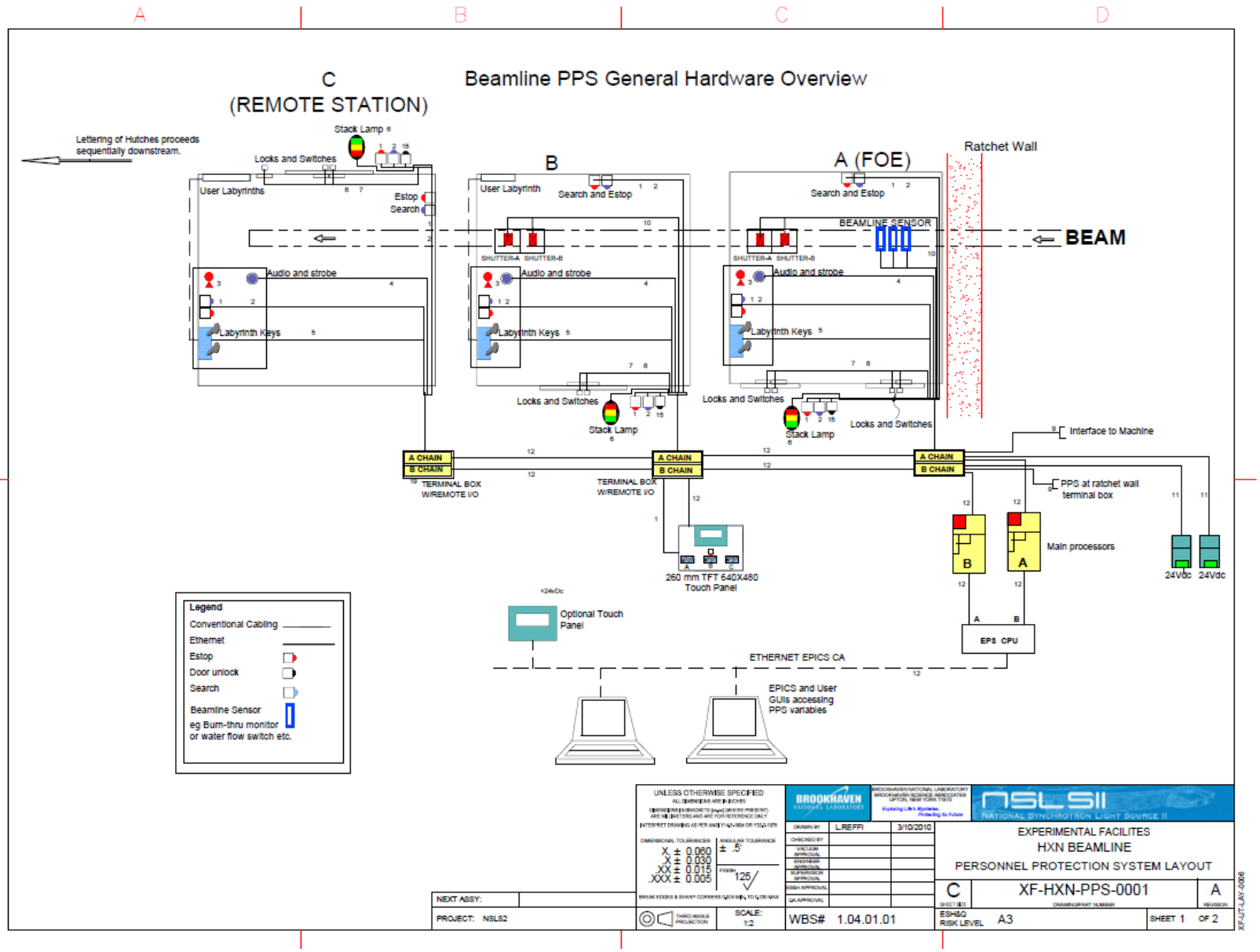

Figure A2.9: Personnel Protection System schematic layout for the Hard X-ray Nanoprobe Beamline

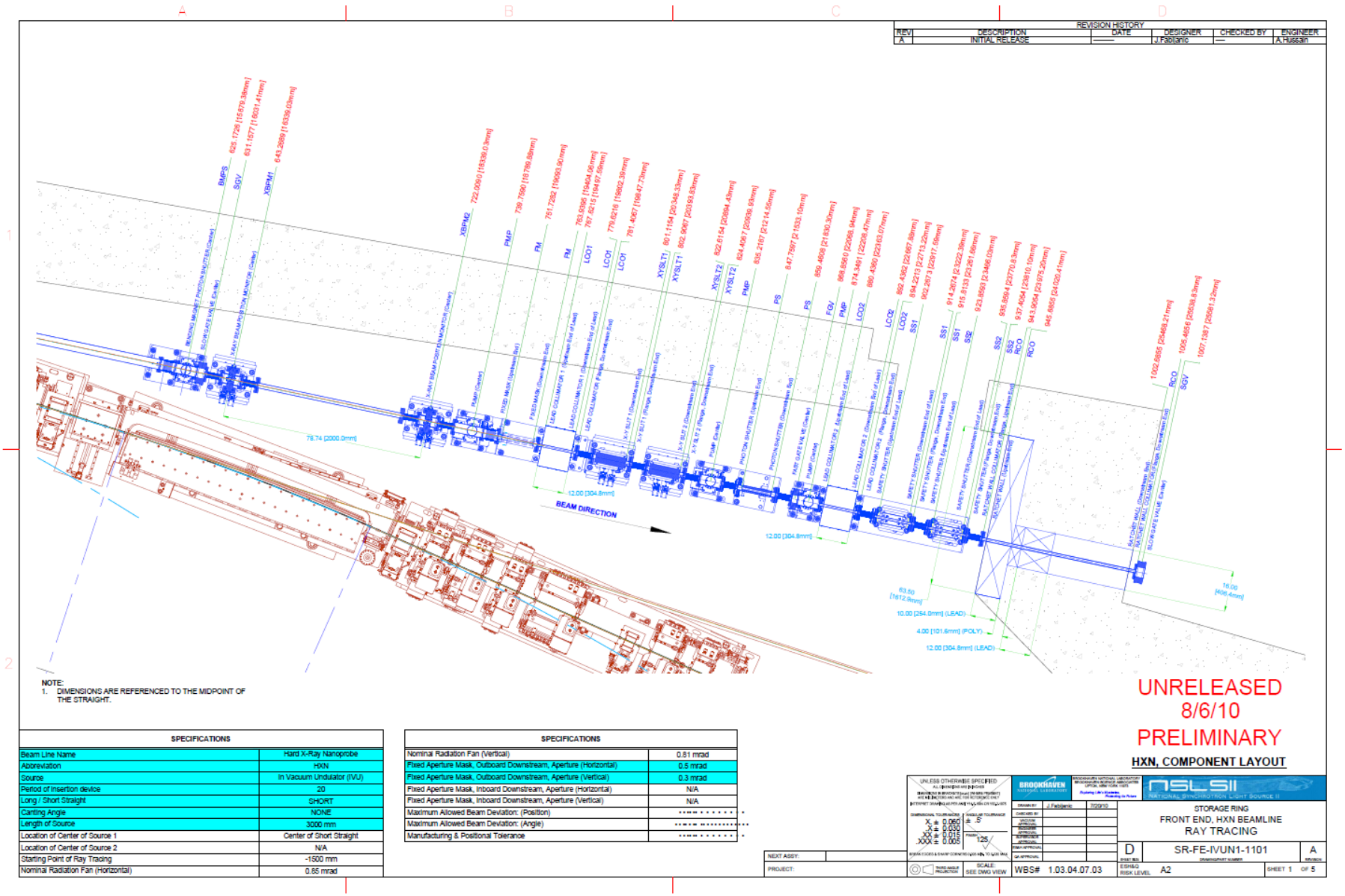

SPECIFICATIONS	
Beam Line Name	Hard X-Ray Nanoprobe
Abbreviation	HXN
Source	In Vacuum Undulator (IVU)
Period of insertion device	20
Long / Short Straight	SHORT
Canting Angle	NONE
Length of Source	3000 mm
Location of Center of Source 1	Center of Short Straight
Location of Center of Source 2	N/A
Starting Point of Ray Tracing	-1500 mm
Nominal Radiation Fan (Horizontal)	0.85 mrad

SPECIFICATIONS	
Nominal Radiation Fan (Vertical)	0.81 mrad
Fixed Aperture Mask, Outboard Downstream, Aperture (Horizontal)	0.5 mrad
Fixed Aperture Mask, Outboard Downstream, Aperture (Vertical)	0.3 mrad
Fixed Aperture Mask, Inboard Downstream, Aperture (Horizontal)	N/A
Fixed Aperture Mask, Inboard Downstream, Aperture (Vertical)	N/A
Maximum Allowed Beam Deviation: (Position)	.....
Maximum Allowed Beam Deviation: (Angle)	.....
Manufacturing & Positional Tolerance	.....

Figure A2.10: Preliminary front end component layout (note beam direction is from left to right)

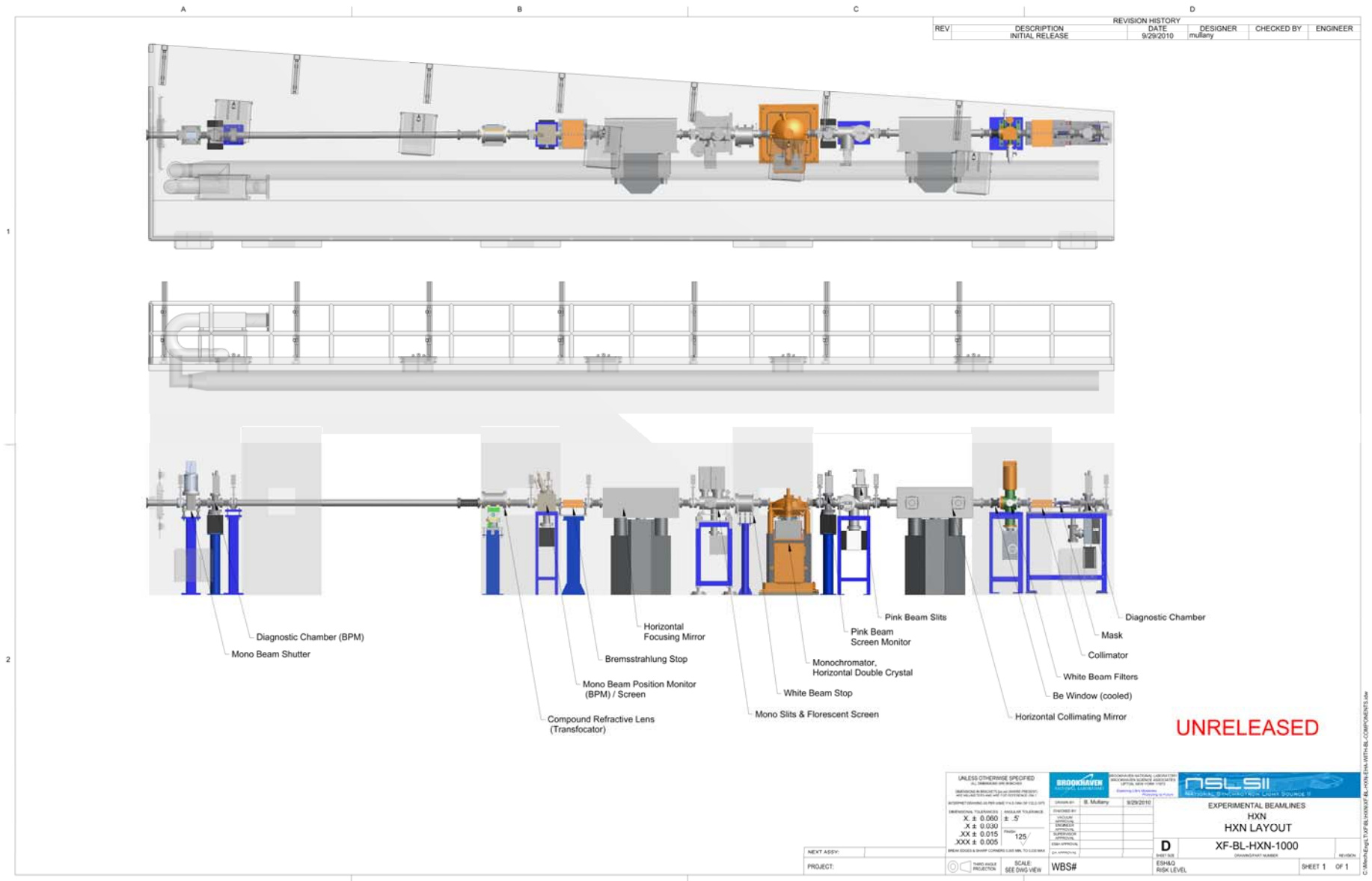

Figure A2.11: Beamline Layout – Experimental Station 3-ID-A

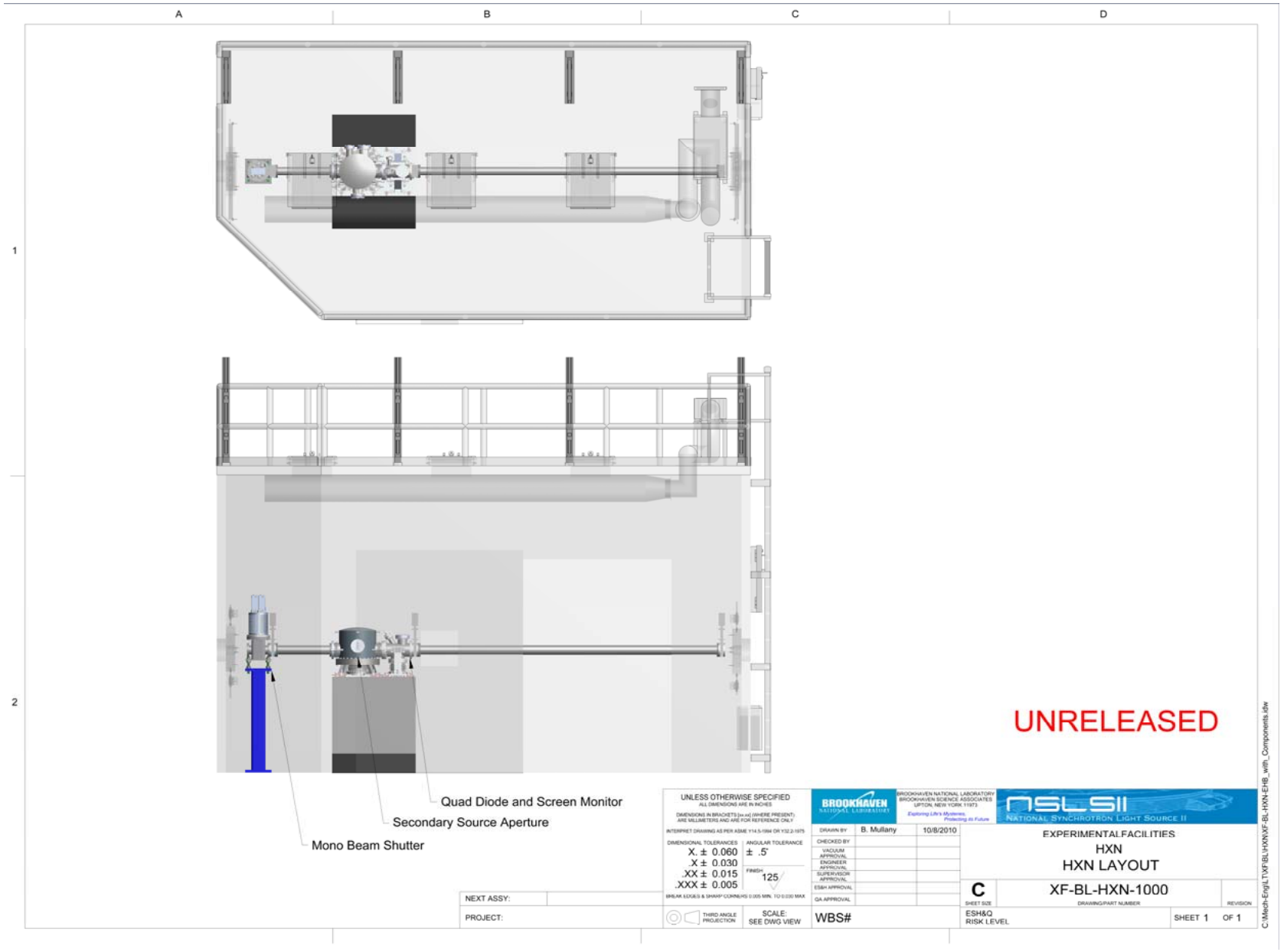

Figure A2.12: Beamline Layout – Experimental Station 3-ID-B

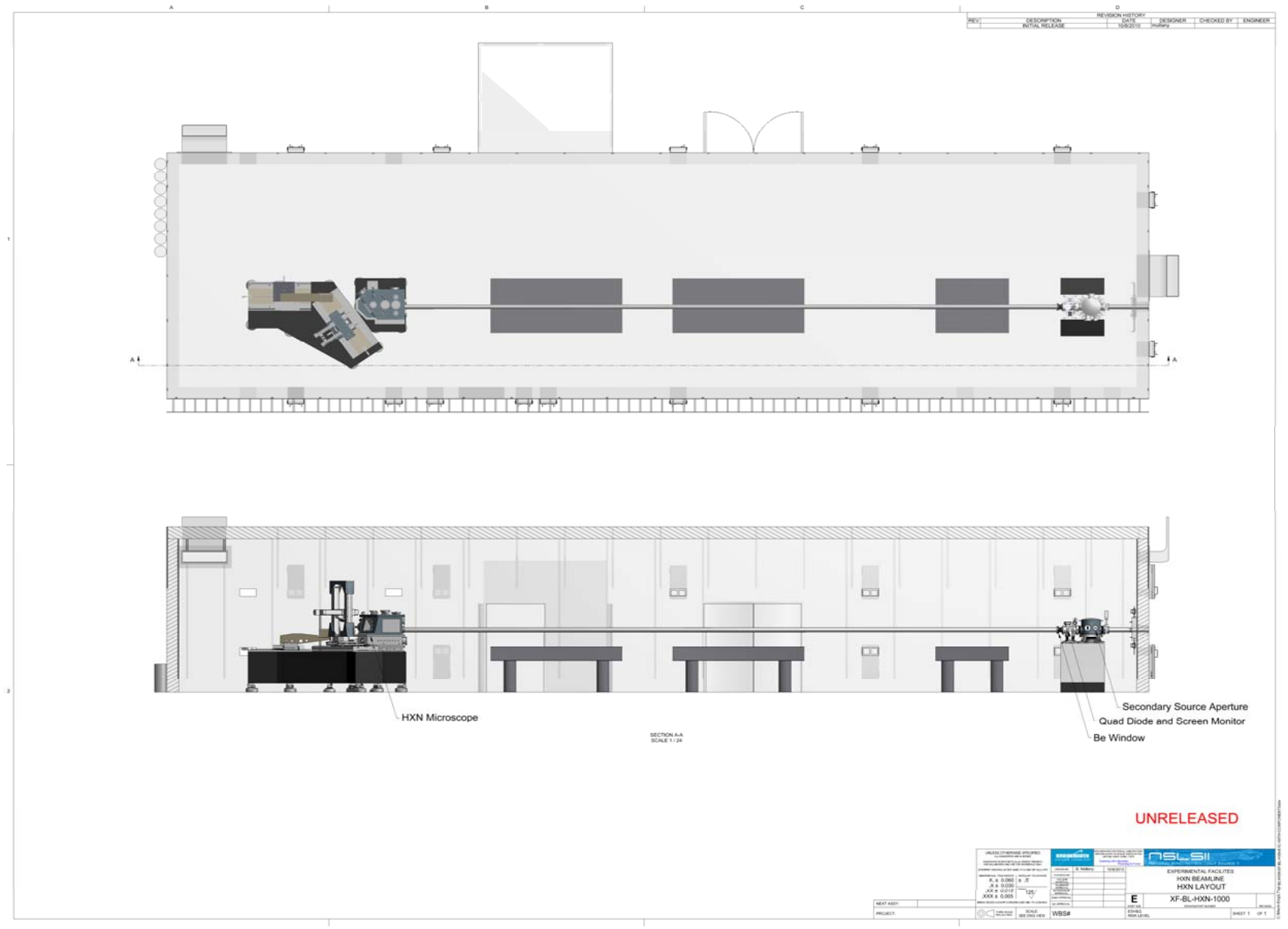

Figure A2.13: Beamline Layout – Experimental Station 3-ID-C

APPENDIX 3: MULTILAYER LAUE LENS (MLL)

A multilayer Laue lens (MLL), at first glance, can be considered as a 1D zone plate (ZP). It consists of many alternating layers (zones) made of two different materials (i.e., spacer and scatterer) so that there is a phase change π as x-rays pass through two adjacent zones. Positions for individual zones follow the zone plate law [A3.1], resulting in wide zones at the center and progressively thinner zones in the outer region. Such a structure diffracts an incoming plane wave into spherical waves converging to multiple foci of the lens. The diffraction-limit focus size scales with the outmost zone width. In order to achieve 1nm focusing for hard x-rays, a 1nm outmost zone with a substantially high aspect ratio (the ratio of thickness to zone width) up to 10^3-10^4 must be fabricated (see Figure A3.1a). This high aspect ratio is required for high efficiency. For a 2D ZP, fabrication with conventional lithography methods is quite difficult. Maximum aspect ratios of ~20 have been produced for high-resolution zone plates [A3.2]. In contrast, the 1D structure of a MLL is fabricated by a thin-film deposition technique such as sputtering deposition, which is capable of depositing nanometer-size zones with almost limitless aspect ratios. The technical feasibility of fabricating nanometer-size zones with extremely high aspect ratios is the fundamental driving force for developing MLL optics for hard x-ray nanofocusing. To date, 1D focusing of 16 nm [A3.3] and 2D focusing of 25 x 27 nm have been demonstrated experimentally [A3.4].

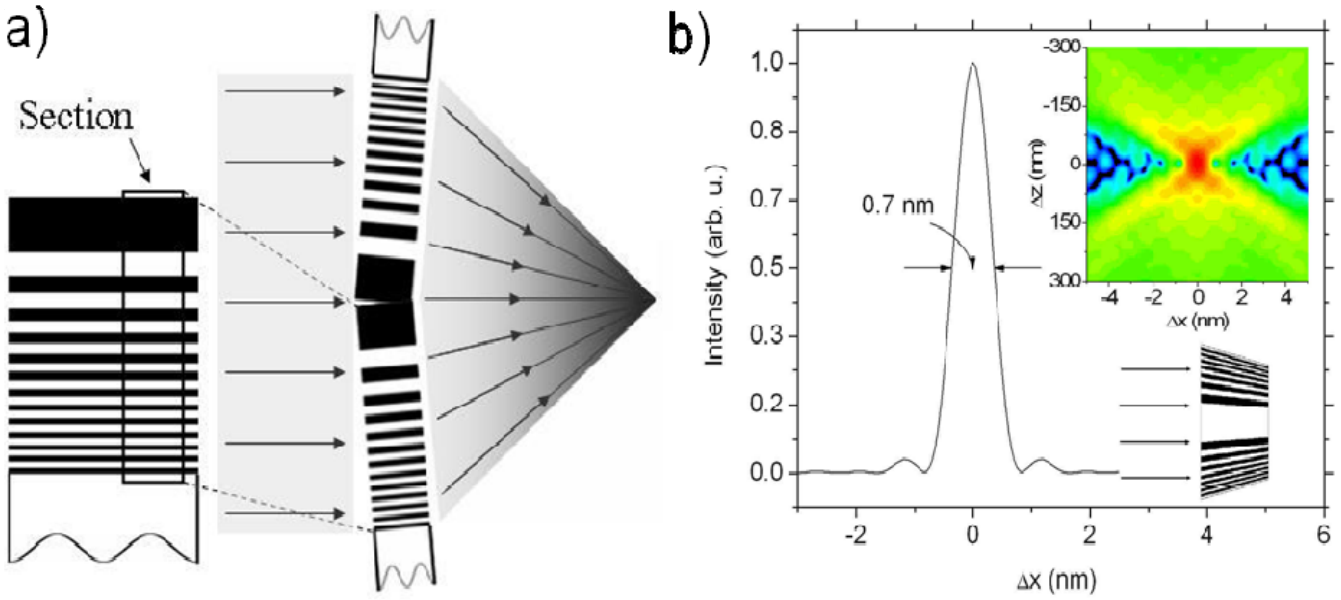

Figure A3.1: a) A schematic of a MLL and a pair of tilted half MLLs to satisfy the Bragg condition. b) (inset on bottom) The focus profile of a wedge MLL with 0.8 nm outmost zone width. The inset on top is the intensity isophotes near the focus.

Due to the high aspect ratio required for efficient hard x-ray nanofocusing, MLLs are no longer optically "thin." That is, the dynamical diffraction effect has to be fully taken into account. The geometrical theory [A3.5], assuming "pencil x-rays inside a lens," is invalid. A full-wave dynamical diffraction theory is required to properly describe its focusing properties. Since in a local region the MLL structure is nearly periodic, the diffraction from a multilayer stack is akin to crystal diffraction in the Laue case. As a result, MLL performance is heavily dependent on the "Bragg" condition, where the resonant scattering occurs [A3.6]. We take advantage of the dynamical effect to improve the performance of a MLL. By tilting the MLL slightly with respect to the incident beam to satisfy the "local" Bragg condition, efficiency is greatly enhanced. Figure A3. 1 shows a pair of half MLLs tilted intentionally for this purpose. However, the diffraction effect has an adverse effect, too; it will limit the achievable NA (numerical aperture) of a MLL. Since the d-spacing (i.e., layer-spacing) of a MLL varies significantly, at a fixed tilting angle, the Bragg condition is satisfied over a small region. For those regions where the deviation from the Bragg condition is too large for resonant scattering, the diffraction intensity goes down to zero, reducing the

effective NA of the MLL. Based on dynamical models, a 5nm focus can be achieved using a pair of two tilted half-MLLs (as shown in Figure A3.1) and a 10nm focus can be achieved by a single tilted half-MLL [A3.7, A3.8].

Dynamical diffraction effects can be fully utilized with the observation that the Bragg condition can be fulfilled approximately everywhere if the individual zones are tilted progressively. Such arrangement leads to a wedged zone profile (inset of Figure A3.1b) and is called the wedged MLL (wMLL) [A3.8, A3.9]. Dynamical diffraction calculations have shown that wMLL can achieve 1-nm focusing with over 60% efficiency for hard x-rays. as shown in Figure A3.1b.

[A3.1] Janos Kirz, "Phase zone plates for x rays and the extreme UV," *J. Opt. Soc. Am*. **64** (3), 301-309 (1974).

[A3.2] Gung-Chian Yin, Yen-Fang Song, Mau-Tsu Tang, Fu-Rong Chen, Keng S. Liang, Frederick W. Duewer,Michael Feser, Wenbing Yun, and Han-Ping D. Shieh, "30 nm resolution x-ray imaging at 8 keV using third order diffraction of a zone plate lens objective in a transmission microscope," *Applied Physics Letters* **89** (22), 221122-221123 (2006).

[A3.3] H.C. Kang, H.F. Yan, R.P. Winarski, M.V. Holt, J. Maser, C.A. Liu, R. Conley, S. Vogt, A.T. Macrander, and G.B. Stephenson, "Focusing of hard x-rays to 16 nanometers with a multilayer Laue lens," *Applied Physics Letters* **92** (22), 221114 (2008).

[A3.4] Hanfei Yan, Volker Rose, Deming Shu, Enju Lima, Hyon Chol Kang, Ray Conley, Chian Liu, Nima Jahedi, Albert T. Macrander, G. Brian Stephenson, Rodney Porter, Martin Holt, Yong S. Chu, Ming Lu, and Jörg Maser, "Two Dimensional Hard X-ray Nanofocusing with Crossed Multilayer Laue Lenses," submitted.

[A3.5] Max Born and Emil Wolf, *Principles of optics*. (Cambridge University Press, Cambridge, 1999).

[A3.6] André Authier, *Dynamical Theory of X-ray Diffraction*. (Oxford University Press, Oxford, 2002).

[A3.7] H.C. Kang, J. Maser, G.B. Stephenson, C. Liu, R. Conley, A.T. Macrander, and S. Vogt, "Nanometer Linear Focusing of Hard X Rays by a Multilayer Laue Lens," *Physical Review Letters* **96** (12), 127401-127404 (2006).

[A3.8] H.F. Yan, J. Maser, A. Macrander, Q. Shen, S. Vogt, G.B. Stephenson, and H.C. Kang, "Takagi-Taupin description of x-ray dynamical diffraction from diffractive optics with large numerical aperture," *Physical Review B* **76** (11), 115438-115413 (2007).

[A3.9] R. Conley, C. Liu, J. Qian, C.M. Kewish, A.T. Macrander, H. Yan, H.C. Kang, J. Maser, and G.B. Stephenson, "Wedged multilayer Laue lens," *Review of Scientific Instruments* **79** (5), 053104 (2008).

APPENDIX 4: MLL FABRICATION CAPABILITIES

The NSLS-II project has started a significant R&D program for the development of next-generation MLL nanofocusing optics. To overcome the current limits in MLL growth (namely, total growth thickness, interfacial roughness, and layer placement), a custom linear deposition system shown in Figure A4.1 has been designed, procured, and commissioned. This state-of-the-art deposition system took 9 months of designing and 15 months of construction. This deposition system utilizes nine circular permanent-magnet sputtering cathodes that are arranged in a horizontal plane for side-growth on a vertically-oriented sample that is raster-scanned using a unique UHV linear translation system. All sensors and process accessories were selected for the highest available stability and accuracy. Integral to the machine is a high-precision linear motion platform that utilizes an in-vacuum linear servo motor mounted to a one-piece rail that has been aligned to less than ±1.5 μm of vertical trajectory error. In order to meet the eventual goal of 1nm focusing optics, a vertical sample trajectory error of less than 10 μm must be maintained for wedged MLL growth. The raster-scanning stage has been independently tested to maintain velocity stability to less than 0.0025% over 1 order of magnitude of velocity ranges. This is at least a factor of 10 improvement over the highest performance deposition systems currently in service[A4.1], and this high-precision stage combined with the target geometry, growth process, and overall system stability puts NSLS-II into the position of owning the best laboratory in the world for the fabrication of MLL optics.

MLLs are fabricated by deposition of thousands of layers, with materials of alternating density and sectioned to allow for side-illumination [A4.2]. Figure A4.2 shows an SEM micrograph of a MLL with a minimum layer spacing of ~2.8 nm. The initially targeted MLLs for the HXN beamline require more than 18,000 layers; achieving 1nm spatial resolution will require an approximate 10-fold increase in the number of layers. The challenges related to MLL growth are best split into two categories that can be converged later; these are 1) to grow very thick, flat (or tilted) MLLs to solve the challenges related to extremely thick multilayer growth, and 2) to grow wedged MLLs to solve the challenges related to growth of extreme film thickness gradients while maintaining adequate interface roughness [A4.3]. Successful fabrication of both subgroups of MLLs requires extremely precise knowledge of deposition rate decay due to target erosion. Furthermore, in order to grow thicker zones (layers), a better understanding of the growth dynamics for very thick layers will be needed.

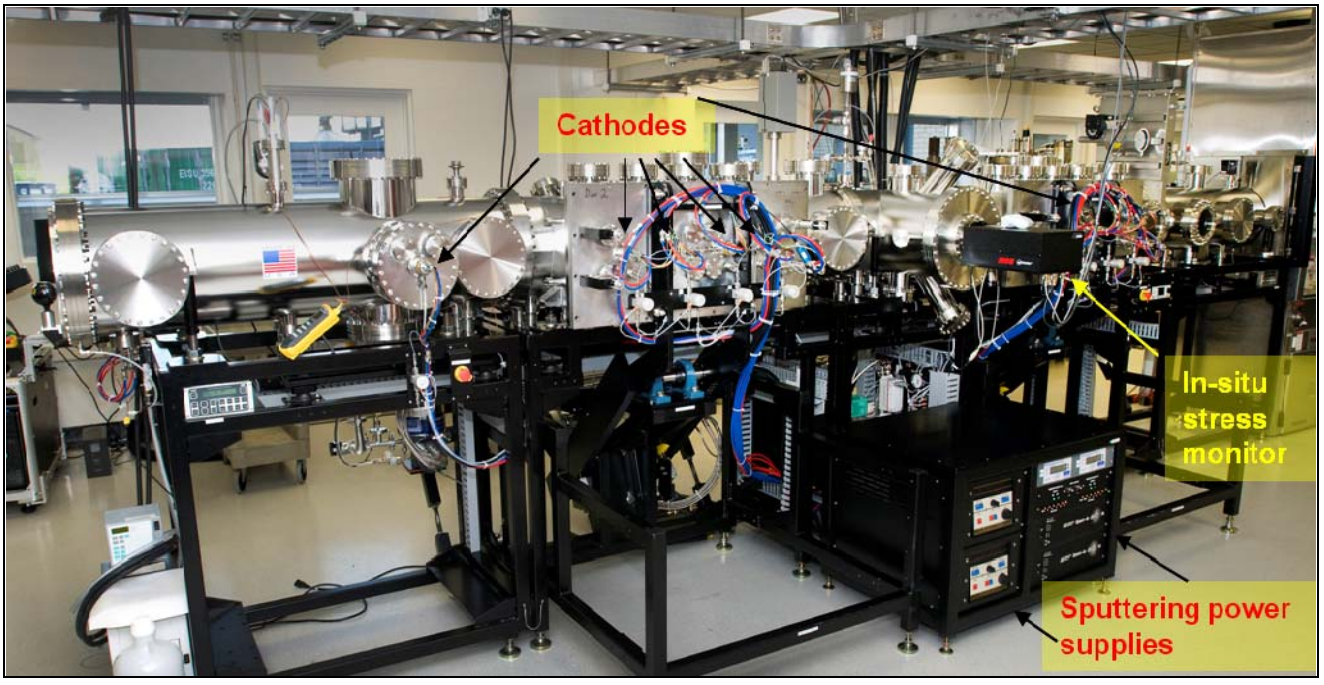

Figure A4.1: The NSL-II multilayer deposition system capable of fabricating flat and wedged MLLs.

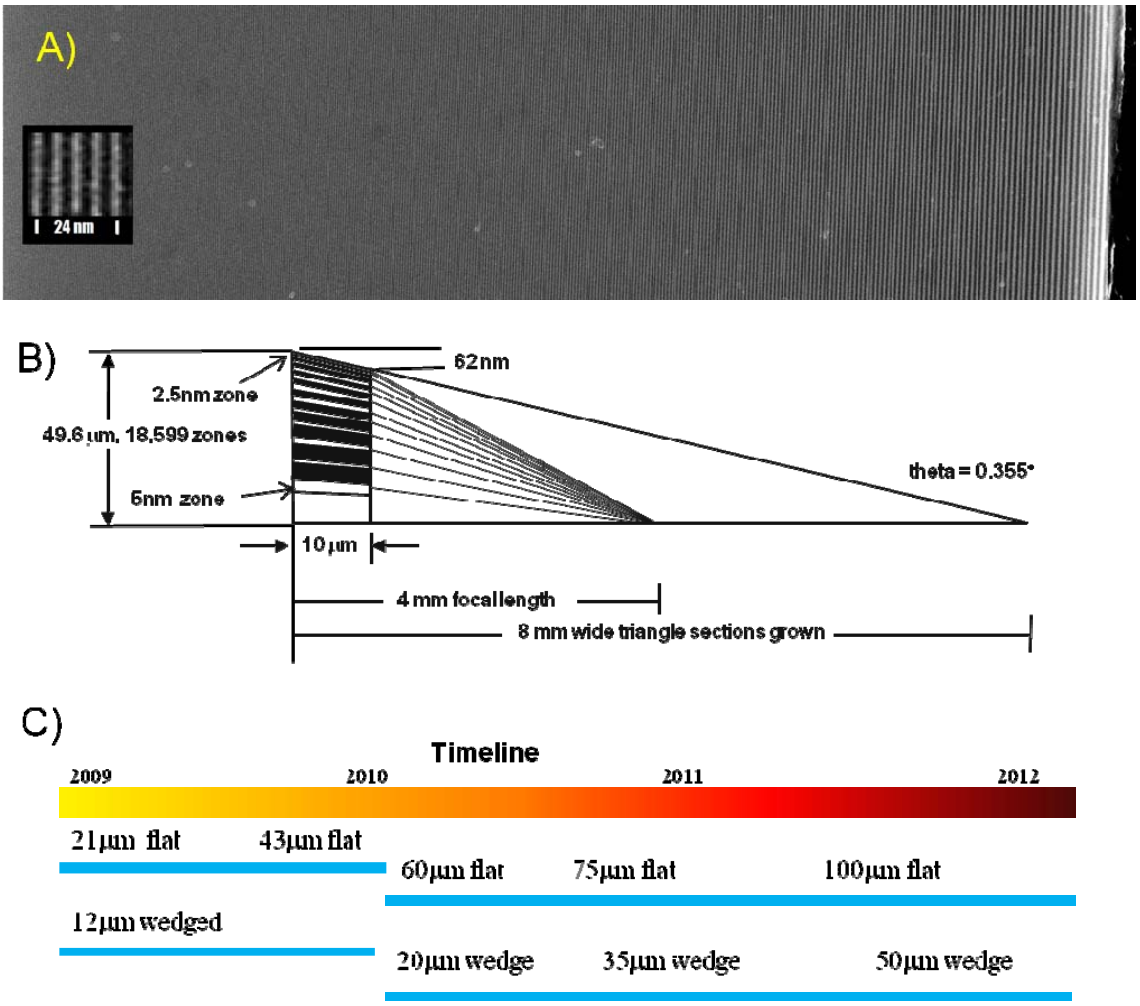

Figure A4.2: A) SEM micrograph of a deposited MLL with ~2.8nm minimum layer thickness. B) Schematic diagram for fabricating a wedged MLL. C) MLL development timeline showing present achievements and future goals. .

The HXN beamline team plans to use a wedged MLL with parameters outlined in Figure A4.2, based on parameters shown in Table 3.2.1. Fabrication of wedged MLLs requires growth of the entire wedged structure (a graded growth with a width of about 8 mm from 49.6 µm to 0 µm, as shown in Figure A4.2B) and subsequent sectioning of the optic at a location specific to the wavelength desired. The MLL R&D program has produced 1) periodic multilayers with a minimum layer thickness of 8.5Å with high contrast, and 2) a flat (for use in tilted geometry) half-structure MLL with 6,510 layers and 42.25µm thickness. The requirements for the fabrication of an optic that can realize 1nm x-ray focusing are challenging, but the NSLS-II program is well on the way to finding the answers to the material science questions in order to achieve this goal. Figure A4.2C outlines a timeline with present achievements and future goals.

[A4.1] "Multilayer Growth in the APS Rotary Deposition System," R. Conley, C. Liu, C.M. Kewish, A.T. Macrander, C. Morawe, *Proc. SPIE* 6704 (2007).

[A4.2] "Nanometer linear focusing of hard x-rays by a multilayer Laue lens," H.C. Kang, J. Maser, G.B. Stephenson, C. Liu, R. Conley, A.T. Macrander, S. Vogt, *Phys. Rev. Lett.* 96, pp. 127401 (2006).

[A4.3] "Wedged Multilayer Laue Lens," R. Conley, C. Liu, J. Qian, C. Kewish, A.T. Macrander, H. Yan, H.C. Kang, J. Maser, G.B. Stephenson, *Rev. Sci. Instrum*. 79 (2008) 053104.

APPENDIX 5: VIBRATION STABILITY CONSIDERATIONS

A key element in achieving the desired performance of the HXN beamline is the level of stability of the endstation floor that supports sensitive instruments. Stability or floor vibration at the HXN is influenced by a number of external factors such as the natural ground vibration that exists at the site, the cultural noise that reaches the site, and the particular location of the HXN station. The location criteria are further influenced by operations in nearby facilities, nearby vehicle traffic, NSLS-II operations in the form of sources of mechanical noise of systems and, finally, external conditions such as wind loads on the superstructures of both the HXN endstation and the overall NSLS-II complex of buildings.

To establish and quantify the stability and vibration criteria for the HXN endstation floor and supports, a series of integrated studies ranging from extensive field measurements to sophisticated ground vibration propagation simulations and interaction analyses were performed. These studies were correlated to Vibration Criteria (VC curves) guidelines [A5.1] that are widely used in vibration-sensitive facilities,. The interconnected studies were conducted in an effort to influence the final layout and design of the HXN endstation and also qualify as well as quantify the anticipated HXN floor vibration.

Described in more detail below are the desired stability goals for the HXN endstation, the optimization effort to establish the final HXN location relative to the NSLS-II ring including the contributing field studies, the evolution of the HXN endstation design influenced by the desire to reduce the vibration effects of natural and cultural sources, sensitivity studies and quantification of the effect of in-house operational sources on the HXN floor such as noise emanating from the nearby NSLS-II service buildings and reaching the HXN floor and, finally, the special structural interfaces adopted between the HXN endstation envelope and the ring structure as well as the nearest laboratory office building (LOB) where noise transmission and wind load effects are the driving parameters.

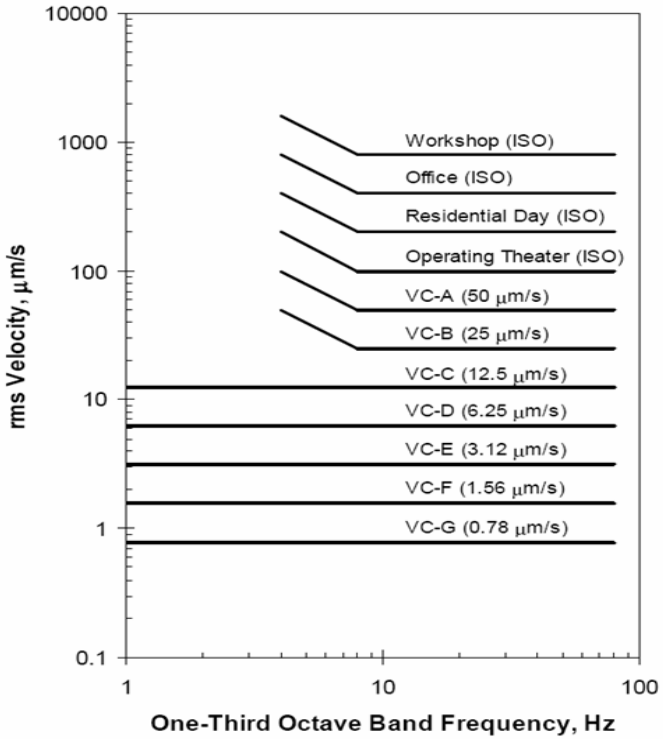

Figure A5.1.1: VC Criteria curves of RMS velocity in 1/3rd octave bands

A5.1 HXN stability criteria and goals

To ensure that 1nm resolution at the HXN endstation can be achieved, stringent stability criteria were adopted for the support floor where the sensitive instruments will rest. The desired vibration levels expressed through the criteria influence both the design of the overall HXN structure and its interfaces with the substrate and the ring. Specifically, the design incorporates structural features that both data and detailed analyses have shown will help mitigate cultural and natural vibration and ensure that established stability criteria are met. For the HXN floor the wide-band VC-F criteria expressed as RMS velocity values in one-third octave bands that translate to 1.56 μm/sec velocity were adopted as the HXN design driver, with the VC-G criteria of 0.78 μm/sec as a desired level for optimal performance. Figure A5.1.1 depicts the VC criteria curves that are being widely used in vibration-sensitive facilities. In addition to the wide-band criteria, similar narrow-band criteria used for the NSLS-II ring (expressed in terms of integrated floor displacement) are also desirable for the HXN floor. These criteria call for 25nm integrated floor displacement in the frequency range of 4-100 Hz.

A5.2 Stability-driven HXN design evolution

To enable the final HXN structural configuration (floor and envelope structure) to contribute toward the mitigation of ground vibration and effects from structure-to-structure interaction, a number of design features were considered during the evolutionary process of arriving at what now represents the final HXN layout. The primary feature around which the design was evolved was the "floating" instrument floor that is completely separated from the enveloping structure. Shown in Fig A5.2.1 is one of the considered designs, depicting the floating character of the isolated 1m-thick endstation floor as well as special vibration features such as a noise-attenuating concrete layer of CONCREDAMP™ [A5.2]), and isolating trenches.

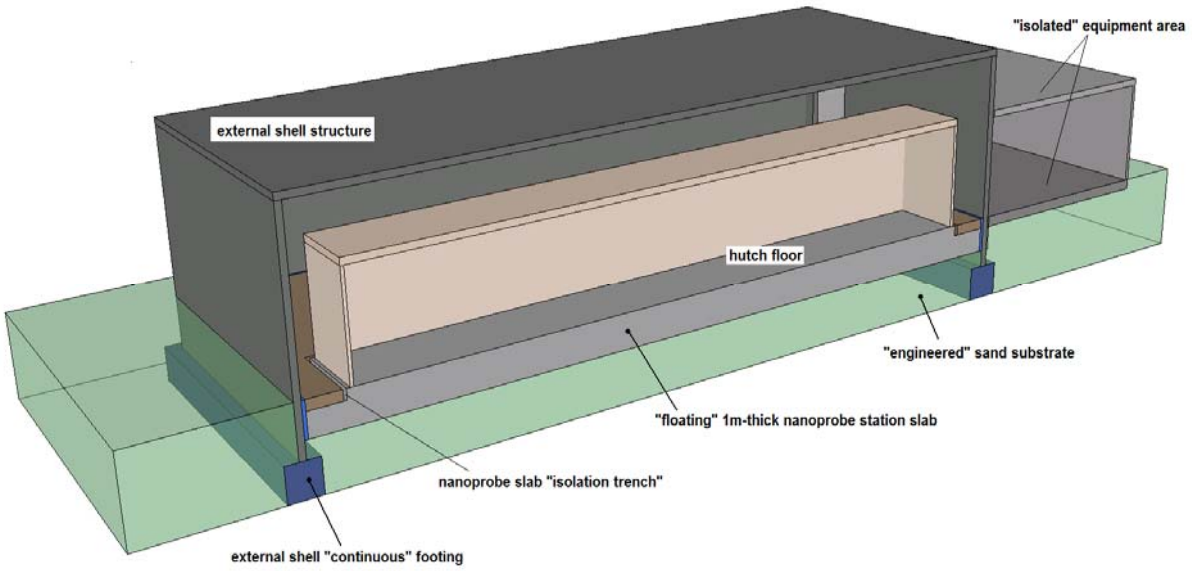

Figure A5.2.1: Early HXN design concept, depicting isolation-enhancing features for the support slab.

Following an extensive sensitivity study that incorporated both vibration mitigation (including coupling to the NSLS-II ring structures) and endstation functionality, a final concept design has been deduced which maintained both the "floating" nature of the endstation slab and its complete isolation from its envelope structure. Basic details of the final design concept implemented in the engineering design of the HXN endstation are shown in Figure A5.2.2.

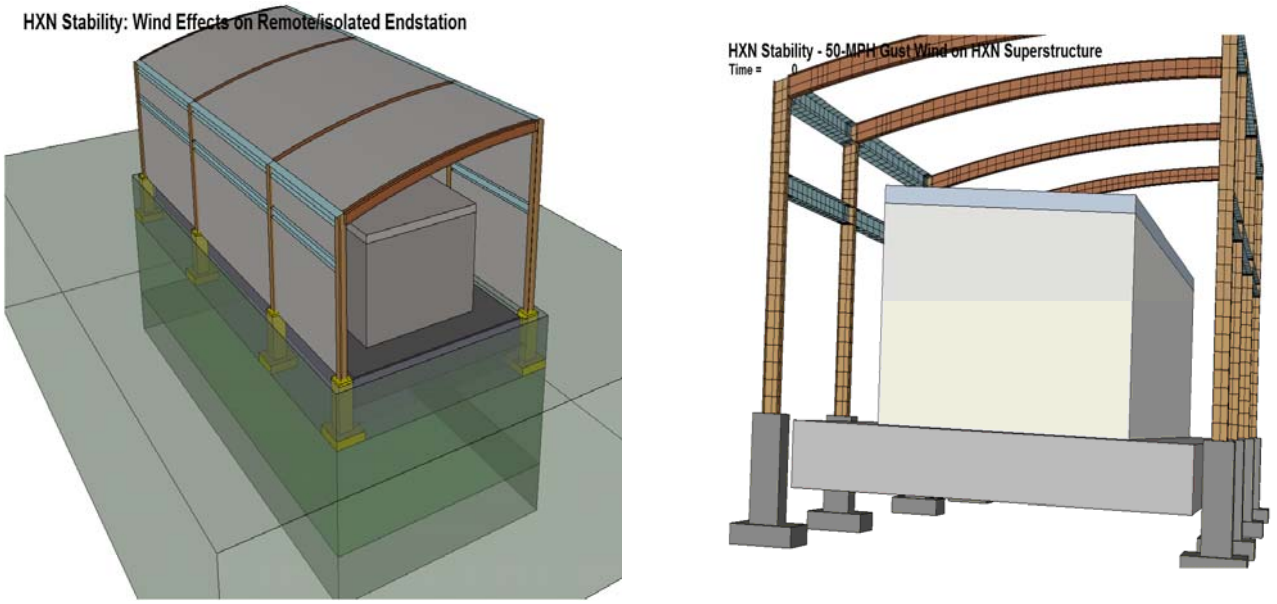

Figure A5.2.2: Adopted design concept of the HXN endstation depicting the "floating" character of the 1m-thick slab, the hutch structure layout, and the isolation from the envelope structure.

A5.3 HXN and NSLS-II ring – optimization of HXN location

One of the crucial steps towards the final design of the HXN endstation was the "optimization" of the location in reference to the NSLS-II ring structure. Factors influencing the HXN location were the "proximity" to the ring structure and the influence of the cultural noise associated with its operation, its proximity to the lab office building(s) and their noise sources and its orientation/distance from the site cultural noise sources such as local and highway traffic-borne ground vibration. The goal of the multi-faceted effort was to identify the most appropriate ring sector and long beamline option for the HXN endstation including its spatial location relative to the ring and LOB structures. While the natural ground vibration was anticipated to be quite uniform over the site, thus not influencing its location relative to the ring, the ground vibration induced by the heavy traffic in the vicinity and in the nearby highway was identified as a driving parameter. To address the issue and arrive at a location decision extensive field studies that addressed (a) the attenuation of the highway-borne ground vibration and (b) the effect of local heavy traffic were conducted. In evaluating the two options for the HXN location (depicted as NP_a and NP_b in Figure A5.3.1) it was concluded from the field studies that the highway effects were very similar and therefore the local traffic effects were a dominant factor. A special field test using a heavy truck as a vibration source was conducted leading to an assessment of ground vibration attenuation as well as the benchmarking of a state-of-the-art numerical model which in turn was used to optimize the HXN location.

In conjunction with the above, results of extensive studies, discussed in more detail in Section A5.4 and addressing the effects of ring and LOB operations, indicated that the NP_b location is optimal from vibration stability considerations and was adopted in the final design.

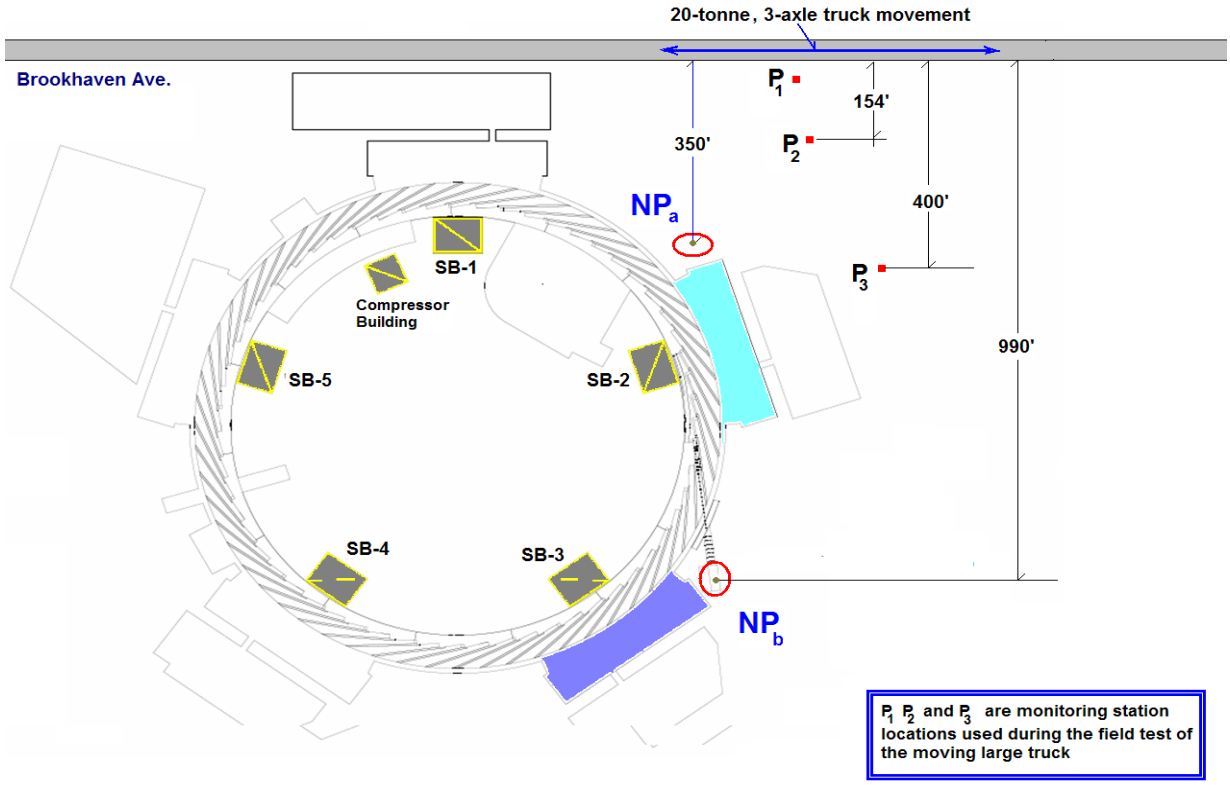

Figure A5.3.1A: Evaluated HXN locations relative to the NSLS-II ring and the local traffic sources including field test layout.

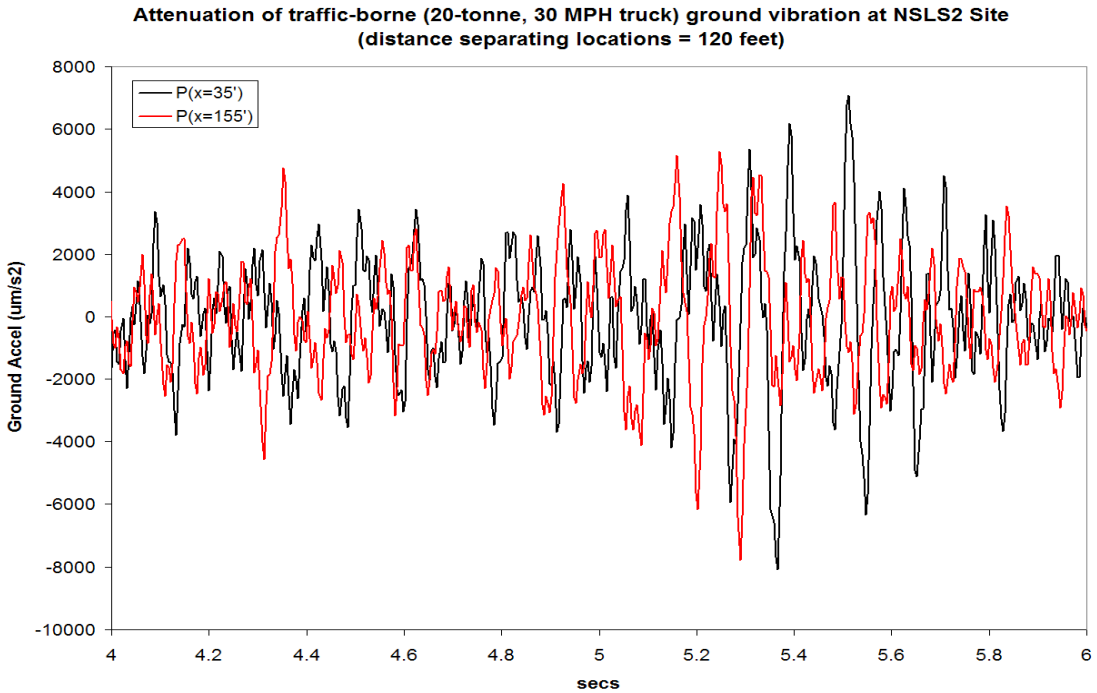

Figure A5.3.1B: Recorded ground motions during field tests of traffic-borne vibrations and site attenuation characteristics

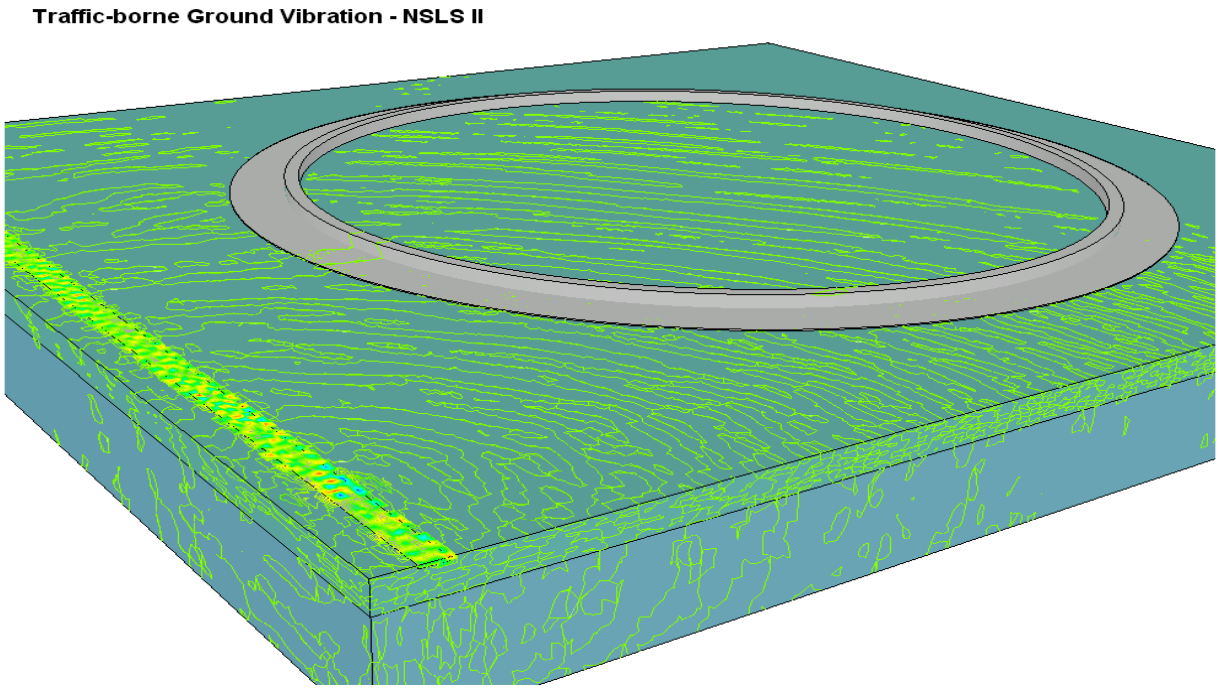

a

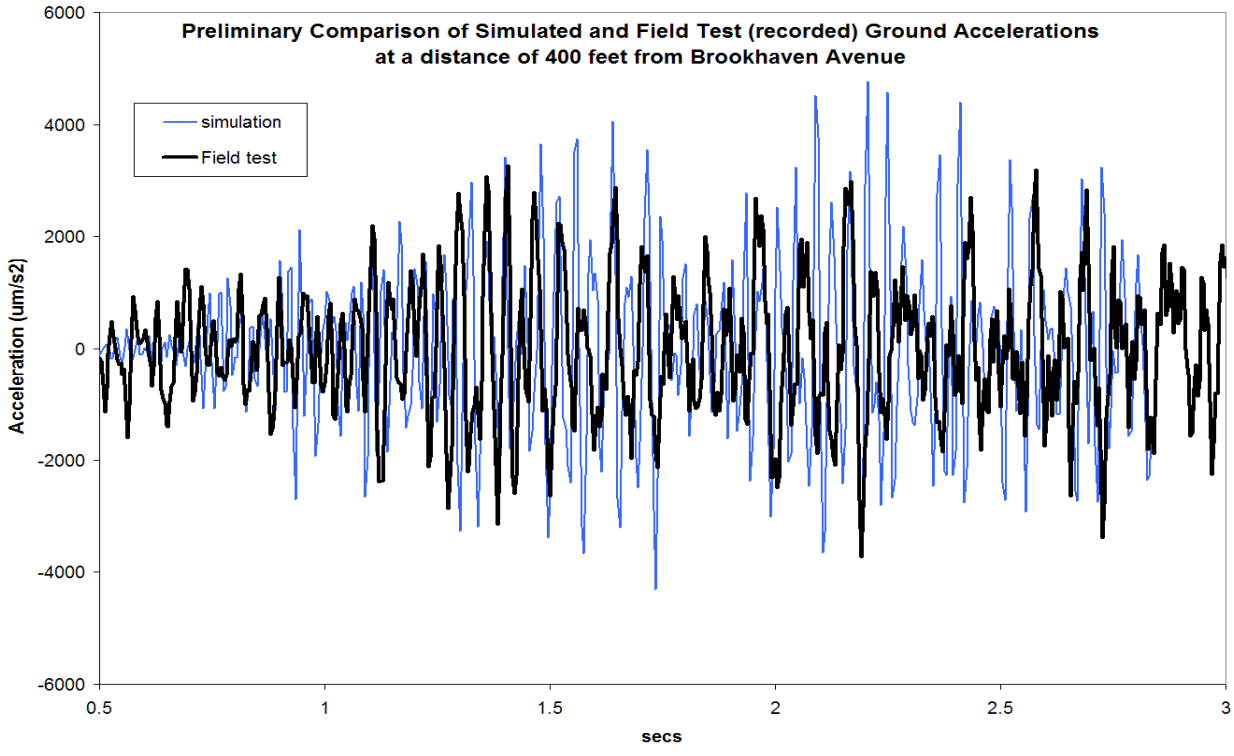

b

Figure A5.3.2: Ground motion effects. a) Simulation model used to benchmark field tests and subsequently quantify effects at the two HXN location options (NP_a and NP_b). b) Comparison of predicted and measured ground vibration acceleration for the test, assuring the validity of the numerical analysis as a tool for establishing the optimal HXN location.

A5.4 HXN and ring/LOB interface design considerations

Significant contributors to the design of the HXN are, in addition to its location relative to the ring, are the structural coupling/interfaces with the ring structure and the nearest LOB. Cultural noise generated by operating systems in support of the ring and housed in the service buildings and in the LOB will propagate towards the HXN and affect its stability. The types of structural interfaces or isolating features that are introduced in the final engineering design will greatly influence the observed effect on the HXN floor. In addition, external loads in the form of wind pressure on the superstructures will generate ground motions that may adversely affect the experimental activities on the HXN floor.

In an effort to quantify these effects and assist the engineering design of both the HXN endstation and of its coupling to the ring and LOB structures extensive studies that include field measurements and large-scale simulations were performed. In particular, through sensitivity studies the integration of the HXN superstructure to the LOB was evaluated and the effects to the HXN slab were quantified leading to the adoption of the final design interface.

Shown in Figure A5.4.1 are (a) the rendering of the HXN location and interface with the LOB and ring buildings, (b) a numerical representation of the coupling between the LOB and the HXN superstructure, (c) a representation of the cultural vibration stemming from service building operations and LOB air-handling activity, and (d) a detailed numerical description of the LOB/HXN coupling. The numerical representations that were utilized in both the sensitivity analyses and the quantification of the effects anticipated on the HXN floor are based on a sophisticated finite element model that has incorporated all important structural details leading to an exact representation of the final NSLS-II structure.

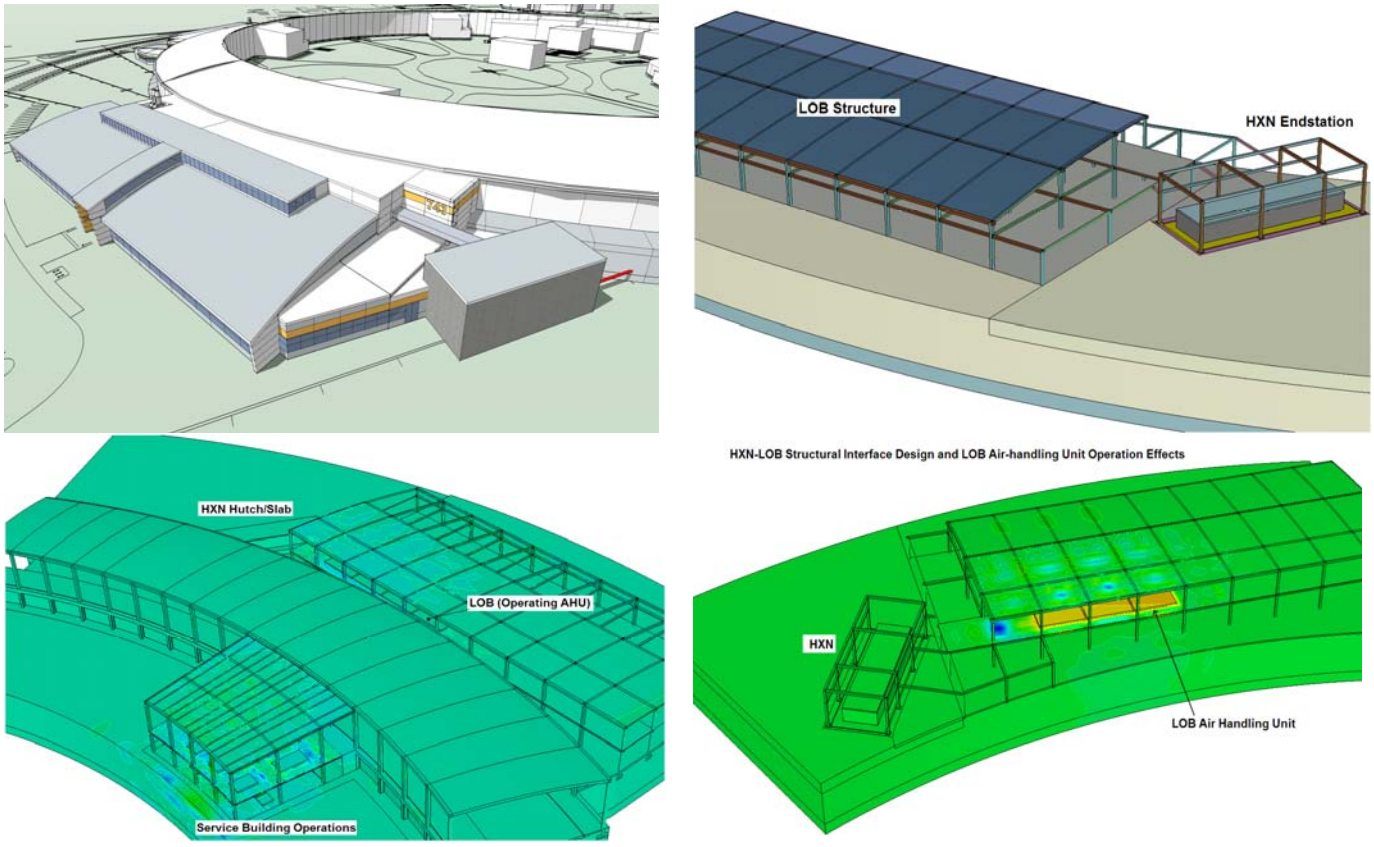

Figure A5.4.1: Numerical representations of the HXN structure and its interfaces with the ring and LOB buildings used to evaluate the effects of facility operations and wind loads on the HXN experimental floor.

In addressing the effect of the facility operations (both at the ring service buildings and the air-handling unit located on the mezzanine of the LOB and which represents the closest vibration source) field measurements of similar capacity units operating at other facilities were used for a more realistic representation of the HXN floor effects. The charts in Figure A5.4.2 depict HXN floor vibrations induced by the facility operations in a form that allows comparison with the desired stability criteria. In Figure A5.4.2a the resulting floor vibration is compared with the wide-band criteria expressed by the VC-F curve and in Figure A5.4.2b the integrated rms floor displacement indicates that for the complimentary narrow-band criteria, the induced floor vibration levels are well below 25 nm for the 4 to 100 Hz range.

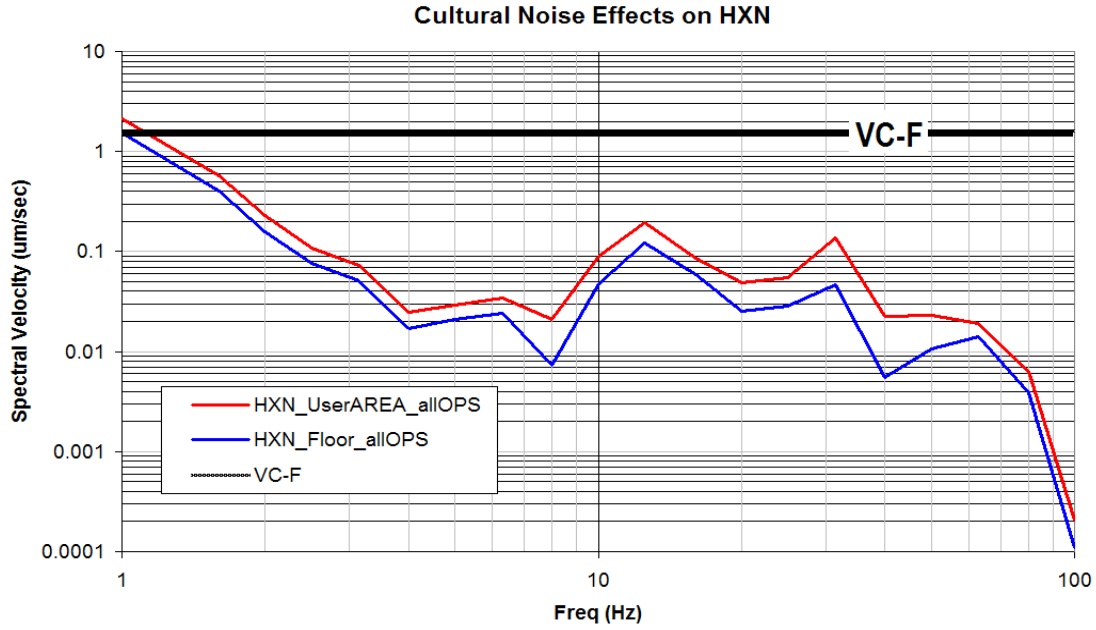

a

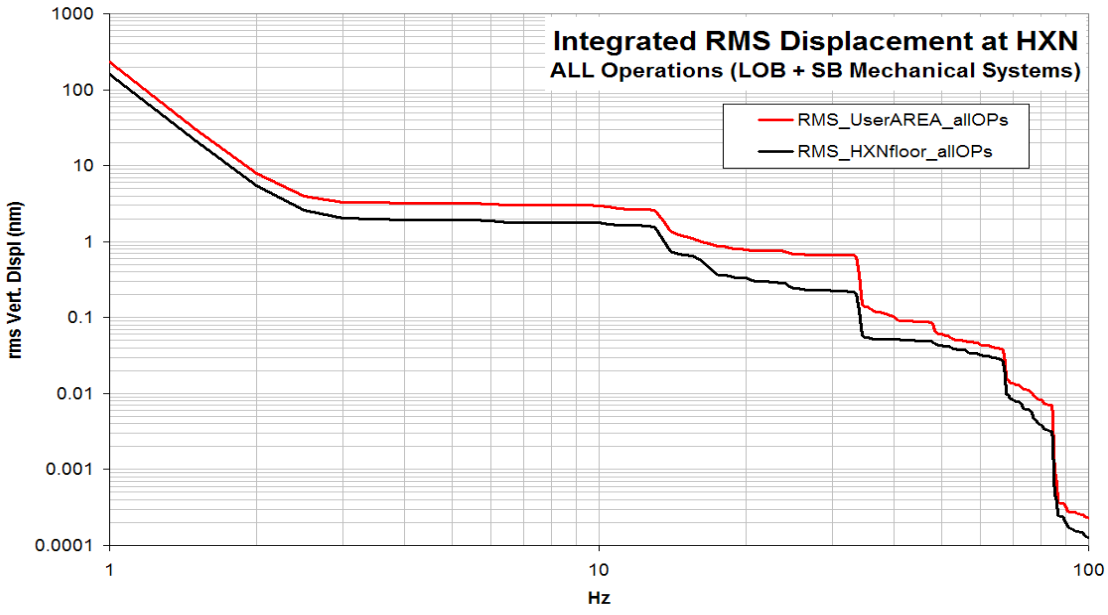

b

Figure A5.4.2: HXN floor vibration levels induced by NSLS-II ring service buildings and LOB operations. a) Floor velocity levels in 1/3d Octave bands compared to VC-F wide-band stability objective. b) Floor integrated vertical displacement compared to the narrow-band 25nm goal level.

Wind loads acting on the ring and LOB buildings and the HXN envelope structure will induce ground vibration emanating from the buried footings of the structures and propagate towards the HXN floor. While the substrate sand is attenuating in nature motion of large wavelengths due to the size of the superstructures will travel significant distances. Due to the size of the HXN floor, however, large wavelengths will be less detrimental since they are expected to cover the entire floor slab. To quantify the potential impact wind load intensities will have on the HXN floor and assess the performance of both the structural interfaces between the HXN and the ring and LOB buildings and of the isolating features an array of large-scale analyses were performed. The studies focused on gust winds of very short duration (~1 sec) with intensities up to 50 mph as a reasonable threshold for experimental activities on the HXN floor. It should be noted that the actual structures are designed to withstand 120 mph winds driven by the Category 2 class of the NSLS-II structures. Important consideration in these studies, which in turn influenced the decision on structurally coupling the HXN envelope structure to the LOB, was the effect of the physical connection between the two buildings (see Figure A5.4.1).

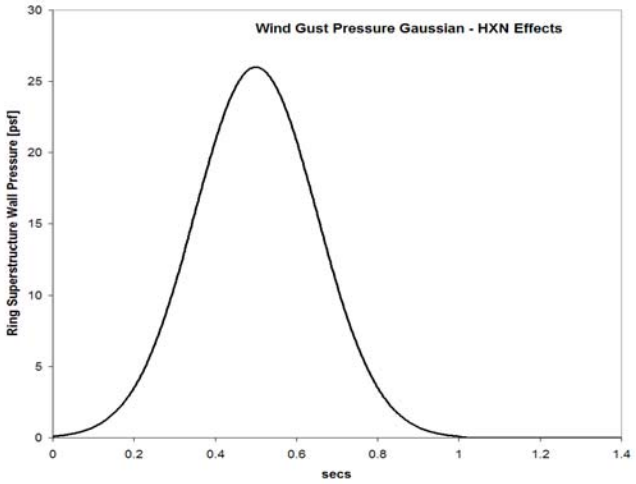

Figure A5.4.3: Wind load Gaussian pressure transient

Figure A5.4.3 depicts the wind transient duration and shape applied in the form of pressure on the shell surfaces of the structures including their roofs and according to ASCE criteria. In Figure A5.4.4, the numerical representation of the structures used to evaluate the effect on the HXN floor along with the application of the wind loads are shown.

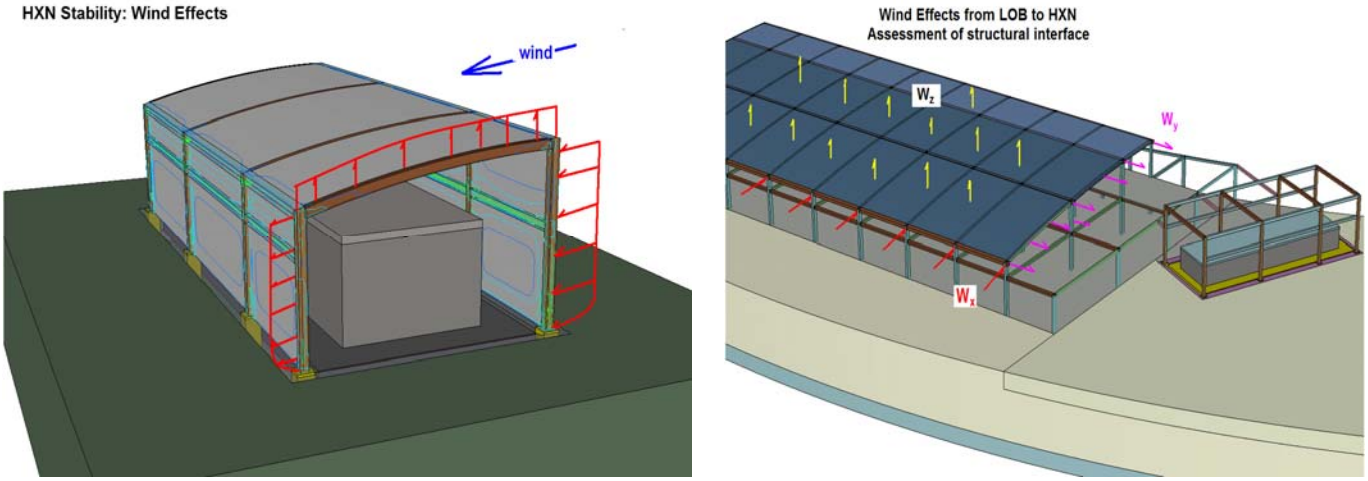

Figure A5.4.4: Numerical models utilized to quantify wind effects on the HXN floor. This figure shows the numerical representation of the structures used to evaluate the effect on the HXN floor along with the application of the wind loads.

Figure A5.4.5 shows the quantification of the wind effects in terms of HXN floor velocity spectra and its comparison with the desired stability criteria. While the simulations show that the desired VC-F criteria may be exceeded during a rare event of an intense, short-duration wind gust acting on the surrounding superstructures, this is of no consequence to the operation of the HXN since exceedance is only observed at very low frequencies where the induced ground motion wavelengths are large. Under such rare conditions which will last a very short time (~2 secs), the HXN slab will follow the induced wave in a coherent fashion and with uniform displacements throughout and thus leading to no experiment disruption. Based on the results of the extensive wind-effect studies on the HXN it is assessed that the adopted HXN design will meet the desired stability goals.

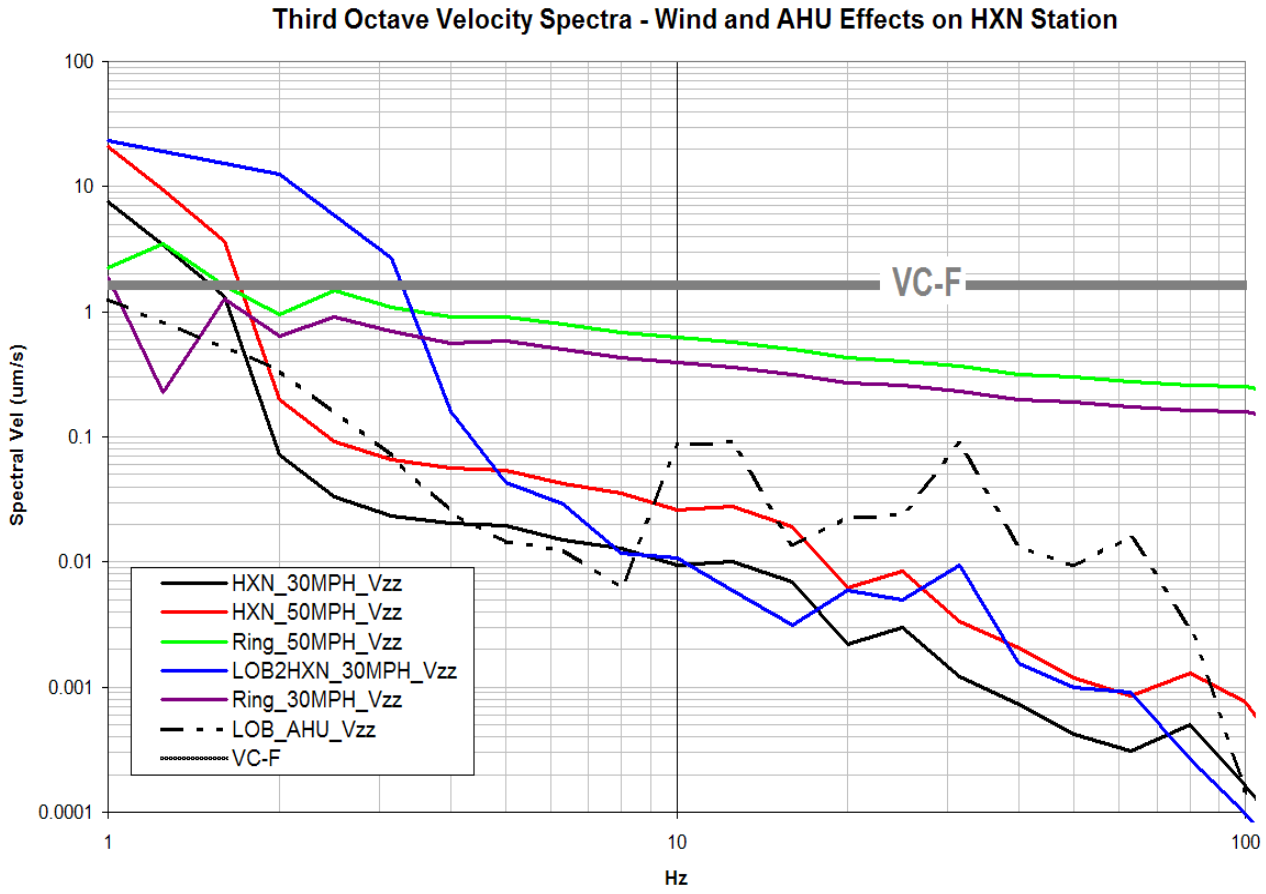

Figure A5.4.5: HXN floor velocity spectra induced by wind loads on the various structures in the vicinity of the endstation and comparison with the VC-F criteria representing the design goal. As noted in the figure, the VC-F criteria are exceeded at low frequencies due to large wavelengths generated by the swaying of the large structures. The impact, however, on the HXN performance is minimal due to the fact that the entire floor slab is experiencing the same and strongly coherent movement.

[A5.1] Gordon, C.G., "Generic criteria for vibration-sensitive equipment," *Proceedings of SPIE Conference on Vibration Control and Metrology*, pp. 71-85, San Jose, CA (November 1991).
[A5.2] CONCREDAMP™ Concrete Vibration Dampener, http://www.concredamp.com.

APPENDIX 6: PARTIALLY-COHERENT WAVEFRONT PROPAGATION CALCULATIONS FOR THE HARD X-RAY NANOPROBE BEAMLINE

Over the past decade, many novel experimental techniques relying on x-ray coherence either for scattering or for imaging have emerged. Evidently, traditional beamline ray-tracing analysis has to be extended beyond geometrical optics -- to include accurate calculation of wave-optical characteristics of SR sources, and to allow for simulation of full- and partially-coherent SR wavefront propagation through optical elements of a beamline. After the first wave-optics computer codes for simulation of transversely-coherent SR wavefront propagation became available [A6.1-A6.3], they have quickly found a number of important practical applications, such as optimization of infrared beamlines in 3rd generation SR sources [A6.4,A6.5], simulation and analysis of free-electron laser wavefronts [A6.7, A6.8], and electron beam diagnostics [A6.3, A6.9, A6.10]. In most of these applications however, fully transversely coherent wavefronts were treated. First, we numerically illustrate the basic properties of partially-coherent x-ray range UR, paying special attention to distinctions from van Cittert-Zernike theorem and Gaussian model [A6.11, A6.12], Second, we extend and complement the partially-coherent UR wavefront calculations and analysis that were performed recently [A6.13] for the conceptual design parameters of the NSLS-II Hard X-ray Nanoprobe (HXN) beamline. Our calculations are based on the general method of summing-up intensities after numerical propagation of frequency-domain UR electric field emitted by individual (macro-) electrons, distributed in 6D phase space of the electron beam. The calculations were performed using SRW code [A6.2, A6.3].

It is important to point out that the optical parameters used in the simulation are close to but not identical to the design values for the HXN beamline. In addition, the energy bandpass of the monochromator was not considered in the simulation.

A6.1. Apparent Divergences and "Source Sizes" of Partially-Coherent Undulator Radiation Beam

For a large number of beamline design tasks, accurate values of horizontal and vertical angular divergences and "source sizes" of UR beam are necessary. These values have to include contributions of the divergences and diffraction-limited source sizes of single-electron UR, as well as divergences and sizes of finite-emittance electron beam. Even though approximate values of the divergences and source sizes can be obtained from analytical formulas [6.14], more accurate values may require numerical partially-coherent wavefront propagation calculations. An example of such calculations, performed for two different photon energy values at the 5th harmonic of radiation from a U20 in-vacuum undulator of NSLS-II, is presented in Figure A6.1. One value is the on-axis resonant photon energy of the single-electron emission (10.009 keV), and the other is a bit lower, closer to the peak of the UR spectral flux collected through a 100 μrad (h) x 50 μrad (v) angular aperture (Figure A6.1A). The intensity distributions at these two photon energies are calculated for a 30 m observation distance from the undulator (Figures A6.1B and C), and for the image plane of a 1:1 focusing scheme, consisting of one ideal lens (Figures A6.1D and E). For these partially-coherent wavefront propagation calculations, the "day 1" horizontal and vertical emittances and energy spread of the electron beam (0.9 nm, 8 pm and 8.9×10^{-4} respectively), and nominal horizontal and vertical beta-function values of a NSLS-II low-beta straight section (2.02 m and 1.06 m respectively) were used. The intensity distributions at 30 m were used for characterizing the horizontal and vertical apparent angular divergences, and the distributions in the 1:1 image plane (i.e. at a "waist") -- for characterizing the apparent source sizes. The obtained FWHM values of the horizontal and vertical divergences and source sizes are shown in Figures A6.1F through I.

In addition to the observation that the maximal UR flux from a finite-emittance electron beam collected through a finite aperture doesn't correspond to the on-axis resonant photon energy of single-electron UR, we also note that in the vertical plane, the multi-electron UR intensity distributions both at a distance from the undulator (Figures A6.1B, C, and G), and in the 1:1 image plane (Figures A6.1D, E, and I) differ from Gaussian, especially for photon energies not equal to the on-axis resonant energy of a single-electron UR harmonic.

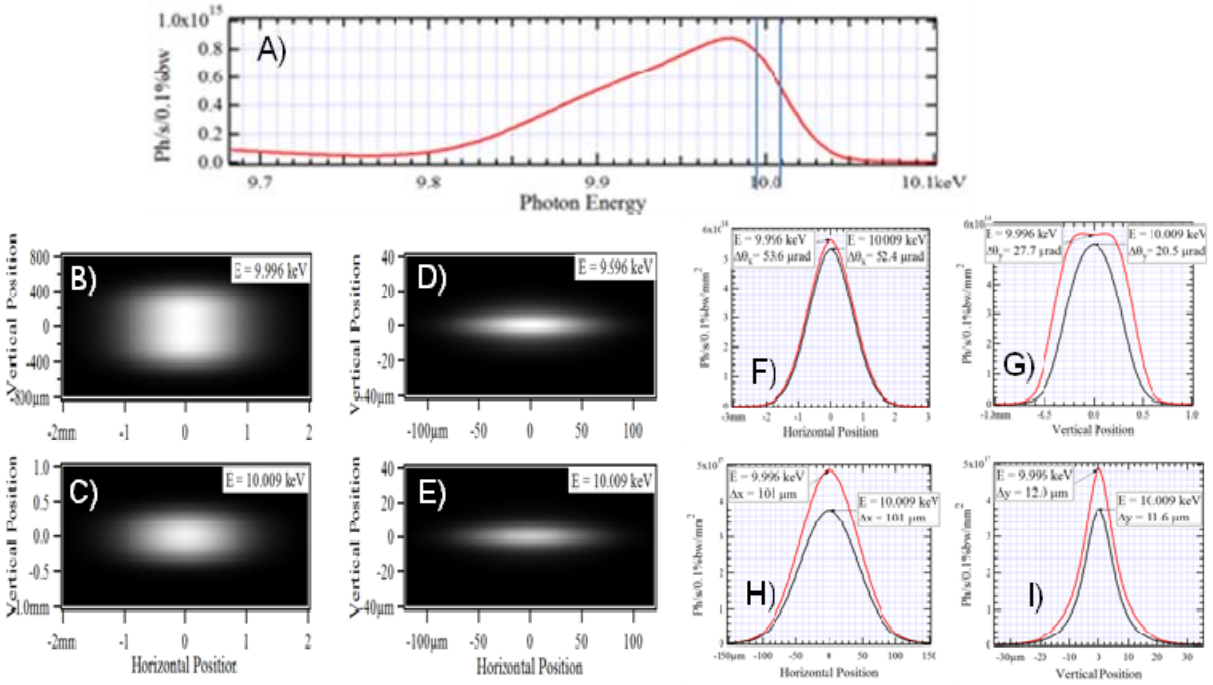

Figure A6.1: Spectral intensity distributions of radiation from a U20 undulator tuned to have the 5th harmonic at ~10 keV: A) spectral flux collected through 100 μrad (h) x 50 μrad (v) angular aperture; B, C) intensity distributions at 30 m from the undulator at 9.996 keV photon energy (shown by left line in A) and at 10.009 keV photon energy (shown by right line in A); D, E) intensity distributions in the 1:1 image plane; F, H) horizontal cuts of intensity distributions at 30 m from the undulator (F) and in the 1:1 image plane (H); G, I) vertical cuts of intensity distributions at 30 m from the undulator (G) and in the 1:1 image plane (I).

It can be useful to estimate apparent "phase-space volume" occupied by this partially-coherent UR beam and to compare it to the well-known values for the fully-coherent Gaussian beam at the same wavelength ($\lambda/4\pi$). Such comparisons, performed both for RMS ($\sigma_{ph}\sigma'_{ph}$) and FWHM ($\Delta_{ph}\Delta'_{ph}$) values of the corresponding intensity distributions, are presented in table 1. In the second column of table 1, ratios of the horizontal and vertical electron beam emittance (ε_e) to the phase-space volume of a fully-coherent Gaussian beam at ~10 keV photon energy are given. We see that in the horizontal plane, the phase-space volume of the resulting photon beam is dominated by the volume occupied by the electron beam. On the other hand, in the vertical plane, the electron beam emittance is small, and the "excessive" phase-space volume of the resulting photon beam (compared to that of the coherent Gaussian beam), is explained by deviation of the single-electron UR distribution from Gaussian, and by contribution of the electron beam energy spread to the UR angular divergence and the source size. From the phase-space volumes presented in Table A6.1 and the spectral flux shown in Figure A6.1A, one can estimate apparent brightness and "coherent flux" of the partially-coherent UR source. For the resonant photon energy (10.009 keV), the estimated apparent brightness is ~2.9 x 10^{20} ph/s/.1%bw/mrad^2/mm^2 and coherent flux ~1.1 x 10^{12} ph/s/.1%bw; for the considered "red-shifted" photon energy (9.996 keV) the corresponding values are ~3.3 ph/s/.1%bw/mrad^2/mm^2 and ~1.3 x 10^{12} ph/s/.1%bw.

Table A6.1: Comparison of the apparent phase-space volume occupied by partially-coherent UR beam at ~10 keV photon energy (at 5th undulator harmonic) to that of fully-coherent Gaussian beam, for the case of 0.9 nm (8 pm) horizontal (vertical) emittance and 8.9x10^{-4} relative energy spread of 3 GeV electron beam. * In terms of harmonic number (n = 5), number of undulator periods (N = 150) and on-axis resonant wavelength of n-th harmonic ($\lambda_n \approx 1.2387$ Å), this off-resonance wavelength value is: $\lambda \approx (1+0.97/(nN))\,\lambda_n$ ** Because of slow convergence, the RMS values for the vertical plane were calculated for the portions of intensity distributions containing ~99% of total flux.

Phase-space volume ratios	$\varepsilon_e \cdot 4\pi/\lambda$	$\sigma_{ph}\sigma'_{ph} \cdot 4\pi/\lambda$		$\Delta_{ph}\Delta'_{ph} \cdot 4\pi/(2.35)^2/\lambda$	
		$\lambda = \lambda_n$	$\lambda \approx 1.0013\lambda_n$ *	$\lambda = \lambda_n$	$\lambda \approx 1.0013\lambda_n$ *
For horizontal plane	91.2	97.3	99.5	97.2	99.3
For vertical plane	0.81	~5.1**	~6.5**	4.4	6.1

A6.2. Performance Estimation of the Hard X-ray Microscopy Beamline

The conceptual optical scheme of the NSLS-II HXN beamline is presented in Figure A6.2. The beamline will be using radiation from a 3 m long 20 mm period in-vacuum undulator installed in a low-beta straight section of NSLS-II. The first optical element is a Horizontal Collimating Mirror (HCM) located at ~27.2 m from the (center of) the undulator. The HCM provides a nearly parallel x-ray beam on the horizontally-deflecting Monochromator (MONO). After the monochromator, the x-ray beam is focused by Horizontally-, and then Vertically-Focusing Mirrors (HFM and VFM) located at ~31.3 m and ~32.8 m from the undulator. The secondary source, i.e. anastigmatic waist in the horizontal and vertical planes, "improved" by a rectangular Secondary Source Aperture (SSA), which can be located either at ~62-65 m or at ~92-94 m from the undulator by appropriate choices of the HFM and VFM focal lengths. The final nanofocusing optics -- zone plate or multilayer Laue lens -- are located at ~105-109 m from the undulator.

The results of partially-coherent wavefront propagation calculations performed for two cases are presented in Figure A6.3. In the first case, the SSA is located at 62 m from the undulator, and it's horizontal size is 50 μm (in the vertical direction the SSA is fully open), and a hypothetical nanofocusing optics with ~18.14 mm focal length and 150 μm aperture diameter is located at 105 m (the wavefront propagation simulation results for that case are shown in Figures A6.3A, B, C and D). In the second case, SSA is at 94 m, it's horizontal and vertical sizes are 12 μm and 16 μm respectively, with the nanofocusing optics located at 109 m (simulation results for that case are presented in Figures A6.3A, E, F and G). All beamline optics and nanofocusing optics were simulated by ideal perfectly-transmitting lenses. However, geometrical apertures of all optical elements were carefully respected. Such approximations were used purposely, in order to "observe" pure effects related to partial coherence of the source, and to trace losses on apertures. The undulator was assumed to provide a spectral peak of the 5th harmonic at ~10 keV photon energy, as this was the case in the calculations discussed in the previous section.

Figure A6.3A shows the UR intensity distribution at the HCM, with the mirror geometrical aperture indicated by a rectangle in the image plot (on the left) and by vertical lines in the intensity cuts graph (on the right). Figures A6.3B, C and D present the intensity distributions just before the SSA (which is indicated by lines and rectangle); Figures A6.3C and F give the intensity distributions in the plane of the nanofocusing optics, with the small circles in the image plots representing the aperture of these optics; and Figures A6.3D and G provide the intensity distributions "at the sample". The spectral flux, obtained using the approximations described above, is ~7.4×10^{14} ph/s/.1%bw after the HCM, ~2.9×10^{14} (~1.7×10^{13}) ph/s/.1%bw after the SSA, and ~2.0×10^{12} (~3.6×10^{12}) ph/s/.1%bw within the nanofocusing optics aperture in the first (second) simulation case.

We note that the sizes of intensity distributions "at the sample" (Figures A6.3D and G) are close to the diffraction limit: in the first simulation case, the horizontal FWHM spot size is ~22 nm (for a 50 μm horizontal SSA size), and the vertical FWHM size is ~16 nm; in the second case, the both the horizontal and vertical FWHM sizes are ~17 nm. The estimated FWHM diffraction-limited spot size for the considered nanofocusing optics is ~15 nm at a 10 keV photon energy.

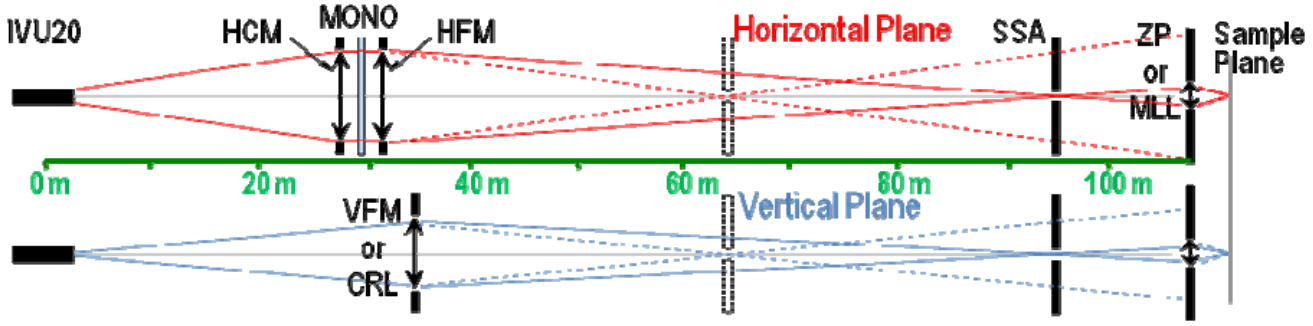

Figure A6.2: Conceptual optical scheme of NSLS-II Hard X-ray Nanoprobe beamline. X-ray beam travels from left to right in this figure

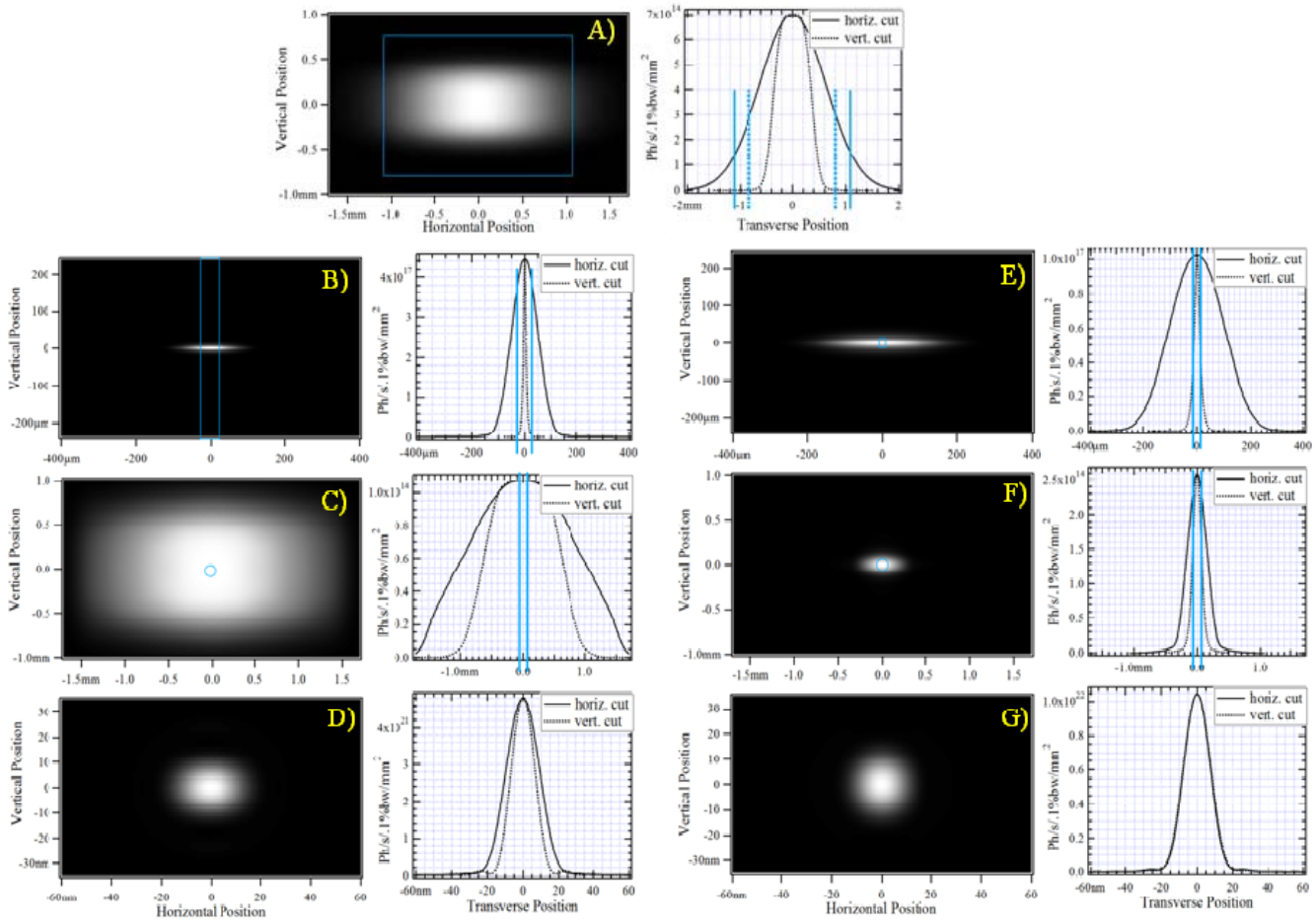

Figure A6.3: Intensity distribution image plots (on the left) and horizontal and vertical intensity cuts (on the right), at different beamline locations: A) at HCM; B) before SSA located at 62 m from the undulator; C) before nanofocusing optics in the case of 50 μm horizontal size of the SSA located at 62 m; D) at sample for the SSA location and size as in B and C; E) before SSA located at 94 m; F) before nanofocusing optics in the case of 12 μm horizontal and 16 μm vertical size of the SSA located at 94 m; G) at sample, for the SSA location and sizes as in E and F.

Since the diffraction-limited spot size at the sample can be reached only by a coherent wavefront, it is interesting to estimate degree of transverse coherence of the wavefront within the aperture of nanofocusing optics. Such estimations can be done, e.g. by simulating wavefront propagation through Young's 2-slit interference scheme, with the slits located at a longitudinal position of the nanofocusing optics. Figure A6.4A shows the visibility of fringes in a scheme with two vertical (horizontally separated) slits vs. the horizontal size of the SSA located at 94 m, in comparison with predictions of the Zernike theorem, assuming that a fully incoherent extended constant-brightness source is located at the SSA. We can notice only a small difference between the partially-coherent UR wavefront propagation simulation results and the Zernike theorem predictions, because the intensity distribution at the SSA in that case is almost constant in the horizontal direction within the horizontal SSA sizes used at these calculations (see Figure A6.3E), and because the photon beam coherence in the horizontal direction is relatively poor. The horizontal FWHM spot size obtained for nanofocusing optics simulated by an ideal lens with an 18.14 mm focal length and 150 μm aperture diameter, and the flux within the aperture of the nanofocusing optics are shown in Figure A6.4B, also as functions of the horizontal SSA size (at a 30 μm vertical SSA size). The visibility of fringes in the vertical plane, vertical spot size and flux within the nanofocusing optics aperture vs. vertical SSA size (at a 20 μm horizontal SSA size), are presented in Figures A6.4C and D. We see a significant deviation from the Zernike theorem in that case, which is explained by the small size and relatively high degree of coherence of the photon beam in the vertical direction at the SSA.

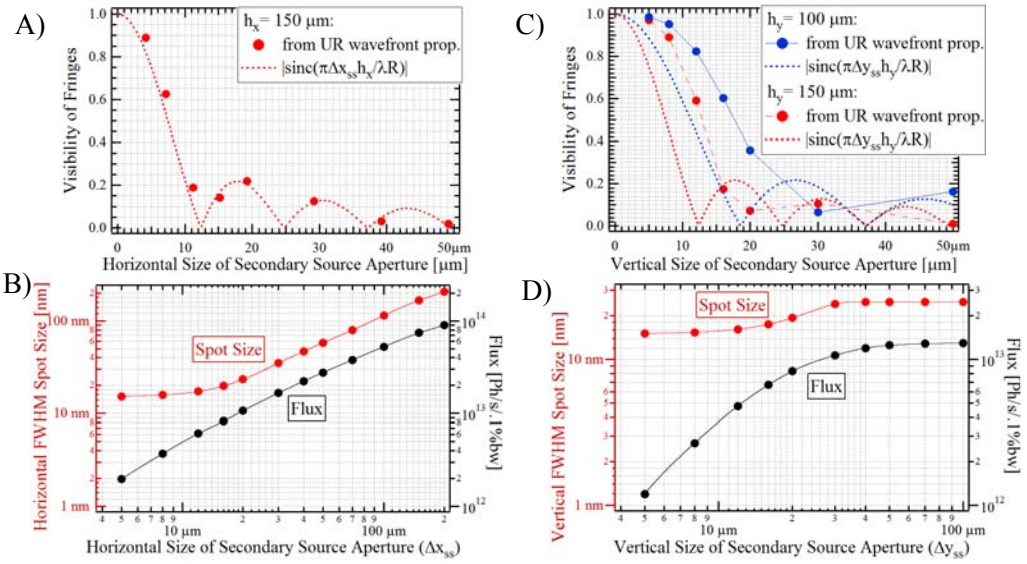

Figure A6.4: A) Visibility of fringes in interference patterns calculated for virtual Young's schemes with two vertical slits, separated by h_x = 150 μm horizontal distance, as a function of horizontal SSA size; B) horizontal FWHM spot size and flux within 150 μm aperture of the nanofocusing optics as a function of horizontal SSA size at 30 μm vertical SSA size; C) visibility of fringes in interference patterns of virtual Young's schemes with two horizontal slits separated by h_y = 100 μm and 150 μm vertical distance as a function of vertical SSA size; C) vertical FWHM spot size and flux vs vertical SSA size at a 20 μm horizontal SSA size (SSA is located 94 m, nanofocusing optics at 109 m in all cases).

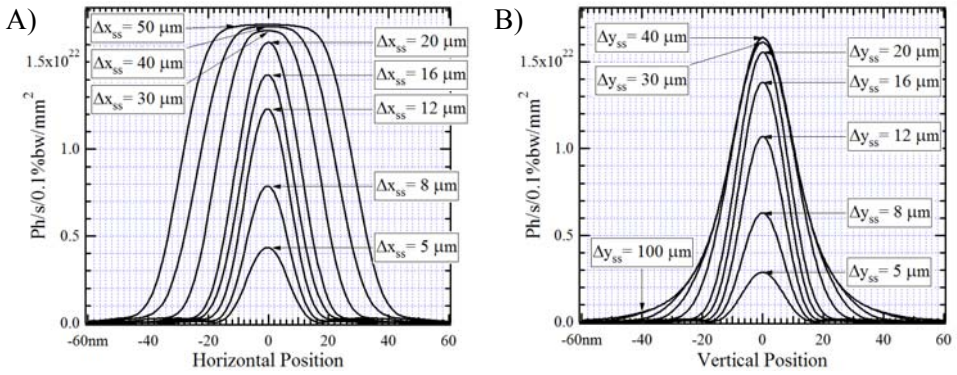

Figure A6.5: A) Horizontal and B) vertical cuts of intensity distributions at sample for different horizontal (Δx_{ss}) and vertical (Δy_{ss}) sizes of the SSA located at 94 m, assuming final focusing by ideal lenses with 18.14 mm focal length and 150 μm aperture diameter.

Finally, in Figure A6.5 we present horizontal (vertical) cuts of intensity distributions "at the sample" at different horizontal (vertical) SSA sizes. From these graphs, one can trace variations of the intensity distribution shapes in different regimes, from the diffraction limit to "high throughput". In the high throughput regime (e.g. at SSA sizes larger than ~30 μm), the horizontal and vertical intensity cuts differ in shape. We note that the use of the vertical SSA with ~20-30 μm size reduces the useful flux in the spot at the sample quite insignificantly (see Figure A6.4D), however, it substantially removes "tails" of the intensity distribution in the vertical direction.

Two important conclusions can be drawn from the simulation investigation. First, the observed visibility in the vertical direction (Figure A6.4C) is considerably larger than the prediction that the secondary source is incoherent. This means that a larger vertical aperture can be used to achieve the desired coherent illumination condition described in sections 2.4 and 2.10. Consequently, the flux estimates outlined in section 2.10 should be considered as "conservative estimates". Second, the focus size and the focus flux are not linear near the diffraction-limited

condition as shown in Figures A6.4B and D. Therefore, slight relaxation of the diffraction-limited condition results in significant gain in the focused flux.

[1] J.Bahrdt, *Applied Optics* **36** (19), p.4367 (1997).
[2] O.Chubar and P.Elleaume, Proc. EPAC-98, pp. 1177-1179.
[3] O.Chubar, P.Elleaume, S.Kuznetsov and A.Snigirev, Proc. SPIE Int. Soc. Opt. Eng. 4769, 145 (2002).
[4] P.Dumas, et. al., *Infrared Physics & Technology* **49**, 152-160 (2006).
[5] P.Roy et. al., *Infrared Physics & Technology* **49**, 139-146 (2006).
[6] O.Chubar et. al., Proc. SRI-2006, AIP Conf. Proc. vol. 879, pp.607-610.
[7] J. Bahrdt, *Phys. Rev. ST - Accel. Beams* **10** (2007) 060701.
[8] O.Chubar et. al., *Nucl. Instr. and Meth.* **A 593**, 30-34 (2008).
[9] O.Chubar et. al., Proc. DIPAC-2001, pp. 88-90.
[10] M.-A.Tordeux et. al., Proc. DIPAC-2007, pp. 180-182.
[11] R. Coisson, *Applied Optics* **34**, No. 5, 904-908 (1995).
[12] G. Geloni et. al., *Nucl. Instr. and Meth.* **A 588**, 3, 463 (2008).
[13] O.Chubar, Y.S. Chu, K.Kaznatcheev, H.Yan, Proc. of SRI-2009, AIP Conf. Proc. vol. 1234, pp.75-78 (2010).
[14] K.-J. Kim, AIP Conf. Proc. vol. 184, pp. 565-632 (1989).